



Swansea University
Prifysgol Abertawe

Corrosion Behaviour of Additively Manufactured High Entropy Alloys

Submitted to Swansea University in fulfilment of the requirements for the
Degree of Doctor of Philosophy

Matthew Ritchie (██████████)

Swansea University

2023

Abstract

Additive manufacturing (AM) is a modern manufacturing technique that facilitates the production of components layer by layer from CAD files, with more recent developments in the field leading to the ability to create these components from metal. Laser powder bed fusion (LPBF) is one of the many techniques used to manufacture metallic components and has drawn significant attention for its ability to create parts with high degrees of complexity, exceptional strength-to-weight ratios and internal structures. However, parts produced by AM are documented to suffer from build defects such as porosity, which can negatively affect not only its mechanical properties but its corrosion resistance, particularly its resistance to pitting corrosion. Whilst the mechanical properties of components produced through metal AM have been well documented since the technology's inception, there are significant knowledge gaps in understanding the corrosion behaviour of metals produced in this way. This thesis aims to expand upon the current understanding of this manufacturing method with a particular focus on its corrosion resistance.

High Entropy Alloys (HEAs) are a class of advanced materials that differ from conventional alloys in composition. Traditional alloys usually consist of one or two principal elements with smaller amounts of additional elements to impart specific properties. In contrast, HEAs are characterised by the presence of multiple principal elements in roughly equal proportions. HEAs' complex and disordered structure can result in unique mechanical, thermal, and magnetic properties. HEAs have shown promise in exhibiting high strength, hardness, and corrosion resistance, making them attractive for various engineering applications. Studies of HEAs have been increasing over recent years; however, significant knowledge gaps are still associated with this classification of materials, especially concerning their corrosion resistance. This lack of knowledge is intensified when discussing the properties of these alloys when manufactured by AM methods.

LPBF was used to produce parts in 316L with process induced porosity by manipulating the process parameters to investigate the effect density has on the corrosion resistance of AM parts. The corrosion resistance of these parts were compared to their wrought counterpart using potentiodynamic polarisation. It was observed that increasing the porosity in the AM parts resulted in poorer corrosion resistance, both by weaker performance across key metrics and a greater degree of unreliability. It was also found that the AM parts proved to have a greater corrosion resistance than the wrought material. However, the decreased consistency in this resistance is often cited as a barrier these components must overcome to supplant conventionally manufactured components.

316L was also produced through induction casting as well as a schedule more representative of industry that consisted of a solution anneal at 1080 °C followed by water quenching followed by a cold rolling reduction by 70 %, and a final anneal at 900 °C. The microstructures and corrosion resistance of these were investigated using SEM-EDS, XRD and potentiodynamic polarisation, and whilst the corrosion resistance of the cold rolled sample had increased, it was less than expected due to the formation of detrimental chromium carbides.

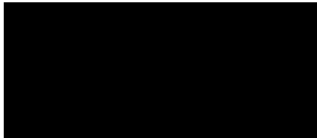
A Swansea University developed AlCrFeMnNi HEA was put through the same 3 manufacturing processes to investigate their effect on the microstructure and corrosion resistance. It was found that, unlike 316L, the HEA suffered less from pitting corrosion and more from a generalised corrosion attack. Very similar corrosion results were seen across the manufacturing methods; however, the cast sample was observed to have the most consistent display of corrosion resistance.

Based on the pitting resistance equivalent number, which relates the amount of Cr and Mo by wt.% in a stainless steel to its corrosion resistance, it was theorised that the addition of Mo to this HEA could also increase its corrosion resistance. The results were inconclusive; however, better corrosion resistance was seen in the AM sample of the HEA with the addition than in the AM sample without.

Declaration

This work has not previously been accepted in substance for any degree and is not being concurrently submitted in candidature for any degree.

Signed:

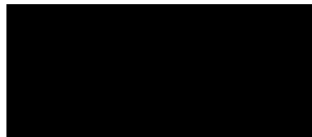
A solid black rectangular box used to redact the signature of the author.

Date: 21/06/24

Statement 1

This dissertation is the result of my own independent work/investigation, except where otherwise stated. Other sources are acknowledged by giving explicit references. A bibliography is appended.

Signed:

A solid black rectangular box used to redact the signature of the author.

Date: 21/06/24

Statement 2

I hereby give consent for my dissertation, if accepted, to be available for photocopying and for interlibrary loan and for the title and summary to be made available to outside organisations.

Signed:

A solid black rectangular box used to redact the signature of the author.

Date: 21/06/24

Acknowledgements

Firstly, I'd like to begin by thanking my primary supervisor and whip-cracker, Nick Lavery, who manages to find 26 hours in a 24-hour day to help all those who step foot across his threshold. I am incredibly grateful for the opportunities that he has provided me with, the level of faith that he's put in me during this process, and for dragging me over the line at the end. Next is my current second supervisor, Jim Sullivan, who, as my undergraduate 3rd year project supervisor, gave me my first insight into the world of academic research. Whilst our contact has been limited recently, he made himself available until the last moment, for which I will always be thankful. And to Natalie Wint, who took me on at the beginning of the PhD and set me on the course I am on today. I would also like to thank the EPSRC and Swansea University for funding this project.

I'm not the same person I was when I started this PhD. I'm fatter, my forehead's become more prominent, and there are bags under my eyes. However, I'm convinced that has all happened in the last few weeks. There are countless people that I have come into contact with throughout this PhD that, in one way or another, have contributed to my work or made this whole crazy process more enjoyable. Firstly, the MACH1 team, who, over the years, have come and gone but have always been incredibly helpful in the labs, from training me on equipment to assisting in planning experiments. I could not hope for a better group of colleagues that, at the drop of a hat, would stop what they were doing to help me out. So, to Dan Butcher, Shahin Mehraban, Rhodri Rees, Talal Abdullah, Ed Palmer, Steve Milward, John Cullen and Jordan Rosser, to name a few, thank you. To those in AIM and SPECIFIC who have stood by with patience as I've asked why my SEM image is wobbling for the 10th time, and to technicians like Ian Hemming and Gareth Davies, who have always been available to discuss anything from heat treatments and etching to Formula 1, I'll always be grateful for your help. To my friends who have kept me sane over the last 4 and a bit years, there are too many of you to name; this is all you're getting - cheers. And finally, to my family. To Mum and Dad, I will deny the following to the hilt. I see myself as one of the worst receivers of gifts ever, so I definitely don't say this enough, but I am incredibly grateful for all the opportunities you have given me over the years. For pushing and supporting me at school and university, for convincing me 4 years ago that this would be a good idea, for giving up your evenings and weekends taking me to swimming, football, cricket, rugby, tennis, or whatever other sport I was playing at the time, it means the world. Thank you. To the rest of you, Eleanor, and beyond, thank you for everything. Here's to never having to ask me again when I'm handing in my thesis.

I'm sure there are many people I am missing that deserve a mention here, but that's what corrections are for, right?

Table of Contents

| | |
|--|-----------|
| Abstract | 2 |
| Declaration..... | 4 |
| Statement 1..... | 4 |
| Statement 2..... | 4 |
| Acknowledgements | 5 |
| List of Figures | 10 |
| List of Tables | 13 |
| Nomenclature | 14 |
| Abbreviations..... | 15 |
| 1 Introduction | 16 |
| 1.1 Aims and Objectives..... | 18 |
| 1.2 Publications..... | 19 |
| 2 Literature Review | 20 |
| 2.1 Additive Manufacturing | 20 |
| 2.1.1 Current State of Industry | 20 |
| 2.1.2 Benefits of AM | 22 |
| 2.1.3 AM Obstacles | 22 |
| 2.1.4 Additive Manufacturing Methods..... | 25 |
| 2.1.5 Applications..... | 28 |
| 2.1.6 Process Parameters..... | 31 |
| 2.1.7 Powder Parameters | 33 |
| 2.1.8 Temperature Parameters..... | 33 |
| 2.1.9 Powder Metallurgy..... | 34 |
| 2.1.10 Post Processing | 36 |
| 2.2 Metallurgy..... | 39 |
| 2.2.1 Steels..... | 39 |
| 2.2.2 Microstructure | 40 |
| 2.2.3 Available steels..... | 43 |
| 2.2.4 Cold Rolling | 44 |
| 2.2.5 AM Corrosion | 44 |
| 2.2.6 316L Corrosion | 45 |
| 2.3 High entropy alloys | 46 |
| 2.3.1 History of High Entropy Alloys | 46 |

| | | |
|----------|--|-----------|
| 2.3.2 | The Four Effects of High Entropy Alloys..... | 47 |
| 2.3.3 | Methods for Alloy Design..... | 50 |
| 2.3.4 | High Entropy Alloys Studied for Corrosion | 51 |
| 2.3.5 | In-Situ Alloying of HEAs..... | 52 |
| 2.4 | Corrosion..... | 53 |
| 2.4.1 | General Corrosion Theory..... | 53 |
| 2.5 | The Electrochemical System | 55 |
| 2.5.1 | Electrode Potentials..... | 55 |
| 2.5.2 | Practical Corrosion | 56 |
| 2.6 | Mechanisms of Corrosion | 58 |
| 2.6.1 | Crevice Corrosion..... | 58 |
| 2.6.2 | Pitting Corrosion | 59 |
| 2.6.3 | Bimetallic corrosion | 60 |
| 2.7 | Kinetics of Corrosion | 60 |
| 2.7.1 | Polarisation | 61 |
| 2.8 | Evans Diagram..... | 62 |
| 2.9 | Passivity..... | 63 |
| 2.10 | Pourbaix Diagram..... | 64 |
| 2.11 | Electrochemical Techniques | 65 |
| 2.11.1 | Potentiodynamic Polarisation..... | 65 |
| 2.12 | Scanning Techniques..... | 67 |
| 2.12.1 | Scanning Vibrating Electrode Technique (SVET)..... | 68 |
| 2.12.2 | Time-lapse Microscopy | 68 |
| 2.13 | Summary | 69 |
| 3 | Experimental Procedures | 70 |
| 3.1 | Introduction | 70 |
| 3.2 | Powder Mixing..... | 70 |
| 3.2.1 | HEAX..... | 70 |
| 3.3 | Particle Size Distribution Analysis..... | 70 |
| 3.4 | Rheometry | 71 |
| 3.5 | Reduced Build Volume..... | 72 |
| 3.5.1 | Installation | 73 |
| 3.5.2 | Operation | 73 |
| 3.6 | Additive Manufacturing Process Parameters | 74 |

| | | |
|----------|---|-----------|
| 3.7 | Casting..... | 75 |
| 3.8 | Drop Casting..... | 77 |
| 3.9 | Heat Treatments | 77 |
| 3.9.1 | Solution Anneal..... | 77 |
| 3.9.2 | Post-Rolling Anneal | 77 |
| 3.10 | Cold Rolling | 78 |
| 3.11 | Sample Preparation for Optical Microscopy and SEM and Corrosion | 78 |
| 3.11.1 | Cutting..... | 78 |
| 3.11.2 | Mounting & Polishing..... | 79 |
| 3.11.3 | Corrosion Preparation..... | 79 |
| 3.12 | Etching..... | 82 |
| 3.13 | Density Analysis | 82 |
| 3.13.1 | Bulk..... | 82 |
| 3.13.2 | Optical | 83 |
| 3.14 | SEM EDS | 83 |
| 3.14.1 | Loading and Initial Operation | 83 |
| 3.14.2 | EDS | 84 |
| 3.14.3 | Grain Size Analysis..... | 84 |
| 3.15 | X-ray Diffraction | 85 |
| 3.15.1 | Loading & Alignment..... | 86 |
| 3.15.2 | Test Set-up | 86 |
| 3.15.3 | Phase Identification & Analysis..... | 87 |
| 3.16 | OCP & Potentiodynamic Polarisation | 88 |
| 3.16.1 | Solution Preparation | 88 |
| 3.16.2 | Experimental Setup..... | 88 |
| 3.17 | Additional Notes | 89 |
| 4 | An Investigation into the Effect of Density Variation on the Corrosion Performance of Additively Manufactured 316LSS | 90 |
| 4.1 | Introduction | 90 |
| 4.2 | Powder Analysis..... | 91 |
| 4.3 | Optimisation and Experimental Setup..... | 93 |
| 4.3.1 | Optimisation..... | 93 |
| 4.3.2 | Build Setup..... | 94 |
| 4.4 | Bulk Density Analysis | 95 |

| | | |
|----------|--|------------|
| 4.5 | Optical Density Analysis | 98 |
| 4.6 | Microstructure | 101 |
| 4.6.1 | Additive Manufacturing | 101 |
| 4.6.2 | Wrought | 104 |
| 4.7 | Corrosion Testing | 106 |
| 4.8 | Discussion..... | 111 |
| 4.9 | Conclusions | 113 |
| 5 | An Investigation into the Different Manufacturing Methods of 316L Stainless Steel and their Effects on Microstructure and Corrosion Resistance..... | 115 |
| 5.1 | Introduction | 115 |
| 5.2 | Density Analysis | 115 |
| 5.3 | Thermocalc..... | 116 |
| 5.4 | XRD..... | 118 |
| 5.5 | Microstructure | 119 |
| 5.5.1 | AM..... | 119 |
| 5.5.2 | Cast..... | 119 |
| 5.5.3 | CR | 123 |
| 5.5.4 | Grain Size Analysis..... | 126 |
| 5.6 | Corrosion Testing | 128 |
| 5.7 | Discussion..... | 130 |
| 5.8 | Conclusions | 132 |
| 6 | An Investigation into the Different Manufacturing Methods of a High Entropy Alloy (HEA1) and their Effects on Microstructure and Corrosion Resistance | 133 |
| 6.1 | Introduction | 133 |
| 6.2 | Powder Analysis..... | 134 |
| 6.3 | Optimisation and Build Setup | 136 |
| 6.4 | Density Analysis | 137 |
| 6.5 | Thermo-Calc..... | 139 |
| 6.6 | XRD..... | 141 |
| 6.7 | Microstructure | 143 |
| 6.7.1 | AM..... | 143 |
| 6.7.2 | Cast..... | 147 |
| 6.7.3 | CR | 150 |
| 6.8 | Corrosion Testing | 154 |

| | | |
|-----------|--|------------|
| 6.9 | Discussion..... | 158 |
| 6.10 | Conclusions | 160 |
| 7 | An Investigation into the Different Manufacturing Methods of a High Entropy Alloy (HEA1) with a 2.4 wt.% Molybdenum Addition and their Effects on Microstructure and Corrosion Resistance | 161 |
| 7.1 | Introduction | 161 |
| 7.2 | Powder Analysis..... | 162 |
| 7.3 | Optimisation and Build Setup | 165 |
| 7.4 | Density Analysis | 166 |
| 7.5 | Thermocalc..... | 167 |
| 7.6 | XRD..... | 168 |
| 7.7 | Microstructure | 170 |
| 7.7.1 | AM..... | 170 |
| 7.7.2 | Cast..... | 177 |
| 7.7.3 | CR | 181 |
| 7.8 | Corrosion Testing | 185 |
| 7.9 | Discussion..... | 188 |
| 7.10 | Conclusions | 190 |
| 8 | Final Discussion | 191 |
| 9 | Conclusions and Future Work..... | 193 |
| 9.1 | Conclusions | 193 |
| 9.2 | Future Work..... | 194 |
| 10 | References..... | 195 |

List of Figures

| | | |
|-----------|--|----|
| Figure 1 | Chart displaying the approximate percentage revenues received by industrial machine manufacturers from each industrial sector [6]..... | 21 |
| Figure 2 | Stratasys H2000 Infinite Build 3D printer [17] | 24 |
| Figure 3 | Part density vs laser energy density for 316L [48]..... | 32 |
| Figure 4 | Melt pool geometry vs energy density [50]..... | 33 |
| Figure 5 | Gas atomisation and plasma atomisation [52] | 34 |
| Figure 6 | Particle size variation over the rebuild period for 316L [48] | 35 |
| Figure 7 | Isothermal transformation diagram for iron-carbon alloy 0.76 %C [59] | 38 |
| Figure 8 | Diagram of BCC structure [59] | 41 |
| Figure 9 | Diagram of FCC structure [59]..... | 41 |
| Figure 10 | Iron-carbon phase diagram [59] | 42 |
| Figure 11 | Gibbs Free Energy diagram for a metal [143] | 54 |

| | |
|--|-----|
| Figure 12 Schematic of oxygen reduction and metal oxidisation [144] | 57 |
| Figure 13 Schematic of pitting corrosion [144]..... | 60 |
| Figure 14 Polarisation vs current density [144] | 61 |
| Figure 15 Polarisation vs current [144]..... | 62 |
| Figure 16 Polarisation vs current density for metal in aerated water [144] | 62 |
| Figure 17 Evans diagram for zinc in hydrochloric acid [156] | 63 |
| Figure 18 Pourbaix diagram for zinc [159]..... | 64 |
| Figure 19 Potential vs current [159] | 65 |
| Figure 20 Example of a full cyclic potentiodynamic polarisation sweep [163]..... | 66 |
| Figure 21 Schematic of potentiodynamic polarisation set-up..... | 67 |
| Figure 22 SVET plots of current density vs location [165,166] | 68 |
| Figure 23 Density cube used for optimisation and corrosion testing..... | 75 |
| Figure 24 Diagram of the experimental set-up within the glove box for casting, including a scissor lift, boron nitride block and crucible..... | 76 |
| Figure 25 Corrosion sample holder - iteration 1 (A), specimen prepped for testing (B)..... | 80 |
| Figure 26 Corrosion specimen setup - iteration 2 | 81 |
| Figure 27 Da Vinci set up for divergent slit XRD analysis..... | 86 |
| Figure 28 XRD analysis of Bakelite | 88 |
| Figure 29 SEM micrographs of 316L powder at 250x (a) and 1000x (b) magnification..... | 91 |
| Figure 30 316L powder PSD | 92 |
| Figure 31 5x9 build setup for 316L density cubes..... | 94 |
| Figure 32 Bulk density of 316L cubes..... | 96 |
| Figure 33 Graph of VED vs average bulk density | 97 |
| Figure 34 Bulk and optical density comparison for 316L..... | 98 |
| Figure 35 Binary images of (a) AM samples 19 and (b) 22 post thresholding | 100 |
| Figure 36 SEM micrograph of AM 316L in the XZ plane at 500x magnification | 101 |
| Figure 37 EDS point scan map of AM 316L in the XZ plane at 4000x magnification | 102 |
| Figure 38 Optical microstructure of wrought 316L at 500x magnification..... | 104 |
| Figure 39 SEM micrograph of wrought 316L at 4Kx magnification | 105 |
| Figure 40 OCP data from 316L AM samples 1, 3, 7 ,10, 22 and 29 over 600s | 106 |
| Figure 41 Cyclic polarisation plots for 316L AM sample 1 | 107 |
| Figure 42 Cyclic polarisation plots for 316L AM sample 10 | 108 |
| Figure 43 Cyclic polarisation plots for 316L AM sample 22 | 109 |
| Figure 44 Cyclic polarisation plots for 316L AM sample 29 | 109 |
| Figure 45 Optical density vs key corrosion metrics for 316L AM..... | 110 |
| Figure 46 Cyclic polarisation plots for 316L wrought samples | 111 |
| Figure 47 Volume fraction of all phases for 316L produced by Thermo-Calc..... | 116 |
| Figure 48 XRD scans for wrought, CR, AM, and cast 316L samples | 118 |
| Figure 49 EDS Maps of cast 316L at 1000x magnification | 120 |
| Figure 50 EDS point scan map of cast 316L | 121 |
| Figure 51 EDS point scan map of CR 316L at 10kx magnification | 123 |
| Figure 52 EDS Maps for CR 316L on the sample area shown in Figure 51 | 125 |
| Figure 53 Histogram of 316L AM grain size analysis..... | 127 |
| Figure 54 OCP plots for 316L AM 22, cast and CR over 600s..... | 128 |
| Figure 55 Cyclic polarisation plots for cast 316L..... | 129 |

| | |
|---|-----|
| Figure 56 Cyclic polarisation plots for CR 316L..... | 130 |
| Figure 57 SEM images of HEA1 powder at 250x and 1000x magnification | 134 |
| Figure 58 HEA1 powder PSD | 135 |
| Figure 59 Measured bulk density vs VED during HEA1 optimisation | 137 |
| Figure 60 Thermo-Calc prediction of HEA1 in 2021..... | 139 |
| Figure 61 Volume fraction of all phases for HEA1 produced by Thermo-Calc..... | 140 |
| Figure 62 XRD scans for CR, AM, and cast HEA1 samples..... | 141 |
| Figure 63 SEM micrograph of HEA1 produced by AM in the XZ plane | 143 |
| Figure 64 SEM micrograph of HEA1 produced by AM in the XY plane | 144 |
| Figure 65 Point scan EDS for HEA1 AM XZ at 1000x magnification | 145 |
| Figure 66 EDS linescan one HEA1 across a melt pool boundary at 2000x magnification..... | 146 |
| Figure 67 SEM BSD of cast HEA1 and accompanying EDS maps for Cr and Ni at 750x magnification..... | 147 |
| Figure 68 BSD EDS point scan map of cast HEA1 at 1000x magnification | 148 |
| Figure 69 BSD SEM of CR HEA1 at 1500x magnification | 150 |
| Figure 70 EDS maps of CR HEA1 area in Figure 69..... | 152 |
| Figure 71 EDS point scan map of CR HEA1 at 12.6kx magnification | 153 |
| Figure 72 OCP plots for HEA1 AM, cast and CR over 600s..... | 154 |
| Figure 73 Cyclic polarisation plots for HEA1 AM, sample 2 | 155 |
| Figure 74 Cyclic polarisation plots for cast HEA1..... | 156 |
| Figure 75 Cyclic polarisation plots for CR HEA1 | 157 |
| Figure 76 SEM micrograph of Mo powder used for in-situ addition | 162 |
| Figure 77 SEM micrograph of HEAX powder | 163 |
| Figure 78 HEAX powder PSD | 164 |
| Figure 79 Initial build setup for HEAX on the RBV | 165 |
| Figure 80 Successful build layout for HEAX on the RBV..... | 166 |
| Figure 81 Volume fraction of all phases for HEAX produced by Thermo-Calc | 167 |
| Figure 82 XRD scans for CR, AM, and cast HEAX samples | 168 |
| Figure 83 SEM micrograph of AM HEAX in the XY plane | 170 |
| Figure 84 EDS maps for AM HEAX..... | 171 |
| Figure 85 SEM micrograph and point scan map of AM HEAX at 750x magnification..... | 172 |
| Figure 86 SEM image of AM HEAX corrosion sample with point scan locations at 250x magnification | 174 |
| Figure 87 EDS maps for HEAX corrosion sample..... | 175 |
| Figure 88 Rectangular area around the region of high Mo in AM HEAX | 177 |
| Figure 89 SEM image of cast HEAX at 1000x magnification | 177 |
| Figure 90 EDS maps of cast HEAX at 1000x magnification | 178 |
| Figure 91 SEM micrograph and point scan map of cast HEAX at 750x magnification..... | 179 |
| Figure 92 SEM micrograph of CR HEAX at 1500x magnification..... | 181 |
| Figure 93 EDS maps of CR HEAX | 182 |
| Figure 94 EDS point scan map of CR HEAX | 183 |
| Figure 95 OCP plots for HEAX AM, cast and CR over 600s..... | 185 |
| Figure 96 Cyclic polarisation plot for AM HEAX | 186 |
| Figure 97 Cyclic polarisation plots for cast HEAX..... | 187 |
| Figure 98 Cyclic polarisation plots for CR HEAX..... | 188 |

List of Tables

| | |
|--|-----|
| Table 1 Chemical composition ranges for stainless steel 316L [70] | 43 |
| Table 2 Configurational entropies of equiatomic alloys with constituent elements between 5 and 13 [91] | 47 |
| Table 3 A Selection of electrode reduction reactions and their respective electrode potential [144] | 55 |
| Table 4 Desired Composition of HEAX | 70 |
| Table 5 Flow rate sensitivity and its associated powder type | 72 |
| Table 6 The structure of L9 and L25 arrays..... | 74 |
| Table 7 Cold rolling reductions, target and achieved (mm)..... | 78 |
| Table 8 Polishing Recipe Used for All Materials Tested..... | 79 |
| Table 9 Etchant details..... | 82 |
| Table 10 XRD setup ranges for 316L and HEAs | 87 |
| Table 11 Manufacturing processes and their production notes..... | 89 |
| Table 12 EDS point scan analysis of Figure 29 (b) (wt.%) | 92 |
| Table 13 Particle size by volume for 316L powder | 93 |
| Table 14 Rheometric characteristics of the 316L powder | 93 |
| Table 15 L9 Taguchi array for parameter selection | 94 |
| Table 16 316L build parameters for repeated samples 1-9..... | 95 |
| Table 17 Mass analysis for 316L by cube and block number (g)..... | 95 |
| Table 18 Density analysis for 316L by cube and block number (%)..... | 96 |
| Table 19 Density measurements from bulk and optical analysis | 98 |
| Table 20 Spectrum analysis data for SEM image in Figure 37 (wt.%)..... | 103 |
| Table 21 EDS composition of wrought 316L | 105 |
| Table 22 Compositional point scan summary of wrought 316L (wt.%)..... | 105 |
| Table 23 Summary of corrosion data for AM and wrought 316L samples ordered by density..... | 107 |
| Table 24 Optical density of 316L samples produced by optimum AM, cast, and CR | 115 |
| Table 25 Composition of selected 316L phases at their highest respective volume fraction (wt.%) | 117 |
| Table 26 XRD data extracted from scans shown in Figure 48..... | 119 |
| Table 27 Composition of cast 316L from EDS map..... | 121 |
| Table 28 Point scan analysis of cast 316L shown in Figure 50, (wt.%)..... | 122 |
| Table 29 Composition of CR 316L from EDS Maps in Figure 52 | 125 |
| Table 30 Point scan analysis from spectrum in Figure 51 (wt.%) | 126 |
| Table 31 Grain size analysis of AM, cast, and CR specimens | 127 |
| Table 32 Summary of 316L corrosion data for each manufacturing method..... | 128 |
| Table 33 Composition of the target, actual, and EDS HEA1 Powder, in w.%..... | 135 |
| Table 34 Particle size by volume for HEA1 powder | 136 |
| Table 35 Rheometric characteristics of the HEA1 powder | 136 |
| Table 36 Optimum parameter set used for HEA1..... | 137 |
| Table 37 Bulk density analysis of AM HEA1 cubes..... | 138 |
| Table 38 Optical density measurements for AM, cast, and CR HEA1 | 138 |
| Table 39 Composition of selected HEA1 phases at their highest respective volume fraction (wt.%) | 141 |
| Table 40 XRD data extracted from scans shown in Figure 62..... | 142 |
| Table 41 Major phase ratios for HEA1 CR, cast and AM..... | 142 |
| Table 42 Composition of AM HEA1 from EDS maps | 144 |

| | |
|---|-----|
| Table 43 Summary of point scan EDS on HEA1 AM on the XZ plane (wt.%)..... | 145 |
| Table 44 Summary of linescan EDS on HEA1 AM on the XY plane (wt.%) | 147 |
| Table 45 Composition of cast HEA1 from EDS maps in Figure 67..... | 148 |
| Table 46 Point scan data for HEA1 cast in Figure 68 (wt.%) | 149 |
| Table 47 Composition of CR HEA1 from maps in Figure 70..... | 152 |
| Table 48 Composition summary of CR HEA1 point scans in Figure 71 (wt.%)..... | 153 |
| Table 49 Summary of HEA1 corrosion data for each manufacturing method..... | 155 |
| Table 50 Particle size by volume for HEAX powder | 164 |
| Table 51 Rheometric characteristics of the HEAX powder | 164 |
| Table 52 Laser parameters used for AM HEAX | 166 |
| Table 53 Optical density measurements for AM, cast, and CR HEAX..... | 166 |
| Table 54 Composition of selected HEAX phases at their highest respective volume fraction (wt.%) | 168 |
| Table 55 XRD data extracted from scans shown in Figure 82..... | 169 |
| Table 56 Major phase ratios for HEAX CR, cast and AM..... | 169 |
| Table 57 Composition of AM HEAX from EDS (wt.%) | 171 |
| Table 58 Point scan spectrum analysis relating to the HEAX AM sample in Figure 85 (wt.%) | 173 |
| Table 59 Composition of AM HEAX corrosion sample from EDS maps | 176 |
| Table 60 Point scan analysis of AM HEAX corrosion sample (wt.%)..... | 176 |
| Table 61 Composition of cast HEAX from EDS maps (wt.%)..... | 179 |
| Table 62 Point scan analysis of cast HEAX shown in Figure 91(wt.%) | 180 |
| Table 63 Composition of CR HEAX from EDS maps in Figure 93..... | 182 |
| Table 64 Point scan analysis of CR HEAX shown in Figure 94 (wt.%)..... | 184 |
| Table 65 Summary of HEAX corrosion data for each manufacturing method | 185 |

Nomenclature

| | |
|-------------------------|---------------------------------|
| atm | Atmosphere |
| at.% | Atomic Percent |
| BFE | Basic Flowability Energy (mJ) |
| CBD | Conditioned Bulk Density (g/ml) |
| I_{corr} | Corrosion Current (A) |
| E_{corr} | Corrosion Potential (V) |
| I | Current (A) |
| K | Degrees Kelvin |
| ET | Exposure Time (μs) |
| FRI | Flow Rate Index |
| R | Gas Constant (8.314 J / mol·K) |
| HS | Hatch Spacing (μm) |
| LT | Layer Thickness (μm) |
| M | Moles |
| OCP | Open Circuit Potential (V) |
| E_{pit} | Pitting Potential (V) |
| PD | Point Distance (μm) |
| E | Potential (V) |
| P | Power (W) |

| | |
|-------------|--|
| E_r | Repassivation Potential (V) |
| SMD | Sauter Mean Diameter (μm) |
| σ | Sigma Phase |
| SE | Specific Energy (mJ/g) |
| φ_i | Volume Fraction |
| VED | Volumetric Energy Density (J/mm^3) |
| wt.% | Weight Percent |

Abbreviations

| | |
|-------------|----------------------------------|
| AM | Additive Manufacturing |
| BSD | Backscatter Diffraction |
| BCC | Body-Centered Cubic |
| CR | Cold Rolled |
| CAD | Computer-Aided Design |
| CP | Cyclic Polarisation |
| EBSD | Electron Backscatter Diffraction |
| EDS | Energy Dispersive Spectroscopy |
| FCC | Face-Centered Cubic |
| HEA | High Entropy Alloy |
| HIP | Hot Isostatic Pressing |
| LPBF | Laser Powder Bed Fusion |
| PSD | Powder Size Distribution |
| RAP | Rapid Alloy Prototyping |
| RBV | Reduced Build Volume |
| SEM | Scanning Electron Microscope |
| SS | Solid Solution |
| SD | Standard Deviation |
| SHE | Standard Hydrogen Electrode |
| WRT | Wrought |
| XRD | X-ray Diffraction |

1 Introduction

Corrosion is a global issue that infiltrates many aspects of today's society. Its implications can vary, from degrading the aesthetic appeal of metallic cladding to negatively impacting a component's mechanical properties and structural integrity. There are also many indirect costs associated with corrosion, such as risk to human safety and environmental consequences. Many studies have been commissioned over recent years in an attempt to quantify the cost of corrosion to society financially. One such study was the International Measures of Prevention, Application and Economics of Corrosion Technology (IMPACT), commissioned by the National Association of Corrosion Engineers (NACE). As of 2013, it estimated that the global cost of corrosion was \$2.5 trillion annually, equating to approximately 3.4 % of global GDP [1]. This cost stems not only from the replacement of corroded components, but also the preventative measures such as coatings and paints, and lost production due to out-of-service plants [2].

The nature of corrosion depends, not only on the material of the component on which it occurs but also on how it was manufactured. The term corrosion is used to describe the degradation of the properties of a material. This overarching phenomenon does not occur in the same way for all metals, nor are its effects felt equally by each material. Environmental and structural factors also have a significant impact on the type and severity of corrosion. Different manufacturing methods result in components with different properties, even if the material used is the same. New, innovative manufacturing methods and alloys are being developed with numerous associated benefits, but with these developments come several hurdles that must be overcome.

One means by which components can be manufactured is through additive manufacturing (AM). The adopted definition for AM set out by ASTM F42 F2792 – 12a is "a process of joining materials to make objects from 3D model data, usually layer upon layer, as opposed to subtractive manufacturing methodologies" [3]. Synonyms for these manufacturing processes include additive fabrication and additive layer manufacturing (ALM).

AM, as we know it today, originated in the early 1980s with the invention and first patent of the Stereo-Lithographic Apparatus (SLA) by Charles 'Chuck' Hull [4,5]. SLA is a process whereby layers of an ultraviolet (UV) light-sensitive liquid polymer are solidified to create the desired geometry using a solid-state crystal laser. It was initially envisaged that AM would be used for rapid prototyping within research and development, replacing the often complex, tedious, and expensive processes linking an initial design conception through the maze of developmental iterations to the final marketable product. However, as the list of usable materials, general output quality and possible complexity of

the parts produced increased, the goalposts have shifted towards functional components, replacing those made by conventional manufacturing methods.

Throughout the 1990s, other additive processes were developed, including Laser Sintering (LS) and Material Deposition Extrusion. Only around the turn of the millennium did efforts become more focused on the development of laser powder bed fusion (LPBF) techniques [4]. This, along with other modern technology, has allowed the list of manufacturable materials to extend into metals, which has, in turn, significantly increased the possible usable avenues for the manufacturing technique.

As the interest, investment, and capability of general AM machinery has increased over time, so has the level of research into the field, the number of patents filed for new equipment and the revenue generated by the industry. Until recently, this research has mainly focused on the optimisation of the AM process to ensure that the mechanical properties associated with built components are similar to those of components manufactured using subtractive or net-shape methods. Many components made using AM processes can now compete mechanically with those manufactured through traditional methods; as such, research is now turning towards the serviceable lifetime of these components. One of the main difficulties in predicting the service lifetime of metal AM parts is their variability in corrosion resistance compared to those made using conventional methods.

Their impacts must be understood and validated to advance the field further, increase the components' failure predictability, and develop techniques to overcome such issues.

In materials science, the emergence of High-Entropy Alloys (HEAs) has ushered in a new era of exploration and innovation. Unlike traditional alloys, HEAs defy conventional norms by incorporating four or more principal elements in nearly equal proportions, resulting in a complex and disordered atomic structure. This departure from the well-established principles of alloy design has opened up a vast compositional space, offering tantalising possibilities for engineering materials with unprecedented properties.

The inherent benefits of HEAs are multifaceted. Their equimolar composition contributes to a high degree of structural disorder, leading to unique and often superior mechanical, thermal, and magnetic properties. HEAs have demonstrated exceptional strength, hardness, and corrosion resistance, making them highly attractive for a myriad of applications ranging from structural materials to specialised coatings.

Despite the remarkable strides made in understanding and harnessing the potential of HEAs, the research landscape into these alloys remains largely unexplored. While their benefits are evident, critical gaps exist in our comprehension of HEAs, necessitating a closer examination. Whilst there are

gaps in the knowledge around HEAs made by conventional manufacturing methods, these are even more substantial when manufactured by AM. Significant work needs to be done to bring the scientific community's knowledge of these alloys processed by this method to a level where they can begin to replace other, more documented materials such as steel.

1.1 Aims and Objectives

This work aims to develop an understanding of the links between composition, microstructure and processing on the corrosion behaviour of alloys used in AM, particularly high entropy alloys used in a LPBF process.

By studying the behaviour of 316L stainless steel alloy as a baseline, the alloy will be processed in three ways: casting, LPBF, and casting with cold-rolling and annealing. In all cases, the microstructures will be characterised and tested for corrosion properties. It is known that porosity from LPBF strongly affects corrosion, but by looking at other processing routes, the full extent of the processing on corrosion can be put into context for a given alloy chemistry.

The knowledge gained on the behaviour of the baseline 316L stainless steel will be compared to that of HEAs processed similarly. It has been suggested that high entropy alloys may have an inherent corrosion resistance. This hypothesis will be tested on a novel HEA (e.g. AlCrMnNiFe) developed at Swansea and prepared by gas atomisation as a pre-alloyed powder in the 15 – 45 μm size specific for processing by LPBF. The HEA will be processed the same way as the 316L stainless steel (i.e., by casting, LPBF and cold rolling), using the alloy powder as feedstock to ensure identical composition.

Finally, minor modifications will be made to the HEA alloy, adding elements such as Mo to see if the corrosion resistance changes. In the final step of this work, a Rapid Alloy Prototyping (RAP) route will be used, and modifications to the HEA will be explored via thermo-calc, casting, and in-situ LPBF builds. Corrosion testing will be undertaken on the HEA variants in cast, LPBF, and rolled form to determine the effects on corrosion resistance.

Whilst porosity is expected to be a leading cause of corrosion variability in LPBF, by covering three different processing routes with lower porosity and different microstructures, it is hoped that the extent to which processing competes with composition in a standard alloy can be better understood. Furthermore, while it may not be possible to determine to a full extent whether HEAs are inherently more corrosion resistant than other alloys, it will allow an incremental verification for the alloys studied here.

1.2 Publications

M. Ritchie, S. Mehraban, S.G.R. Brown, D. Butcher, J. Cullen, M. Calvo-Dahlborg, N.P. Lavery., “In-situ Modification of a High Entropy Alloy With 2.4% Molybdenum Using LPBF, and its Effect on Microstructure and Corrosion Resistance” in *Annual International Solid Freeform Fabrication Symposium*, Austin, Texas, USA, 2022.

E. Palmer, J. Rosser, M. Ritchie, C. Bromley, S. G. R. Brown, N. P. Lavery., “Controlling Grain Evolution of IN625 Parts Produced by LPBF-AM” in *Annual International Solid Freeform Fabrication Symposium*, Austin, Texas, USA, 2022.

N.P. Lavery, S. Mehraban, D. Butcher, J. Cullen, D.W. Hardwicke, M. Ritchie, M. Calvo-Dahlborg, S.G.R. Brown., “The development and testing of a customised high entropy alloy (AlCrMnNiFe) for Laser Powder Bed Fusion”. To be published in the *Journal of Alloys and Compounds* 2024

2 Literature Review

2.1 Additive Manufacturing

AM uses 3D models initially generated using computer-aided design (CAD) software to fabricate digital geometries out of the desired material layer-by-layer [6–9].

2.1.1 Current State of Industry

Since 1988, there has been strong and consistent growth in the industry year on year, with only 3 years of negative growth in that time [6]. The level of research into AM in recent years has considerably increased, with interest and investment emanating from many different industries, organisations, and governments. This is shown through an average revenue growth rate over the last 29 years of 26.6 % and, more recently, an average year-on-year growth of 24.9 % between 2014 and 2017 [6]. The intention of many industries, such as automotive and aerospace, to incorporate AM into their production processes is demonstrated by the 12.6 % increase in industrial AM system sales (systems valued at \$5000 or more) from 2016 to 2017. Furthermore, the average annual growth for industrial system sales between 1989 and 2017 was 28.2 %, showing a significant and consistent sector expansion [6].

One segment of AM technology that has recently enjoyed substantial growth in popularity and sales is that of metal AM systems. Since the turn of the century, the number of these machines sold per annum has risen from 16 to 1768, increasing by 79.9 % between 2016 and 2017. This recent, dramatic increase in sales can be linked to the heightened research and commercialisation of these systems and the components they produce, as well as the arrival of cheaper metal AM systems, many originating in Asia. Due to their complexity and relative infancy, the average selling price of these machines was \$407,883 in 2017, down from \$551,585 in 2016 [6]. This decrease in average selling price can be attributed to the emergence of relatively low-cost metal AM systems entering the market.

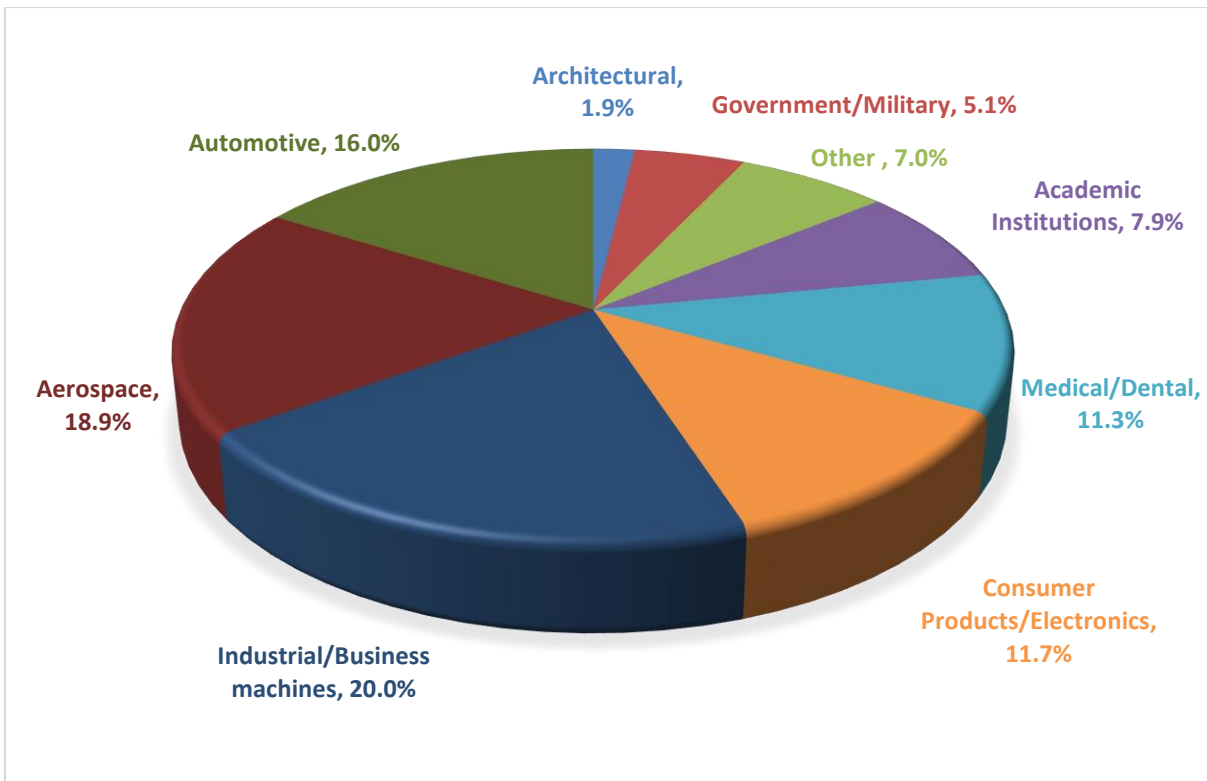


Figure 1 Chart displaying the approximate percentage revenues received by industrial machine manufacturers from each industrial sector [6]

Figure 1 shows the approximate revenue received from the sales of industrial AM systems from each sector as a percentage. For the 5th year in a row, the most significant revenue is obtained from the industrial/business sector. This broad category incorporates many sub-classifications, from industrial automation equipment to document printers and computers. A similar level of variation is contained within the consumer products/electronics grouping. Therefore, from this data, it can be ascertained that a large share of the AM industrial machine revenue is generated by the aerospace, automotive and medical/dental industries, which collectively hold a market share of 46.2 % [6].

Patent applications are also a valuable indication of industry growth. Regarding AM, patents are generally related to the development of new technological advancements, sometimes representing design patents for components produced by AM machines. Between 2015 and 2017, there were 4,957 published applications to the US Patent and Trademark Office, averaging 1,652 a year compared to 2,218 in the 15 years preceding. This dramatic increase represents the progression of the technology and the heightened level of interest, research, and investment in AM.

The transfer of data between research groups, universities, and industry through partnerships and publications is vital for increased technology development. Governmental intervention can assist with creating centres such as the ‘America Makes’ and the ‘High Value Manufacturing Catapult Centres’, formed by the US and UK governments, respectively [6].

2.1.2 Benefits of AM

AM opens the door to previously considered impossible, unfeasible, or uneconomic applications. The possibility of mass customisation means that bespoke parts remain cost-effective. AM has developed over time, and the list of usable materials, geometric accuracy, and overall output quality has improved [9].

The list of benefits for AM over traditional manufacturing methods such as machining, drilling, grinding, and casting is extensive. To begin with, parts made through AM use less material than those produced by subtractive methods, leading to less waste product. This is compounded as the size and complexity of part geometries are increased. Complex structures often need many support structures when produced through AM, but when designed correctly, the material wastage is still significantly less than in other manufacturing methods [5,9–11].

In line with AM's initial objective of rapid prototyping, changes can be made to designs quickly and cost-efficiently simply by editing the CAD file and beginning a new build [9,12]. The only costs in this process are materials and the energy used to create the part. Comparatively, subtractive manufacturing operations will need to be redesigned to create the new part. This can be far more time-consuming as additional machining steps may be required to complete the new geometry. Furthermore, extra material is also wasted because of this. Changing a casting manufacturing process is also very costly and time-consuming. Even when small, casting moulds are expensive and, even when made in-house, require extra time for manufacture and delivery.

Potential part complexity and part reduction are other benefits of the AM process compared to traditional manufacturing methods [13,14]. Net-shape processes such as casting and injection moulding are associated with fast cycle times, leading to increased production at a lower cost. However, their use is limited by the complexity of the geometries the moulds can produce, and intricate parts must be divided into multiple smaller components, each requiring its own mould. Only after an arduous assembly procedure requiring several time-consuming joining processes is the desired part completed.

2.1.3 AM Obstacles

2.1.3.1 Running Costs

AM machines, particularly those that can operate on an industrial level and produce components of a quality that rivals those made by traditional methods, are exceedingly expensive. As mentioned, the average cost of an industrial metal AM system in 2017 was over \$400,000. This is partly due to the

complexity of the machines and the technology they employ but also due to the industry's infancy, market competition, and the relatively low volume being sold [6].

After purchasing the necessary machinery, another cost associated with AM is the elevated material cost compared to that needed for standard manufacturing methods. Some manufacturers only offer machine warranties on the proviso that the customer will solely use material purchased from that company, reducing competition. Thermoplastics used in material extrusion processes are produced at a relatively similar cost to those used in injection moulding. However, the cost of production of metallic powder for use in powder bed fusion far exceeds that of its traditional counterpart due to the complex and expensive processes that were undertaken to create them. Each type of machine will have its own running costs comprising of those related to operation, such as an inert gas like argon and electricity, or consumables such as new filters between builds and other clean-down procedures [5,6,9,10].

2.1.3.2 Cost justification

AM rarely makes business sense if assessed on a like-for-like cost comparison with conventional processes. However, the price of the technology cannot be constricted to this dictatorial approach of cost at the point of purchase, and many of the financial benefits AM offers are realised through a component's lifespan [15]. For example, a traditionally made part for use in a vehicle may cost half that of its AM equivalent. However, a weight reduction of 30 % may mean that the savings over its operation lifetime are more significant than the initial price differential, and AM suddenly becomes more economically viable. Additionally, significant savings have been realised in industry case studies, for example, turbine blade repair, airframe component material utilisation, and forged engine components [10].

2.1.3.3 Machine throughput

Increasing AM component throughput will reduce the cost of AM parts, allowing the machine depreciation to be distributed across a more significant number of parts over its lifetime. Current build chamber volumes limit both the size of individual components and the number of parts that can be produced in one build cycle and, therefore, the effective throughput. The processes that must be carried out between builds for many systems are time-consuming, and reducing these instances will increase production. Increasing operating speeds naturally increases throughput and can be achieved in powder bed fusion systems with the use of multiple lasers working simultaneously to fabricate the part [6]. This is a relatively new technology and requires further research to determine its effects on component properties.

One conceptual technology that is making promising developments is those of continuous production techniques, an example of which is shown in Figure 2. These would allow parts to be made continuously, with the only intervention being the resupply of the build material and required maintenance. This would drastically increase production and also allow for the construction of much larger components [16].



Figure 2 Stratasys H2000 Infinite Build 3D printer [17]

2.1.3.4 Certification & Quality Assurance

As with any new technology entering a market, AM must be assessed to make sure it complies with the rigorous quality control that governs the sector. These are particularly stringent in the highly regulated medical and aerospace industries, where the certification of new designs, processes and materials are often time consuming, complex, and expensive [10,18]. These components must meet or surpass the existing international standards that govern the industry, which often relate to materials' properties or the level of defects. Part quality is not always the challenge for parts produced through AM methods; however, inconsistency over long production runs is well documented due to issues such as porosity, cracks, un-melted regions, and surface roughness [6,19].

2.1.3.5 Corrosion Resistance

Metallic parts produced through various AM processes are renowned for having greater variability in corrosion resistance than their traditionally manufactured counterparts. This is predominantly due to the physical and chemical processes undergone during their fabrication and the effect these have on the microstructure. As mentioned previously, the majority of research into AM metal components has focused on their mechanical properties, bringing them to the point where they can replicate the

performance of conventional parts. Therefore, work still needs to be done to improve the corrosion resistance of AM parts and the consistency of this failure method [9].

2.1.4 Additive Manufacturing Methods

2.1.4.1 System Classification

Several processes can build parts using additive layer manufacturing (ALM), creating the designed geometry by adding material layer by layer. Due to the nature of each manufacturing process, each ALM technology is bound to a specific list of materials that it can administer. Broadly speaking, these are plastics, composites, ceramics, and metals. Within these processes, the parameters they employ to create the desired parts cause large variability in the output's specification [8,20]. These include part density, geometrical accuracy, and surface roughness. For metal-based AM systems, the feedstock can be separated into 3 different categories, namely those of powder bed, powder fed and wire fed [4–6,9].

The main types of metal AM processes found and the technology they use are those of:

- Powder Bed Fusion (Direct metal laser sintering/Electron beam melting/Selective laser melting (SLM))
- Binder Jetting (Powder bed/Inkjet head printing)
- Direct Energy Deposition (Laser metal deposition)
- Sheet Lamination (Laminated object manufacturing/Ultrasonic consolidation)

Other processes include:

- Binder Jetting (Plaster-based 3D printing)
- Material Extrusion (Fused deposition modelling)
- Material Jetting (Stereolithography)
- VAT Polymerisation (Digital light processing)

However, these manufacturing methods are limited to the production of polymers, ceramics and composites.

2.1.4.2 Powder Bed Fusion

The term 'powder bed fusion' (PBF) is used to define all processes that use concentrated energy in the form of an electron beam (EBM) or LPBF to selectively melt or sinter material in powder form, fusing the layers of powder together to create the desired geometry over time. This technology can be used

for an extensive list of materials; however, the method used to melt the powder must be tailored to the material in use and its melting point [5].

All PBF processes share a fundamental set of characteristics. These include a thermal source, usually in the form of a laser (commonly referred to as laser sintering), to induce fusion between the powder particles and a method of controlling the direction of such a source with a focusing lens [21]. They also require a system to evenly and smoothly distribute the powder across the build plate at a predefined layer thickness (LT), often made up of a powder dispenser and a roller/rake. The construction of parts by this technique occurs in an enclosed chamber that is filled with an inert gas, usually nitrogen or argon [21,22]. These help to minimise the oxidation and degradation of the powder. More advanced machines may use apparatus to direct the flow of the inert gas across the build plate to carry away any 'balling', spatter or unwanted gases created during the sintering of the powder. Also, prior to the build cycle, the build chamber is bereft of oxygen using a vacuum pump, again to minimise oxidation of the part during building [22].

For polymers, the neighbouring powder acts as scaffolding for the part and therefore, additional support structures are rarely required. For metal parts, support structures are required to anchor them to the build plate [10,21,22]. The geometries associated with some parts can also necessitate the use of supporting constructs, often those at an angle greater than 45 °. Thermal gradients are high within the build chamber and can lead to large thermal stresses and distortion if these fixtures are not used [23].

2.1.4.3 Binder Jetting

Binder jetting works by depositing a liquid binder onto a powder layer by layer. Depending on the material, other processes, including curing, sintering, infiltration, and consolidation, are used to complete the part [24–26].

Binder jetting can create parts built from a range of materials, from polymers and metals to composites and ceramics. It can also be used to rapidly manufacture casts from sand. The process begins with the CAD file being imported into the printer, and the powder for the part to be built from is poured into the hopper. An initial layer of the powder is distributed evenly across the build plate at the designated thickness, and then the printer head moves across the plate, depositing the liquid binder where necessary to create the geometry at that layer. That layer is then briefly cured before the build plate is lowered by an amount equal to the LT, and these steps are repeated until the part is constructed[24].

Once the binder is dry, a fragile binder-material mix remains. The build must then be removed and placed in a furnace to cure the part to give it its mechanical strength. The parameters of this step depend on the type of binder in use. Composites, polymers, ceramics, and sand moulds can usually move straight to post-processing steps after this is complete. When cured, metal parts produced by binder jetting require sintering to sinter the loose powder and burn off the loose powder. However, this leaves a highly porous part requiring infiltration or consolidation to increase its density.

Binder jetting machines are capable of building parts at relatively high speeds and at low cost; however, metal parts will take longer due to the necessity for sintering and infiltration/consolidation [25,26]. Due to the relative lack of research in the field, the materials currently available to manufacture with binder jetting technology are limited compared to DED and PBF. Resultant parts created by this method often have a limited level of accuracy and poor surface finish, requiring work afterwards [24].

2.1.4.4 Direct Energy Deposition

Direct Energy Deposition (DED) processes use focused thermal energy, similar to that of powder bed fusion technology, in the form of a laser or electron beam to fuse the materials into the desired geometry by melting [27,28]. These processes differ from LPBF in that the material, in the form of a fine powder or wire feedstock, is melted as it is being deposited. The heat source also simultaneously melts the substrate to which the feedstock is deposited. This process has been referred to as blown powder AM, laser cladding and Laser Engineered Net Shaping (LENS). Polymer and ceramic parts can be formed using this technology, but it is predominantly used for metal powders. Those DEP machines that use a wire-based feedstock are essentially extensions of standardised welding technology, feeding a solid wire into a molten pool.

One significant and unique benefit of DED is that multiple materials can be deposited simultaneously on the build surface, allowing the possibility for functionally graded parts. Another is that the deposition head on most DEP systems is on a multi-axis motion system or robotic arm, meaning the build process is not limited to uniaxial builds as in other processes like PBF [27,28].

As with PBF, the build chamber is confined for safety reasons and to allow for a controllable atmosphere. While nonreactive metals do not necessarily require the chamber to be filled with an inert gas, a shielding gas aimed at the melt pool is sufficient to remove the risk of oxidation.

2.1.4.5 Sheet Lamination

Sheet lamination creates the predefined geometry by stacking sheets of the chosen material and bonding them. It joins these sheets through the use of either adhesively joined or metallurgically bonded through the use of brazing, diffusion bonding, laser welding, resistance welding or ultrasonic consolidation [23]. After each layer is bonded to the substrate, it is machined to create the required geometry at that designated layer. This is less efficient than other additive processes, as waste material is created. However, most methods allow the production of complex parts that cannot be manufactured by conventional subtractive or net shape methods, such as overhangs and concealed geometries.

Sheet lamination, like PBF and Binder jetting processes, has the ability to construct parts from the four main material groups: metals, polymers, ceramics, and composites. The bonding method employed is dependent on the material to be built with [6,9].

Some benefits of the parts built by this technology include the speed at which it can make large parts with a relatively good surface finish and at low cost. However, it can lead to parts with anisotropic properties, and there is still a need for post-processing. Also, adhesively bonded parts are more susceptible to tensile and shear loading conditions in the plane perpendicular to the build direction.

Ultrasonic consolidation is widely regarded as one of the more promising techniques for producing parts through sheet lamination and is advantageous when attempting to create parts made with metal composites by using alternate sheets of dissimilar metals. Many AM processes also allow for the possibility of smart structures such as electronics, actuators, or heat pipes to be integrated into a component during the build, and ultrasonic consolidation offers several advantages. UC is currently the only mainstream technology that can form metal structures without subjecting them to extreme temperatures, and large internal cavities can be designed to enable the placement of these smart structures [23].

2.1.5 Applications

The automotive, aerospace, and medical/dental/veterinary industries provide the driving force behind the development of metallic AM [6,9,23,29]. These sectors are, therefore, the areas where metal AM's growth is most pronounced and closest to being manufactured on a larger scale [30]As the technology's development gains even more momentum, the cost of these processes will decrease while the range of applications and quality of components will increase.

2.1.5.1 Automotive

Product development within the automotive industry is critical but is often expensive and time consuming. Commercial automotive companies have been using AM technology to create prototypes, which has shortened their product development cycles and lowered costs.

More recently, as the technology has developed and the costs of the processes have decreased, they have also been using AM for low quantity fabrication of structural and functional parts, often for luxury or low volume production vehicles [12]. It can also be beneficial in the aftersales market for producing spare parts on demand and replacing components that have been discontinued because the model's production line is deceased.

Motorsport has long been at the forefront of technology, and its approach to AM is no different. The incredibly low scale production, as well as the complexity of components, means that AM is well suited for this sector and allows designers more manufacturing freedom, without the restrictions of traditional processes. These freedoms can incorporate anything from lighter components to complex internal geometries, which can enhance internal flow path efficiency in fluid systems and reduce demand on other parts, in some cases by up to 250 % [31].

Within Formula 1, the Fédération Internationale de l'Automobile (FIA) technical regulations for the 2020 season state that the car's mass, excluding fuel, must be above 745kg. This figure must include the mass of the driver, which in turn must be no less than 80kg [32]. While this must be obeyed, if parts, particularly those deemed non-critical, can be lightened through AM, other, more essential parts can be increased in size to enhance reliability and strength. Mass could also be added to different areas of the car to improve the weight distribution, all while remaining at the minimum threshold demanded by the regulations.

Motorsport races occur across the globe throughout the year. This requires the transportation of race-ready cars and a significant number of spare parts, amongst other items, around the world at eye-watering expense. Often, updates in aerodynamic parts occur between race weekends, sometimes within a weekend itself, and new components must be flown directly to a track. Through further research and technological advancement, AM could be utilised in the event of a crash or failure to manufacture replacement parts on-site, thus reducing the number of components requiring transport between tracks. This is particularly relevant when the sport is making significant changes to reduce its emissions and lower operating costs.

2.1.5.2 Aerospace

The requirements of the aerospace industry are often far greater than those of other sectors, particularly when discussing the complex geometries and advanced materials required by their in-service components. Materials such as titanium alloys, nickel superalloys and high temperature ceramics are often used due to the extreme conditions undergone during a normal operation and these can be expensive and time consuming to manufacture using standard methods. Additionally, the production of aerospace components usually occurs in much lower quantities compared to other industries. This works within one of the current limiting factors of AM, that larger scale production of parts becomes uneconomically viable beyond a certain point.

One early example of the use of AM for an end-use component within the aerospace industry occurred on the 5th of November 2015. On this date, Rolls-Royce concluded the first test flight of one of the largest aero-engine components produced by ALM at that time in their new Trent XWB-97 engine. The 48 stators housed at the inlet, which guide the air into the compressor, were made from titanium by ALM [33].

Boeing and Bell helicopter have also been using additively manufactured polymer parts for non-structural parts since the mid-1990s on both military and commercial aircrafts. Space agencies such as NASA, the ESA and SpaceX are utilising AM's capabilities to produce vital components for rocket engines like igniters and combustion chambers [6].

2.1.5.3 Medical/Dental/Veterinary

The medical, dental, and veterinary industries best demonstrate AM's practicality for mass customisation and bespoke designs. In these industries, the need for the production of two identical parts is incredibly rare, with each patient requiring anything from minute to major adaptations to an initial design to optimise it for their needs and specifications.

The list of possible applications within these industries is extremely extensive, including both intrusive procedures and external aids.

There is a huge market in these sectors for orthopaedic implants, prosthetics development, surgical and diagnostic aids, and tissue engineering [30,34]. The capability to fabricate trabecular structures for implants increases osteointegration, with the porous surface creating a better environment for bone tissue to grow into [6,29].

Due to the nature of the environments they reside in, the materials feasible for these components are largely restricted. When in place, they must not cause any internal damage, both physical and through

other means, such as the chemical composition of the component. There is currently a limited number of approved polymer materials that are classified as safe for invasive procedures; however, metal systems are used regularly for a wide range [34–36]. Often, titanium is the material of choice, but it is very costly. Cobalt chromium and stainless steels with higher concentrations of elements such as molybdenum are both plausible alternatives, provided they have the required biocompatibility for the application.

2.1.6 Process Parameters

The processes employed in the fabrication of AM parts have a dramatic effect on the physical and microstructural characteristics of the final part, as well as the inclusion of defects. These include part density and porosity, residual stresses, and grain boundary variation. A huge amount of work has gone into understanding the impacts these process parameters have on the mechanical and electrochemical properties through both computational and experimental methods [37–47].

The process parameters for LPBF systems can be allocated into four classifications:

- Laser parameters
- Scanning parameters
- Powder parameters
- Temperature parameters

Laser parameters include laser power (P), spot size, and exposure time (ET), with the scanning parameters including scan speed (V), hatch spacing (HS), and scan pattern (the path the laser traverses when melting the powder). These, when combined with the LT and through the use of equation 1, gives the volumetric energy density (VED) of the laser.

$$VED = \frac{P \times ET}{PD \times HS \times LT} \quad 1$$

VED has a direct relationship with the final part density, as shown by the graph in Figure 3. The optimum laser parameters and energy density value fluctuate for different materials, but the trend displayed can be observed across all metals that have been successfully processed by AM.

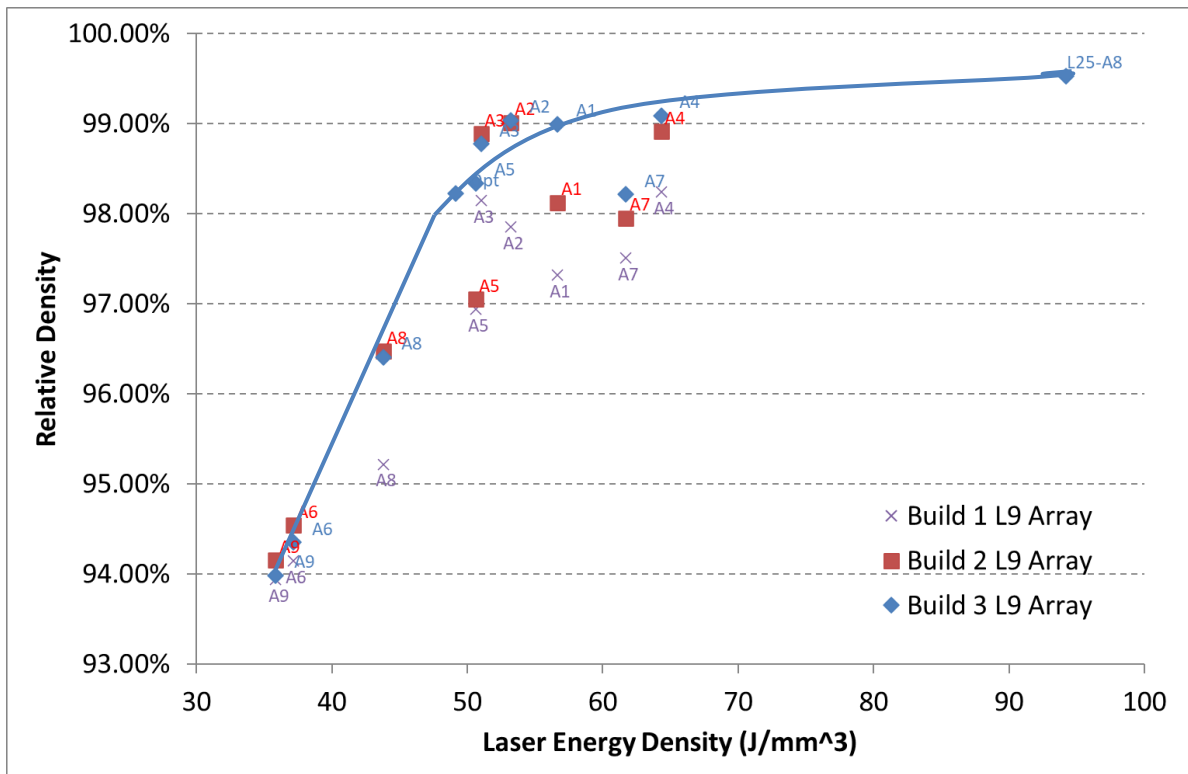


Figure 3 Part density vs laser energy density for 316L [48]

Figure 4 shows a graphical representation of melt pool formation from two different orientations, also depicting how different energy densities generate distinct melt pools. A preferential melt pool uniformly overlaps all surrounding pools, leaves no unmelted powder, and is achieved by using a machine's optimum parameters for the given material. It is highlighted in the figure as 'normal'. These constraints will likely produce a part with the highest density. Increase the energy density further, and keyholing is often seen, with the laser penetrating much deeper into the substrate and creating pores. This higher energy density can also cause vaporisation of the metal, the gas of which cannot escape, forming gaseous cavities within the part. If an insufficient energy density is incident on the powder, the melting will be incomplete [49].

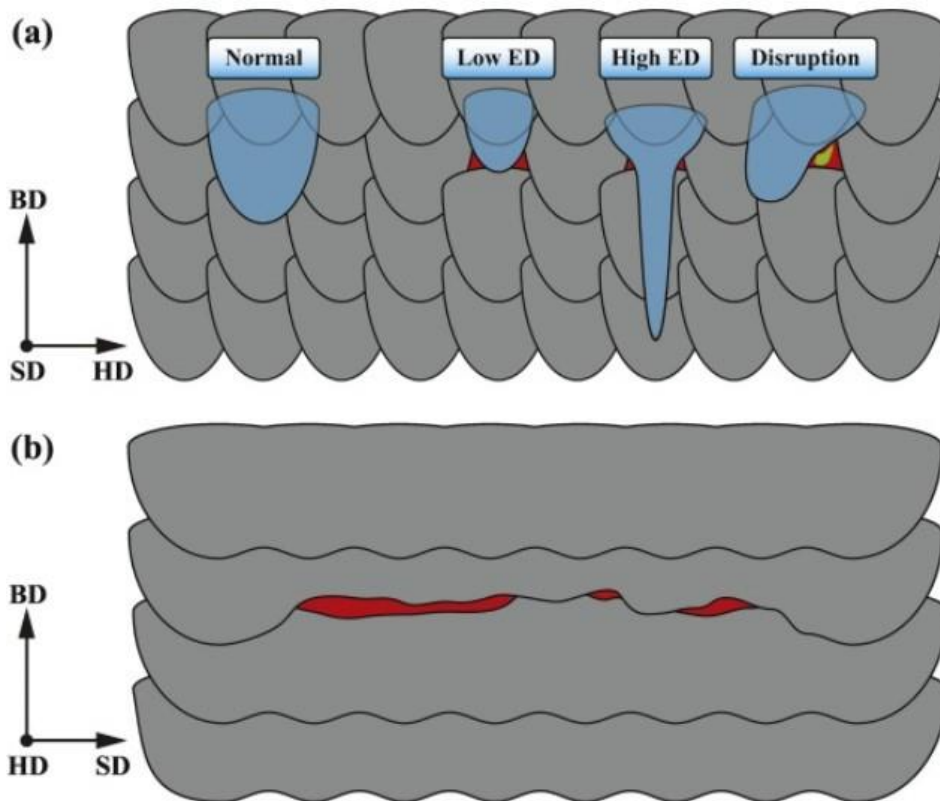


Figure 4 Melt pool geometry vs energy density [50]

2.1.7 Powder Parameters

Powder parameters are important to consider when building through LPBF, as they have a direct effect on the final quality of the part. Generally, a higher-quality powder, which is to say, a powder with smaller and more spherical particles, creates parts of superior quality compared to those made with a powder consisting of larger, irregularly shaped particles. Finer particles are also known to absorb laser energy more efficiently than rougher particles, reducing the input required to create the part.

Higher quality powder, along with an effective, uniform powder distribution mechanism, has a significant effect on powder bed density, which typically ranges from between 50 % and 60 % for most commercially available powders, as well as being crucial for surface quality [20]. A higher powder bed density naturally translates to a higher final part density as well as higher thermal conductivity and, therefore, beneficial properties, provided all other variables are controlled [9].

2.1.8 Temperature Parameters

The temperature of the build plate and the temperature of the atmosphere within the build chamber can both be controlled during the build. Often, inbuilt systems are used to preheat the chamber atmosphere and build plate prior to and during the process. This has been shown to reduce the laser

power requirements for the build and help diminish the effects of any nonuniform thermal expansion or contraction instigated throughout the parts construction [23].

With all these parameters, trade-offs must be made between dimensional accuracy, electrochemical and mechanical properties, build rate, surface finish and cost, among others. With regards to which ones to prioritise, it depends completely on the application of the final part, and the level of post processing that can be performed to enhance its properties.

2.1.9 Powder Metallurgy

The quality of the metallic feedstock, and in this case the powder used in AM practices, influence the quality of the final part. Powder quality is controlled by the size, shape, composition, and internal porosity. The causality of these differences stems from the processes used to produce the powder.

2.1.9.1 Powder Production

The two main methods used in powder production are those of gas and plasma atomisation, which utilises induction heating and plasma torches, respectively, to melt the metal. Both these processes occur within an inert gas or vacuum to minimise oxide or other contamination and are displayed in Figure 5. High-velocity gas is directed at a stream of molten metal, breaking it into droplets which, as they fall into a collection chamber, solidify in spherical formation. Variations in the parameters involved will influence the shape and diameter of the particles formed, as well as their uniformity [51]The production method used depends on the material to be atomised, the production volume, and the level of purity required. Novel methods for powder production are being developed to reduce the cost of creation while still providing the requisite quality.

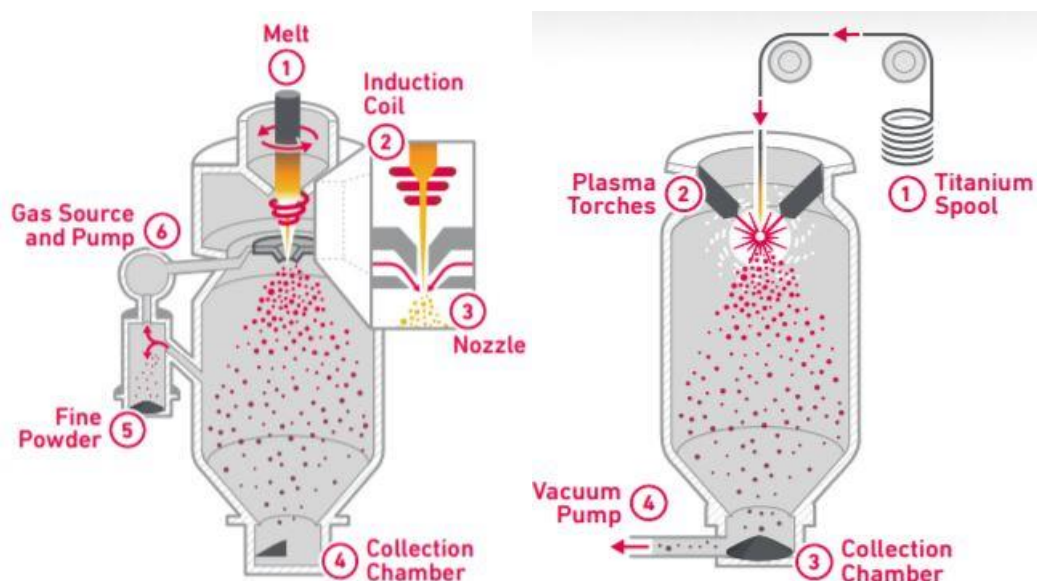


Figure 5 Gas atomisation and plasma atomisation [52]

2.1.9.2 Powder Recycling

As mentioned previously, one of the main expenses incurred during AM is the cost of building materials. During the fabrication of parts created by powder-based mechanisms, all the powder that is not fused to create the geometry would theoretically be wasted. In builds with tall, intricate parts, the unused powder can make up the majority of the building mass, the loss of which would amount to high operational costs and leave the technology uneconomically viable [53].

To circumvent this expenditure, operators can employ powder recycling, thus lowering the quantity of new powder that must be used to create each part. This can be done simply by collecting the unused powder from the build chamber and replacing it in the hopper. However, this approach can allow for larger and more irregular particles, formed through effects such as balling, to be recycled. To avoid this, sieving is used to only allow particles with a certain diameter to be reincorporated. [53]. This slightly increases the level of waste; however, it is beneficial to the quality control of parts to be made from this powder. The feedstock is then topped up with virgin powder.

The possible effects of powder recycling have been researched, and the general consensus is that, with the use of sieving, particle size distribution (PSD) remains fairly constant, regardless of the number of times it is reused. This is displayed in Figure 6, which shows minimal change in 316L PSD over a 30-build sample period. Some reports suggest an increase in the flowability, possibly due to the reduction of smaller particles and, therefore, reducing the packing factor [54].

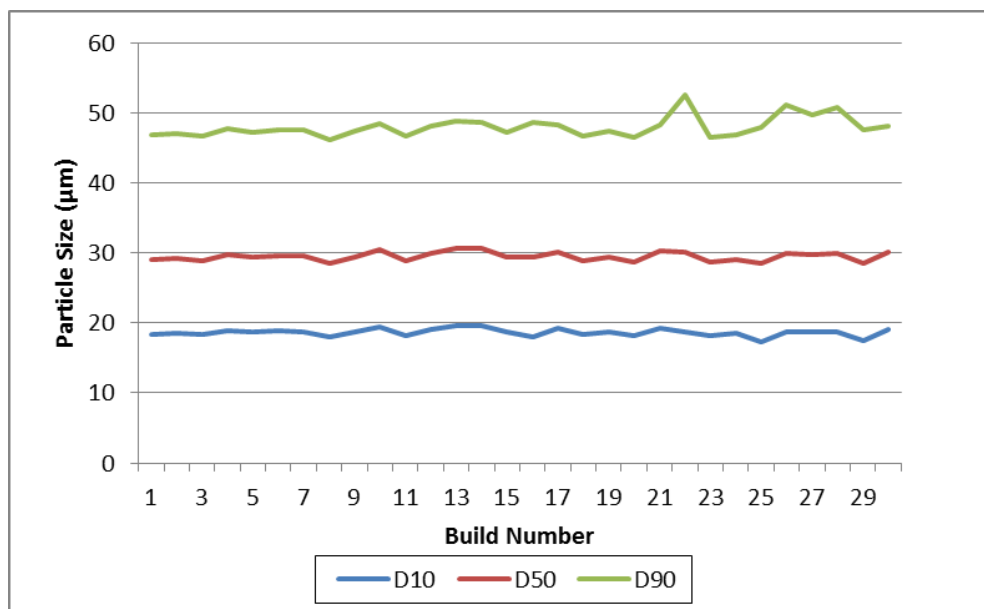


Figure 6 Particle size variation over the rebuild period for 316L [48]

2.1.10 Post Processing

The post-processing of AM parts is an important stage in the manufacturing production line and is used to a far greater extent than parts made by conventional methods. The degree to which it is required is dependent on the technology and process parameters used to fabricate it, as well as its intended application. Different AM processes generically cause a certain quality of surface finish, density, and microstructure. These are important consequences that must be considered when choosing the technology used in the creation of a component. A process that requires a greater level of post-processing to bring it to a level that meets the stringent requirements of engineering applications will incur higher production costs as well as increase the throughput time of the part [6,9,55].

Mechanical operations are used to remove the parts from their build plate and increase the quality of the surface finish to the desired level. To affect the part on a microstructural level, thermal processes, in the form of heat treatments and hot isostatic pressing (HIP) are used.

2.1.10.1 Surface Treatments

AM processes often result in a poor surface finish, which is often unsuitable for certain applications [6]. The unsatisfactory quality must be improved upon as, aside from affecting the aesthetic appearance of the part, high surface roughness can have detrimental effects on the part's fatigue and frictional properties, as well as possibly acting as crack initiation points [55]. Often, it is difficult to characterise overall surface roughness in AM parts due to varying surface qualities that are dependent on build orientation. Treatments to improve the surface quality include the sole use of mechanical actions, such as machining, media blasting and shot peening. Mechanical processes combined with chemicals, such as electropolishing, can also provide desirable qualities [56,57].

Initially, media blasting is normally used to clean the part and remove any remaining residual powder from its fabrication. The mediums usually used for this process consist of sand or glass beads. Shot peening is essentially an extension of this, using compressed air to fire small steel ball bearings (or a comparable media) against the part to flatten the surface. It is often described as having a micro-forging effect, smoothing the surface as well as having the capacity to strengthen it [6].

The methodology for machining AM parts is the same as that for conventionally manufactured parts. Machining is the removal of material, so extra material is usually added when necessary to a CAD design where machining will be required. Micromachining combines a chemical reaction on the surface of the material with fluid flow to remove all waste material.

Other, more complicated methods, such as anodising, plasma spraying, and electroplating, can be used to produce a very high-quality surface finish. Plasma spraying, in particular, can improve corrosion protection and wear resistance and give preferential electrical characteristics [58]. These processes, however, are infrequently used due to their high cost, and therefore, a part's final application and environment must be considered when assessing the surface treatments to be employed.

2.1.10.2 Post-Heat Treatments

Once any material removal required to create the final geometry has occurred, thermal processes are usually used to alleviate residual stresses generated during the additive process, as well as impart superior mechanical and chemical properties [6,9]. Residual stress within parts of metal AM is unavoidable due to the rapid temperature changes they undergo during fabrication. As the metal endures these variations, it expands and contracts within microseconds while still being constrained by the structure around it. When contraction occurs, shear forces between layers are produced. Depending on the power of the fusion method, multiple layers beneath the surface may be re-melted during the process.

Each specific metal alloy is likely to have a 'recipe' involving temperature, hold time and cooling method. These recipes have been optimised so that once the process has been undertaken, it leaves behind a material with preferential properties. Materials often have recipe variations so that the microstructure and other properties will be affected in different ways, depending on the application.

The cooling process is as important as the heating of the alloy as it can have a significant effect on the microstructure and characteristics of the final alloy. A slow cooling rate of 1-20 °C/s through the austenitic region is used in the annealing of metals. This requires a furnace with controlled cooling, as exposing the metal to the air outside the chamber will cause it to cool at a faster rate. The aim of a full anneal on steel is to raise the temperature of the alloy above its austenitic temperature for a sufficient time so that it forms a fully austenitic grain structure. Once this is achieved, the slow cooling mentioned previously aims to transform the microstructure from austenitic to pearlite. Pearlite is made up of a lamellar structure comprising of ferrite and cementite. This results in the alloy becoming more malleable and ductile but compromising other mechanical properties such as yield strength and hardness.

Other microstructures are achievable with the application of different temperatures and cooling rates. TTT and CCT diagrams are useful tools when designing a heat treatment recipe to manipulate the microstructure of a metal to achieve the desired result. A crucial factor to consider when using these

diagrams for steels, alongside phase diagrams, is the carbon content in the metal. Hypoeutectoid steels are steels with less than 0.76 wt.%C, and those with greater are designated hypereutectoid. Increased carbon composition results in greater formation of cementite through the treatment, increasing hardness and strength but compromising ductility and toughness. Another is the alloying additions to the metal and their effect, as different elemental compositions will cause variations in the eutectoid temperature.

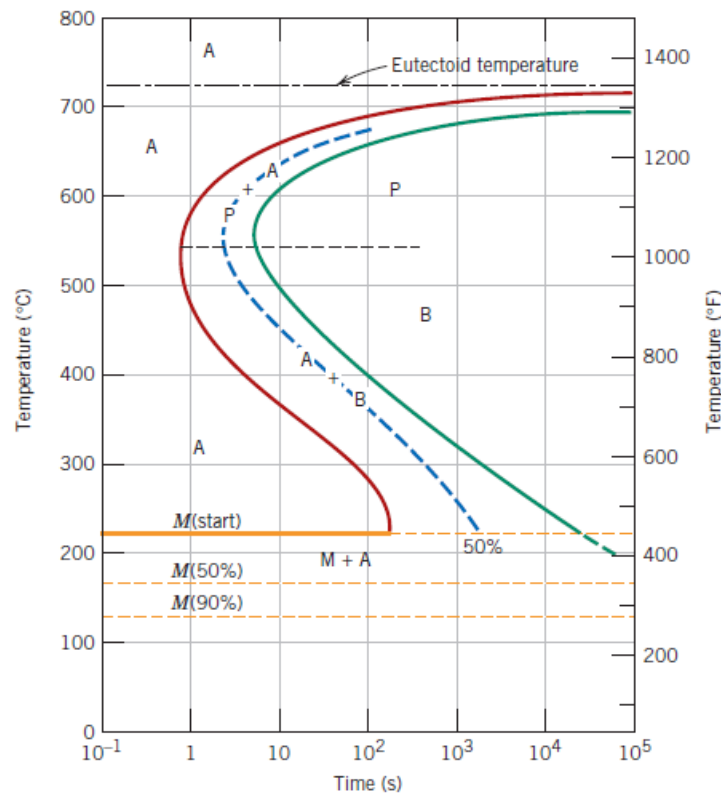


Figure 7 Isothermal transformation diagram for iron-carbon alloy 0.76 %C [59]

Figure 7 shows the TTT diagram for an iron-carbon alloy. The initials 'A', 'B', 'P', and 'M' represent the austenite, bainite, pearlite and martensite regions, respectively. The beginning of the transformation is designated by the red line and the end by the green, with the dashed curved line representing the point at which a 50/50 split is achieved, either between austenite and pearlite or austenite and bainite. At higher temperatures of transformation, the carbon diffusion rate is also higher, leading to a coarser structure. Once austenite has partially or fully transformed into pearlite or bainite, it cannot be transformed further unless the alloy undergoes austenitisation. For iron-carbon alloys with different elemental compositions, a proeutectoid phase is likely to coincide with pearlite.

Martensite is a non-equilibrium phase and, therefore, does not appear on the iron-carbon phase diagram. It can be seen that the formation of martensite for this particular alloy in Figure 7 occurs instantaneously at approximately 215 °C. As further cooling occurs, the alloy becomes less austenitic

and more martensitic, as shown by the phase composition at 165 °C and 125 °C being 50 % and 90 % martensitic, respectively.

TTT diagrams are, however, not the most practical to use in real life as the alloy must be rapidly cooled but then maintained at a controlled, elevated temperature. This is exceptionally hard to dictate. They can be modified for the use of continuous cooling methods by delaying the time it takes for the reactions to begin and end, as well as lowering the temperatures they occur at. This creates the CCT diagram. A slow, continuous cooling process is likely to result in a coarser pearlitic structure, whereas a faster cooling time will produce a finer formation. Due to the nature of continuous cooling, bainite will not typically form when plain carbon steel is cooled to room temperature using this method. This is because the austenite will have fully transformed into pearlite before the bainitic transformation becomes possible.

For alloyed steel, there is a critical cooling rate which, when exceeded, will produce a totally martensitic structure. Slower rates will produce structures with a combination of martensite and pearlite unless they are slow enough to create a 100 % pearlite formation.

2.1.10.3 Hot Isostatic Pressing

Hot isostatic pressing is a form of heat treatment that also incorporates a high, uniformly distributed pressure to improve a material's properties. Usually, an inert gas, such as argon, is used in the containment vessel so that the material does not react chemically whilst undergoing the procedure. The HIP process variables include the temperature/s and pressure/s that the atmosphere is taken to, the time the atmosphere is held at these levels, and the method used to cool the material.

The technique is usually applied to sintered and cast parts to increase their density, which is closer to the theoretical value. The advantages of hipping are well known; aside from increasing the density, it can eliminate surface and internal porosity, improve mechanical properties, and create a finer grain structure, among other improvements [60,61]. These will take the part's metallurgical properties closer to that of its conventionally made counterpart [62]. HIP is regularly used on AM parts that are to be employed in critical applications, such as in the aerospace industry, which has much finer tolerances, as part failure can be catastrophic.

2.2 Metallurgy

2.2.1 Steels

Metals can be separated into two categories: ferrous and non-ferrous; the former means the composition is dominated by iron, and the latter is not. Steel is ferrous and is one of, if not the most

common metals used in engineering applications due to its low cost, high strength, and good formability. Steel can be classified into 4 sub-groups: plain carbon steels, low alloy steels, tool steels and stainless steels. Plain carbon steels can be further devolved into low carbon, medium carbon, and high carbon steels, containing up to 0.25 wt.%C, 0.25 – 0.6 wt.%C, and >0.6 wt.%C, respectively. Iron-based alloys containing greater than 2 wt.%C are no longer classed as steel. Instead, they are branded as cast irons [63].

Steels have an immense variety of uses, with the carbon content being a significant contributor to these. Lower carbon steels have high ductility and toughness properties, as well as reasonable strength, and accounts for the lion's share of global steel production [63]. Medium steels are often used for applications such as casting, forging, and axles, while the hardness and strength of high-carbon steels make them the choice material for tools and dies.

Steels can be further alloyed with a large number of other metallic elements to provide useful mechanical, chemical, and conductive properties specific to the end application, meaning the number of possible combinations is immeasurable.

One major negative of standard steel is that it corrodes freely under a range of standard atmospheric conditions, with its characteristic red rusting due to iron.

2.2.2 Microstructure

Steels are comprised of different microstructures, namely ferrite, austenite, cementite, pearlite, martensite, and bainite. These different microstructures, when occurring at varying levels, provide the steel with distinct characteristics. For example, ferritic microstructures are associated with strength, corrosion resistance, and stress-corrosion resistance, whilst austenitic microstructures offer increased toughness and weldability. Duplex stainless steels utilise all of these credentials as they generally comprise of a 50/50, ferritic/austenitic split.

In iron, the element that steels comprise the most of, two main types of crystal structures are present, body centred cubic (BCC) and face centred cubic (FCC). The former is present at temperatures below 910 °C (α -Fe) and above 1400 °C (δ -Fe), with the latter (γ -Fe) occurring at the intermediate temperatures. These structures are illustrated in Figure 8 and Figure 9, respectively [64].

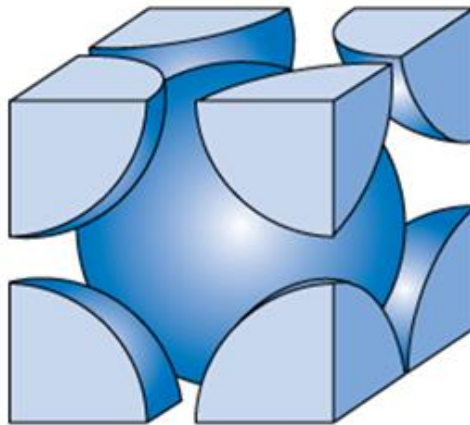


Figure 8 Diagram of BCC structure [59]

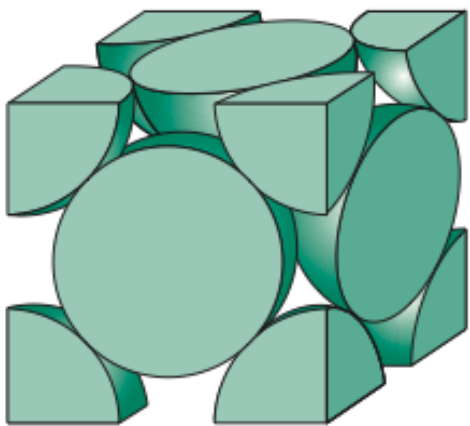


Figure 9 Diagram of FCC structure [59]

The type of microstructure or phase can be manipulated through the use of heat treatments, compositional changes, and external pressures. The lines on the iron-carbon phase diagram in Figure 10 represent the boundaries between these at certain temperatures and compositions. The key focus of this system is the degree to which carbon is dissolved in interstitial solid solution. FCC structures have larger interstitial holes than their BCC cousins, leading to a much lower solubility in BCC microstructures (ferritic) than FCC (austenitic).

Figure 10 indicates that, in the α -Fe phase, the solubility of carbon is at its minimum of 0.005 wt.%C when at 0 °C, and a maximum of 0.022 wt.%C at 727 °C. As the temperature is increased past 912 °C, the lattice structure becomes FCC as it enters the austenitic phase which has a much higher solubility for carbon. It maxes out at 2.14 wt.%C at 1147 °C and a minimum of 0.76 wt.%C at 727 °C, the temperature, prior to any further decrease, which would take it back into the α -Fe phase. The δ -Fe phase, whilst still ferritic, has carbon solubility over 4 times higher than that of the α -Fe, at 0.09 wt.%C, occurring at 1493 °C, just before the melting point of pure iron at 1534 °C.

Finally, the diagram also indicates that a fully cementite microstructure is only present once the carbon solubility surpasses 6.7 wt.%, at which point the alloy becomes iron carbide.

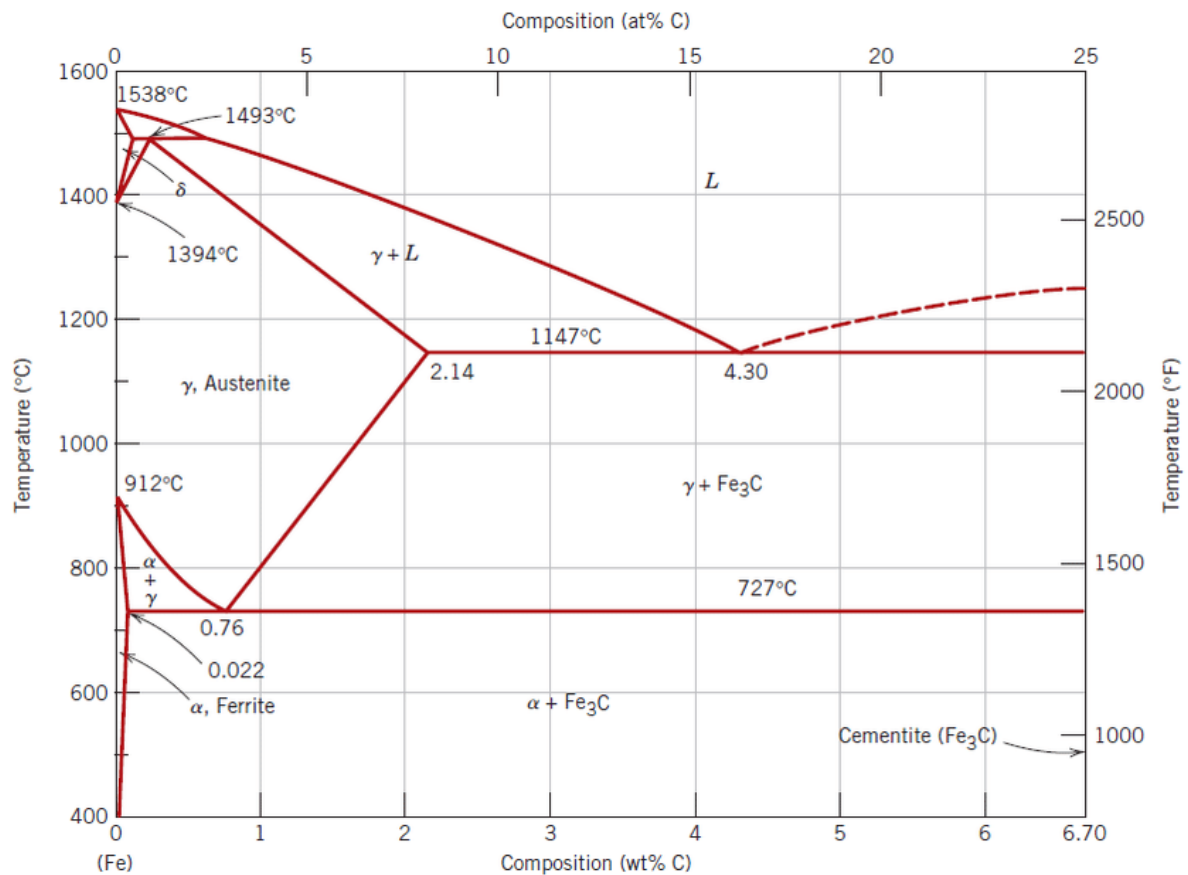


Figure 10 Iron-carbon phase diagram [59]

The eutectic reaction occurs at 1147 °C, where liquid iron containing 4.3 wt.%C forms γ-Fe with 2.14 wt.%C, and cementite with 6.7 wt.%C. The eutectoid point is the point at which the austenitic microstructure produces α-Fe with a carbon solubility of 0.02 wt.% and Fe₃C, again with 6.7 wt.%C. This latter reaction occurs when the alloy is in a completely solid state. Additional alloying elements have significant effects on the eutectic and eutectoid temperatures.

It is important to understand this diagram and others such as Isothermal transformation diagrams (TTT) and Continuous cooling transformation diagrams (CCT) as, whilst phase diagrams show how an alloy proceeds towards an equilibrium state depending on its composition, there is no indication of the time required to achieve it.

2.2.3 Available steels

2.2.3.1 Stainless Steels

Stainless steels differ from generic steels due to the alloying addition of chromium, with the minimum quantity of Cr required for it to be classed as stainless being 11 wt.%Cr [65]. This supplement provides the steel with a superior level of corrosion resistance, as a passive layer of chromium oxide forms to cover the damaged surface or corroding site, protecting it from further attack [66]. Duplex and super duplex stainless steels contain substantial amounts of alloyed chromium (22 % and 25 %, respectively), providing them with significant pitting corrosion resistance, even in the harshest of environments. Chromium is, however, very expensive and due to this, its use is limited where possible. Large amounts of it can also compromise the material's mechanical properties and workability [67].

The designations for each wrought steel grade are most commonly known by the three-digit number prescribed to them by the American Iron and Steel Institute (AISI). For example, numbers in the 200 range contain all manganese and nitrogen austenitic stainless steels, whereas those in the 300 range represent those austenitic stainless steels containing nickel. The 'L' notation succeeding some numbered grades denotes that it contains a low carbon content, <0.3 %. This lower carbon content is often associated with increased corrosion resistance as well as slightly lower strength at extreme temperatures. The global production of stainless steel was circa 52.2 million metric tonnes in 2019, over 27 million more than it was ten years before [68].

2.2.3.2 316/L Stainless Steel

Grade 316 stainless steel is the second most common austenitic grade after 304 and is widely regarded as the 'marine grade' stainless steel due to its increased resilience to chloride-rich environments [69,70]. Grade 316L differs from standard 316 as its chemical composition contains a lower percentage of carbon. The benefits of this include its immunisation from sensitisation, greater corrosion resistance, and the inhibition of carbide precipitation at grain boundaries. It is, therefore, often used in components that require a degree of welding [29,70]. The chemical composition ranges for 316L stainless steels can be seen below in

Table 1.

Table 1 Chemical composition ranges for stainless steel 316L [70]

| Element | C | Mn | Si | P | S | Cr | Mo | Ni | N | Fe |
|---------|------|-----|------|-------|------|------|------|------|------|-----|
| Min | - | - | - | - | - | 16.0 | 2.00 | 10.0 | - | Bal |
| Max | 0.03 | 2.0 | 0.75 | 0.045 | 0.03 | 18.0 | 3.00 | 14.0 | 0.10 | Bal |

Large quantities of nickel are often found in stainless steel to increase its ductility, weldability, and formability [71]. The addition of molybdenum is used to further increase the alloy's control of pitting corrosion.

Due to its strength and corrosion resistance, 316 is often used in applications such as aerospace, pharmaceuticals, cutlery, and marine, with 316L used for those environments with more corrosive properties [72,73].

2.2.4 Cold Rolling

Cold rolling is a process used in the production of metal sheets, strips, and coils, where the metal is passed through a series of rollers at room temperature or below. The process is called "cold" because it does not involve heating the metal above its recrystallisation temperature. During cold rolling, the metal is gradually deformed as it passes through the rollers. The process can be used to reduce the thickness of the metal, create a smoother surface finish, and improve the mechanical properties of the metal, such as its strength and hardness. Cold rolling is commonly used to produce steel sheets and strips, but it can also be used with other metals, such as aluminium, copper, and brass. The resulting metal sheets and strips are used in a wide range of applications, including automotive parts and construction materials. Cold rolling, accompanied by heat treatments, has also been shown to increase the corrosion resistance of alloys when the right level of deformation is achieved [74–77].

2.2.5 AM Corrosion

As referenced earlier in this review, one significant obstacle to the industrialisation of metal AM is its increased irregularity to corrosive processes compared to its traditionally manufactured counterparts. Research into the causes of this has significantly trailed behind the development of the mechanical properties of AM components since their introduction, as the latter is the industry focal point.

There are many theories as to why this transpires, some stemming from the thermal processes involved during manufacture, initiating consequences such as internal residual stresses, unique microstructures, and dislocation cells [78]. As the layers of powder and substrate are repeatedly heated and rapidly cooled, the diffusion of its constituent elements occurs at distinct locations and different speeds. This has been shown to cause higher concentrations of certain elements around the perimeter of the melt pool, which, in turn, can increase its susceptibility to corrosive environments, especially if these areas include those elements added to improve corrosion resistance, such as chromium and molybdenum [29,79,80]. Surface finish defects, whilst present across the majority of manufacturing processes, are more prominent where metal AM is concerned. However, this is

correctable to a degree with the techniques described previously. Much focus, though, is directed to the porosity that occurs during the fusion stage of the AM procedure.

AM porosity can be divided into two sub-categories: porosity caused by incomplete fusion and porosity caused by trapped gas during the melting process. The overall porosity can be varied by optimising certain manufacturing conditions such as laser energy density, scan strategy and other process parameters [81]. The effect of varying the laser energy density incident on the metallic powder has on the relative density of the part produced is displayed in Figure 3.

Much of the relevant literature suggests that increasing the energy density applied has the effect of reducing porosity until such a point is reached that further increasing results in vaporisation and balling of the metallic powder. This has been observed to increase porosity by causing gases to become trapped within the build [82]. Prior to this energy density, the porosity present is prominently due to the incomplete fusion of the powder.

Small, porous sites on the surface of AM metals provide an ideal environment for pitting corrosion to occur. Pitting is particularly common throughout AM corrosion studies and regularly occurs at sites of high porosity; however, more research must be conducted to understand why it initiates at certain sites more frequently.

2.2.6 316L Corrosion

As previously mentioned, 316 stainless steel has a greater resistance to chloride environments when compared to other grade variations in the 300 series, particularly with regard to pitting and crevice corrosion. This is partly due to the alloying addition of molybdenum (2-3 %) [69]. 316L further increases this corrosion resistance with the benefit of lower carbon content. Some literature reports that AM 316L, due to its finer grain structure compared to its wrought equivalent, had better barrier characteristics due to an increase in its passive film growth rate [83].

In some instances, corrosion of AM 316L has been shown to dramatically increase the surface roughness of the sample compared to a traditionally made specimen under the same conditions [84]. Mass loss under the same conditions is also experienced to a greater by the AM specimens, an important quantifier in the lifespan of a material, as significant mass loss will, while potentially compromising the aesthetic appeal of a component, can, more importantly, lead to its mechanical failure. This was also shown over a 2184 hr exposure to a 0.75 M sulphuric acid solution by Miller et al. where the LPBF specimen's tensile strength and strain measurements were affected significantly more than the traditionally manufactured [72].

Again, due to the thermal processes undergone during the melting and rapid cooling of the metallic powder during fabrication, essential elements alloyed to specifically increase corrosion resistance are known to congregate along grain boundaries. This elemental segregation, when compared to the often homogenous structure of wrought metals, can lead to increased susceptibility to corrosion in the areas where metallic additions such as chromium and molybdenum are deficient [29].

Trelwicz et al. reports that AM 316L, when undergoing a potentiodynamic scan in a solution of deaerated 0.1M HCl, demonstrated a substantially reduced passive region and a greater passive current density than the wrought specimen [85]. Both of these results implicate a weakened corrosion resistance for the LPBF sample when compared. It is also suggested that these disparities were more due to the AM specimen's microstructural inconsistencies than its porosity. This again brings the discussion forward as to what the main protagonist for corrosion among AM alloys is.

Literature suggests that AM 316L, when undergoing cyclic polarisation, displays a higher pitting potential (E_{pit}) than that of the wrought 316 SS. It is hinted that this is due to the impacts that the SLM process has on limiting the size and concentration of inclusions on the surface of the metal. It also indicates that an increase in the level of porosity within a sample results in a lowering of the repassivation potential (E_r) as well as increasing the frequency that metastable pits occur [86].

2.3 High entropy alloys

2.3.1 History of High Entropy Alloys

Traditional alloy development has focused on selecting the main metal component of the alloy based on the most desirable properties. Alloying elements are then added in various quantities to provide it with additional preferential properties [87–90]. Stainless steel is an example of this, with Fe making up the bulk of composition as the primary element for its strength properties, with Cr added to increase the corrosion resistance.

Modern multi-principal element alloy (MPEAs) research began as the undergraduate thesis of Alain Vincent and his supervisor Brian Cantor in the late 1970s at Sussex University. During this time, Cantor developed the base equiatomic alloy FeCrMnNiCo, known as the 'Cantor alloy' [91]. This research was continued by Peter Knight as another undergraduate project at the University of Oxford in 1998 before being repeated again by Isaac Chang in 2000 at the same institution [91]. The work was combined with his predecessors, refined, and published in 2004 [87]. Initially, 20 and 16-element alloy systems were investigated, with each element present in equal atomic proportions, at 5 at.% and 6.25 at.%, respectively [87,91]. Both resulted in alloys that were multiphase and brittle. However, their phases

were predominately single FCC primary. Further research was completed on equimolar alloys consisting of between 5 and 9 elements [87].

HEAs were proposed in 1996 by the Alloy Research Group, National Tsing Hua University, to escape this conventional method of alloy innovation in order to increase the degrees of freedom and to explore the possible manipulation of solid solution phase stability through the regulation of configurational entropy [89,92]. The classic compositional definition of a HEA is an alloy system containing five or more constituent elements, with each of these elements existing in quantities ranging between 5 at.% and 35 at.%. Based on this principle, alloys consisting of up to 20 elements could be created [89,91–94]. There is also a secondary definition, motivated by the ‘high entropy’ segment, which states that the configurational molar entropy of the alloy ‘ $S^{SS,ideal}$ ’ be greater than $1.61R$ for an alloy with 5 components (where SS refers to solid solution phases and R is the gas constant) [92]. This value increases with the number of constituent elements, as shown in Table 2, below. This definition is, however, flawed, with factors such as temperature and pressure affecting an alloy’s entropy.

Table 2 Configurational entropies of equiatomic alloys with constituent elements between 5 and 13 [91]

| N | 5 | 6 | 7 | 8 | 9 | 10 | 11 | 12 | 13 |
|-------------------|---------|---------|---------|---------|--------|--------|--------|---------|---------|
| ΔS_{conf} | $1.61R$ | $1.79R$ | $1.95R$ | $2.08R$ | $2.2R$ | $2.3R$ | $2.4R$ | $2.49R$ | $2.57R$ |

Since then, the level of research interest in HEAs has been gathering pace, with significant effort going into understanding the complex thermodynamic effects taking place in these alloys as well as how their relatively unexplored benefits compare to traditional alloy systems [95–101].

2.3.2 The Four Effects of High Entropy Alloys

The effects that the microstructure and properties of HEAs are subjected to differ from those that conventional alloys undergo. Those undergone by the former are high entropy, severe lattice distortion, sluggish diffusion, and cocktail effects.

2.3.2.1 High Entropy

Many describe the high entropy effect as the most important of the four discussed effects. This is because it can improve the formation of solid solutions, making the microstructures produced simpler and with less likelihood of intermetallic formation. This is attributed to their high mixing entropies [91,92,102,103]. This high degree of disorder in HEAs can lead to unique microstructures and several exceptional properties, such as high strength, excellent ductility, and good resistance to wear and

corrosion. It is widely accepted that, due to this effect, the number of phases in the alloy created is far lower than the Gibbs phase rule. This states that given an alloy at constant pressure in equilibrium, the number of phases (P) will be equal to the number of components (N) plus 1 minus the number of thermodynamic degrees of freedom (F), as shown by Equation 2 below [91,103].

$$P = C + 1 - F \quad 2$$

Contrary to this, however, it has been observed that on analysis, HEAs composed of compatible elements are comprised of fewer solid phases than expected and as low as one single phase, a characteristic credited again to their high mixing entropies [102].

Overall, the high entropy effect in HEAs represents an innovative approach to the design and synthesis of advanced materials, which has the potential to revolutionise a wide range of industries, including aerospace, automotive, and energy.

2.3.2.2 Severe Lattice Distortion

The severe lattice distortion effect in HEAs refers to the significant disruption of the crystal lattice due to the random arrangement of multiple elements in equimolar or near-equimolar proportions. The random distribution of various elements in HEAs creates a highly disordered structure, which leads to significant local lattice distortions [104,105].

The severe lattice distortion effect has important implications for HEAs' mechanical and physical properties. First, the high degree of lattice distortion creates a large number of lattice defects, such as dislocations and vacancies, which contribute to HEAs' high strength and ductility. Second, the severe lattice distortion can lead to the formation of complex microstructures, such as nanocrystalline and amorphous phases, which contribute to the exceptional properties of HEAs, such as high corrosion resistance and excellent wear resistance.

The severe lattice distortion effect is believed to arise from a combination of factors, including the high degree of compositional complexity, the suppression of intermetallic compound formation, and the formation of solid solutions between multiple elements. This effect is one of the critical characteristics of HEAs and has been extensively studied in recent years as part of efforts to understand the unique properties of these materials and to develop new, high-performance alloys for a range of applications [92].

2.3.2.3 Sluggish Diffusion

The sluggish diffusion effect in HEAs refers to the phenomenon where the diffusion of atoms within the material is slower than in conventional alloys due to the high degree of compositional complexity and the resulting high configurational entropy. This effect is caused by the fact that in a HEA, many different elements are randomly distributed throughout the crystal lattice, which can create local compositional fluctuations and impede the diffusion of atoms [92].

In conventional alloys, the diffusion of atoms is relatively fast and follows well-established diffusion paths. However, as previously mentioned, in HEAs, the large number of elements and their random distribution create a highly disordered structure, which can lead to diffusion pathways that are not well-defined. The difference in these neighbouring atomic structures creates varying energies across sites, with atoms in lower energy regions essentially becoming trapped and unable to move to a higher energy vacancy.

The sluggish diffusion effect has important implications for the properties of HEAs. For example, it can lead to the formation of complex microstructures and the suppression of phase transformations, which can contribute to the high strength, ductility, and resistance to wear and corrosion that are observed in many HEAs. However, it can also make it more challenging to process and fabricate HEAs, as it can lead to the formation of unwanted phases or the segregation of elements during processing.

2.3.2.4 Cocktail Effects

The cocktail effect in HEAs refers to the synergistic or combined effects of multiple elements in the alloy on its properties. In a HEA, many different elements are randomly distributed throughout the crystal lattice, which can lead to a wide range of compositions and a high degree of compositional complexity. As a result, the interactions between the different elements can lead to unique and often unpredictable properties, which are not observed in conventional alloys [104,105].

The cocktail effect arises from the fact that a HEA's properties are not simply a linear combination of the properties of its constituent elements but rather the result of the complex interactions between these elements. For example, the addition of a small amount of a particular element to a HEA can have a significant effect on its mechanical, physical, or chemical properties, even if the individual element itself does not have a strong effect.

The cocktail effect, a key concept in the design and synthesis of High Entropy Alloys (HEAs), has revolutionized the field of materials engineering. By strategically selecting the composition and distribution of the constituent elements, we can now create alloys with customized properties for

specific applications. This breakthrough has sparked significant interest in HEAs, a novel class of materials that hold the potential for superior properties compared to conventional alloys.

2.3.3 Methods for Alloy Design

The selection methods used when designing new HEAs differ from that of conventional alloy systems with a base metal, mainly due to the 4 effects highlighted above. It's a complex process with plenty of factors that need consideration, including its desired properties, cost, and applications. Experimentation was the only way to understand these effects in the early years of HEA development. This involved synthesising every composition and characterising the resultant alloy through optical analysis or mechanical testing. This is, however, incredibly time-consuming, even for a few compositions, and so it is impractical as a method to understand more about these new alloy systems. It was, therefore, essential to narrow down compositions that would give the desired properties before manufacturing them.

Early work in the 1920s by metallurgist William Hume-Rothery led to some simple rules on the solubility of an element when it is dissolved into a host metal. Firstly, the radii of the solvent's atoms must not differ by more than 15 % from that of the solute. Developing this rule further, complete solubility can be achieved when the size factor is kept to less than 8 % [91]. If the constituent elements have atomic radii within these bounds, solid solutions are more likely to form instead of intermetallic compounds. These formations have an effect on the lattice distortion of the alloy created. Secondly, the solubility of a solute in its host is likely to decrease when there is a more significant difference in electronegativity, as intermetallic compounds are likely to form. Finally, increased solubility is expected to occur if the crystal structures of the elements are the same and if the solute and solvent have the same valency [91]. Once predictions have been made and compositions chosen, RAP can make these alloys in small quantities with high throughput whilst replicating the mechanical properties of alloys made through traditional methods [106–115].

However, it is concluded that these criteria cannot be taken in isolation to predict the formation and characteristics of the resultant alloy. Further thermodynamic and topological parameters can be used alongside these methods to predict the solid solution formation conditions in HEAs.

2.3.3.1 Entropy of Mixing

The entropy of mixing (ΔS_{mix}) is a thermodynamic parameter used in the development and characterisation of HEAs to evaluate the degree of disorder or randomness associated with mixing constituent elements in an alloy. It is defined as the change in entropy that occurs when two or more elements are combined to form a solid solution.

The ΔS_{mix} is related to the formation and stability of HEAs. In general, HEAs with high entropy of mixing tend to have better mixing and form single-phase solid solutions. In contrast, those with low entropy of mixing tend to have poor mixing and form multiphase or multiplex alloys.

Miracle et.al discuss an operational designation for HEAs as an alloy with either an ideal or regular configurational entropy with maximum $\Delta S_{\text{mix}} \geq 1.5R$, where R is the gas constant = $8.314\text{J}\cdot\text{mol}^{-1}\cdot\text{K}^{-1}$ [92].

2.3.3.2 Enthalpy of Mixing

Enthalpy of mixing is another thermodynamic parameter used in developing and characterising HEAs to evaluate the energy associated with the random mixing of constituent elements in an alloy. It is defined as the difference in enthalpy between the mixed alloy and the hypothetical reference state where the constituent elements are separate and at the same temperature and pressure.

The enthalpy of mixing is related to the formation and stability of HEAs. In general, HEAs with low enthalpy of mixing tend to have better mixing and form single-phase solid solutions. In contrast, those with high enthalpy of mixing tend to have poor mixing and form multiphase or multiplex alloys. A negative enthalpy of mixing is also associated with the formation of intermetallic compounds, with the inverse leading to clustering and elemental segregation [91].

Other methods of selection for alloy systems are based on parameters such as the non-dimensional Ω , atomic size mismatch, valence electron concentration, and finally, the itinerant electrons per atom and average atomic radius, also known by the e/a and \bar{r} [116–118].

2.3.4 High Entropy Alloys Studied for Corrosion

HEAs that have been manufactured and studied for their corrosion resistance cite many different properties associated with HEAs that increase their corrosion resistance to a level greater than their individual alloying elements would suggest, and beyond that of some widely used stainless steels [119–124]. HEAs often incorporate large quantities of elements with inherent corrosion resistance, such as chromium, nickel, and molybdenum. These elements form protective oxide layers on the alloy surface, acting as a barrier against corrosive environments. These properties include the fact that HEAs are often characterised by a single-phase, homogeneous microstructure, which reduces the presence of interphase boundaries [125,126].

Traditional alloys often have distinct phases and grain boundaries that can act as preferential sites for corrosion initiation. The absence of such features in many HEAs contributes to their improved corrosion resistance. However, it is reported that in some cases where secondary or intermetallic

phases form, such inhomogeneity can result in micro-galvanic localised corrosion due to elemental segregation [127–129].

304 SS is the most commonly used stainless steel in the world but comparing its corrosion resistance to a $\text{Cu}_{0.5}\text{NiAlCoCrFeSi}$ HEA provides mixed results. It is reported that the HEA is more resistant to general corrosion at room temperature in the deaerated H_2SO_4 and NaCl solutions tested, but once corrosion has been initiated, the rate of corrosion is faster than the 304 SS due to weak passivation. Additionally, an elevation in experimental temperature appears to affect the HEA to a greater extent, increasing its corrosion rate [130,131]. Additional research reiterates the strong corrosion resistance of a variety of HEAs that have been shown to be significantly more noble than carbon steels and aluminium alloys and some nobler than austenitic stainless steels such as 304 SS [132]. Multiple investigations into the corrosion resistance of single phase AlTiVCr HEAs report excellent results, and whilst returning a less noble E_{corr} than 304 SS, its passive region and E_{pit} achieved far exceeded it, the latter by 1142 mV [133,134]. Analysis of the passive film noted an unusual mixture of metallic ions and oxides, the latter predominantly Al with decreasing quantities of Cr_2O_3 and V_2O_3 [134]. This particular HEA highlights the exceptional corrosion resistance HEAs can exhibit with the right composition and microstructure, outperforming traditional alloys.

Similar to stainless steel, the addition of Cr to the alloy system is noted to improve corrosion resistance; however, some manufacturing processes can lead to Cr segregation, which increases the bulk matrix's susceptibility to corrosion [29]. Research citing elemental segregation, whether to a secondary or intermetallic phase or precipitating out of the matrix, as having a negative effect on the corrosion resistance of HEAs is repeated regularly in literature and highlights the importance of single-phase solid solution [126–129,132]. This is due to these phases acting as preferential sites in localised or galvanic corrosion but also due to a weakening in the passive layer, the latter more prevalent with Cu segregation [127,129,133].

2.3.5 In-Situ Alloying of HEAs

Traditional fabrication through LPBF uses a pre-alloyed powder. However, to increase the exploration of HEAs for AM, gas atomisation of individual compositions would be time-consuming and expensive, thus compromising the large degree of compositional flexibility associated with HEAs. In-situ alloying within AM refers to creating alloys directly during manufacturing rather than using a single, pre-alloyed powder. This process offers several benefits, including increased customisation, flexibility, innovation, and sustainability. For AM processes, the in-situ alloying tends to work by using a pre-alloyed powder as a foundation before adding an additional element in powder form [135–137]. It has, however, also been conducted using purely elemental powders to create refractory HEAs, but

with noted vaporisation of lower melting point elements [138–140]. The in-situ modifications can take advantage of the exceptional customisability of HEAs, allowing the tailoring of existing alloys to suit a desired application. These additions can be made rapidly, with limited waste, reducing costs and increasing the sustainability of the development process. An example of this principle has been shown with the additions of Mo to an HEA and alloyed in an induction furnace, strengthening the corrosion resistance as the Mo concentration is increased [119].

However, this process has encountered issues when the alloying addition fraction is greater than 5 at.%, as the additional elements tend to stay unalloyed, particularly in the LPBF process [136,140]. Even at lower proportions, additions have been shown to induce swelling and cracking, increase brittleness, and result in poor chemical homogeneity [141,142]. It is also important to use a powder with a similar particle size to reduce processing issues. It is also clear that different elemental additions do not respond the same when sintered in-situ to pre-alloyed powder during LPBF, with a 3.52 % magnitude difference in relative density between Ti and Cu additions on the same CoCrFeNi alloy with optimised parameters [137].

2.4 Corrosion

2.4.1 General Corrosion Theory

Corrosion, a complex electrochemical process, involves the degradation of material properties through reactions with the surrounding environment [143,144].

This phenomenon is commonly classified into two categories: 'wet' and 'dry'. Dry corrosion is less prevalent and predominantly influenced by factors such as high temperature and gases (e.g., in furnaces). The majority of present research focuses on wet corrosion. Due to this, wet corrosion is the focal point of this thesis. In wet corrosion, the material is exposed to an environment where water or other solutions facilitate the movement of ions, enabling electrochemical reactions to take place. The liquid medium can contain dissolved salts, acids, or other corrosive substances that enhance the corrosive process. Factors such as humidity, temperature, and the specific chemical composition of the liquid play crucial roles in influencing the rate and extent of wet corrosion [145].

Wet corrosion is a significant concern in various industries, as it can compromise the structural integrity and functionality of materials and components over time. Understanding the mechanisms and factors influencing wet corrosion is essential for developing effective corrosion prevention and mitigation strategies, especially in applications where moisture is prevalent, such as in marine environments or chemical processing industries. This classification is pivotal for understanding the corrosion mechanisms relevant to AM components in real-world applications.

The fundamental driving force behind metal corrosion lies in the higher free-energy level of the metallic state compared to the resulting corrosion products. The thermodynamics of metal formation from ore contribute to the inherent instability of the resultant metal. The formation of metals from their ore is an endothermic process, with the resultant metal being in a thermodynamically unstable state [146]. Local conditions that elevate the metal's energy state above the activation energy threshold (ΔG^*) initiate corrosion. As a consequence, there is a reduction in the metal's Gibbs free energy as it undergoes a transformation into corrosion products. These energy transformations are displayed in Figure 11.

Redox reactions are integral to corrosion processes, wherein the metal functions as both the anodic and cathodic cells in the presence of an electrolyte, facilitating the transfer of ions. The occurrence of minute surface or environmental differences can create similar electrochemical cells, adding a layer of complexity to corrosion dynamics. A simple example of a redox reaction is that of the corrosion of iron to form hydrated iron oxide (rust). At the anode, iron is oxidised, and water is reduced in the presence of oxygen at the cathode, as shown by equations 3 and 4, respectively. These reactions combine in equation 5, creating rust. The metal completes the electrical circuit, allowing charge to flow between the two sites, and the electrolyte permits ion transfer.

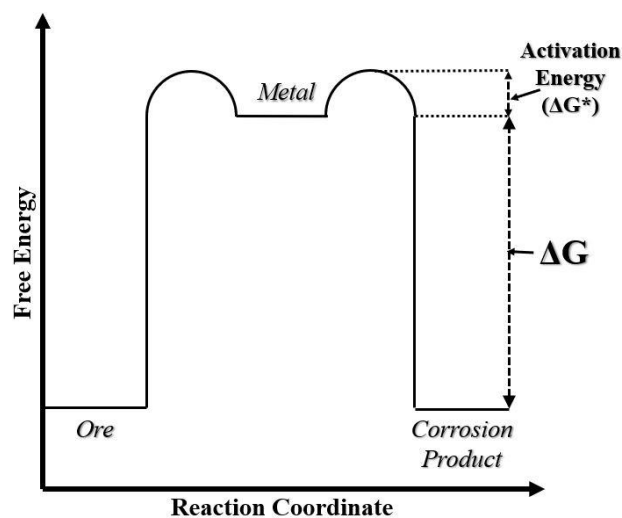
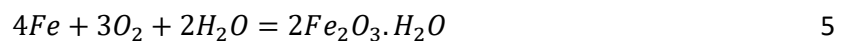


Figure 11 Gibbs Free Energy diagram for a metal [143]

2.5 The Electrochemical System

2.5.1 Electrode Potentials

An electrode potential is the measure of the thermodynamic stability. More specifically, it is a measure of the tendency of a chemical species to undergo reduction or oxidation in an electrochemical cell. All metals have different electrode potentials that are regulated against the standard hydrogen half-cell. Those pure metals with the most positive potentials are in the most stable state and are the easiest to extract from their ore, with the most negative being the most thermodynamically volatile with a higher tendency to corrode.

These electrode reduction potentials are linked to the Gibbs Free Energy, ΔG , through Faraday's law in equation 6, where n represents the number of electrons transferred, F is the charge on one mole of electrons, and E is the electrode potential.

$$\Delta G = -nFE \quad 6$$

Table 3 A Selection of electrode reduction reactions and their respective electrode potential [144]

| Electrode reduction reaction | E⁰/V |
|--|------------------------|
| Au⁺ + e = Au | +1.68 |
| Pt²⁺ + 2e = Pt | +1.20 |
| Cu²⁺ + 2e = Cu | +0.34 |
| 2H⁺ + 2e = H₂ | 0.00 |
| Sn²⁺ + 2e = Sn | -0.14 |
| Ni²⁺ + 2e = Ni | -0.25 |
| Fe²⁺ + 2e = Fe | -0.44 |
| Cr³⁺ + 3e = Cr | -0.71 |
| Zn²⁺ + 2e = Zn | -0.76 |
| Al³⁺ + 3e = Al | -1.67 |
| Mg²⁺ + 2e = Mg | -2.34 |
| Na⁺ + e = Na | -2.71 |
| Ca²⁺ + 2e = Ca | -2.87 |

Table 3 details a selection of reduction reactions and their respective electrode potentials. Platinum (Pt), with a potential of +1.20 V, has a much lower predisposition to corrode when compared to aluminium (Al) at -1.67 V. The standard hydrogen electrode (SHE) is often used as a reference electrode, and its electrode potential is defined as zero. The electrode potential of other half-reactions is measured relative to the SHE. If a species has a positive electrode potential, it tends to be reduced (gain electrons), while a negative electrode potential indicates a tendency to be oxidised (lose electrons).

The electrode potential of a half-reaction is a measure of the electric potential (voltage) generated by that half-reaction when it operates as a reduction reaction under standard conditions. Standard conditions typically include a concentration of 1 M for all ions involved, 1 atm pressure, and a temperature of 25 °C.

The hydrogen half-cell is connected to the metal/metal salt redox couple to be measured by an external circuit containing a voltmeter which will record the potential and it is submerged in a 1 mol dm⁻³ solution of its own metal ions. Depending on the setup, a salt bridge or porous separator is used to complete the electrical connection between the two halves of the cell.

If a sample of Fe was dipped into a solution containing Pt ions, the Fe will be oxidised due to its more negative potential. This is outlined in equations 7 and 8.



The overall displacement reaction is given by equation 9.



The overall cell potential E_{cell} is calculated with the addition of these half-cell potentials, consequently $E_{cell} = 1.64 V$. Because the cell potential is highly positive, this reaction is thermodynamically favourable and is likely to occur of its own accord without any external energy.

2.5.2 Practical Corrosion

As mentioned previously, wet corrosion is generally the mechanism by which metals undergo chemical degradation and requires 4 electrochemical components to occur. The chemical cells created to support corrosion comprise of:

- Anode – Metal oxidation occurs
- Cathode – Reduction reaction occurs
- Electron flow between the electrodes
- An electrolyte or aqueous medium to facilitate the electron flow

The cell cannot function if one of these components is interrupted.

The Pt plating of Fe described earlier is corrosion in an artificial sense, with the positive iron anode oxidised, losing electrons to the negative platinum cathode, which is reduced. Often under normal

operation, a metal will instead be subjected to an atmosphere consisting of oxygen and water acting as a cathode, as opposed to another metal.

The generic anodic reaction undergone by metals in this case is shown in equation 10 where M is the metal, n refers to the number of electrons, and e denotes the electron being transferred.



Hydrogen evolution in equation 11 is the predominant cathodic reaction which occurs in a strongly acidic environment (with a pH much lower than 7) or in the absence of oxygen.



At a pH of around 7 and above, and in the presence of oxygen, the oxygen reduction reaction (ORR) is more likely to occur via equation 12.



Figure 12 below, illustrates how the ORR occurs on the surface of a metal, with the flow of electrons from the anode to the cathodic site.

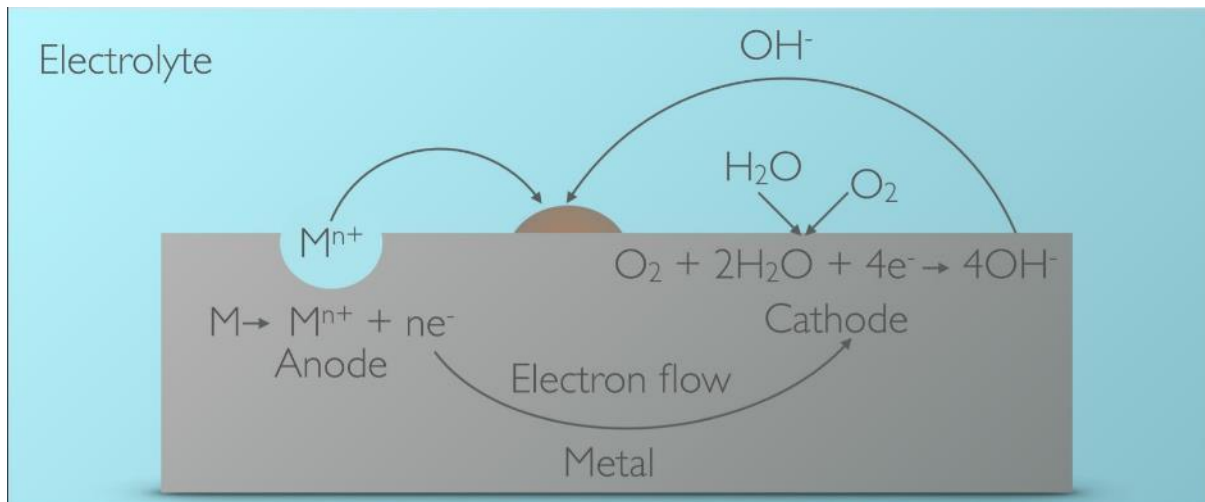


Figure 12 Schematic of oxygen reduction and metal oxidation [144]

Corrosion initiation is contingent upon the negativity of the ΔG in the global reaction, leading to the dissolution of the metal at the anodic site. This process results in the release of metal ions into the electrolyte, accompanied by an excess of electrons. Functioning as an electrical circuit, the metal facilitates charge flow from the anode to another site on its surface. At the cathode, a combination with water occurs, reducing oxygen and yielding hydroxide ions. Subsequently, the metal and hydroxide ions combine on the surface through the electrolyte intermediate, forming the characteristic metal hydroxide associated with metallic corrosion.

The spatial distribution of anodic and cathodic sites is variable, ranging from ubiquity across the surface to individual sites with relatively larger separations. The latter scenario gives rise to localised corrosion environments capable of inducing more extensive damage due to the emergence of anodic focal points. Minute disparities in surface potential, originating from subtle chemical or physical irregularities, determine the locations of the anodic and cathodic sites. These irregularities include discontinuities in protective films, nonuniform chemical composition, and fluctuations in oxygen concentration and pH.

While the electrode potential of a reaction serves as an indicator of the thermodynamic likelihood of corrosion, it does not elucidate the rate at which corrosion will manifest. As previously discussed, variables such as temperature and concentration are influential factors in this regard. The presence and quality of coatings, paints, or films also contribute to rate determination. The literature further indicates that environmental factors, including humidity, electrolyte thickness, and exposure to ultraviolet radiation, exert notable impacts on corrosion rates [147–153].

Corrosion can have a detrimental effect not only on the aesthetic appeal of a material but also on its mechanical properties.

2.6 Mechanisms of Corrosion

2.6.1 Crevice Corrosion

Crevice corrosion is a localised form of corrosion that occurs in confined spaces or crevices between two surfaces in close contact, where access to corrosive agents is restricted. This type of corrosion typically manifests in gaps, joints, or overlaps between metal surfaces, creating an environment with limited exposure to the external environment. These restricted areas can lead to a chemically inhomogeneous electrolyte composition as well as oxygen depleted zones, causing metal dissolution within it at the anodic site and oxygen reduction over the rest of the metal surface [144].

Initially, both the anodic and cathodic processes occur at equal rates on the metal, irrespective of location. A large number of these sites are created on the surface, and electrons flow between them. To balance the charge change, the metal ions develop along with those created at the cathode due to oxygen reduction. The oxygen levels in the electrolyte region within the confined environment are diminished as it is consumed by the reaction at the cathode, and more oxygen diffuses through the electrolyte to replenish these sites. However, the oxygen is not distributed uniformly, with the surfaces outside the crevice serviced first, creating a differential aeration cell.

Without oxygen in the crevice, the cathodic reaction cannot occur, and it becomes the focal point for anodic activity, with the more accessible areas of the metal surface becoming the cathodic sites. The site fills with positively charged metal ions, creating a net positive charge to the electrolyte within the crevice and triggering a potential difference. Negative ions, often chloride, are attracted to the area, forming a metal chloride, which in turn reacts with the water in the electrolyte, producing H⁺ ions and an aggressively acidic environment. An autocatalytic environment has been created that will support itself and become more destructive.

2.6.2 Pitting Corrosion

Pitting corrosion stands as a distinctive and potentially destructive form of localised corrosion, characterised by the development of small pits or craters on the metal surface. This phenomenon poses a significant challenge due to its propensity to cause notable damage even when the overall corrosion rate is relatively low. It can be caused by inconsistencies such as a physical defect in a protective layer/coating or the metal itself, as well as impurities like inclusions or precipitates. It is one of the more destructive forms of corrosion, with pits often equal to or deeper than their diameter, making it difficult to detect [145].

It differs from crevice corrosion in that, where crevice corrosion is instigated due to variable oxygen concentrations within the electrolyte stemming from the geometry of the metal, pitting occurs due to metallurgical processes. Once initiated, however, it propagates in a similar way.

A schematic for pitting corrosion is depicted in Figure 13. Once initiated, the mechanism of propagation is similar to that of crevice corrosion and the Fontana Greene mechanism. Within the pit, oxygen is used up and is replaced at the surface instead of the pit, with the anodic site forming within the cavity and creating a differential aeration cell. As metal hydroxide is formed from the metal ions and water, the corrosion products form over the top of the pit, concealing it from the environment. This further restricts oxygen diffusion into the pit, but allows passage for smaller ions like Cl⁻, which stabilise it. Many pits die due to poor coverage from their corrosion product around the anodic site, allowing oxygen into the cavity and reducing the rate of reaction. Like crevice corrosion, pitting is also deemed to be autocatalytic, provided the environment is sustained [154]. Alloy composition and microstructure, particularly the concentration of elements like Cr and Mo, play crucial roles in influencing pitting resistance [155].

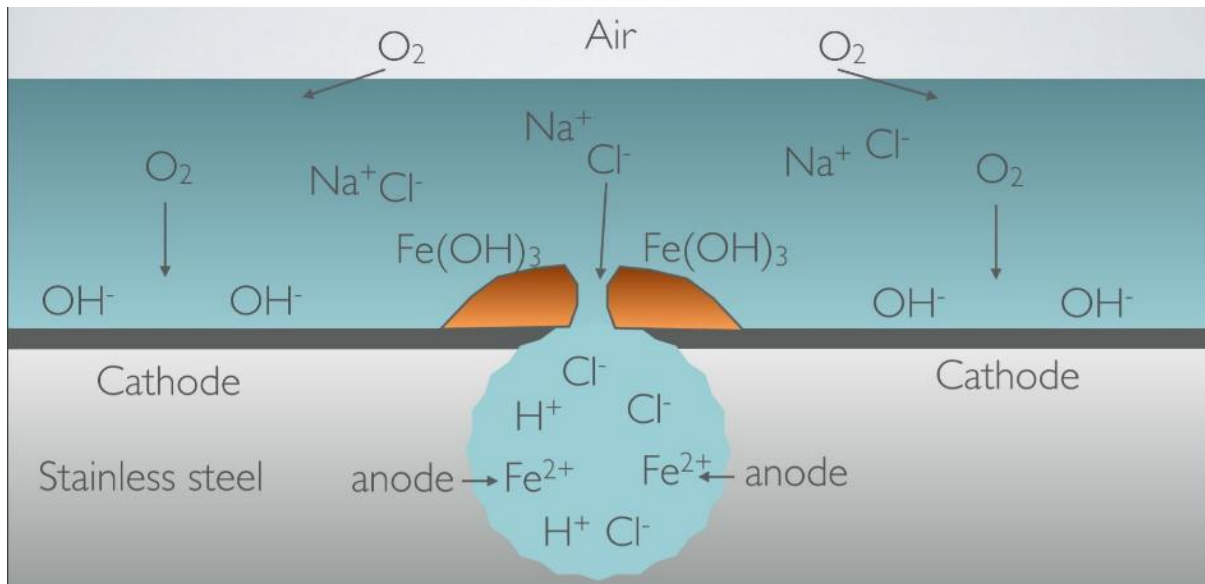


Figure 13 Schematic of pitting corrosion [144]

2.6.3 Bimetallic corrosion

Bimetallic dissimilar metal or galvanic corrosion occurs when metals with different electrode potentials are in direct physical contact, creating an electrical connection in the presence of an electrolyte. It is a very common corrosion classification due to many components and structures comprising multiple metals and metallic joining methods. The metal with the most negative electrode potential, and therefore the most easily oxidised, forms the anode and the other acts as the cathode. The metal harbouring the anodic site corrodes preferentially to that of the cathode and, critically, does so at a faster rate than if it was on its own. It does, however, leave the cathodic site unaffected, leading to a useful benefit of this phenomenon [144].

Sacrificial metals can be used to protect another, more structurally significant metal through bimetallic corrosion, provided it has a more negative electrode potential. In the event that the more important metal is exposed, the sacrificial metal will develop the anodic site and corrode preferentially to the other metal, acting as the cathode and leaving it unscathed. The corrosion product would then form over the damage, protecting the integral metal from further harm. The quantity of sacrificial metal required to perform this role depends on the aggressiveness of the electrolyte present.

Galvanised steel uses zinc to this end, with a thin layer of it on the surface of the iron, which corrodes preferentially due to it having a more negative E_{cell} value, as shown in Table 3.

2.7 Kinetics of Corrosion

The rate at which corrosion occurs is dependent on the environmental conditions present in the system. Variables such as temperature, solution of concentration and pressure are just some known

to do as such. An increase in temperature increases the kinetic energy of the particles, which, in turn, increases the number of successful collisions [145]. Similarly, an increase in the concentration of the corrosive medium raises the number of corrosive particles in the system, again increasing the number of successful collisions. The presence of a catalyst in a system will also increase the rate of reaction in a system by providing it with an alternate reaction pathway with a lower activation energy. The rate of corrosion has a direct relationship to the current flowing between the anode and cathode and, therefore, also the rate of electron transfer between the two.

Each reaction involves the transfer of electrons between the two sites; therefore, a current is associated with each. Anodic current and cathodic current can be denoted as 'i_a' and 'i_c' respectively, with the exchange current density or equilibrium current, as 'i₀'. Under equilibrium conditions, equations 12 and 13 apply, and there is no net metal loss.

$$i_a = -i_c = i_0 \quad 13$$

$$i_a - i_c = 0 \quad 14$$

2.7.1 Polarisation

Enforcing a power source upon a metal will move its potential away from its equilibrium potential (E_{eq}) to a new potential, E. The difference between the E_{eq} and E equates to the polarisation, η. Artificially manipulating the potential value associated with a metal away from its equilibrium value will alter the rate of metal dissolution at the anode or metal replating at the cathode site. A graph with axis of overpotential and current density, including data for anodic and cathodic current density when subjected to different levels of polarisation provides the graph seen below in Figure 14.

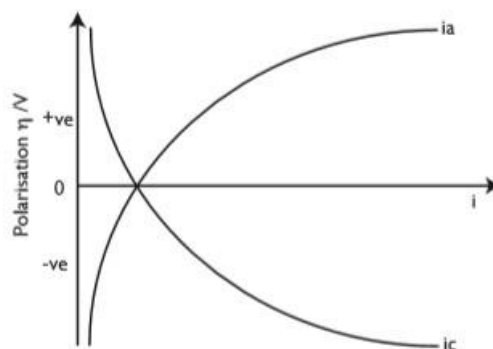


Figure 14 Polarisation vs current density [144]

The connection between i_c and i_a, with the inclusion of polarisation, is defined by the Tafel equations 15 and 16 for anodic and cathodic reactions respectively, where α is a constant related to the relevant electrode material.

$$i_a = i_0 \exp\left(\frac{(1-\alpha)nF}{RT}(E - E_{eq})\right) \quad 15$$

$$i_c = i_0 \exp\left(\frac{(-\alpha)nF}{RT}(E - E_{eq})\right) \quad 16$$

These equations and the graph in Figure 14 show an exponential relationship between polarisation and current. This data can be linearised by taking the natural log of current to produce the graph in Figure 15, for a metal submerged in its own ions. This is the beginning of the Evans diagram.

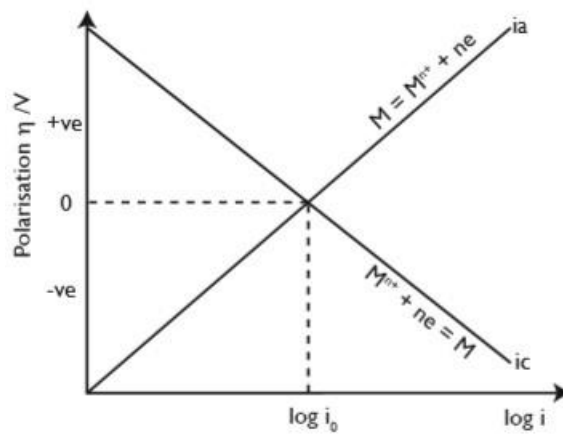


Figure 15 Polarisation vs current [144]

2.8 Evans Diagram

Under normal conditions, a metal rarely experiences dissolution in an environment consisting of its own aqueous ions. Figure 16 also shows Tafel plots associated with the oxidation and reduction reactions to show how the metal will interact with water.

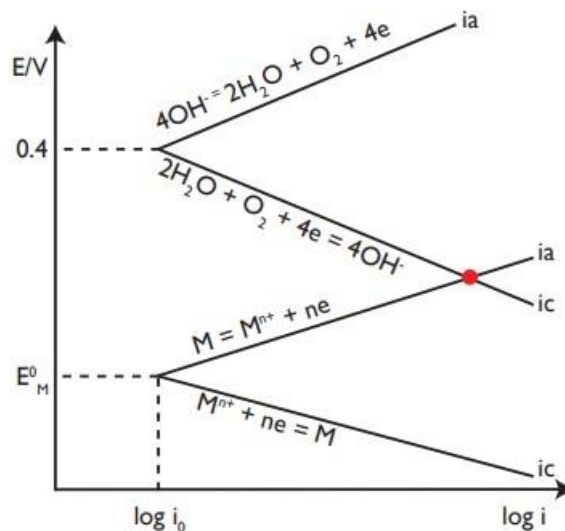


Figure 16 Polarisation vs current density for metal in aerated water [144]

Figure 16 shows that the standard reduction potential of the metal E^0_M is lower than that of the oxygen/water system and that it is, therefore, likely to be the anode in the couple. The E^0 of the water and metallic systems are different, and the potential of the system must increase or decrease to adopt a potential that they both share. This is the point in Figure 16 where the anodic dissolution and cathodic reduction (i_a and i_c) lines meet, this is called the mixed potential.

As previously stated, the chemical reactions which occur during the corrosion process are oxidation and reduction electrochemical reactions. The Evans diagram is a simple representation of these reactions in a straightforward electrochemical system [156]. It requires straight lines representing both the cathodic and anodic activity of the system. Where these lines converge reveals the point of corrosion potential (E_{corr}) and corrosion current density (i_{corr}). This, on an Evans diagram for a zinc electrode in hydrochloric acid, as seen in Figure 17, is where the hydrogen reduction and zinc oxidation lines meet.

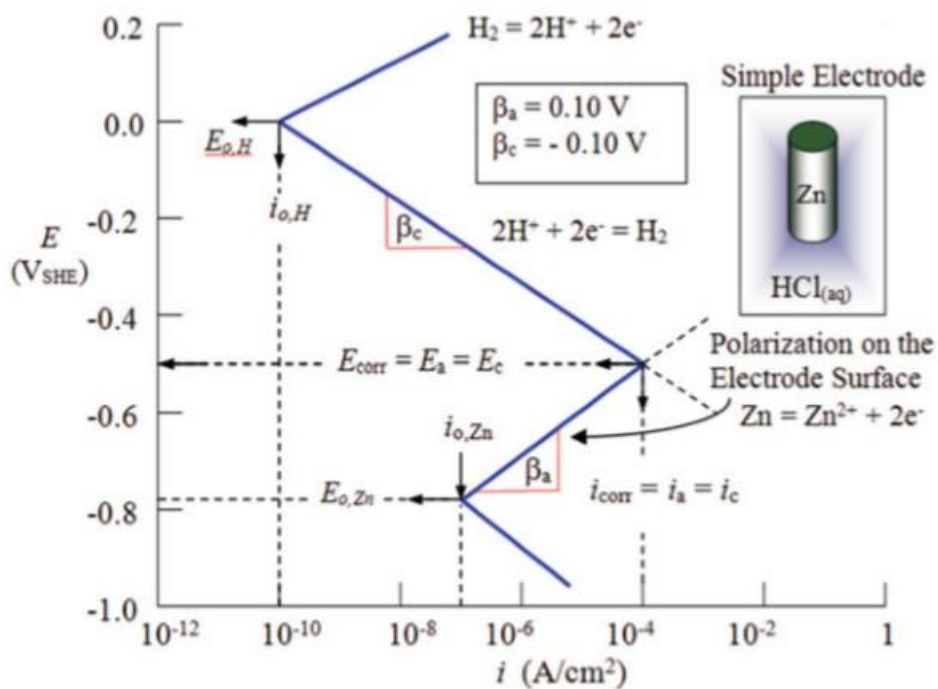


Figure 17 Evans diagram for zinc in hydrochloric acid [156]

2.9 Passivity

Passivity in corrosion refers to the ability of certain metals and alloys to resist corrosion through the formation of a protective oxide layer on their surface. This passive film acts as a barrier, preventing further corrosion by isolating the metal from the surrounding corrosive environment. The passive film is typically a thin layer of metal oxide, nitride, or other compounds that adhere tightly to the metal surface [157]. A characteristic of passive films is their ability to self-heal. If the passive film is damaged or disrupted by external factors, it can regenerate under favourable conditions, restoring the

protective barrier. The presence of a passive film significantly reduces the corrosion rate of the metal. The film acts as a physical and chemical barrier, hindering the access of corrosive agents to the underlying metal.

Chromium is well known as an efficient passivator which is alloyed in varying quantities into a wide range of stainless steels, such as duplex and super duplex stainless steels, to improve corrosion resistance. It combines with oxygen to create a thin chromium oxide/hydroxide layer that reduces the speed of anion and cation transfer [158].

2.10 Pourbaix Diagram

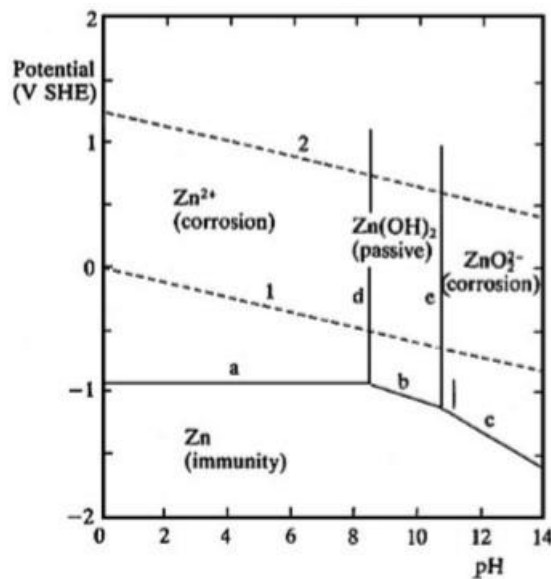


Figure 18 Pourbaix diagram for zinc [159]

Pourbaix, or potential-pH diagrams, were conceived by Belgian chemist Marcel Pourbaix. They summarise the pH and potential dependent nature of a metal and whether it is in an active, passive, or immune state. The lines are calculated using the Nernst equation, and the regions are determined by the potential and pH of the environment. They allow for the quick interpretation of a metal's thermodynamic condition with respect to its environmental condition and its suitability for a particular purpose, specifically those involving pH and potential restrictions. Similar to an electrode potential, the Pourbaix diagram does not show the speed at which the metal will corrode.

Figure 18 shows the Pourbaix diagram for zinc, with corrosive regions between the pHs of 0 and 8, and 11-14, with a passive region in between. Dashed lines labelled 1 and 2 represent the boundaries for water oxidation and reduction lines, respectively, with hydrogen evolution tending to occur preferentially at the cathode below 1 and oxygen reduction favoured when the environment lies between 1 and 2.

The Pourbaix and Evans diagrams can be combined to show which state a metal is in with respect to its potential and current density, whether active, passive, or transpassive. Figure 19 shows a simplistic model for a typical anodic metal dissolution curve.

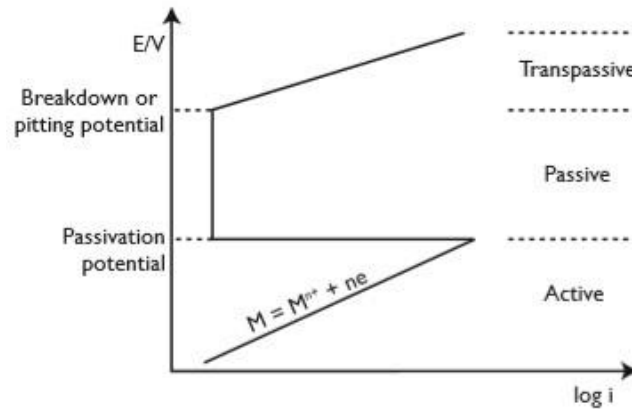


Figure 19 Potential vs current [159]

The plot shows that, as the polarisation increases, the metal moves through an initial active phase with increasing current density until it reaches its passivation potential. The inclination of this slope is dependent on the metal involved and is explained by the Tafel constant, β . The passivation potential is the point at which the anodic site/s becomes covered in a corrosion product that forms a protective layer and causes the current to reduce radically. As the potential increases further, the metal remains within the passive region until it reaches its pitting potential. This is the point at which the potential is great enough to eradicate the passive layer, triggering corrosion to reoccur.

2.11 Electrochemical Techniques

Electrochemistry can be defined as the science concerned with the mutual transformation of chemical and electrical energy. Electrochemistry plays key roles in various fields, from corrosion and batteries to fuel cells and electroplating [82,160]. A visual or theoretical appreciation of a material's chemical, surface, and electrical properties limit the understanding of the user dramatically compared to the information that can be offered through the use of electrochemical techniques. They have a place in many other fields of science, particularly when understanding many essential biological processes [160]. As mentioned previously, electrochemical processes are responsible for metallic corrosion, which causes \$2.5 trillion worth of damage annually. Understanding these processes will help engineers design solutions to reduce this expense.

2.11.1 Potentiodynamic Polarisation

When studying corrosion, most existing electrochemical tests consist of enforcing an external potential on the working electrode and measuring the subsequent current density. This is required

because under normal, even optimum environmental conditions, any perceptible degradation of most metals will take years to occur, if ever [161,162].

This is no different for potentiodynamic polarisation. The applied potential is varied from a starting value, during which the current/current density are monitored. After the initial sweep to a predetermined value of potential or current density is achieved, the scan can be reversed, with the variables remaining under continued examination. The generic effect of a polarisation sweep can be seen in Figure 20, with the change of curve inclines explained by the phases it undergoes, previously mentioned in Figure 19.

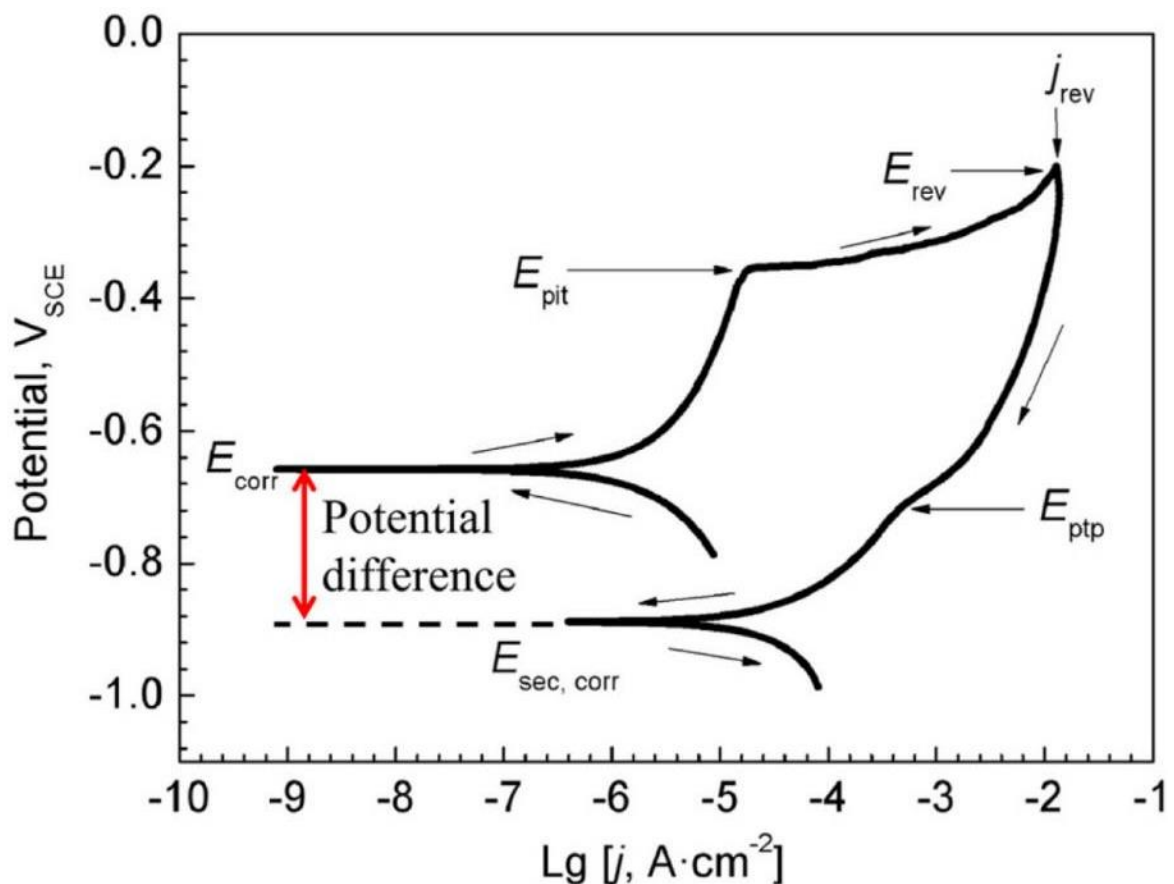


Figure 20 Example of a full cyclic potentiodynamic polarisation sweep [163]

The E_{corr} , shown through this method, can be used to predict the localised corrosion vulnerability of metals. Predetermined values for the E_{rev} and I_{rev} dictate the point at which the potential begins to reduce, usually whichever condition is met first. These points can be relative to the open circuit potential (OCP) of the system or to the readings taken by the reference electrode. After the E_{pit} occurs following the initial active and passive stages, the current density rapidly increases with minimal increase in potential. The scan is then reversed, with the current density reducing as potential is decreased, producing a curve with a similar shape to that of a tensile bar that has undergone plastic deformation. Some metals, under certain conditions, may repassivate during this stage, reforming a

protective layer over the localised corrosion site. Other quantitative data such as the pitting transition potential E_{ptp} and corrosion potential $E_{\text{sec,corr}}$ can also be gleaned from cyclic polarisation scans.

Potentiodynamic experiments comprise of a 3-electrode cell, the working electrode that measures the potential of the specimen is measured relative to the reference electrode, often filled with a KCl solution. The third is the counter electrode with an insert metal such as Pt. The latter two electrodes are immersed in the aqueous solution whilst an electrical connection must be made between the working electrode and the metal to be tested, which is also submerged [82]. The atmosphere in test chamber can be left to its own devices however, nitrogen and other gases can be used to purge it of oxygen. A diagrammatical representation of the set-up described is shown in Figure 21.

Some parameters that may affect the potentiodynamic curve include the scan rate, inclusion of aggressive ions, pH, temperature, and surface defects.

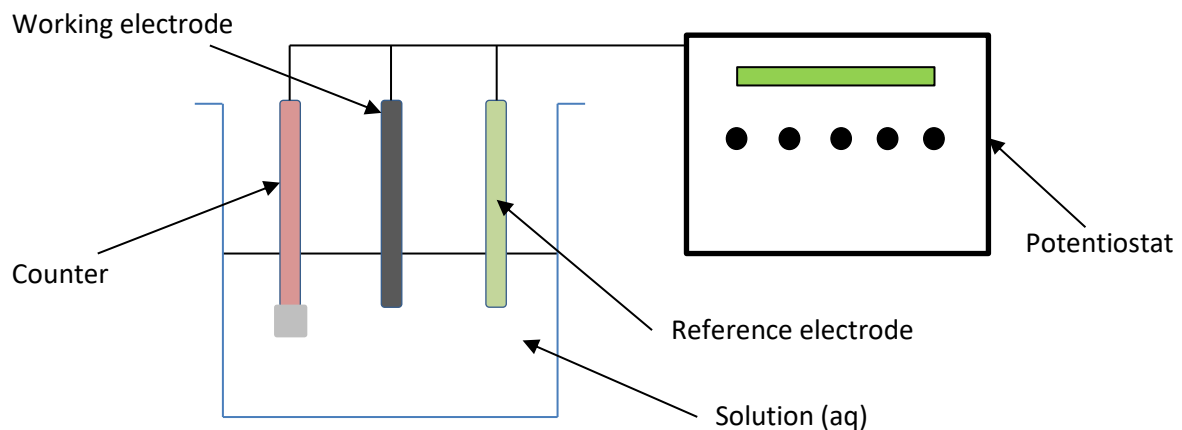


Figure 21 Schematic of potentiodynamic polarisation set-up

2.12 Scanning Techniques

Scanning electrochemical techniques, when used to study metallic corrosion, usually necessitate the use of a scanning microtip electrode a small distance above the metallic surface to be analysed. The referenced electrode can be inert or made to vibrate with a relatively small amplitude perpendicular to the scanning directions.

The electrode can be used to measure localised values for the potential or current as it traverses the surface of the corroding surface, the data from which can be used to create a visual representation of localised disparities in the measured parameters with the help of computational facilities. This highlights one of the advantages of these methods, which is the ability to resolve differences in variables such as surface reactivity and reaction rate which is particularly useful as metallic surfaces are rarely homogenous.

When compared to a potentiodynamic sweep, these techniques provide information regarding the electrochemical reactions in much greater detail than merely providing average potential and current readings across the whole metallic surface.

2.12.1 Scanning Vibrating Electrode Technique (SVET)

The scanning vibrating electrode technique (SVET) is a descendant of the early scanning reference electrode technique, in which the scanning electrode microtip is vibrated relative to the examined surface [82]. At known points, the vertical component of flux is measured above a corroding metal surface in a solution [164]. The microtip functions potentiometrically, with the electrode registering the vibration frequency proportional to the electrical field strength. The field is generated by the ionic current flux passing through the electrolyte, the signal of which is, therefore, proportional to the current density. A greater current density stems from an area of elevated anodic activity, signifying an elevated level of corrosive activity.

As the electrode traverses the parallel air space above the corroding surface, discrete variations in these signals are identified, depending on the electrochemical reactions taking place. From this, different topographical maps can be created, such as the one in Figure 22, to represent changes across the surface over time.

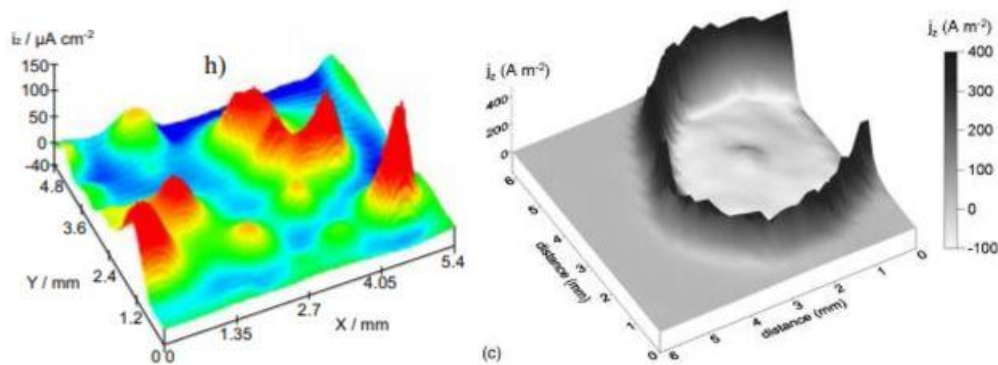


Figure 22 SVET plots of current density vs location [165,166]

2.12.2 Time-lapse Microscopy

Time-lapse microscopy (TLM) is used to observe any progressive visual changes undergone by a system at a microscopic level. It has been used in previous work specifically to view cellular processes and cell interactions as well as the corrosion of metals [167–169]. It works by taking images at designated intervals, enabling the operator to compress the visuals of an experiment lasting hours, days, and sometimes weeks into a matter of minutes.

Many systems that can conduct this procedure are built in-house, adapting current microscopes or creating customised jigs with the required capabilities.

To monitor corrosion cells, some systems operate a flow-cell setup with the microscope lens outside the electrolyte. Constantly flooding the system with fresh electrolyte replicates a real-world atmosphere, such as rainfall or a chloride environment. A failure of this can be that appropriate magnification and focus cannot be obtained by the microscope due to the distance between the lens and the sample surface. The microscope cannot be submerged as it will disrupt the flow of the electrolyte.

Other systems use a submerged lens with a waterproof sheath to observe the corroding surface. Setups such as these require the sample to be fully immersed in a static pool of electrolyte. This negates the failure of the flow-cell setup, allowing the lens to get close enough to the surface to observe it in the required detail.

2.13 Summary

Traditionally manufactured stainless steels show excellent corrosion resistance, a trait that is replicated and reportedly heightened in parts produced through AM processes such as LPBF. However, this notion of increased performance cannot be applied generically across all additive components, with processing parameters, post-processing, and experimental setup all reportedly affecting the final corrosion resistance. Literature suggests that, of these conditions, porosity in the final part is most detrimental to corrosion resistance as it creates a preferential site for pitting corrosion to initiate. This highlights the importance of optimising the processing parameters in addition to utilising post-processing methods to minimise porosity, thus achieving parts with maximised corrosion resistance.

HEAs are a relatively new class of alloys founded on the principles of a composition consisting of 5 or more elements occurring at between 5 at.% and 35 at.%. These alloys are reported to exhibit properties that outperform those of traditional alloys such as steel due to four key effects: high entropy, lattice distortion, sluggish diffusion, and the cocktail effect, resulting in a lower likelihood of forming intermetallic phases and an increased chance of establishing a single solid solution. In-situ additions through AM have been studied, both with traditional alloys and HEAs, in an attempt to tailor the material properties to meet specific requirements. However, limitations of this method have been encountered, including the maximum magnitude of the addition before processing complications are realised. Work still needs to be done, both with AM and HEAs, before they are integrated into engineering applications more frequently.

3 Experimental Procedures

3.1 Introduction

Below is an examination of the methodologies used for the gathering of data for this thesis.

3.2 Powder Mixing

3.2.1 HEAX

To create the mixture, it was calculated that, for every 1000 g of HEA1, 24.59 g of Mo would be needed to achieve the required composition. It was determined that approximately 5kg of powder would be needed to complete 2 optimisation builds, 2 builds containing cylinders to be remelted for casting, and potentially one for tensile specimens if required. 122.950 g of Mo was weighed out and added to the powder mixer containing 5 kg of HEA1. This was then run for 2 hours to allow for good integration of the powders. Often, it is standard procedure to heat the mixture to 50 °C for a period of time to remove any moisture. However, this was not necessary as both the HEA1 alloy and Mo had been sealed and stored under argon since their production.

The predicted composition of the powder mixture based on the addition is presented in Table 4.

Table 4 Desired Composition of HEAX

| Element | Fe | Cr | Ni | Mn | Al | N | Si | C | Mo |
|-------------------|-----------|-----------|-----------|-----------|-----------|----------|-----------|----------|-----------|
| Desired w% | 31.55 | 27.23 | 22.10 | 9.72 | 5.39 | 0.74 | 0.74 | 0.13 | 2.40 |

3.3 Particle Size Distribution Analysis.

PSD was investigated using a Malvern Mastersizer 3000 Hydro EV. To begin, a large beaker was filled to approximately 500 ml with distilled water, making sure that the inlet/outlet and stirrer were suitably immersed. If agglomeration could potentially occur, a surfactant can be added to disperse the particles more effectively. Manual measurement was selected in the toolbar before naming the sample and selecting its particle type from the drop-down menu of spherical, non-spherical and opaque. In the tab for material properties is a bank of pre-loaded materials that can be selected to provide their refractive and absorption index. If the desired material, or one similar, is not pre-defined, custom materials can be made. The last setup stage was to select the dispersion solution used and the stirrer speed, which were set to distilled water and 2000 rpm, respectively. Some optimisation may be needed for the stirrer speed, as escalating it can increase the number of bubbles produced, potentially interfering with the analysis. Too low, however, and the powder may not be fully dispersed within the solution.

On the measurement screen, 'initialise instrument' is selected before the background interference is read. The powder to be evaluated is slowly added to the solution until the obscuration level reaches approximately 14 %. Once this has been completed, 'measure sample' is selected, which runs 10 successive tests, printing the D_v (10), (50) and (90) values after the test is finished. An average of the 10 tests is produced, summarising the results, which can be exported to Excel or as a PDF. Other values calculated are $D [3,2]$ and $D [4,3]$, which are the Sauter Mean Diameter (SMD) and the De Brouckere Mean Diameter, respectively. The former is more relevant for a finer particle size distribution and is, therefore, more pertinent for assessments of LPBF powder where the common size fraction is between $15 \mu\text{m} - 45 \mu\text{m}$. A tween surfactant was added to the distilled water dispersant when testing HEAX to reduce the agglomeration of the smaller Mo particles, as seen in Figure 76.

3.4 Rheometry

To understand the flow characteristics and other rheological properties of the powders tested, they were subjected to two tests that studied their stability and variable flow rate. These tests were carried out on a freemantechology FT4 rheometer using their 25 mm x 25 ml split vessel and 23.5 mm blade. The stability analysis was carried out first to understand whether processing the powder results in any property changes.

Once the test was selected, the blade was inserted into the machine, the split vessel assembly and funnel were locked onto the measuring platform, and the weight on the scales zeroed. The powder to be analysed was subsequently decanted into the vessel so that the split line was no longer visible. The change in mass was recorded, and the test started. The test is made up of a series of conditioning and test cycles. The conditioning cycle was employed prior to every test to negate any variability caused by the operator and remove any residual stress, air pockets, or localised compaction from a previous test. It involved lowering the rotating blade into the vessel to a set depth in an attempt to homogenise the packing of the powder. Once the first conditioning cycle was completed and the carriage was parked, instructions were given to split the vessel and collect the displaced powder before reassembling the vessel. This process ensured that the same volume of powder was tested each time for repeatability and also provided the data for the Conditioned Bulk Density (CBD) to be calculated.

The test was then resumed, with another conditioning cycle occurring before the initial test cycle. The test cycle, like the conditioning, was performed by the carriage lowering the blade into the vessel and rotating it at 100 mm/s blade tip speed. The total energy consumed during this test (forced flow) is recorded, providing the user with the Basic Flowability Energy (BFE) as well as the energy required to lift the blade upwards out of the powder at the end of the test (low stress), offering the powders

Specific Energy (SE). This process is repeated a further 6 times to monitor repeatability and, therefore, stability of the powder.

Once this is completed, the variable flow rate study can commence using the split vessel of powder in its current form. For this study, 4 test cycles are completed in the same manner as the stability study, with the first being with a blade tip speed of 100 mm/s, the second at 70 mm/s, and the 3rd and 4th at 40 mm/s and 10 mm/s, respectively. Conditioning cycles are performed prior to each of these tests as before. This test again provides the total energy used during the test and uses it to calculate the Flow Rate Index (FRI), as shown in equation 17.

$$\text{Flow Rate Index, FRI} = \frac{\text{Energy Test 4}}{\text{Energy Test 1}} \quad 17$$

The FRI is a measure of the powder’s sensitivity to flow rate and is quantified in Table 5.

Table 5 Flow rate sensitivity and its associated powder type

| Flow Rate Sensitivity | FRI | Powder Type |
|--------------------------------|-----------------|--|
| High | > 3.0 | Cohesive |
| Average | 1.5 < FRI < 3.0 | Majority of powders |
| Insensitive | ≈ 1.0 | Large particle size/surface treatments |
| Pseudoplastic/Newtonian | < 1.0 | Powders containing flow enhancers |

3.5 Reduced Build Volume

Reduced Build Volumes (RBV) can be fitted into some LPBF machines and present advantages and disadvantages to the user compared to operating within the machine's full build volume.

Notably, the RBV offers cost savings by minimising the material and energy consumption per manufacturing run. This, combined with faster build times, provides a quick and comparatively cheap pathway to rapid prototyping and proof of concept. To change the powder used for a full build, the entire machine needs to be stripped and cleaned down, a process which can take a small team days to complete. The RBV only requires itself and the chamber it resides in to be cleaned, which is significantly quicker, allowing the rapid testing of novel or unoptimised powders. Due to the dosing mechanism in the RBV and the size of the build plate in which it operates, it is also possible to manufacture components with very small volumes of powder, which is a valuable addition when developing new powders.

As mentioned, however, there are some negatives associated with the use of the RBV. Because the baseplate of the RBV is not heated as it is with the full build volume, heat transfer out of the parts during printing is greater, and, therefore, it is not a true representation of the full manufacturing process. Also, due to the baseplate's small size, part throughput and maximum component size are limited when compared to the full build volume.

3.5.1 Installation

The RBV is most often used when the amount of feedstock available is limited, so a full hopper build is not feasible, or when a limited production run is needed, and a full material changeover would be inefficient.

To use the RBV, it first must be installed, with the unit being placed onto the z-axis and loosely bolted in place. The z-axis is then lowered to -210mm, causing the RBV to seat centrally before raising it to the top and fully tightening bolts, securing the base to the z-axis. After this, it is once again lowered to the previous height, and the taper clamps tightened, securing the top of the RBV so that it remains level with the base of the chamber. 'RBV present' is then selected in the machine's settings. Finally, the full hopper doser must be set to closed to ensure no contamination of powder, and the gas deflectors must be removed, as they have not been optimised for use with the RBV.

3.5.2 Operation

Once installed, the rear dosing chamber has a depth of 67mm, thus determining the maximum build height of the RBV. When the height of the build is known, spacers are added to the doser, decreasing its depth to the minimum level required for the build to be completed. For safety, this is the build height, including any supports and the height of the substrate, plus an additional 3mm. The z-axis is sent to the absolute top, at which point an RBV substrate is placed upon it and fixed in place using 2 screws at the front and back of the plate. The process of measuring the height of the build plate and installing the wiper blade replicates that of the full build procedure.

Once this has been completed, the powder must be loaded into the doser. A sealed container containing the feedstock is placed into the chamber along with the powder compaction tool, and the door is closed. Using the door gloves, the lid is removed, and the powder is poured into the doser in stages. Between each stage, it is compacted to make sure no cavities are present until the doser is completely full, plus an additional 1mm of powder. This additional powder is to facilitate the filling of any and all cavities between the doser and the overflow chute when the wiper blade is first moved forward, whilst demonstrating that at that z-axis height, there is an even distribution of powder across the substrate. When the level of powder deposited in the doser is acceptable, the chamber is flooded

with argon and the remaining powder is sealed within the tub, ensuring that it remains in an inert atmosphere. The tub is then removed from the chamber, and the door is closed, with the remaining machine prep steps following that of a full build.

3.6 Additive Manufacturing Process Parameters

Orthogonal arrays, which come in various forms from L4 to L81, can reduce the need for exhaustive testing by selecting a set of factors and levels to systematically investigate their effects on a given outcome. Each factor level combination appears an equal number of times, ensuring an unbiased evaluation of their effects. Data from these experimental results are analysed to identify significant factors and interactions, subsequently guiding further optimisation. For LPBF, the main variables adjusted when optimising the parameters for new materials are power (P), exposure time (ET), hatch spacing (HS), and point distance (PD), which combine, as outlined in equation 1 with the layer thickness (LT), to give a value for volumetric energy density (VED). L9 and L25 arrays were implemented to determine these optimised parameters, as the former maximised the usable area on the RBV build plate, which could then be expanded to an L25 for the full build volume, as outlined below, to investigate the build parameters in greater detail. The structure of these arrays is displayed in Table 6.

Table 6 The structure of L9 and L25 arrays

| Orthogonal Array | Experimental Runs | Max Number of Factors | Number of levels |
|-------------------------|--------------------------|------------------------------|-------------------------|
| L9 | 9 | 4 | 3 |
| L25 | 25 | 6 | 5 |

The initial development of AM parameters for documented metals began with a baseline. 316L has been well studied in LPBF, and therefore, Renishaw could supply an optimised parameter set compatible with their machine. As with most machines, it could not be taken for granted that any two are exactly the same, and therefore, a supplementary optimisation with the AM400 had to be undertaken, the generic method of which is outlined below.

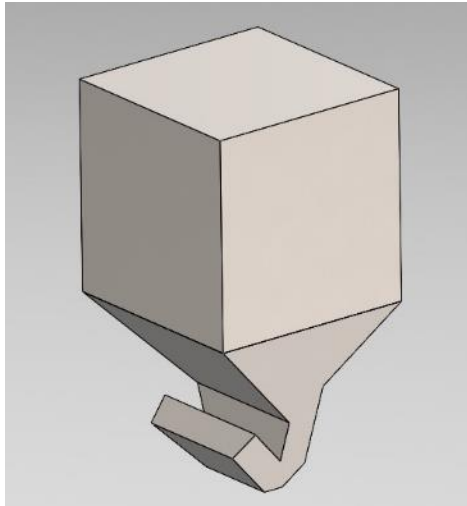


Figure 23 Density cube used for optimisation and corrosion testing

Initial optimisation occurs on the RBV, as it offers much quicker results without needing a complete clean-down and does not require the large quantity of powder used by a full build plate, albeit with some drawbacks. It also establishes whether there are any glaring errors in the parameter set or whether there is an issue with the machine's processing. For preliminary optimisation, an L9 array is prepared based on the initial parameters and applied using QuantAM to density cubes displayed in Figure 23, before the file is transferred to the machine to build. Once built, the cubes are analysed for bulk porosity, with the highest densities sectioned and optically analysed. The data gained from this is used to further hone in on the optimised parameter set. Once the density analysis has taken place, an L25 array is developed for the full build volume to achieve the optimum set, as it did with the RBV.

The specific AM process parameter development will be discussed in more detail in their relevant material sections.

3.7 Casting

To produce cast samples, each material was melted using an induction coil in an argon atmosphere within a glove box. 40g of the material to be cast was initially weighed out in powder form in a fume cupboard. To aid conduction, the powder was then compacted into a cylinder using a Baileigh hydraulic press with 10 to 15 tonnes of force. This was broken down into 2-3 steps, as attempting to compact the entire volume of powder into a billet at once resulted in limited consolidation and structural integrity. Once this was completed, the billets of compacted powder and a ceramic crucible were loaded into a vacuum port connected to a glovebox, ready to be purged to maintain the atmosphere within the chamber.

Once flooded with argon, the contents of the port were transferred into the chamber, with the crucible placed on a boron nitride block, which itself was in the centre of an adjustable stage, as shown in Figure 24.

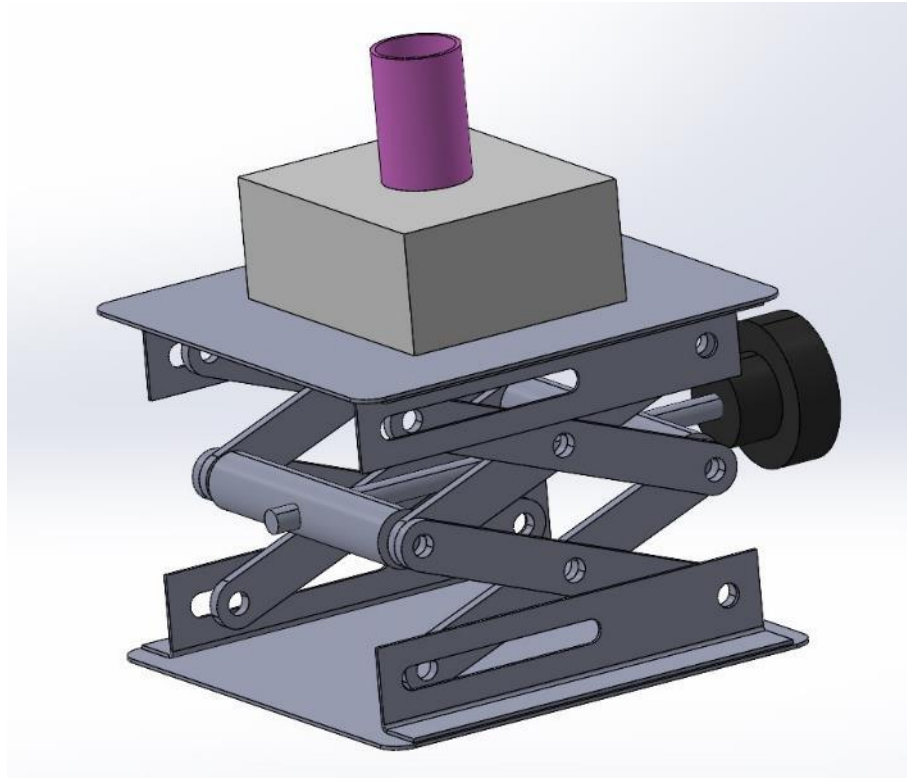


Figure 24 Diagram of the experimental set-up within the glove box for casting, including a scissor lift, boron nitride block and crucible

As much of the material that could be safely placed into the crucible was done before the stage was raised so that the crucible was in the centre of the induction coil, with the pyrometer laser incident on the material within. The pyrometer that was used operates within the range of 350-1800 °C, as temperatures below this are not relevant to the process. Initially, a current of 80A was induced through the induction coil, which was operated using the foot pedal and controlled using the control pad. After approximately 15 seconds, the current was increased by 20A to 100A. When the current is this low, it must be varied based on time, as it is not significant enough to take the temperature of the contents of the crucible into the operating window of the pyrometer. This is then done again so that the current is 120A, at which point the temperature reading starts to increase. From this point onwards, further increases in current were made in 20A increments; however, they were initiated when the rate of increasing temperature began to dwindle.

Once the crucible's contents have begun to melt, there is space for the rest of the material to be added. For safety purposes, this must be done quickly and while no current is flowing through the coil.

It was also standard procedure to drop the current in the coil by 40-60A when restarting the melt after the new material was added, as this, again, would be less likely to result in any thermal shock.

3.8 Drop Casting

The procedure to create drop cast samples followed the same method as that to create standard cast samples, followed by additional steps. As soon as the initial cast is completed, it is allowed to cool by approximately 100 °C to allow some solidification of the alloy before dropping the stage down so that the crucible can be lifted off and placed upon the drop cast mould. The stage is then raised so the crucible is again within the induction coil but predominantly beneath it. This is to focus the current through the top portion of the material, as doing this too low could result in some of the material melting and dropping into the mould before the entire sample is molten, resulting in an incomplete cast. By the time the crucible is within the confines of the coil, the temperature of the alloys processed would drop to approximately 700 °C, so as with adding new material to the cast, the current must initially be dropped prior to resuming the procedure. The metal is reheated until molten, at which point it drops into the mould.

3.9 Heat Treatments

3.9.1 Solution Anneal

The alloys studied in this thesis underwent 2 separate heat treatment cycles. The first was a solution anneal at 1080 °C for 1h per inch thickness before water quenching [74,170,171]. This was achieved by placing 2 samples of each alloy into the furnace at room temperature before increasing the temperature to 1080 °C at a rate of 25 °C/m. Once this temperature was reached, they were held for 35 minutes. After this interval, the first sample was removed and quenched in a large bucket of water whilst the furnace door was resealed and left to return to temperature. This process was repeated for all of the samples to ensure the same quenching temperature for each alloy. Due to the small size of the samples, there was no need to change the water between quenches.

3.9.2 Post-Rolling Anneal

Once each sample had been cold rolled, it was put through an additional annealing cycle where it was held at 900 °C for 35 minutes. This temperature was chosen as it has been shown that this cycle has resulted in a similar yield strength, % elongation, and strain hardening component as the starting material [172].

3.10 Cold Rolling

Cold Rolling was conducted on each alloy tested. The samples to be cold rolled were manufactured through the drop casting route before going through the solution anneal described in section 3.9.1. These samples were then skimmed in the workshop to remove any oxide layers around the exterior whilst leaving as much material as possible. This was to ensure that no oxides were ingrained into the structure during the rolling process.

The initial thickness of the samples was measured prior to rolling to calculate the reduction needed to achieve the desired final depth. The desired total reduction was aimed to be completed in 10 passes, and the reduction per pass was kept the same where possible. This, however, was not always possible, as there were no fixed increments to adjust the gap between the rollers. There was also a degree of slack within the system that was presented when material was passed through the rollers. It was also beneficial to reduce the size of the reduction per pass as the total reduction approached the required level to avoid an overshoot. The total rolling reduction was again chosen based on the information presented by Ravi Kumar. B [172]. The reductions that were realised by rolling for each alloy are shown in Table 7.

Table 7 Cold rolling reductions, target and achieved (mm)

| | 316L | HEA1 | HEAX |
|------------------------------|-------------|-------------|-------------|
| Start | 5.55 | 5.60 | 5.70 |
| 50 % Reduction Target | 2.78 | 2.80 | 2.85 |
| 70 % Reduction Target | 1.67 | 1.68 | 1.71 |
| 50 % Reduction | 2.73 | 2.80 | 2.86 |
| 70 % Reduction | 1.65 | 1.66 | 1.71 |

3.11 Sample Preparation for Optical Microscopy and SEM and Corrosion

3.11.1 Cutting

Once dipped for bulk density analysis, 2mm thick samples were cut from the top face of the AM density cubes using a Buehler IsoMet®4000 linear precision saw. The feed rate was set to 4mm/min and the blade speed to 4900rpm for all cuts. Cast specimens were cut in the same way, whereas drop casts initially had their necks removed via a Buehler AbrasiMet®250 abrasive cutter before then following the same procedure. This was to ensure the specimen cut was representative of the bulk material. For

each method of production, 2 slices of each were initially cut from the bulk material, with one to be prepared for imaging and the other for corrosion analysis.

3.11.2 Mounting & Polishing

Samples for imaging and SEM-EDS went through an additional cutting stage to create an internal face in the XZ and XY planes. These were then hot mounted in conductive Bakelite resin and distinguished using a Dremel engraver.

All samples went through the same 5-stage polishing recipe outlined in Table 8. A head and platen speed of 60rpm and 150rpm were applied at every stage, respectively. Fresh water was used for stage 1, with Buehler MetaDi supreme polycrystalline suspension compounds of diamond size from 9 μm to 1 μm applied for the rest of the polishing pads. All these compounds were deposited using the Buehler automated pipetting system, except during stage 4, where the polishing compound was delivered by hand. Between each stage, the pad, rotating head, and samples were rinsed with water, followed by Isopropyl Alcohol (IPA), with the samples then dried using a hair dryer.

Table 8 Polishing Recipe Used for All Materials Tested

| Stage | Pad | Time (Mins) | Force (N) | Polishing Compound | Head Rotation |
|-------|--------------------|-------------|-----------|--------------------|---------------|
| 1 | Diamond DDG | 10 | 5 | Water | Contra |
| 2 | Hercules H | 10 | 4 | 9 μm | Contra |
| 3 | Trident | 10 | 3 | 6 μm | Comp |
| 4 | Microfloc | 10 | 2 | 3 μm | Comp |
| 5 | Microfloc | 10 | 1 | 1 μm | Comp |

Once this recipe had been followed, the surface finish was analysed using a microscope to see whether any scratches persisted. If they were present, stages 3 to 5 were repeated until the desired finish remained.

Samples for EBSD went through a final polishing stage which comprised of a 90 second polish with colloidal silica before a water stage for the same duration. This procedure slightly etched the samples, revealing some of the microstructure.

3.11.3 Corrosion Preparation

3.11.3.1 Set-up 1

Samples due for corrosion experimentation went through 2 iterations of preparation. For method 1, they were put through the same mounting process as those prepared for imaging; however, once

polished, they then needed to be removed from the resin before an electrical connection could be soldered to the rear of the specimen. Once this was done, the wire connected to the sample was fed through a cavity beneath the platform of the specimen holder shown in Figure 25 and then up through the stem to be connected to the potentiostat. This setup, however, led to multiple problems.

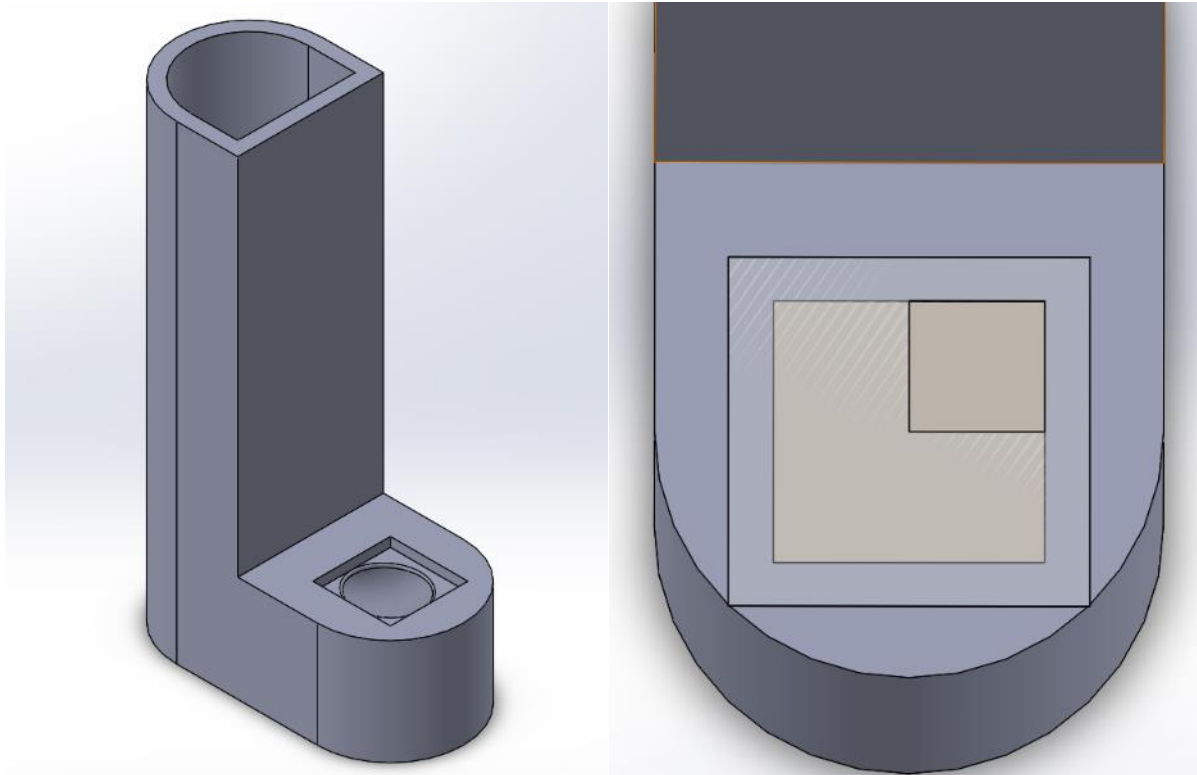


Figure 25 Corrosion sample holder - iteration 1 (A), specimen prepped for testing (B)

Firstly, extracting the samples from the bakelite was a complex undertaking as the only way it had been successfully performed was to wrap the sample in a protective layer of blue roll. It was then clamped in a vice with one side of the resin exposed before using a saw to cut approximately 2mm behind the sample. The remaining bakelite could then be removed with pliers. This was, however, a complicated process that also risked damaging the surface of the sample, requiring it to be re-polished.

Once the sample had been removed, a wire was soldered to its rear, providing the electrical connection needed for the corrosion experiments. However, due to the amount of manoeuvring necessary to thread the wire through the specimen holder, the solder often failed, needing to be redone.

The 0.4356cm² sample area to be tested was removed from a strip of double-sided tape using a Vaessen Creative craft punch. This was then placed in the corner of the sample, as shown in Figure 25

and used to hold it in place in the sample holder with additional tape. Air bubbles present under the tape were extricated using a sawn flat edge of a balsa wood stick.

Once the experiment was running, if there was any significant material degradation during the test, the electrolyte could ingress beneath the tape used to seal it to the holder, down the sides of the sample and into the basin beneath. This caused erratic readings as the electrical contacts on the underside of the sample influenced the readings.

3.11.3.2 Set-up 2

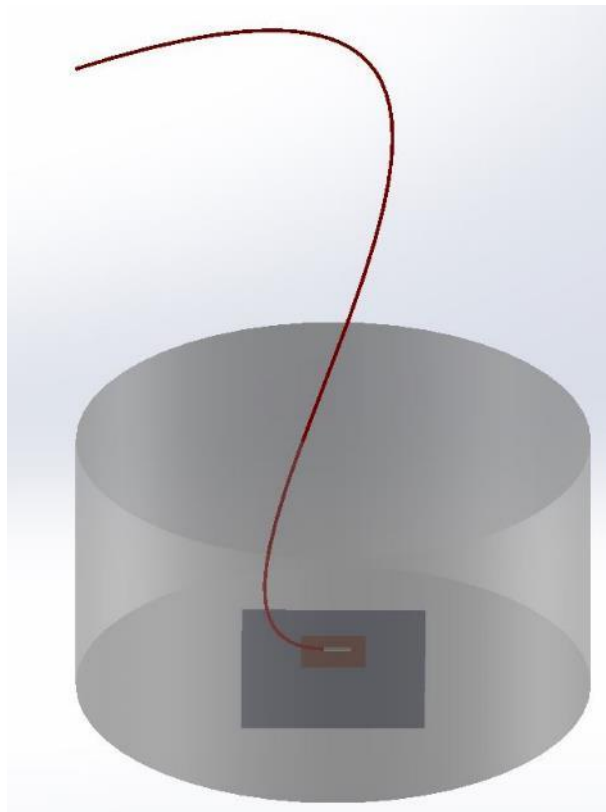


Figure 26 Corrosion specimen setup - iteration 2

To circumvent many of the issues triggered by the first iteration of the setup, a wire was soldered to the rear of the sample prior to mounting in epoxy resin and cured using a hardener. Copper tape was used as an intermediary surface between the wire and metal, as shown in Figure 26, as this aided the soldering process and created a stronger bond. Before the resin was added to the mould, the electrical connection was tested with an ammeter.

Once these samples were polished, they were immediately ready for corrosion experiments. The only further requirement being a test area had to be outlined on the surface, which was achieved using double sided tape and a craft punch as was done in setup 1.

3.12 Etching

Etching is a valuable preparation stage in metallographic analysis, facilitating the observation of the microstructural features of a material, making it easier to examine and analyse under a microscope. Etching creates a differential contrast between various microstructural constituents of a metal or alloy. Different phases, grains, and inclusions may have similar appearances under an optical microscope, but etching selectively reveals these features, making them distinguishable. 316L requires aggressive etchants such as Kalling's No.2, Adler's or Carpenters. Alternatively, electrolytic etching can be employed with a solution of oxalic or nitric acid. Table 9 outlines the etchants used for each alloy and their respective manufacturing methods. Cast samples did not require etching due to an already visible microstructure.

Table 9 Etchant details

| Alloy | Manufacturing Route | Etchant | Condition |
|--------------------------------|----------------------------|------------------|-------------------------------|
| 316L | AM | Kalling's No.2 | Immersion for 5s |
| | Wrought | 70 % Nitric acid | Electrolytic, 75s at 10V |
| | Cold Rolled | | Electrolytic, 1 minute at 10V |
| HEA1 & HEAX | AM | Kalling's No.2 | Immersion for 2-3s |
| | Cold Rolled | 70 % Nitric acid | Electrolytic, 45s at 10V |

In hindsight, a dilution of Kalling's No.2 may have been more practical, as the short immersion times outlined in Table 9 meant over-etching was more likely to occur. Additionally, cold rolled samples in the rolling direction and the surface orientation were mounted within the same mount for ease of analysis. Because these samples were electrolytically etched, the current density was greater on the rolling direction sample due to its smaller surface area which led to faster etching, making it more difficult to achieve an optimal etch on both samples simultaneously.

3.13 Density Analysis

3.13.1 Bulk

Once manufactured, the density cubes were removed from the build plate using a combination of pliers and a mallet. Initial density analysis was conducted using a Biolin Scientific Sigma 700 force tensiometer and Archimedes calculations. Firstly, two equal lengths of dental floss were cut and tied into loops, with one to be used for zeroing the scale and the other to suspend the samples from the machine's hook. The cubes were dipped into a 100ml beaker that was filled with a 50ml solution

containing distilled water and 3 drops of washing-up liquid. The relevant parameters set in the machine's software for the test were a probe speed of 20 mm/min and an immersion depth of 21mm.

The weight of the floss was offset by zeroing the scale with a loop on it; thus, when the cube was suspended, it would give its actual weight, and the calculations would be legitimate. Once the mass of the cube had been recorded, it was manually lowered until it was hanging just above the surface of the water, and the test was started. Once the set immersion depth had been reached, the apparatus returned to its default position, and the change in mass measured was outputted and recorded in Excel. During the dipping cycle, the temperature of the water and surrounding air were also monitored and used in the density calculations.

3.13.2 Optical

Once samples had been polished to the required 1 μ m finish, they were imaged on a Zeiss Observer inverted light microscope. The software's stitching capabilities were used to capture the entire surface of the samples in each image without compromising the quality. Images were captured at 2.5x magnification with a 10x objective lens to provide detailed stitched images without exceeding the file size limit to be exported. These images were then imported to ImageJ to analyse the surface porosity present in each sample.

For this, the image to be investigated is transformed into an RGB image before splitting the individual channels and displaying them. The channel with the best contrast and highest quality was selected, and the image was cropped to achieve the largest area of the sample possible while excluding irregularities. With the AM samples, the outer edges of the samples were removed during the crop, as the boundary parameters for processing had not been optimised and could, therefore, influence the results. Once this has been completed, the threshold of the image is slowly increased from zero, causing the darker areas of the image (the porosity) to turn red. Once all porosity is red, the threshold is applied, and the image is converted to a binary format displaying the porosity in black and the rest of the sample in white before the particles are analysed. Analyse particles was selected from the toolbar with 'display results' ticked, outputting a value for the total area white area, and therefore the density value.

3.14 SEM EDS

3.14.1 Loading and Initial Operation

Polished samples were loaded into the EVO LS25 SEM before the chamber was evacuated and the sample raised to the 10mm analytical position. Once complete, the filament was turned on with an

initial accelerating voltage and probe current of 15 kV and 250 pA set as standard. The brightness, contrast and focus were then adjusted to provide the clearest possible image, followed by optimising the gun shift and tilt to provide the brightest, most stable image for operation before undergoing aperture and stigmatism alignment. The former was achieved by increasing the magnification to 4x greater than the anticipated analytical magnification and focusing on a feature such as a pore or inclusion. The reduced frame tool was activated to maintain image quality whilst decreasing the frame time before selecting the wobble function. The x and y aperture knobs were then adjusted so that the feature in focus remained stationary instead of drifting between frame passes. Once refocused and the wobble function deselected, a stigmatism correction was performed by rotating the x and y rotaries one at a time to achieve the clearest image for both. When a sample area of interest had been identified, the image was refocused before increasing the resolution to 2048x1576 px and decreasing the scan speed to ~ 9 to maximise image quality. The scan was frozen at the end of the frame before saving the image to a report file.

3.14.2 EDS

To complete EDS analysis, the AZtec software was loaded once the initial optimisation and any imaging had been completed. A report file was created before describing the specimen to be analysed, including details such as its compositional elements and any coatings present. An EDS-Map was then run to get an initial insight into the composition of the sample and identify any potential inhomogeneity, such as multiple phases or precipitates. This was achieved by initially taking an image of the desired area and selecting 'automatic lock' to account for any beam drift during the scan. The parameters were then set for the EDS mapping, with conditions such as process time, dwell time, and run time varied in combination to achieve the desired frame time, count rate and dead time. If a low count rate is achieved, increasing the probe current will result in an increase in this number. However, this will be at the cost of resolution. After ~ 30 minutes, the scan is stopped and studied for any heterogeneity. If detected, point scans are placed at these locations to quantify the magnitude of the differences. As with the maps, point scan parameters, such as the process time, are designated prior to investigation to achieve the desired count rate before moving on to the following location.

3.14.3 Grain Size Analysis

Grain Size Analysis was conducted using the EBSD facilities within the same AZtec software as EDS, however there was some additional setup steps. Once the initial alignments, magnification and focus steps had been completed, the sample and its holder were tilted by 70 ° towards the horizontal, before being raised to the analytical position. The focus was re-optimised before adjusting the magnification

to the desired level for the analysis. Once this was complete the proximity sensors were disabled and the EBSD detector inserted into the chamber.

Before deciding on an area for analysis, the crystal structures that make up the respective alloys had to be selected. This let the software know what to look for during analysis and speeds up processing time. Once confirmed, the acquisition area was chosen in conjunction with the step size as both affected the total duration of the analysis. The step size had to be smaller than 10% of the average grain size expected and the area had to be large enough to be fully representative of the material, but not too large as to lead to immense processing time. The test could then be launched.

The software had multiple outputs, but the one of interest was the contrast band, which was exported to a second machine for grain size analysis. Channel 5 was opened, and the file dragged in to the Tango platform, opening the file and allowing the removal of dead spots or spikes. Once this had been done, the detection criteria for a grain was set to a grain boundary angle of greater than 4° before 'analyse grains' was selected and the data output exported to excel. Any grains detected that were less than 3x the step size were discounted, as they didn't have the sufficient reliability. Finally, a MATLAB script was used to plot the data and extract the metrics of minimum diameter (d_{\min}), maximum diameter (d_{\max}), and mean diameter (d_m).

3.15 X-ray Diffraction

X-ray diffraction (XRD) is a non-destructive technique that can be used to investigate single crystal or polycrystalline materials. Simply put, X-rays emitted from a source are reflected through a sample before reaching a detector. The interference these X-rays undergo can be analysed to determine things such as the position and arrangement of the crystal structures of the sample [173]. One particular use is its ability to assist in the identification of a sample's constituent compounds based on the diffraction patterns that are detected [174].

XRD was completed to analyse the crystal structures present in the alloys after each manufacturing process. The XRD divergent slit/Bragg-Brentano 2θ methodology was used for this analysis on a BRUKER D8 Discover with a Cu anode and a 1.5406 \AA wavelength.

Once the program is loaded, the Da Vinci tab is selected. This window and its settings contain a mix of user-defined and automatically updating test parameters. Those that auto-update do so based on things such as the beam path, slit sizes and whether any filters have been applied. The setup used is displayed in Figure 27.



Figure 27 Da Vinci set up for divergent slit XRD analysis

3.15.1 Loading & Alignment

The tested samples underwent the same mounting and polishing procedure as those for SEM and optical analysis. To load a sample, DIFFRAC.SUITE is opened, the Z axis is set to 0, and the positional lasers are turned on. The sample is then placed on the central stage, and its height is increased by placing shims underneath it until the two lasers intersect on the sample's surface to roughly set the z height. The rotary absorber is set to 80.93, the detector to 0D mode, and its opening to 0.075 to improve spatial accuracy. Within the scan type, 'z' is selected and set to test between -1.4 mm and 2 mm at 0.05mm increments to ensure the height of the sample is detected accurately and the test is run. The resultant scan has a drop-off in counts from a maximum to 0 as the top of the sample is reached. To accurately determine the z height of the sample, take half of the maximum value, and where this point crosses the line, the value is selected and then sent to the instrument.

3.15.2 Test Set-up

To set up the test, a blank standard XRD file is opened. Because all the alloys tested contain large quantities of Fe and Mn, within the Da Vinci subsection, the lower discriminator needed to be changed from 0.11 V to 0.19 V to remove much of the background radiation. The z-axis height of the sample found in the previous steps is brought into the program by updating the drives. The scan range for 316L was determined based on significant available literature, whereas those of HEA1 and HEAX as alloys of novel composition went through an initial test of a greater range before reducing it in further tests to reduce scan time. These ranges are displayed in Table 10. All tests contained 3600 steps with a time/step of 1s for high resolution.

Table 10 XRD setup ranges for 316L and HEAs

| | 2Theta (Abs. start) | 2Theta (Abs. stop) | Step Size |
|------------------------|----------------------------|---------------------------|------------------|
| 316L | 35 ° | 80 ° | 0.014 ° |
| HEA1 & HEAX | 30 ° | 95 ° | 0.018 ° |

The file is saved before loading it in the jobs subsection and starting the test. Once completed, the data is automatically saved, and the sample is removed.

3.15.3 Phase Identification & Analysis

The file to be analysed is imported into the DIFFRAC.EVA software and selected in the data tree. Initially, the 'strip kalpa2' tool is used to isolate the stronger kalpa1 wavelengths for investigation. Once isolated, the search/match function is selected, and the 'open crystallography database' is chosen. Within the chemical filter, the elements expected within the composition of the alloy are selected and turned blue, indicating that at least one must occur within the patterns suggested; the rest are excluded before selecting 'match.'

A search list is created from the conditions set out in the database and chemical filter, containing all the structures whose peaks in some way match those in the XRD test data. These matches are then analysed to identify those that best compare with the peaks and selected. In the event that these matches do not perfectly align, a degree of tuning may be applied to centralise the expected peak with that of the observed peak using the 'tune cell' tool. The auto-scale function is then applied to match the intensity of the expected peaks with that of the observed. This process is repeated with multiple elements until all the peaks have been accounted for. As all samples tested were mounted in Bakelite resin, a scan was conducted on a pure Bakelite specimen to observe any background wavelengths that should be excluded. This scan is shown in Figure 28. Whilst there are distinct peaks observed from the Bakelite sample, the counts at these peaks are relatively low compared to those detected when analysing the scans conducted on the alloys presented in this work. Nevertheless, peaks at 35 °, 42.5 ° to 46 °, 54.5 °, 57.5 °, 60 °, 77.5 ° and 84 ° are noted in case they interfere with the data from the tested samples. To remove any potential interference from the Bakelite, its data was initially scaled down in the Y axis, as the counts observed when incident on the sample directly would be greater than those seen when in the background of a metal sample. Once this had been completed, the reduced Bakelite scan was subtracted from the scan data of the metal sample. This provided a more accurate representation of the crystal structures without any unexplained peaks.

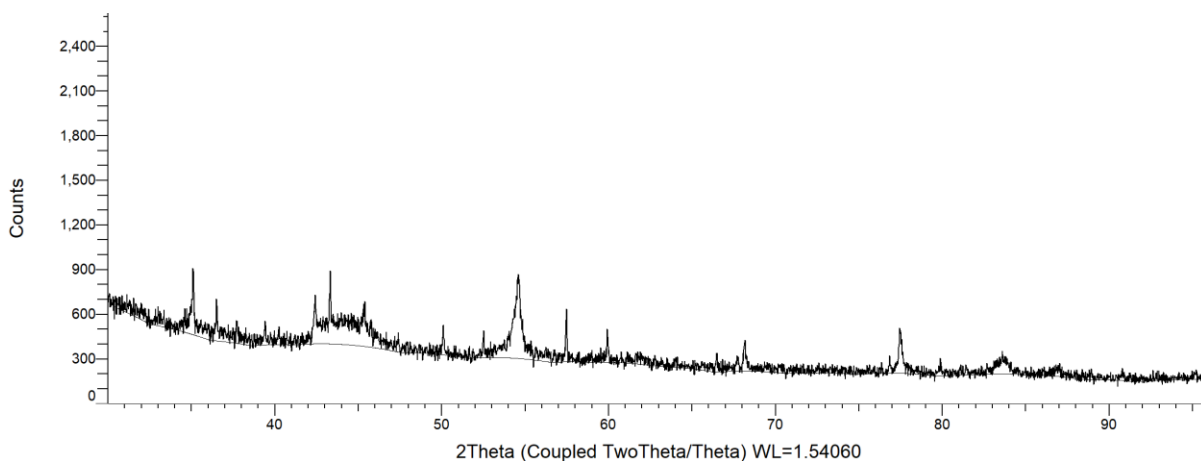


Figure 28 XRD analysis of Bakelite

Once all peaks have been identified, their phase proportions can be plotted on a pie or bar chart, as well as identifying the space group the structure belongs to and its crystal lengths. However, there were failures with this method. Due to the cubic structures identified using the pattern-matching process, the intensities and wavelengths could not be tuned individually, and therefore, deviations were seen when comparing this method of calculating the phase proportions from the sum of the intensities of each peak for some data sets.

3.16 OCP & Potentiodynamic Polarisation

3.16.1 Solution Preparation

All potentiodynamic polarisation experimentation used the same 3.5 %wt sodium chloride (NaCl) solution as the electrolyte. It was created in 1L batches by initially measuring out 1L of deionised water in a beaker before placing it on a magnetic stirrer. 35g of >99.5 % pure NaCl was then weighed out onto a measuring tray before turning the stirrer on and adding the NaCl incrementally to the solution until it had completely dissolved.

3.16.2 Experimental Setup

Setup 2 from the corrosion in Figure 26 was used in all potentiodynamic polarisation tests due to the ease of sample preparation and the comparative lack of problems associated with the experimental procedure. Once the preparation steps had been completed as discussed, the sample is taped face up around the perimeter of the bottom of a wide beaker, with the wire extending out over the rim. This ensures that the sample doesn't move during the experiment and that the exposed wire is removed from the active environment to avoid interference. The reference and counter electrodes are suspended from clamps attached to a retort stand and positioned so that the reference electrode is as close to the sample as possible without contact, and the counter is as far away as possible. The

electrolyte is then steadily poured into the beaker without disturbing the sample until it and the tips of the electrodes are entirely submerged. Any air bubbles present on the test area of the sample must be removed, which was achieved with the end of a pipette so as not to scratch the surface.

Once these steps were completed, the electrodes and sample were connected to their counterpart wires originating from the potentiostat by crocodile clips, and the machine turned on. All tests were conducted on a Gamry Interface 1010 potentiostat using the Gamry Framework™ software provided. The sequence wizard within the software created an experimental framework including an open circuit potential (OCP) and a cyclic polarisation (CP) test that would occur back-to-back without any delay or need for intervention. Each stage needed inputs to set the parameters required. For all open circuit potential tests, the duration was set to 600s to allow the system time to settle and achieve an equilibrium, and the surface area of the test specimen was also input as 0.4356cm².

CView was used to plot the data from each test and extract the key data points. When determining the value of a material's E_{pit} from the plotted data, it was defined as the point at which the current increases rapidly. Where there was no sharp increase and instead a gradual current increase as the potential was increased, the E_{pit} was defined as the value at a predesignated current density. For consistency, this value was chosen as $2 \times 10^{-4} \text{ Acm}^{-2}$. This is a higher current density than often seen for pitting potential; however, it was selected to minimise the chance of defining it too early.

3.17 Additional Notes

For simplicity, the manufacturing processes pursued in this thesis will henceforth be designated as displayed in Table 11.

Table 11 Manufacturing processes and their production notes

| Process | Production Notes |
|----------------|--|
| AM | Manufactured by LPBF, as built with no heat treatments or additional finishing |
| Cast | 40g cast as outlined in 3.7, no heat treatments or additional finishing |
| CR | Drop cast as outlined in 3.8 before solution annealing (3.9.1), cold rolling (3.10), and finally a post-cold roll anneal (3.9.2) |

4 An Investigation into the Effect of Density Variation on the Corrosion Performance of Additively Manufactured 316LSS

4.1 Introduction

This investigation aimed to optimise the LPBF processing parameters for 316L and subsequently introduce deviations from these to impose variations in density across the array. These samples then underwent corrosion testing to understand the effect of porosity on corrosion resistance. The wrought samples in this scheme of work were cut from 2mm thick annealed sheet 316L supplied by Goodfellows. The wrought samples were used as a baseline to compare to the AM samples' corrosion resistance.

4.2 Powder Analysis

Figure 29 presents SEM images of the 316L powder feedstock used to manufacture the cubes in this study.

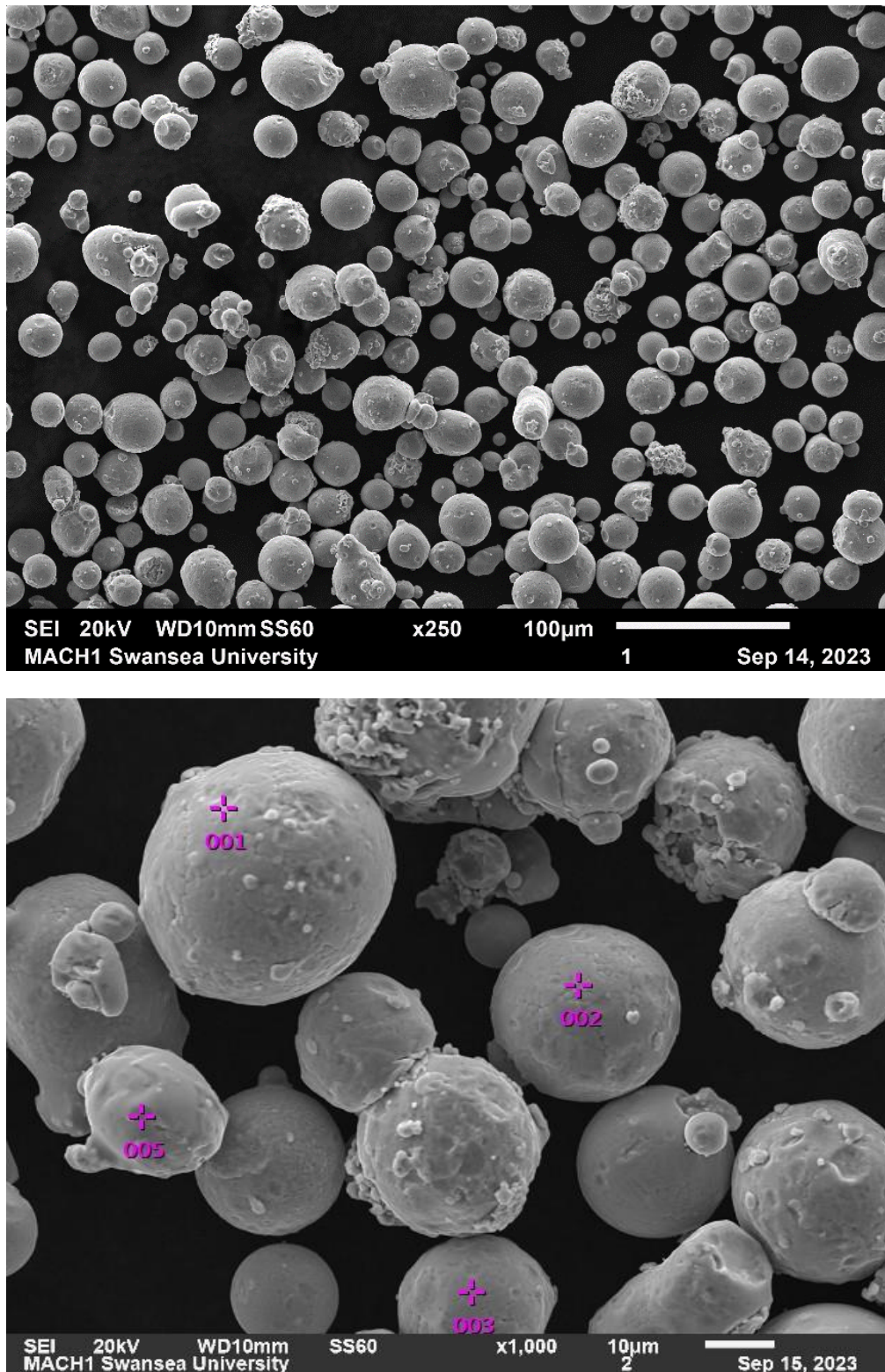


Figure 29 SEM micrographs of 316L powder at 250x (a) and 1000x (b) magnification

Figure 29 observes that the powder used was primarily spherical; however, a small percentage of particles display more irregular, prolate spheroid geometries. There is also evidence of satellites and a degree of agglomeration with smaller particles. An EDS scan was conducted on the powder to check for inhomogeneity, the point scans of which are shown in Figure 29 (b); however, an even compositional distribution was observed across the specimen, as displayed in Table 12.

Table 12 EDS point scan analysis of Figure 29 (b) (wt.%)

| Spectrum | Fe | Cr | Ni | Mo | Mn | Si | S | P |
|------------------|-------|-------|-------|------|------|------|------|------|
| 1 | 67.04 | 17.49 | 10.86 | 1.95 | 1.48 | 0.93 | 0.21 | 0.04 |
| 2 | 67.96 | 17.3 | 10.6 | 1.93 | 1.29 | 0.74 | 0.15 | 0.04 |
| 3 | 67.9 | 17.11 | 10.44 | 1.9 | 1.53 | 0.87 | 0.21 | 0.04 |
| 5 | 66.47 | 17.4 | 11.22 | 2.32 | 1.37 | 1.03 | 0.16 | 0.04 |
| Average | 67.34 | 17.32 | 10.78 | 2.03 | 1.42 | 0.89 | 0.18 | 0.04 |
| Deviation | 0.72 | 0.16 | 0.34 | 0.2 | 0.11 | 0.12 | 0.03 | 0 |

PSD analysis was conducted, the results of which are displayed in Figure 30 and Table 13.

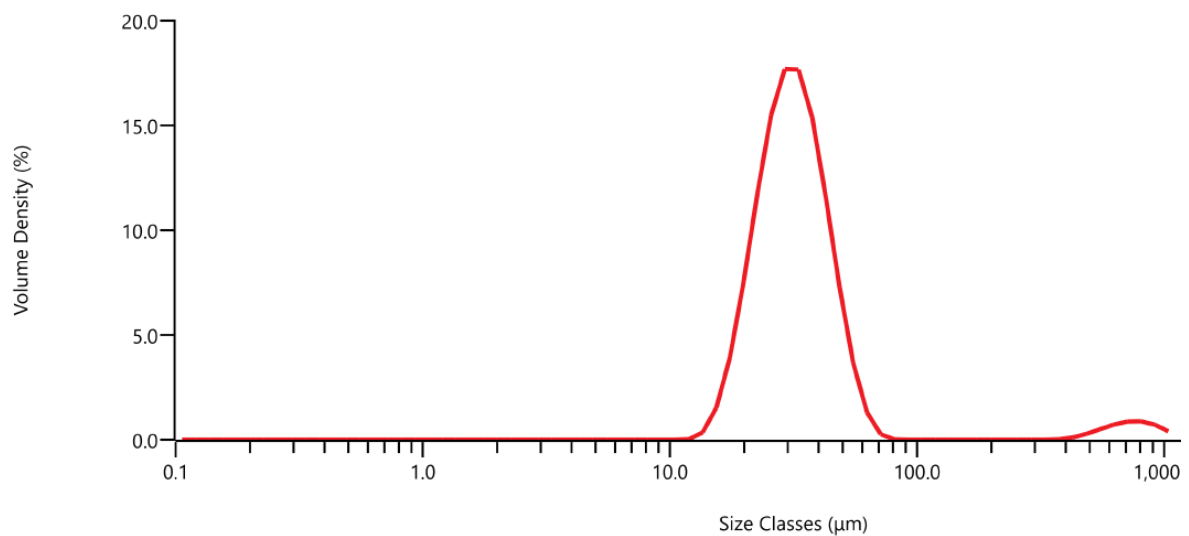


Figure 30 316L powder PSD

Figure 30 shows that the diameter of particles within the powder sample was between approximately 12.7 µm and 66.9 µm. Additional particles were detected with a diameter in excess of 352 µm; however, this is due to air bubbles in the system as a result of the stirrer, with the SMD of 30.6 µm given by D [3,2] in Table 13. Dv (10) and Dv (90) advise that 10 % of the particles analysed lie below 20.8 µm and 90 % below 49.5 µm, which concurs with the fact that the powder size was meant to be within the 15 µm – 45 µm range. Approximately 3.76 % of the total volume is attributed to the bubbles above 352 µm previously discussed.

Table 13 Particle size by volume for 316L powder

| Percentile | Size (μm) |
|------------|------------------------|
| Dv (10) | 20.8 |
| Dv (50) | 31.5 |
| Dv (90) | 49.5 |
| D [3,2] | 30.6 |
| D [4,3] | 59.0 |

A selection of the data produced during stability and variable flow rate testing is presented in Table 14. Comparing the FRI of 1.17 to the flow rate categories in Table 5 suggests that the 316L powder tested was insensitive to flow rate. This implies that the powder behaves consistently when applying a varying driving force.

Table 14 Rheometric characteristics of the 316L powder

| BFE (mJ) | SE (mJ/g) | FRI | CBD (g/ml) | Split Mass (g) |
|----------|-----------|------|------------|----------------|
| 786.46 | 2.89 | 1.17 | 4.29 | 107.29 |

This is important in the LPBF process, as the recoater blade aims to create the most evenly distributed powder bed possible. A low FRI reduces the likelihood of powder agglomeration, providing a consistent material delivery.

4.3 Optimisation and Experimental Setup

4.3.1 Optimisation

Renishaw provided optimum parameters for producing 316L by LPBF for their machine. To confirm these, further optimisation was undergone in the RenAM400 using an L25 array of the density cubes displayed in Figure 23. To do so, the parameter inputs of power (P), point distance (PD), hatch spacing (HS), and exposure time (ET) were varied by 10 % on either side of the optimum, as outlined in the methodology section 3.6. Once the build was completed, the parts were removed from the build plate, and their bulk density was measured 3 times and averaged. The 6 samples with the highest density from this test were sectioned, hot mounted, and polished to a $1\mu\text{m}$ finish, as specified in the methodology. Once prepped, they were optically imaged using the observer microscope and exported to ImageJ for porosity analysis. This optimisation concluded that the parameter set provided by Renishaw was confirmed to manufacture the part with the highest density.

4.3.2 Build Setup

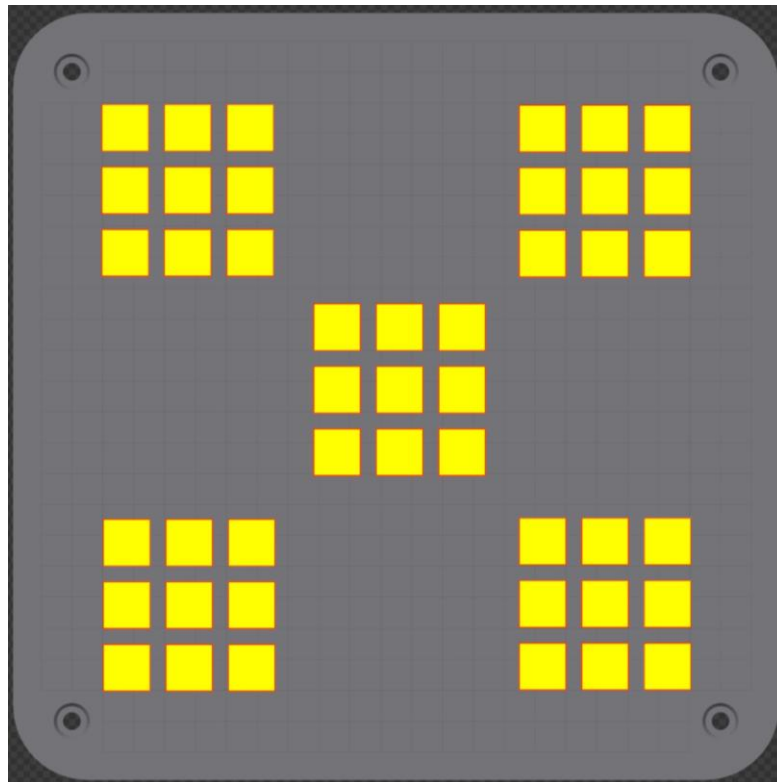


Figure 31 5x9 build setup for 316L density cubes

To conduct this investigation, an L9 array with 5 repeats was created, as shown in Figure 31, with the best parameters confirmed by the optimisation used for the production of sample 4. The other sample's parameters were defined using the Taguchi L9 array setup for 4, 3-level factors outlined in Table 15, with the resultant parameters and calculated energy densities displayed in Table 16. For cube 4, the parameters were overridden from the standard L9 set-up to represent the optimum parameters in the build.

Table 15 L9 Taguchi array for parameter selection

| Cube | PD | HS | ET | P |
|------|----|----|----|---|
| 1 | 1 | 1 | 1 | 1 |
| 2 | 1 | 2 | 2 | 2 |
| 3 | 1 | 3 | 3 | 3 |
| 4 | 2 | 2 | 2 | 2 |
| 5 | 2 | 2 | 3 | 1 |
| 6 | 2 | 3 | 1 | 2 |
| 7 | 3 | 1 | 3 | 2 |
| 8 | 3 | 2 | 1 | 3 |
| 9 | 3 | 3 | 2 | 1 |

Table 16 316L build parameters for repeated samples 1-9

| Cube | PD (μm) | HS (μm) | ET (μs) | P (W) | VED (J/mm ³) |
|------|---------|---------|---------|-------|--------------------------|
| 1 | 65 | 120 | 70 | 175 | 31.41 |
| 2 | 65 | 110 | 80 | 195 | 43.64 |
| 3 | 65 | 100 | 90 | 215 | 59.54 |
| 4 | 60 | 110 | 80 | 195 | 47.27 |
| 5 | 60 | 110 | 90 | 175 | 47.73 |
| 6 | 60 | 100 | 70 | 195 | 45.50 |
| 7 | 55 | 120 | 90 | 195 | 53.18 |
| 8 | 55 | 110 | 70 | 215 | 49.75 |
| 9 | 55 | 100 | 80 | 175 | 50.91 |

4.4 Bulk Density Analysis

Table 17 and Table 18 display the results from the mass and density analysis, respectively, for each cube across the 5 blocks. The error in each cube's reading across the 5 blocks measured by standard deviation is most significant when the mass and density of the components are lowest.

Table 17 Mass analysis for 316L by cube and block number (g)

| Cube | Block 1 | Block 2 | Block 3 | Block 4 | Block 5 | Sample Avg | Std Dev |
|-------------|---------|---------|---------|---------|---------|------------|---------|
| 1 | 30.971 | 31.405 | 31.055 | 31.391 | 31.345 | 31.233 | 0.183 |
| 2 | 31.797 | 31.988 | 31.764 | 32.018 | 31.881 | 31.890 | 0.101 |
| 3 | 31.915 | 31.989 | 31.926 | 32.082 | 32.042 | 31.991 | 0.065 |
| 4 | 31.740 | 31.945 | 31.665 | 31.987 | 31.799 | 31.827 | 0.122 |
| 5 | 31.798 | 31.993 | 31.796 | 31.991 | 31.905 | 31.896 | 0.088 |
| 6 | 31.956 | 32.037 | 31.923 | 32.026 | 31.992 | 31.987 | 0.043 |
| 7 | 31.716 | 31.956 | 31.720 | 31.973 | 31.735 | 31.820 | 0.119 |
| 8 | 31.804 | 32.101 | 31.839 | 32.038 | 31.986 | 31.953 | 0.114 |
| 9 | 31.949 | 32.040 | 31.941 | 31.967 | 32.014 | 31.982 | 0.038 |
| Mean | 31.738 | 31.939 | 31.736 | 31.941 | 31.855 | | |

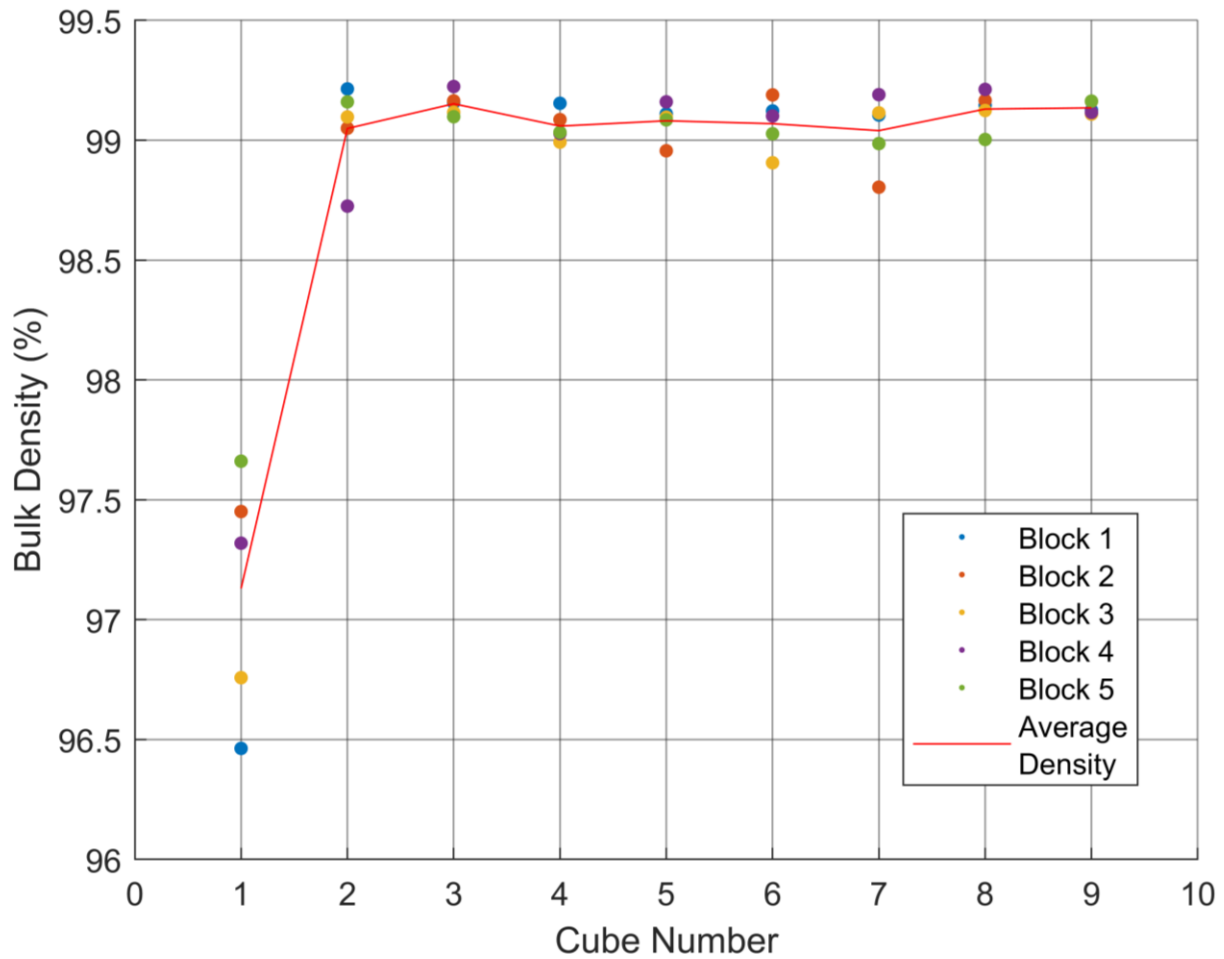


Figure 32 Bulk density of 316L cubes

Figure 32 exhibits the bulk density of each cube from the build, with each L9 block colour-coordinated. Significant variation is experienced in the measurements of the cubes at position 1 in the array, showing that non-optimal parameters result in poorer part quality and decrease the repeatability of these parts.

Table 18 Density analysis for 316L by cube and block number (%)

| Cube | VED (J/mm ³) | Block 1 | Block 2 | Block 3 | Block 4 | Block 5 | Sample Avg | Std Dev |
|-------------|--------------------------|---------|---------|---------|---------|---------|------------|---------|
| 1 | 31.41 | 96.463 | 97.451 | 96.758 | 97.319 | 97.661 | 97.130 | 0.448 |
| 2 | 43.64 | 99.214 | 99.050 | 99.097 | 98.725 | 99.160 | 99.049 | 0.171 |
| 3 | 59.54 | 99.157 | 99.164 | 99.116 | 99.224 | 99.098 | 99.152 | 0.044 |
| 4 | 47.27 | 99.154 | 99.086 | 98.992 | 99.028 | 99.033 | 99.059 | 0.056 |
| 5 | 47.73 | 99.110 | 98.956 | 99.096 | 99.160 | 99.085 | 99.081 | 0.068 |
| 6 | 45.50 | 99.122 | 99.189 | 98.906 | 99.101 | 99.027 | 99.069 | 0.097 |
| 7 | 53.18 | 99.105 | 98.804 | 99.114 | 99.190 | 98.986 | 99.040 | 0.135 |
| 8 | 49.75 | 99.146 | 99.166 | 99.124 | 99.212 | 99.003 | 99.130 | 0.070 |
| 9 | 50.91 | 99.125 | 99.162 | 99.109 | 99.116 | 99.163 | 99.135 | 0.023 |
| Mean | | 98.844 | 98.892 | 98.813 | 98.897 | 98.913 | | |

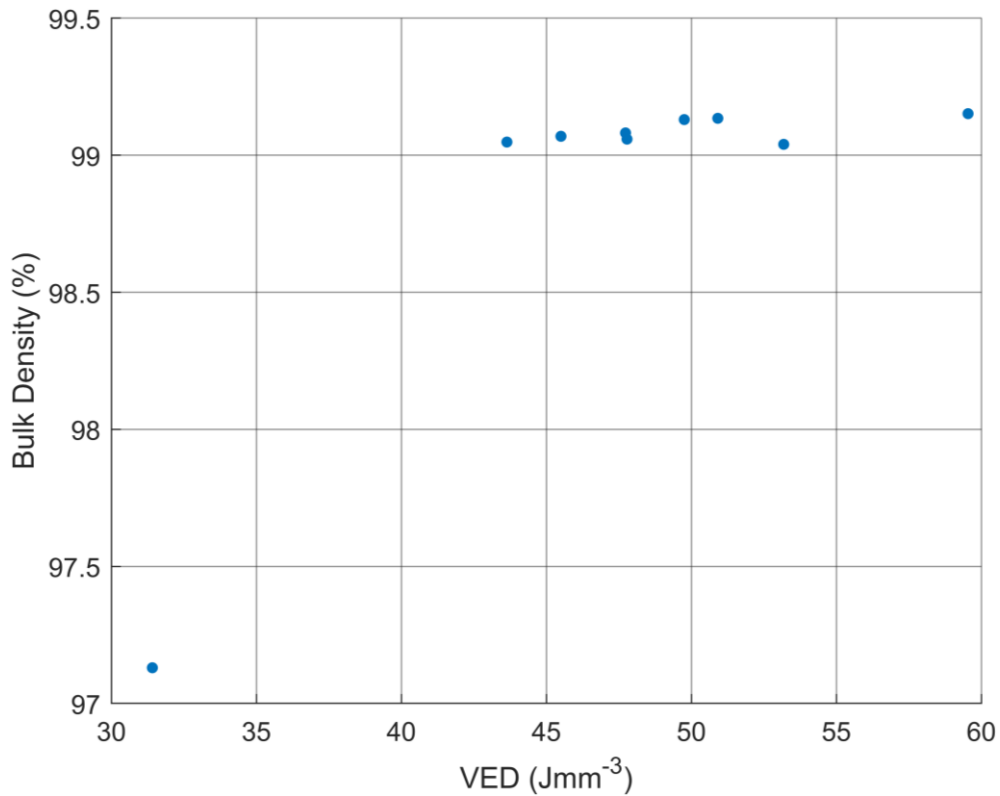


Figure 33 Graph of VED vs average bulk density

Figure 33 shows a correlation between an increased VED resulting in a greater bulk density measurement. The graph reproduces what is seen in literature for 316L, as well as other alloys, that lower energy densities than the optimum result in lack of fusion porosity and consequently, lower part densities. As VED is increased towards the optimum, there is a range in which a high density is achieved, as shown in Figure 33 between 43.64 J/mm³ and 59.54 J/mm³. Beyond this range, it is common for the parts to accrue porosity associated with keyholing and vaporisation. However, this effect is less significant than lack of fusion and is not obvious in the results presented. A more expansive selection of VEDs than exhibited here would be needed to accurately determine at which point lack of fusion is no longer significant, and vice versa for keyholing, but that is not the focus of this study.

4.5 Optical Density Analysis

Table 19 Density measurements from bulk and optical analysis

| Sample | Cube Array | Bulk Density (%) | Optical Density (%) | Difference |
|--------|------------|------------------|---------------------|------------|
| 1 | 1 | 96.46 | 95.11 | -1.353 |
| 3 | 3 | 99.16 | 99.84 | 0.683 |
| 7 | 7 | 99.11 | 99.74 | 0.635 |
| 10 | 1 | 97.45 | 93.05 | -4.401 |
| 16 | 7 | 98.80 | 99.74 | 0.936 |
| 19 | 1 | 96.76 | 90.36 | -6.398 |
| 22 | 4 | 98.99 | 99.88 | 0.888 |
| 25 | 7 | 99.11 | 99.75 | 0.636 |
| 29 | 2 | 98.72 | 99.81 | 1.09 |
| 30 | 3 | 99.22 | 99.81 | 0.586 |
| 37 | 1 | 97.66 | 93.68 | -3.981 |
| 40 | 4 | 99.03 | 99.66 | 0.627 |

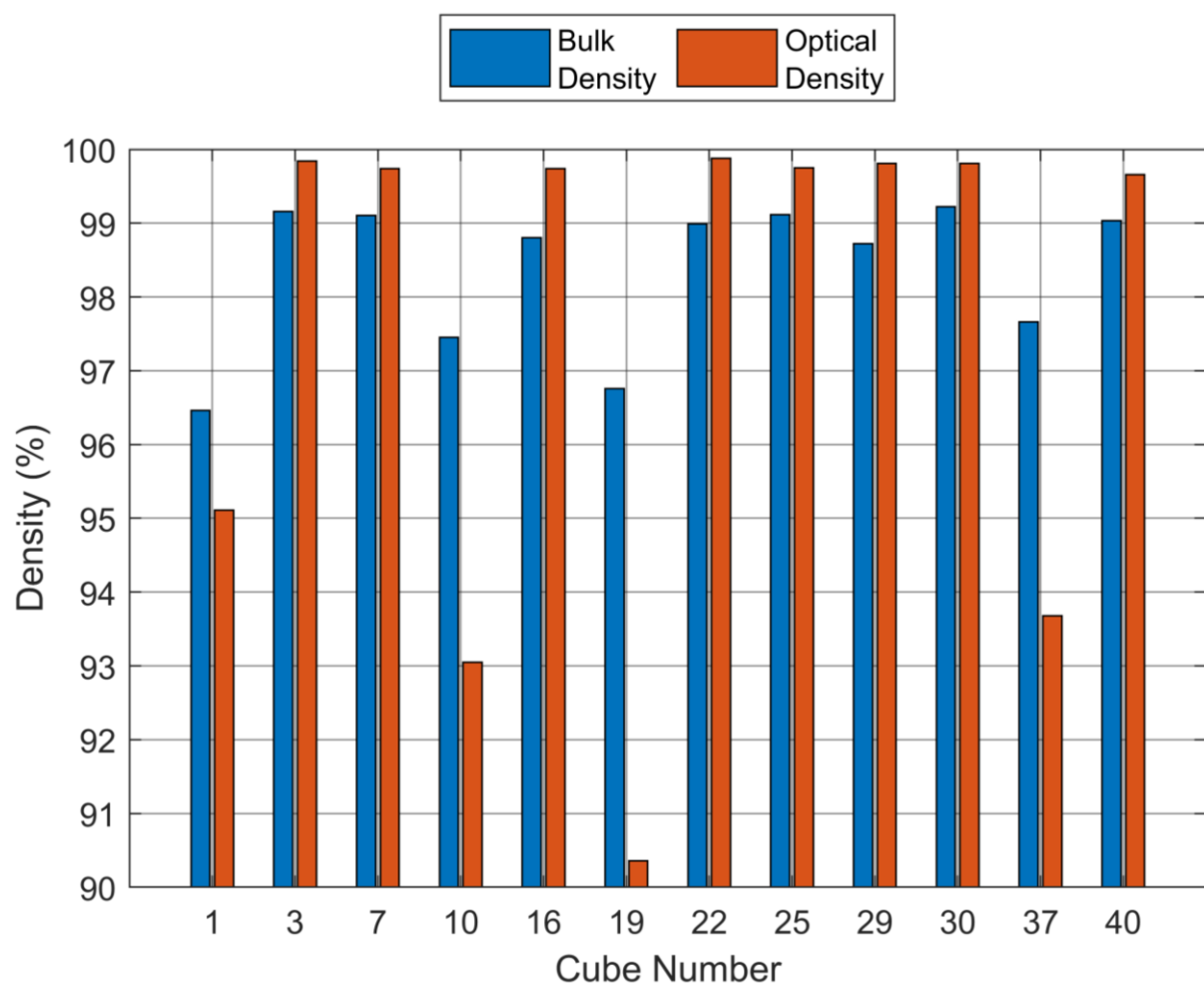


Figure 34 Bulk and optical density comparison for 316L

Table 18 observes that the average bulk density of the cubes built with parameter set 3 was the highest, also exhibiting the highest VED. This contradicts the statement that cube 4 was built with the optimum parameter set in each array. However, the optical analysis presented in Table 19 shows that the highest density was measured at 99.88 % from sample 22, belonging to cube array 4.

Table 19 and Figure 34 show that the bulk density measured using the Archimedes calculation differs consistently from those output from the optical analysis. The optical measurement is consistently higher for the cubes where the bulk density has been observed to be >98 %, whereas the opposite is true for those cubes with a bulk density <98 %. The difference between the two analytical methods is also more pronounced when the density measurement is lower. These results suggest some failures within the methods for one, if not both, of these analytical techniques. The bulk density analysis is calculated on assumptions such as a value for 'theoretical density' as well as repeatability errors encountered when weighing the mass of cubes before dipping. These errors, however, only amounted to a maximum standard deviation of 0.013 once further repeats were conducted. The average standard deviation of the density readings from this method was 0.078. However, multiple samples had to be tested more than the 3 times stated in the methodology to reduce their individual error and single out anomalies.

As mentioned in the methodology, the edges of the samples were cropped out of the final image to be optically analysed, as the boundary parameters had not been optimised. This could be responsible for some of the disparity seen between the two techniques. The optical density is also observed from a single slice or cross-section of the cube, and it, therefore, cannot be stated with absolute certainty that the slice analysed is characteristic of the bulk sample. It is assumed that the porosity present at each layer will be consistent during the build as there are no changes in processing parameters throughout the build. Ultimately, the Archimedes methodology is a non-destructive technique; however, its precision encounters constraints when applied to nearly fully dense components. This limitation arises from the inherent challenge of determining the actual theoretical density of an additive manufacturing alloy, which is dependent on multiple factors. Moreover, the accuracy of measurements may be compromised by variations in surface quality [175,176]. For these reasons, optically analysed density is the authoritative measurement over the dipped density.

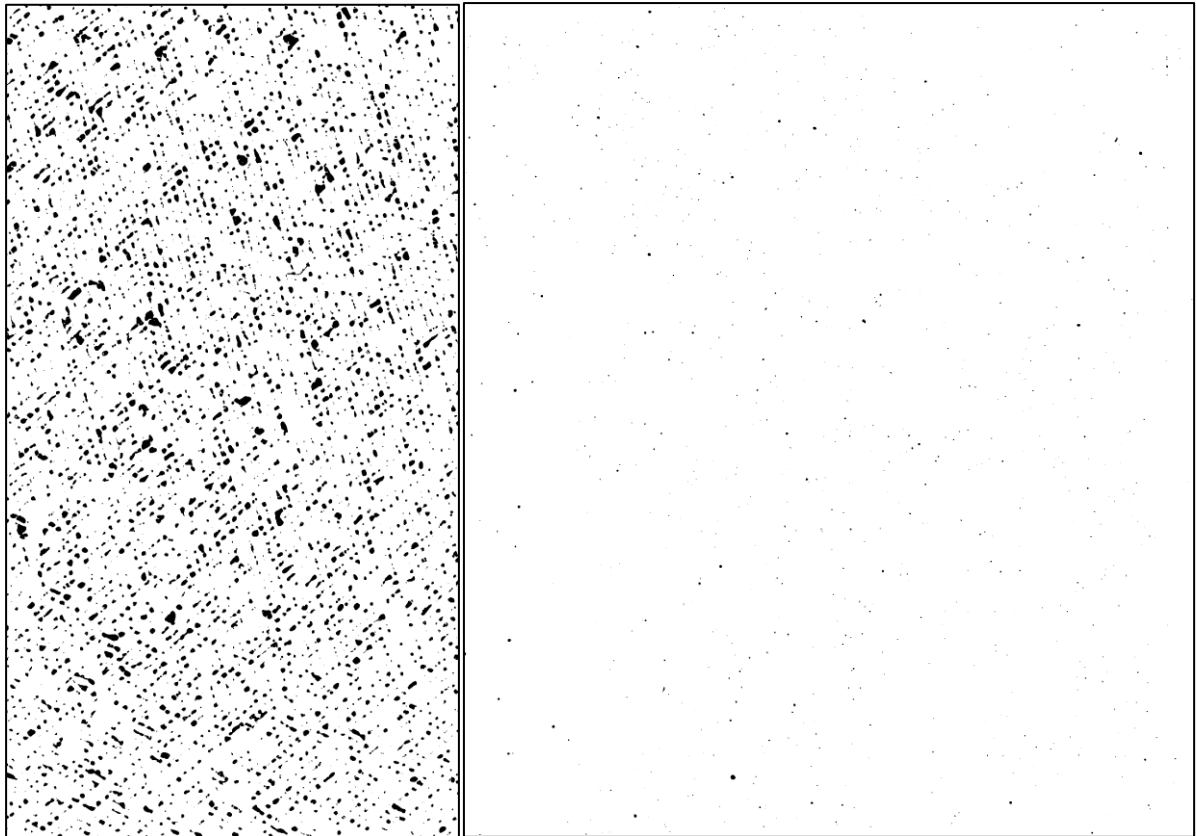


Figure 35 Binary images of (a) AM samples 19 and (b) 22 post thresholding

Figure 35 displays the binary images produced when calculating the density of samples optically. Samples 19 and 22 have been presented to show the clear distinctions between a high and low porosity. Sample 19, with a calculated density of 90.36 %, shows a significant number of irregularly shaped pores with large diameters. They also occur in a regulated formation, appearing to follow the laser scan path, with even larger pores occurring where the laser path from other layers intersect. Conversely, sample 22, with the highest density recorded of 99.88 %, presents comparatively few pores, sporadically located, much smaller in size and with a more circular geometry.

4.6 Microstructure

The microstructure of the 316L AM and wrought samples was investigated using optical microscopy and SEM analysis.

4.6.1 Additive Manufacturing

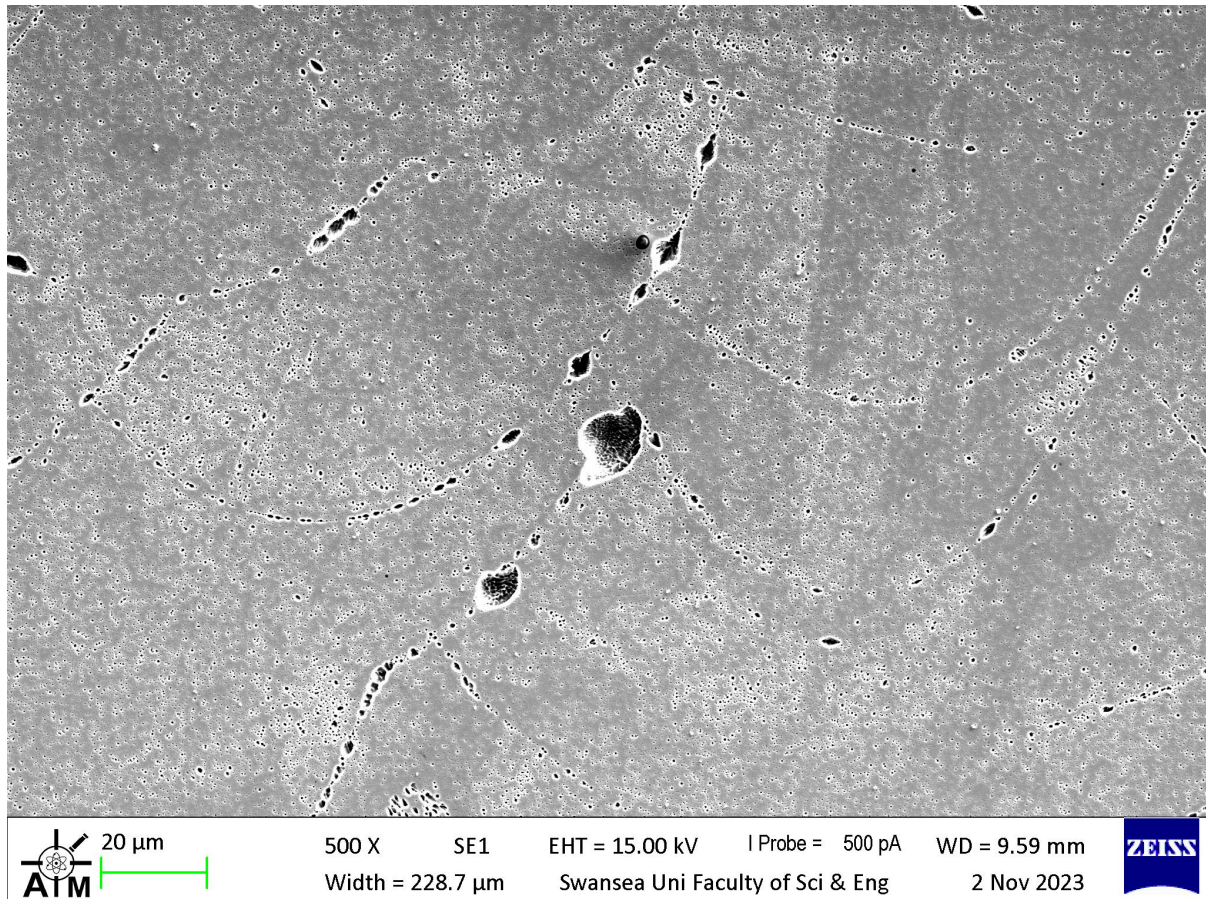


Figure 36 SEM micrograph of AM 316L in the XZ plane at 500x magnification

Particular focus is directed towards the melt pool boundaries of the AM 316L sample depicted in Figure 36. Whilst porosity occurs with certain regularity along the majority of these boundaries, there are regions where significantly larger formations exist. These formations also seem to occur in zones where two or more boundaries intersect and have more of an ellipsoidal geometry than the smaller, circular porosity present along the majority of the boundary. EDS mapping of the area depicted in Figure 36 was undertaken to identify any compositional variations between the bulk material and the boundaries of the melt pool, such as a higher concentration of Cr at the boundary indicating the presence of chromium carbides. However, upon review of the data, no such distinctions appeared other than a diminished count rate at the site of the two largest pores.

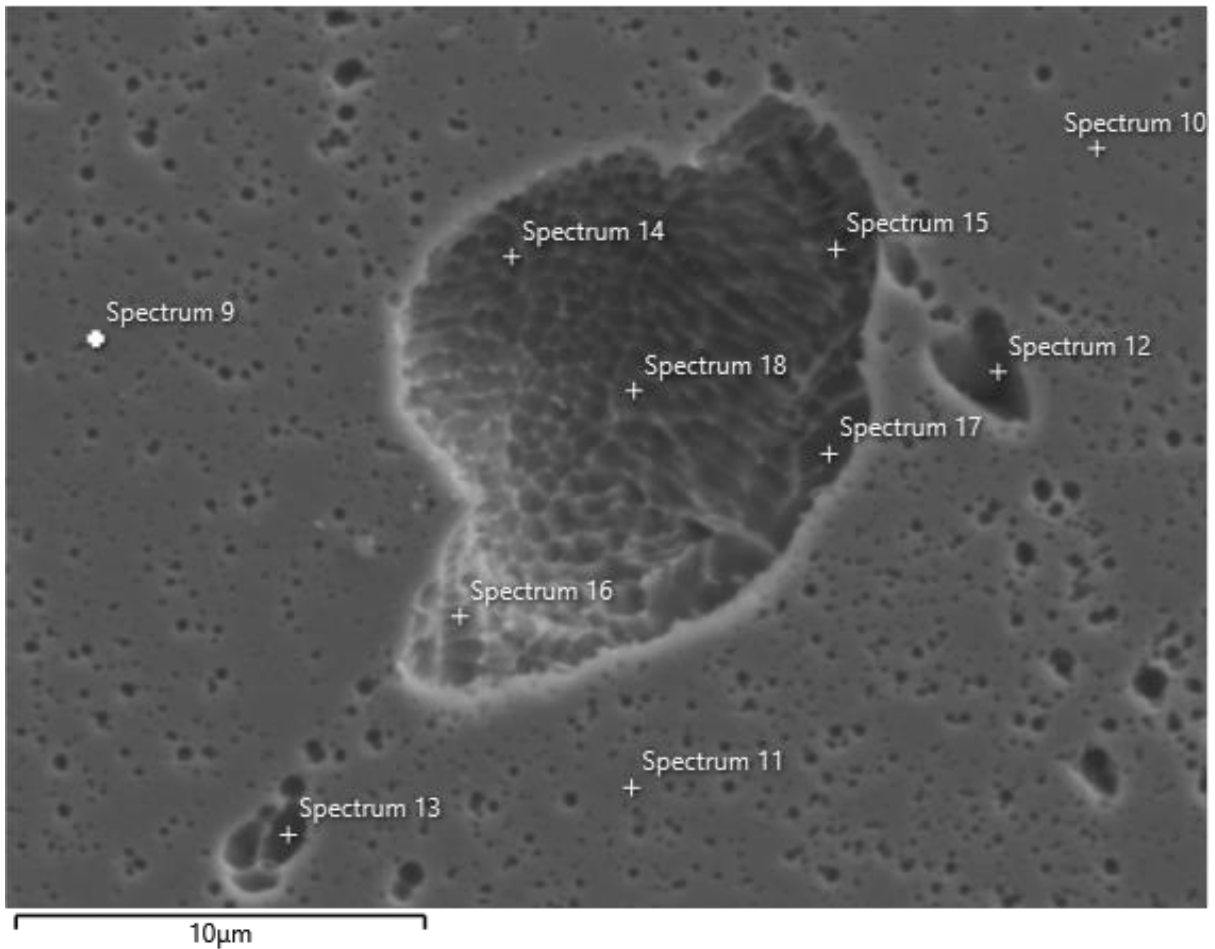


Figure 37 EDS point scan map of AM 316L in the XZ plane at 4000x magnification

Further investigation at greater depth was conducted on the most prominent central pore shown in Figure 37, to examine whether the absent counts resulted from the pore geometry affecting the X-ray detection or a variation in composition. Point scans were taken at spectra 9-11 to acquire a baseline for the bulk material, 12 and 13 to investigate the compositions in the smaller, more regular pores, and 14-18 to map the largest pore.

Table 20 Spectrum analysis data for SEM image in Figure 37 (wt.%)

| Region | Spectrum No. | Fe | Cr | Ni | Mn | Mo | Si | N | S | P |
|---------------------------|--------------|-------|-------|-------|------|------|------|------|------|------|
| Bulk | 9 | 68.33 | 17.00 | 10.42 | 1.64 | 1.59 | 0.84 | 0 | 0.13 | 0.05 |
| | 10 | 67.87 | 17.20 | 10.32 | 1.65 | 1.84 | 0.83 | 0.13 | 0.12 | 0.04 |
| | 11 | 67.07 | 17.25 | 11.11 | 1.65 | 1.88 | 0.79 | 0.1 | 0.10 | 0.05 |
| | Avg | 67.76 | 17.15 | 10.62 | 1.65 | 1.77 | 0.82 | 0.08 | 0.12 | 0.05 |
| Melt Pool Boundary | 12 | 70.56 | 19.66 | 6.98 | 2.21 | 0.35 | 0.14 | 0.05 | 0.04 | 0 |
| | 13 | 67.65 | 18.38 | 10.12 | 1.77 | 1.52 | 0.49 | 0.03 | 0.02 | 0.02 |
| | Avg | 69.11 | 19.02 | 8.55 | 1.99 | 0.94 | 0.32 | 0.04 | 0.03 | 0.01 |
| Ellipsoidal Pore | 14 | 71.39 | 20.10 | 5.83 | 2.43 | 0.16 | 0.06 | 0.02 | 0 | 0 |
| | 15 | 69.72 | 19.70 | 7.63 | 2.39 | 0.43 | 0.09 | 0.01 | 0.01 | 0.02 |
| | 16 | 66.77 | 18.12 | 10.49 | 1.85 | 1.94 | 0.69 | 0.07 | 0 | 0.09 |
| | 17 | 67.44 | 17.79 | 10.25 | 1.77 | 1.97 | 0.76 | 0.02 | 0 | 0 |
| | 18 | 69.49 | 18.42 | 8.82 | 2.01 | 1.03 | 0.2 | 0.02 | 0 | 0.02 |
| | Avg | 68.96 | 18.83 | 8.60 | 2.09 | 1.11 | 0.36 | 0.03 | 0.00 | 0.03 |
| Max | | 71.39 | 20.10 | 11.11 | 2.43 | 1.97 | 0.84 | 0.13 | 0.13 | 0.09 |
| Min | | 66.77 | 17.00 | 5.83 | 1.64 | 0.16 | 0.06 | 0 | 0 | 0 |
| Average | | 68.63 | 18.36 | 9.20 | 1.94 | 1.27 | 0.49 | 0.05 | 0.04 | 0.03 |
| Standard Deviation | | 1.57 | 1.12 | 1.79 | 0.31 | 0.72 | 0.33 | 0.04 | 0.05 | 0.03 |

Evaluating the point scan data in Table 20, the bulk spectra 9 – 11 exhibit an almost homogenous composition, with the only sizable variations being Fe and Ni, with ranges of 1.26 wt.% and 0.79 wt.%, respectively. The region defined as the melt pool boundary and investigated by spectra 12 and 13 show compositional differences compared to the bulk average, with 12 being 2.8 wt.% higher in Fe and a noticeable elevation in Cr and Mn. Ni, Mo and Si are also depleted by 34 %, 80 % and 83 %, respectively, indicating elemental segregation and an inclusion. Spectrum 13, however, presents minimal distinctions from the bulk, implying that not all the points of interest along the grain boundaries can be categorised into one division. When considering the ellipsoidal pore, spectra 14, 15 and 18 show the most significant variations from the bulk, with reduced levels of Ni, Mo and Si balanced with increases in Fe, Cr and Mn. These compositions compare with what was observed at the melt pool boundary in spectrum 12; however, there is little evidence in Figure 37 to explain why spectra 13, 16 and 17 deviate from this trend.

4.6.2 Wrought

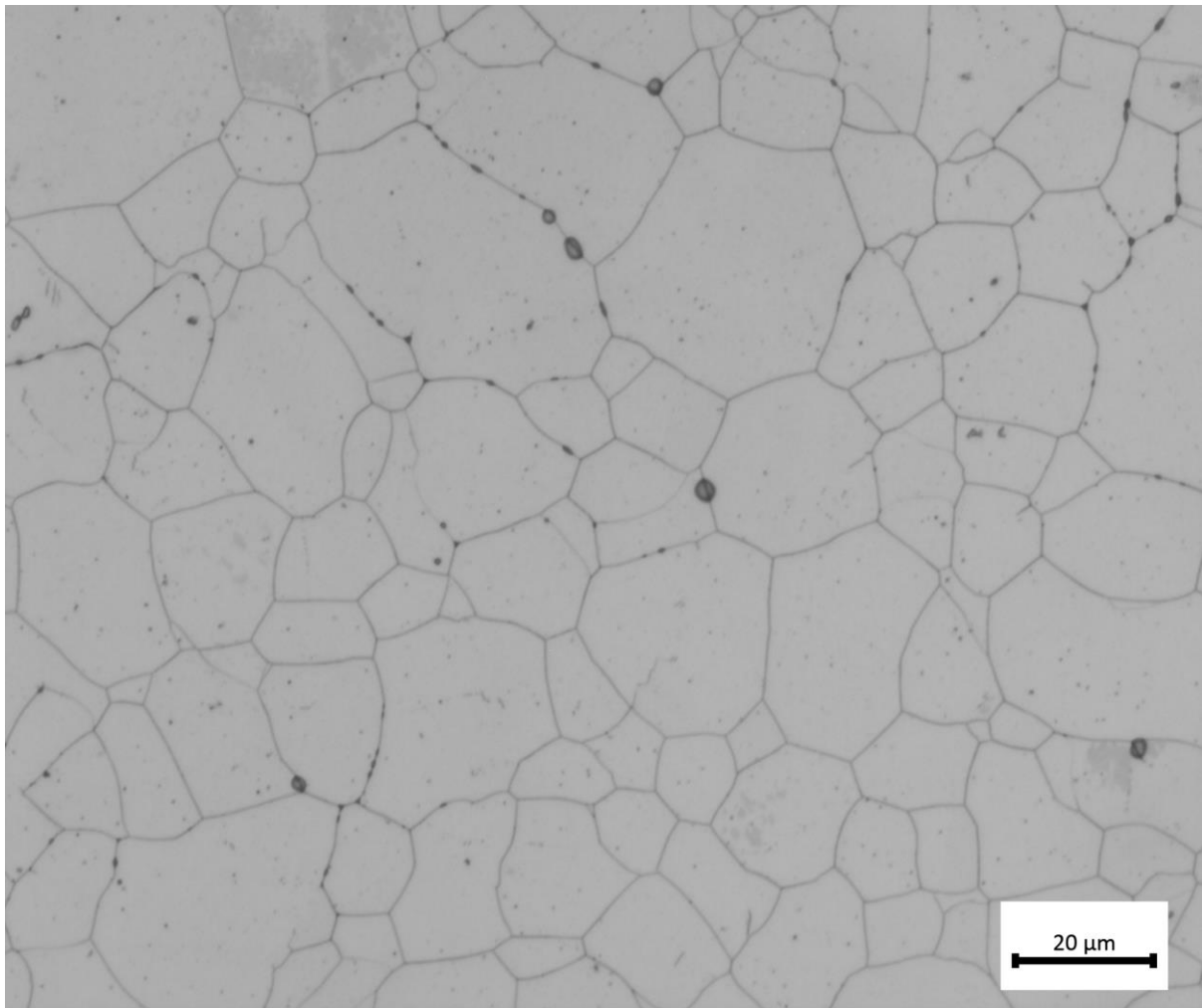


Figure 38 Optical microstructure of wrought 316L at 500x magnification

Figure 38 displays the surface of an annealed wrought sample provided by Goodfellows and prepared by polishing and subsequent electroetching in nitric acid. The optical image shows a cellular microstructure often seen in steels that have been through rolling and annealing treatments, with a grain size range between 5 μm and 50 μm [61,76]. What appear to be defects are observed along the grain boundaries; however, on closer inspection, these seem to be a result of the preparation and not porosity, as the boundary can still be seen within the defect.

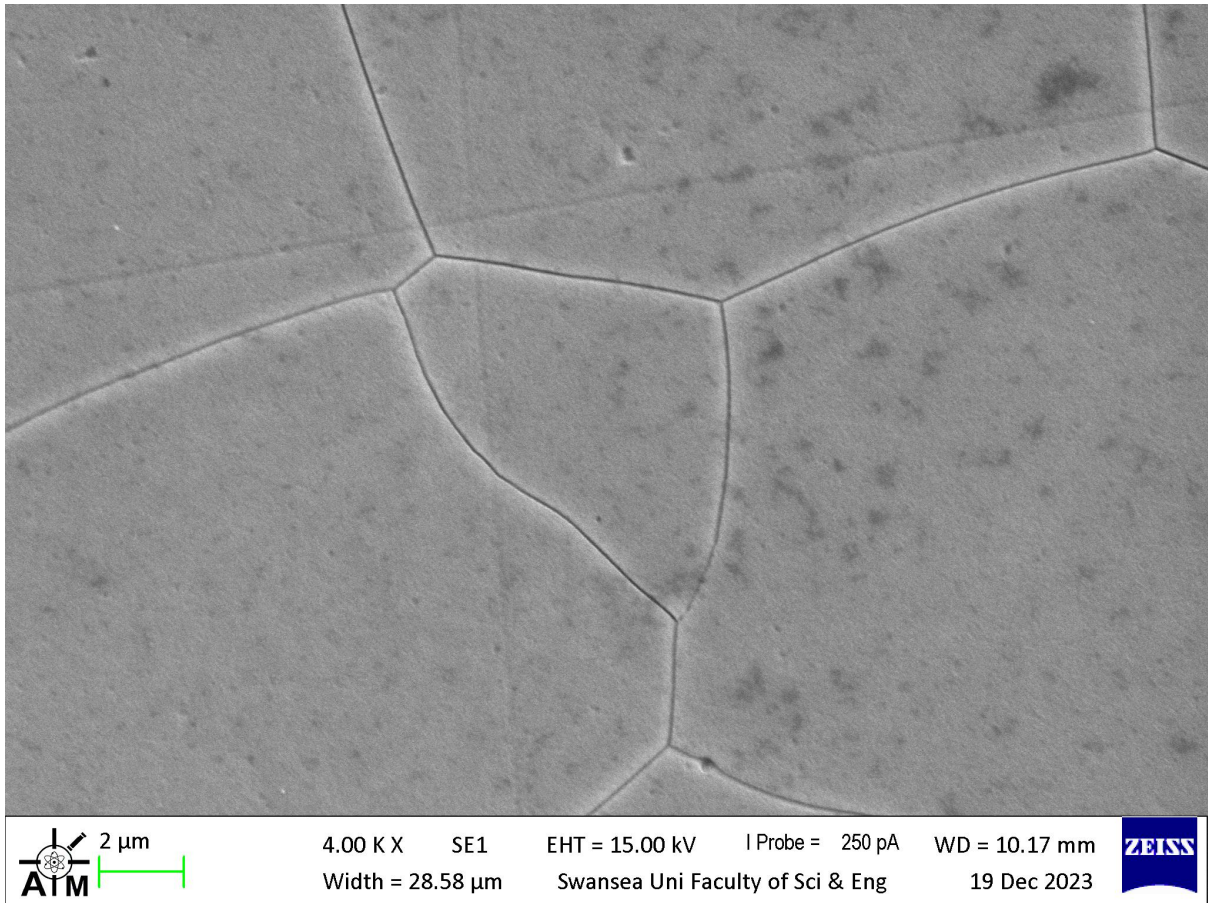


Figure 39 SEM micrograph of wrought 316L at 4Kx magnification

Table 21 EDS composition of wrought 316L

| Element | Fe | Cr | Ni | Mo | Mn | Si | N | P | S |
|-----------------|-------|-------|------|------|------|------|------|------|------|
| Weight % | 68.95 | 17.45 | 9.66 | 1.81 | 1.45 | 0.42 | 0.17 | 0.05 | 0.05 |

To investigate the structure and composition of the wrought samples at greater magnification, SEM-EDS was undertaken on the area in Figure 39, the average composition of which is in Table 21. There were no distinguishable differences in the maps produced by the EDS, with particular attention paid to the grain boundaries. Nevertheless, spectra were taken from across the sample at the bulk and at various points along the boundary, as well as the area immediately adjacent to it, specifically looking for regions rich or depleted in Cr that would indicate the presence of chromium carbides.

Table 22 Compositional point scan summary of wrought 316L (wt.%)

| Statistic | Fe | Cr | Ni | Mo | Mn | Si | N | S | P |
|---------------------------|-------|-------|------|------|------|------|------|------|------|
| Max | 69.29 | 17.97 | 9.76 | 2.34 | 1.76 | 0.45 | 0.42 | 0.17 | 0.08 |
| Min | 68.55 | 17.35 | 9.1 | 1.37 | 1.24 | 0.34 | 0.07 | 0 | 0 |
| Average | 68.95 | 17.62 | 9.5 | 1.71 | 1.44 | 0.41 | 0.25 | 0.08 | 0.05 |
| Standard Deviation | 0.25 | 0.19 | 0.22 | 0.3 | 0.18 | 0.04 | 0.13 | 0.07 | 0.03 |

Table 22 shows the resultant summary of these spectrums. The most significant of these is the standard deviation, which exhibits a tight grouping, suggesting homogeneity across the points sampled. This is consolidated when observing the maximum and minimum compositional values, the most extensive range of which is 0.97 wt.% for Mo.

4.7 Corrosion Testing

Samples 1, 3, 7, 10, 22 and 29 were used for corrosion testing as they provided a wide range of densities from the selection available. OCP and CP tests were carried out on each specimen; the methods and parameters used are outlined in section 3.16.

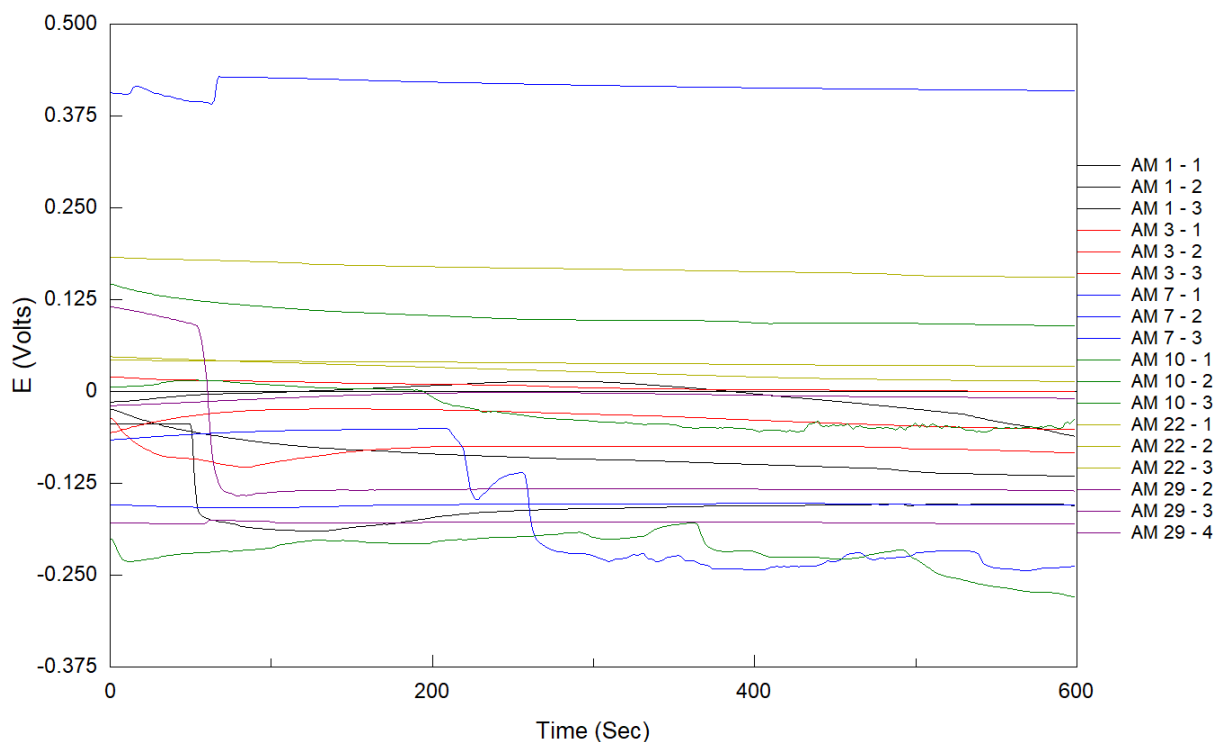


Figure 40 OCP data from 316L AM samples 1, 3, 7, 10, 22 and 29 over 600s

Figure 40 displays the OCP measurements for each test conducted on the AM samples. Across the data plotted, the OCP readings appear stable for the duration of their respective scans, apart from those of AM 1-2, AM 7-2, and AM 29-3, which have a significant drop in potential within the first 5 minutes of the scan, before reaching an equilibrium, likely due to changes in the air formed oxide. The average OCP measurements displayed in Table 23 are a valuable tool in understanding a material's corrosion resistance. Stainless steels, among other alloys, develop a passive oxide layer on their surface that protects them from corrosion. The OCP can indicate the stability and integrity of this passive layer. A more noble (cathodic) OCP suggests that the passive layer is stable and effectively protects the alloy from corrosion. The data shows an overall correlation between the optical density and the OCP. Sample 10, which had the lowest density tested, exhibits the most negative average OCP,

whereas sample 22, with the greatest density of the AM samples, produced the most positive OCP of 0.067 V. The only deviation from this trend is that of sample 7, which produced the second most positive OCP whilst having the 3rd lowest density.

Table 23 Summary of corrosion data for AM and wrought 316L samples ordered by density

| Sample | Optical Density (%) | Avg OCP (V) | Error (SD) | Avg E_{corr} (V) | E_{corr} (SD) | Avg E_{pit} (V) | E_{pit} (SD) | Avg E_r (V) |
|--------|---------------------|-------------|------------|--------------------|-----------------|-------------------|----------------|---------------|
| 10 | 93.05 | -0.112 | 0.169 | -0.109 | 0.158 | 0.808 | 0.468 | -0.232 |
| 1 | 95.11 | -0.110 | 0.047 | -0.141 | 0.041 | 0.727 | 0.155 | -0.238 |
| 7 | 99.74 | -0.032 | 0.051 | -0.172 | 0.015 | 0.964 | 0.178 | -0.190 |
| 29 | 99.81 | -0.108 | 0.088 | -0.131 | 0.068 | 0.969 | 0.061 | -0.216 |
| 3 | 99.84 | -0.045 | 0.042 | -0.111 | 0.058 | 0.953 | 0.179 | -0.156 |
| 22 | 99.88 | 0.067 | 0.077 | 0.024 | 0.098 | 1.018 | 0.096 | -0.183 |
| WRT | 100 | 0.113 | 0.037 | 0.030 | 0.038 | 0.415 | 0.049 | 1.164 |

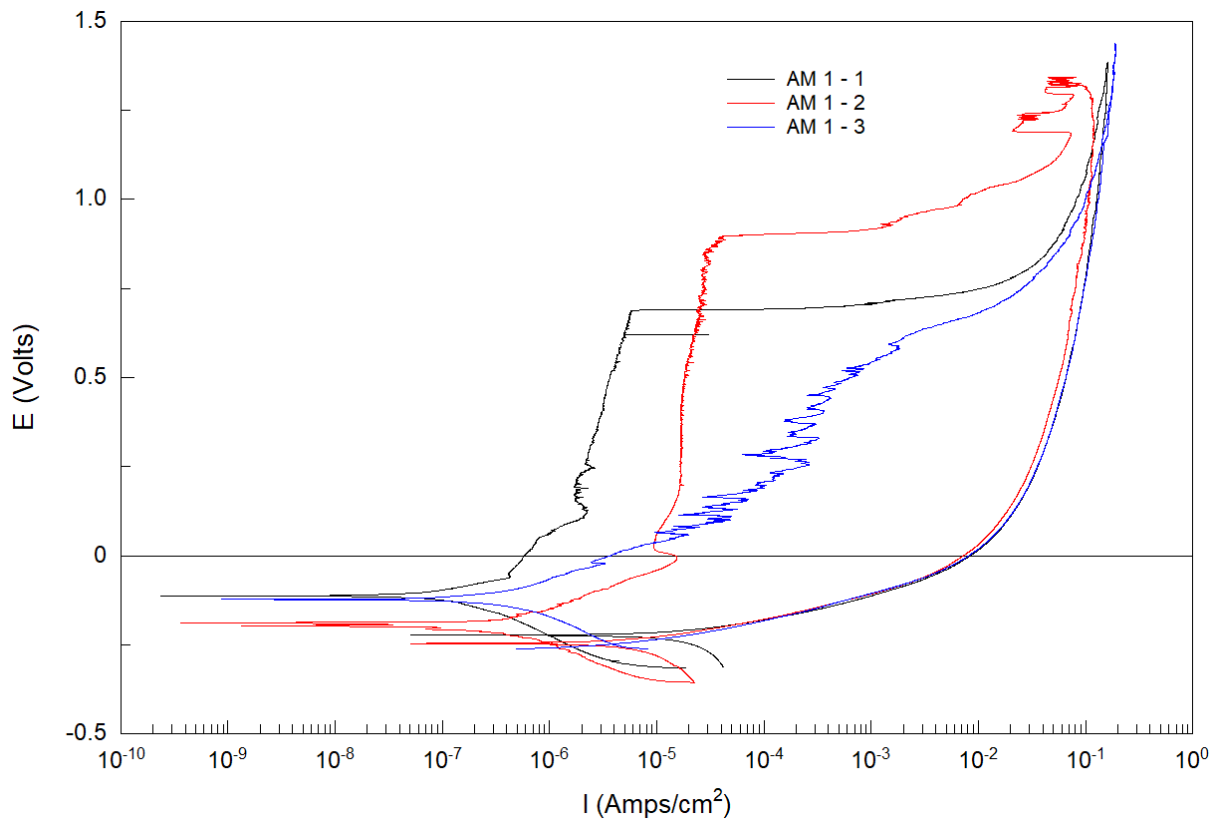


Figure 41 Cyclic polarisation plots for 316L AM sample 1

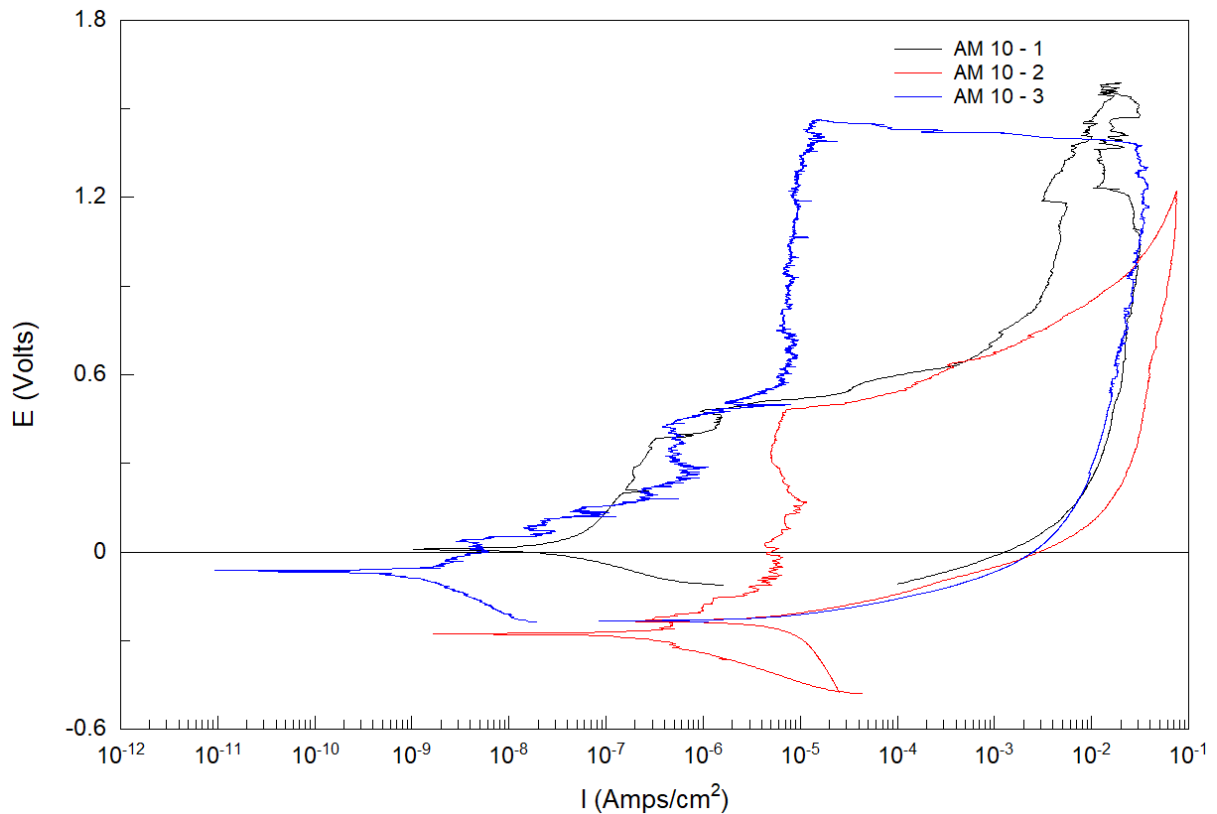


Figure 42 Cyclic polarisation plots for 316L AM sample 10

Figure 41 and Figure 42 display the CP curves for AM samples 1 and 10, which have the two lowest densities of the cubes tested. While some elements of the repeats for each sample display similarity, the overall impression is one of erraticism. Significant metastable pitting is observed between the E_{corr} and E_{pit} sections of the graphs, suggesting either the poor formation of a passive oxide layer over the initial pitting site/s or that other corrosion sites are initiating as the potential is increased across the cell. Of the AM samples tested, 1 and 10 exhibited the lowest E_{pit} values, with sample 10 showing a significantly larger standard deviation for this metric than all other samples. This deviation, as well as lower average E_{pit} values, show that density is a driving factor in not only the corrosion resistance performance but also its repeatability. The latter is often cited as a significant barrier to AM components replacing those made by traditional manufacturing methods.

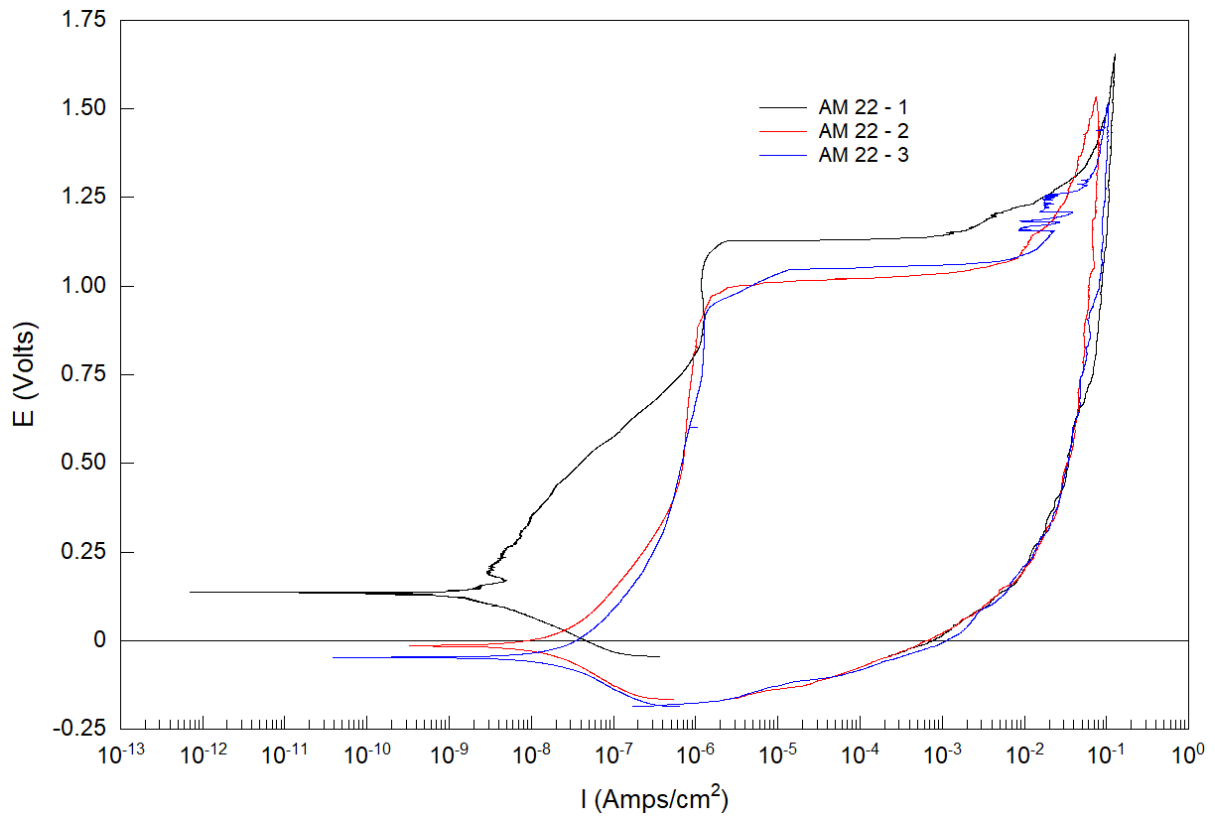


Figure 43 Cyclic polarisation plots for 316L AM sample 22

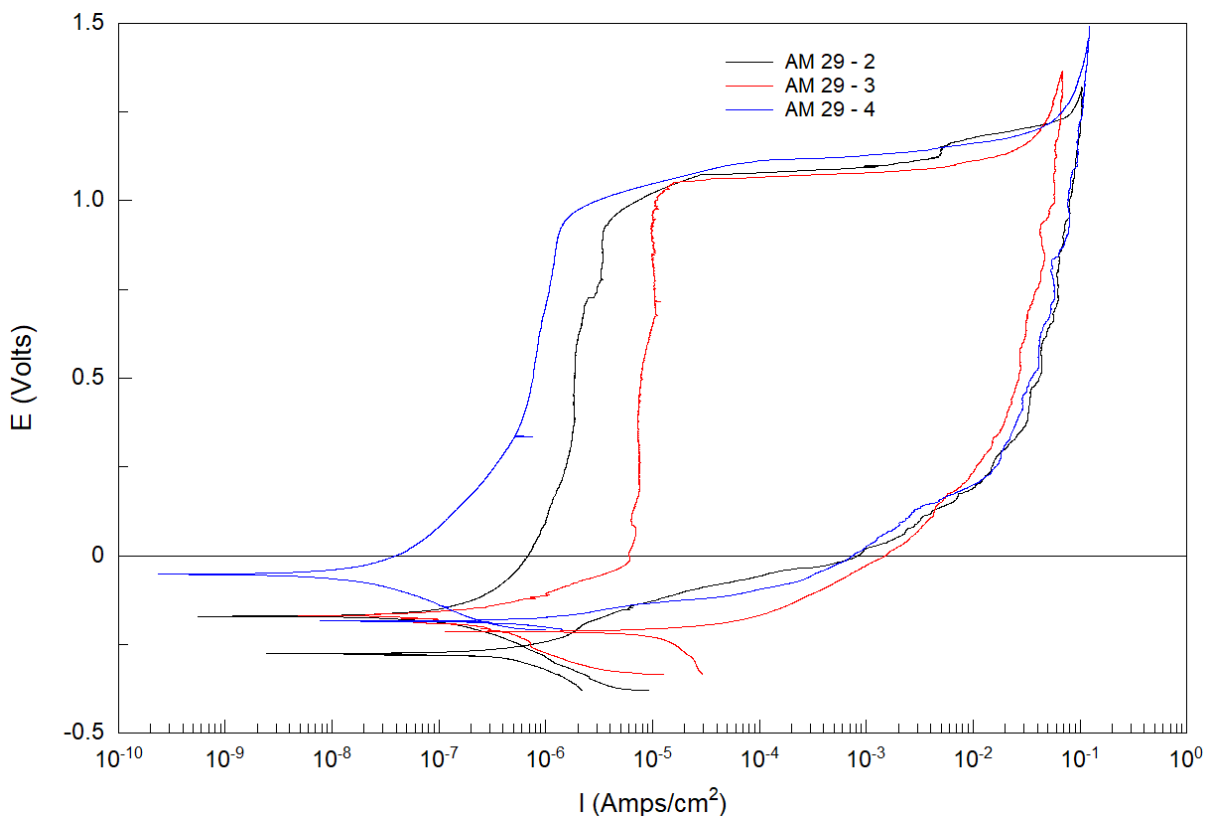


Figure 44 Cyclic polarisation plots for 316L AM sample 29

Comparatively, the CP data produced by AM samples 22 and 29 in Figure 43 and Figure 44 show a significant improvement in corrosion performance and reliability. Looking at the form of the respective

plots, each repeat shows extensive repeatability. The key turning points appear to occur at very similar potentials and currents. The distinct lack of any metastable pitting across the tests is perhaps more significant, showing that the passive layer produced by these samples offers much greater protection from further corrosion than samples 1 and 10.

From Table 23, AM 22 and AM 29's average E_{pit} values are 1.018 V and 0.969 V, respectively, averaging 0.226 V higher than the mean measured on AM 1 and AM 10. Not only this, but the dispersion in the E_{pit} values experienced across the samples with lower density is significantly greater than that of those with higher density, once again reinforcing the reliability issues associated with non-fully dense parts.

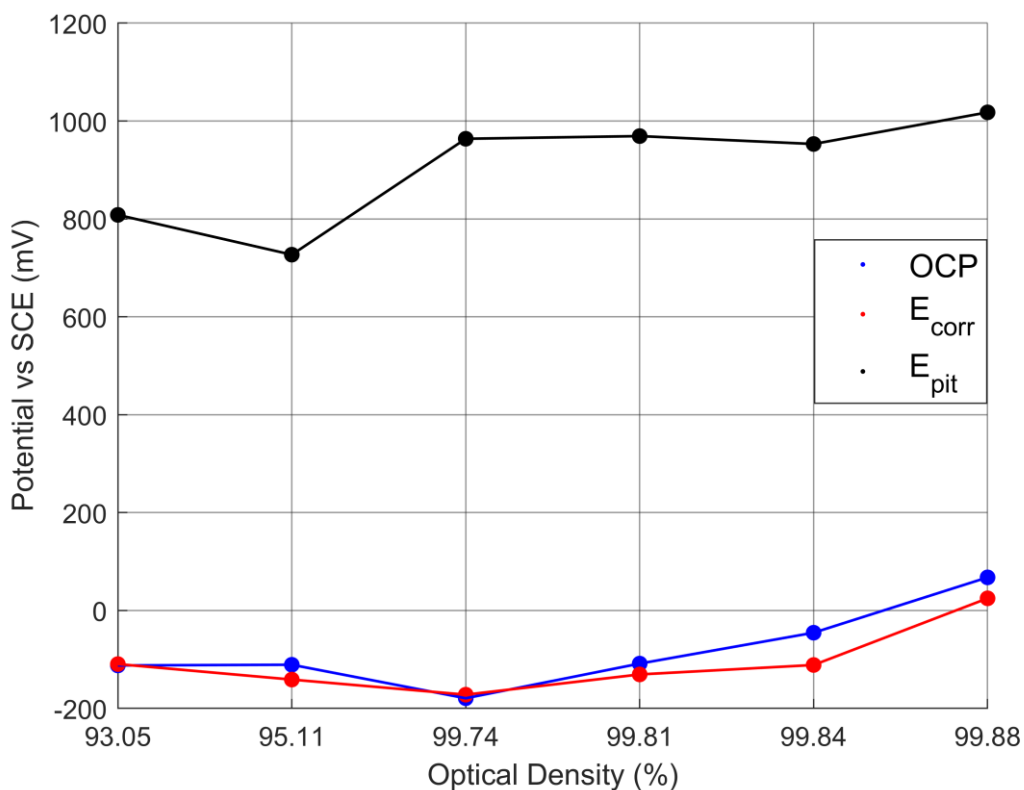


Figure 45 Optical density vs key corrosion metrics for 316L AM

Graphical representations of the 316L corrosion metrics in Table 23 are displayed in Figure 45 against the sample's respective optical densities. This illustration uses a non-linear scale to alleviate the tight distribution that would otherwise be produced due to the small dispersion of the higher optical densities. Whilst this figure does show that an increase in density correlates with an increase in corrosion resistance, it does have some discrepancies and does not encapsulate all the observations that have previously been made. For example, the lack of stability seen between the E_{corr} and E_{pit} values of samples 1 and 10 in Figure 41 and Figure 42 respectively is not represented, so sole reliance on this figure for drawing conclusions on the effect of density on corrosion resistance should be avoided.

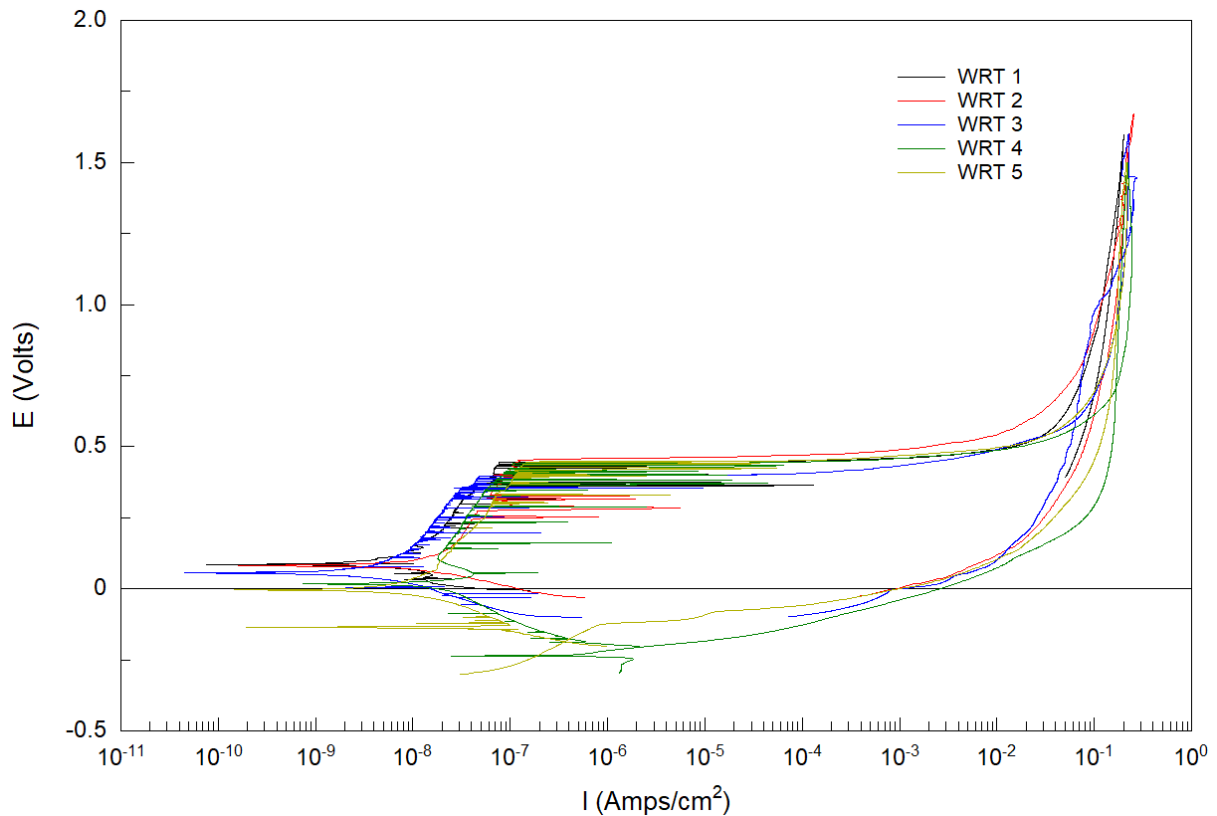


Figure 46 Cyclic polarisation plots for 316L wrought samples

The wrought samples were tested under the same parameters as the AM. The OCP tests yielded the most positive potentials of all the samples tested, suggesting the wrought material had the greatest stability. Not only did it have the most positive OCP, but also the lowest standard deviation. One metric that the wrought samples underperformed in compared to the AM samples was the E_{pit} , which was significantly lower than all the AM densities tested. However, the error for the E_{pit} values, like the OCP again the lowest of all samples tested. The plots produced also appear to be the most reproducible, with every part of the CP scan following a tight cluster of results. The average E_r of the wrought samples is significantly higher than the AM samples. However, this is unreliable due to only some samples repassivating, and of the ones that did, many did so by their return scan profiles crossing by the reversal point before returning to below the forward scan line.

4.8 Discussion

The parameters outlined in Table 16 and subsequent density results presented in Figure 32 display how easily a machine operator can manipulate levels of porosity in AM parts by controlling the input parameters. They also clearly exhibit trends, such as a large parameter operating window for 316L whilst producing components of 99 % density (Archimedes), and the optimisation of these parameters results in the greater repeatability of component quality outlined in literature [177]. The results from the mass and density analysis in Table 17 and Table 18, respectively, show how the location of parts

on the build plate affects the component quality, with the average mass and density of blocks 1 and 3 (furthest from the gas outlet) being 31.737 g and 98.83 %, whereas the same metrics for the blocks closest to the outlet (2, 4) are 31.940 g and 98.89 %. This reinforces what is stated in literature, that an increase in distance from the gas inlet and recoater blade negatively influences part density [178,179].

The corrosion results presented in Table 23 and displayed graphically in Figure 41 - Figure 45 demonstrate the importance that bulk density and surface porosity have on the corrosion resistance of metals, specifically those manufactured by AM. Samples of AM 1 and AM 10, with an average optical density of 94.08 % and investigated by CP, show large variations in corrosion performance at all points of interest. When considering the magnitude of their average OCP and E_{pit} values and comparing them to the wrought data, they come out 0.244 V below and 352.5 V above. What this suggests is a greater predisposition for corrosion within the high porosity AM samples, resulting in a negative OCP well below that of the wrought, but a better passive oxide layer formation once the potential is raised beyond the E_{corr} . This correlates with literature which proposes that this is due to the fine grain structure in AM stainless steels relative to the wrought [66,72]. The average E_{pit} data suggests that even low-density 316L AM specimens have a greater corrosion resistance than their wrought counterparts; however, what is more concerning is the level of reliability in the corrosion mechanisms. Whilst the profiles of all 6 wrought plots in Figure 46 are virtually identical, those of AM 1 and 10 in Figure 41 and Figure 42 show huge variations, with E_{pit} and E_{corr} standard deviations 0.062 and 0.263 higher than the wrought. This level of failure uncertainty in a component increases the risks for those in the AM component supply chain and, therefore, makes it difficult to supplant wrought material where design freedom and mechanical properties are not required.

The high density AM 22 specimen tested in Figure 44, however, shows much more promise for supplanting wrought components. Whilst its average OCP is lower than the wrought by 0.046 V and the standard deviation for this metric is 0.04 higher, it is a significant improvement on the lower density samples mentioned previously. The average E_{pit} of AM 22 diminishes that of the wrought by 0.603 V, and whilst the standard deviation of these values is ~97 % greater at 0.096, there must be a trade-off between the significantly higher overall corrosion resistance and the slight decrease in reliability of high density 316L AM and 316L wrought.

Overall, the trends across every metric measured in Table 23 proposes that a decrease in AM surface porosity results in better corrosion resistance and a more reliable product, with the increased porosity decreasing the stability of the alloy as well as the strength of the passive film [29,81,180]. It is difficult to isolate the effects of pore size and shape from the total porosity surface area with the experimental

work in this study, as the corrosion test sites were often compiled of a combination of both, as displayed in Figure 35. Further work needs to be done to isolate this variable, such as timelapse microscopy [181]. The AM samples did not exhibit any major bulk compositional inhomogeneity across the EDS maps, and whilst some differences were present when pores were investigated with spectrum analysis, these are likely to occur at most sites and, therefore, the greater the number of defects, the greater the heterogeneity. Different corrosion mechanisms were seen between the different density AM samples when observing the surface after exposure to electrochemical testing. Low density samples had a large number of small pitting sites, most likely occurring at pre-existing pores, whereas the high density specimens exhibited degradation more affiliated with crevice corrosion at the boundary of the test area. This is suspected to occur due to the lower frequency, shape, and size of the pores exhibited in the high density samples, as shown in Figure 35, presenting numerous sites for pits to preferentially occur [66,79,81,154]. The increased porosity promotes differential aeration, and thus, the pores act as crevice corrosion initiation sites as they become anodically focussed due to the ease of oxygen diffusion to the bulk metal surface for the cathode compared with more tortuous diffusion of oxygen into the crevice [79,144,154]. This then promotes the establishment of the Fontana Greene crevice corrosion mechanism that can produce acidification in the crevice, leading to accelerated localised corrosion [145]. As the sites in the high density samples are much less frequent and smaller in size, the boundary preferentially corrodes where the site has limited access to the external environment and oxygen depletion and metal dissolution can occur, creating a differential aeration cell.

4.9 Conclusions

- The AM process parameters were successfully optimised for 316L, shown by a maximum achieved optical density of 99.88 %.
- Overall part quality measured by bulk density and component mass was seen to deteriorate as the distance from the recoater blade and gas inlet was increased.
- Process-induced porosity was successfully achieved by altering process parameters in the form of a Taguchi L9 array, resulting in a range of optical densities from 90.36 % to 99.88 %. Clear distinctions are observed between the porosity in low and high density components, such as the size and location of pores.
- Slightly greater compositional heterogeneity is observed with the AM sample vs the wrought. However, this is expected due to the annealing heat treatment performed on the wrought sample, homogenising the microstructure.

- All samples produced by AM had lower OCP values than wrought, indicating greater instability. However, on average, all densities of AM parts outperformed the wrought when analysing the E_{pit} values of each sample, indicating that AM samples produce a superior passive oxide layer that offers impressive protection to pitting sites when formed.
- Whilst all AM densities did display better E_{pit} metrics, the error in these values is of significant concern, particularly for those with suboptimal density. A trend is observed, with an increase in porosity resulting in a decrease in corrosion resistance.
- The highest density AM sample presented significantly better E_{pit} values than the wrought, but with close to twice the error. Whilst this error is not of a large magnitude, it is still a barrier to overcome before the AM components can consistently replace traditionally manufactured components.

5 An Investigation into the Different Manufacturing Methods of 316L Stainless Steel and their Effects on Microstructure and Corrosion Resistance

5.1 Introduction

This chapter, and the subsequent 2, focus on how the manufacturing process affects the microstructure and corrosion resistance of stainless steels and HEAs. The processes investigated are that of AM, cast, and cast with subsequent heat treatments and rolling steps, the latter in an attempt to increase the corrosion resistance of 316L. 316L has been studied in great depth for all 3 of these processes and, therefore, acts as both a subject for method verification and a baseline for other novel alloys. Unlike in Chapter 4, only the optimum parameter set was studied for the AM samples tested. The methodologies for producing the cast and cold rolled samples are outlined in sections 3.7 and 3.10, respectively.

5.2 Density Analysis

Due to the geometry of the samples created by the casting and rolling processes, it was inefficient to use the same bulk density analysis techniques as was used with the AM samples. Therefore, a comparison of optical density measurements was used instead. The process for collecting these was the same as that outlined in section 3.13.2.

Table 24 Optical density of 316L samples produced by optimum AM, cast, and CR

| Sample | AM (22) | Cast | CR |
|----------------------------|----------------|-------------|-----------|
| Optical Density (%) | 99.88 | 99.65 | 99.89 |

The measured densities of the samples are of a comparable level, with a 0.24 % range observed. This suggests that, whilst it should be considered an important variable when discussing each process's corrosion resistance, it is less likely to be a defining factor. The CR sample is seen to have a density higher than that of the cast sample, which could indicate that the mechanical deformation of the cold rolling process has eradicated some of the porosity present.

5.3 Thermocalc

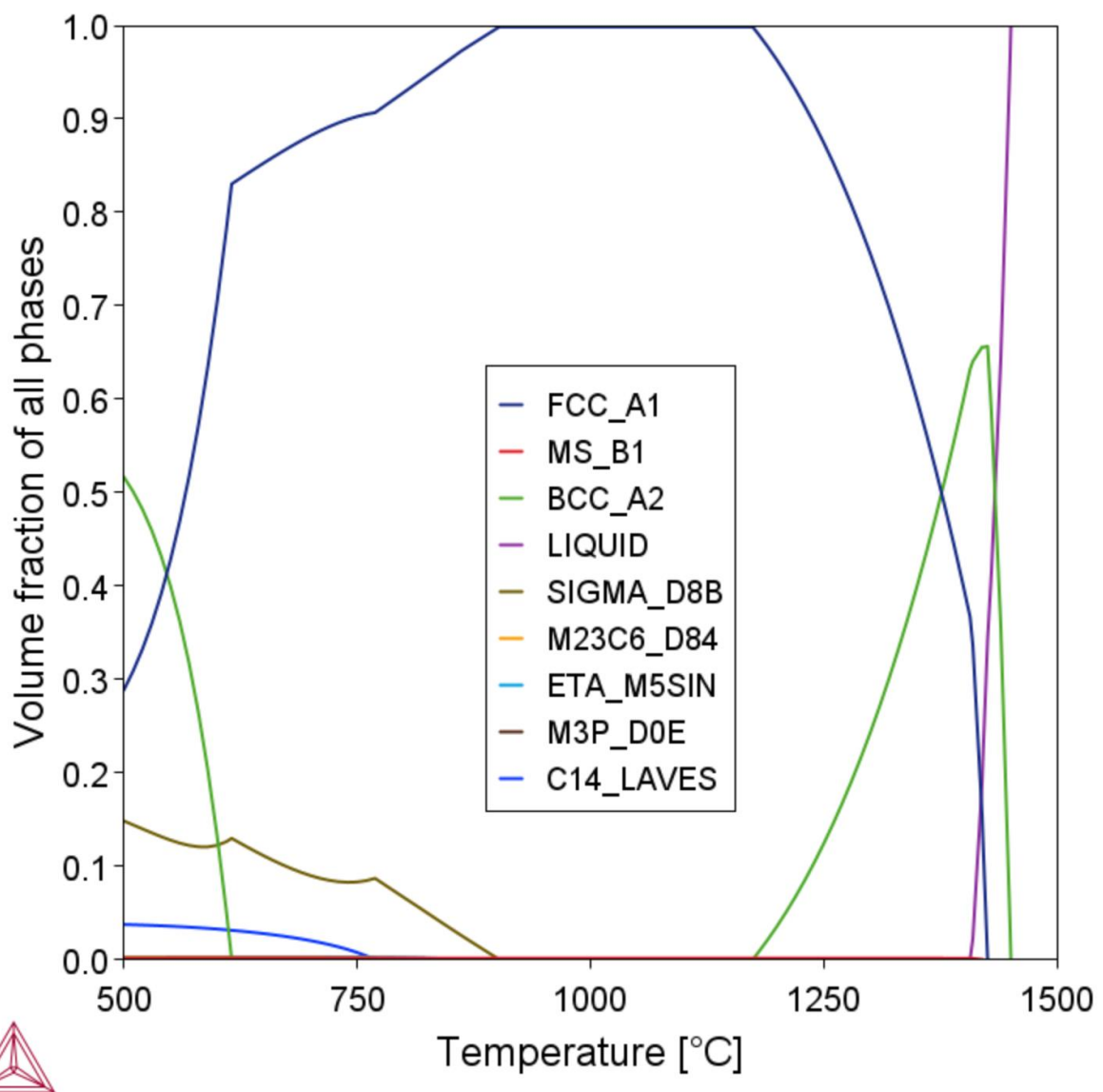


Figure 47 Volume fraction of all phases for 316L produced by Thermo-Calc

Figure 47 shows the simulation result of the volume fraction (φ_i) for 316L for all phases from 500 °C to 1500 °C, produced by Thermo-calc using the TCFE12: Steels/Fe Alloys v12.0 database. As the molten alloy cools from 1450.83 °C, the liquid phase begins to reduce as the BCC_A2 starts to form, which rapidly peaks at a φ_i of 0.657 at 1426 °C, representing the δ -ferrite. The FCC_A1, representing the bulk austenite, then begins to form preferentially, reaching a maximum potential φ_i of 0.998, with no δ -ferrite present and the remaining fraction attributed to MS_B1, referring to a MnS inclusion. As further cooling occurs at 900 °C and below, an σ phase presents before a Mo, Fe, and Cr rich phases designated as C14_LAVES. The compositions of each of these phases at their highest φ_i are outlined in Table 25.

Whilst many factors will affect the volume of these phases and their respective compositions, such as the cooling rate, the element ratio within the phase is a useful tool when analysing other data, such as that from EDS and XRD.

Table 25 Composition of selected 316L phases at their highest respective volume fraction (wt.%)

| | Fe | Cr | Ni | Mo | Mn | Si | N | P | C | S |
|------------------|-----------|-----------|-----------|-----------|-----------|-----------|----------|----------|----------|----------|
| BCC_A2 | 68.99 | 17.56 | 9.18 | 2.12 | 1.44 | 0.69 | 0.007 | 0.012 | 0.003 | 0 |
| FCC_A1 | 67.88 | 17.25 | 10.40 | 2.03 | 1.59 | 0.78 | 0.01 | 0.04 | 0.01 | 0 |
| SIGMA | 47.21 | 44.38 | 3.67 | 0.29 | 4.37 | 0.07 | 0 | 0 | 0 | 0 |
| MnS | 0 | 2.81 | 0 | 0 | 60.28 | 0 | 0 | 0 | 0 | 36.91 |
| C14_LAVES | 33.85 | 19.31 | 0.36 | 46.46 | 0.02 | 0.001 | 0 | 0 | 0 | 0 |
| M23C6_D84 | 5.62 | 70.40 | 0.14 | 18.63 | 0.04 | 0 | 0 | 0 | 5.18 | 0 |

Whilst the BCC and FCC phases differ in composition, these differences are not significant, with the largest absolute variation coming from an increase in Ni from the BCC to FCC of 1.22 wt.%. The σ phase forming below 900 °C presents significantly elevated levels of Cr and Mn as well as large reductions in Fe, Ni, Mo and Si. The phase labelled C14_LAVES's composition appears abundant in Mo with close to average levels of Cr and Fe at a concentration half of what is anticipated in the bulk, with Ni and Mn barely reported. Based on the compositions presented in Table 25, it would be preferential to keep the φ_i of σ and C14_LAVES phases to a minimum to lessen the depletion of corrosion resistant elements such as Cr and Mo from the bulk FCC and BCC phases. Chromium carbides, indicated by the phase M23C6_D84, are suggested to form at 863 °C and below; however, only to a maximum φ_i of 0.002.

5.4 XRD

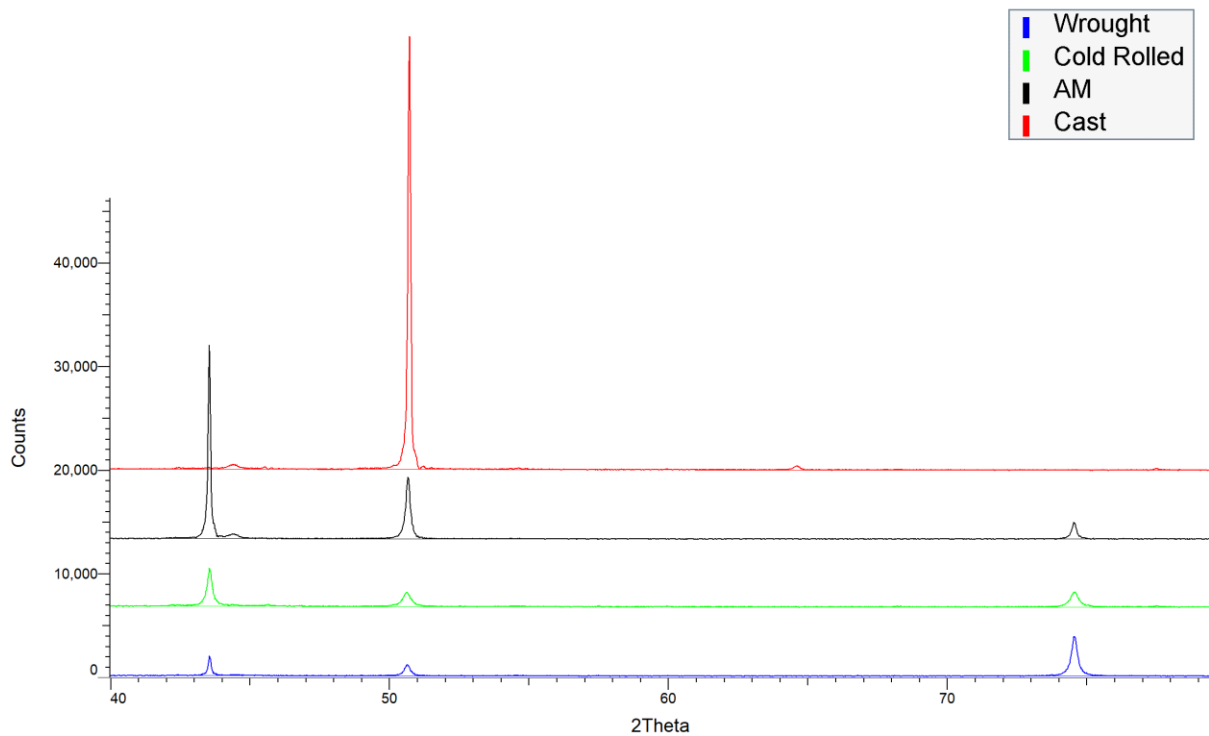


Figure 48 XRD scans for wrought, CR, AM, and cast 316L samples

Figure 48 shows an XRD waterfall plot for the wrought, CR, AM, and cast samples investigated in this work. All specimens were examined using the same process parameters outlined in the methodology section 3.14. The wrought, CR, and AM XRD scans follow similar peak profiles, with obvious peaks at 2θ angles of approximately 43.54° , 50.67° and 74.55° , as correlating with literature [66,182]. For all 3 samples, the first FCC peak at 43.5° exhibits a greater intensity than that of the second FCC by an order of magnitude between 1.7x to 3.12x. The cast sample, however, displays inverse characteristics, with only one significant FCC peak at $2\theta = 50.67^\circ$ at a far greater intensity than any shown by the other manufacturing routes. The BCC peaks, at $\sim 44.42^\circ$ and 64.62° , are also most significant in this sample. However, this is likely due to a higher overall count rate across the sample and not necessarily identifying a higher proportion of BCC within the cast specimen compared to the other process routes. This is reinforced by calculating the phase proportions within each sample in Table 26, showing that similar proportions were achieved across each sample.

Table 26 XRD data extracted from scans shown in Figure 48

| 316L XRD Intensities (cts) | | | | | | |
|----------------------------|--------------------|---------------|---------------|--------------------|---------------|----------------|
| | FCC Peak Intensity | | | BCC Peak Intensity | | |
| | 1 (43.54°) | 3 (50.67°) | 5 (74.55°) | 2 (44.42°) | 4 (64.62°) | FCC/BCC |
| Wrought | 1904.91 | 1074.79 | 3828.83 | 91.2243 | 20.31 | 98.39 %/1.61 % |
| CR | 3658.71 | 1379.04 | 1443.97 | 164.514 | 54.796 | 96.73 %/3.27 % |
| AM | 18523.6 | 5943.48 | 1584.26 | 434.433 | 33.174 | 98.24 %/1.76 % |
| Cast | 29.543 | 41619.5 | 34.22 | 466.49 | 428.348 | 97.90 %/2.10 % |

Table 26 shows the intensities extracted from the XRD scans shown in Figure 48. Intensities are given in counts, the sum of which is used to calculate the FCC/BCC phase ratio. These ratios show that all 4 manufacturing routes have produced samples that are almost fully austenitic with small proportions of δ -ferrite present.

5.5 Microstructure

SEM images and EDS scans were carried out at the end of each manufacturing process, as well as any intermediate stages where a mechanical or heat treatment had been applied, to understand its effects on the microstructure.

5.5.1 AM

The 316L AM microstructure is discussed and analysed in detail in section 4.6.1.

5.5.2 Cast

The cast manufacturing process has significantly slower cooling rates than AM. This allows more time for the elements to diffuse into discrete phases as the alloy cools. The composition of the phases created depends on factors such as the melting points of the elements involved, their solubility, and their affinity for one another. Dendritic structures are present in the EDS maps of cast 316L in Figure 49 and the backscatter representation shown in Figure 50.

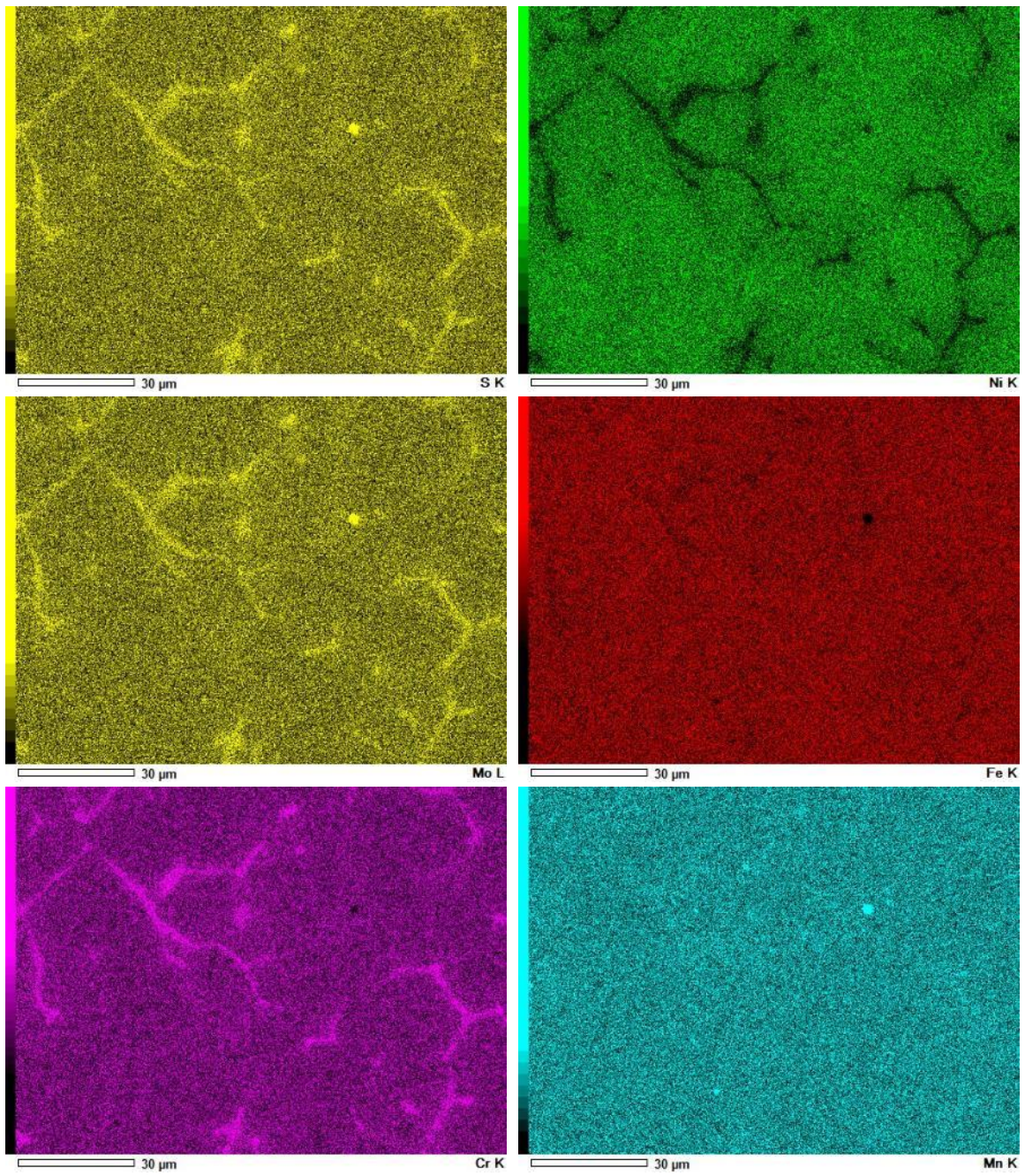


Figure 49 EDS Maps of cast 316L at 1000x magnification

Table 27 Composition of cast 316L from EDS map

| Element | Fe | Cr | Ni | Mo | Mn | Si | N | P | S |
|----------|-------|-------|-------|------|------|------|------|------|------|
| Weight % | 67.66 | 17.17 | 10.52 | 2.15 | 1.58 | 0.78 | 0.07 | 0.04 | 0.03 |

Within the elemental maps in Figure 49, two distinct phases are observed. The dendritic region previously described appears rich in S, Mo, and Cr, whilst also depleted in Ni and Fe. A hotspot, rich in S, Mo and Mn is also observed in these maps. To quantify the variations in composition within these identified regions, point scans were taken respectively, the locations of which are marked in Figure 50, and the results of which are presented in Table 28.

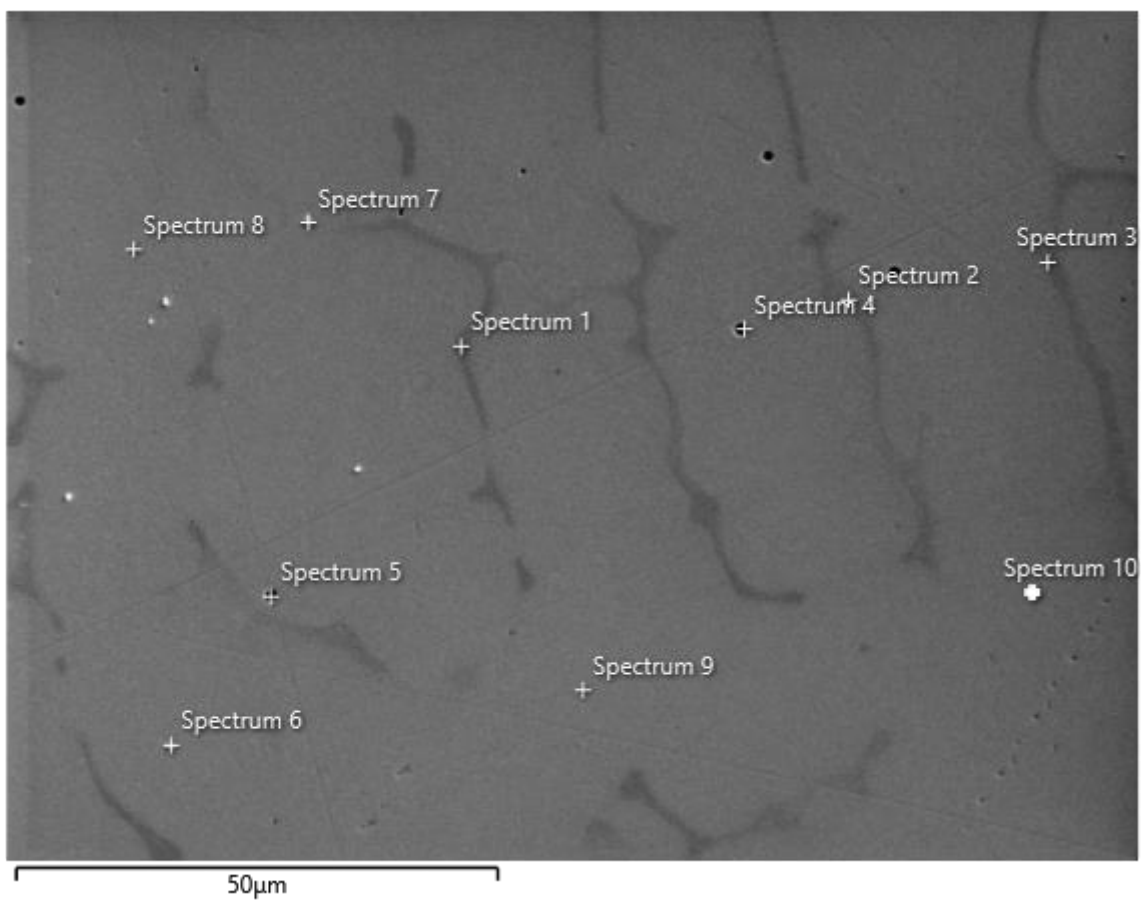


Figure 50 EDS point scan map of cast 316L

Table 28 Point scan analysis of cast 316L shown in Figure 50, (wt.%)

| Region | Spectrum No. | Fe | Cr | Ni | Mo | Mn | Si | N | P | S |
|---------------------------|--------------|-------|-------|-------|------|-------|------|------|------|-------|
| δ-Ferrite | 1 | 65.64 | 23.14 | 4 | 4.79 | 1.38 | 0.92 | 0.12 | 0.02 | 0 |
| | 2 | 65.93 | 22.92 | 4.74 | 3.74 | 1.32 | 0.95 | 0.08 | 0.05 | 0.27 |
| | 3 | 65.94 | 23.12 | 4.11 | 4.43 | 1.48 | 0.89 | 0 | 0.04 | 0 |
| | Avg | 65.84 | 23.06 | 4.28 | 4.32 | 1.39 | 0.92 | 0.07 | 0.04 | 0.09 |
| Inclusions | 4 | 40.94 | 14.04 | 4.93 | 1.6 | 24.85 | 9.22 | 0 | 0.03 | 4.39 |
| | 5 | 17.66 | 9.48 | 1.43 | 2.04 | 43.44 | 9.38 | 0 | 0.1 | 16.47 |
| | 6 | 67.9 | 16.55 | 11.11 | 1.67 | 1.58 | 0.67 | 0.53 | 0 | 0 |
| | Avg | 42.17 | 13.36 | 5.82 | 1.77 | 23.29 | 6.42 | 0.18 | 0.04 | 6.95 |
| Austenite | 7 | 67.25 | 17.42 | 10.21 | 2.39 | 1.45 | 0.75 | 0.39 | 0.06 | 0.08 |
| | 8 | 67.95 | 17.06 | 10.28 | 2.21 | 1.52 | 0.76 | 0.17 | 0.03 | 0.03 |
| | 9 | 67.78 | 15.86 | 11.87 | 2.01 | 1.71 | 0.75 | 0 | 0.03 | 0 |
| | 10 | 67.61 | 16.53 | 11.51 | 1.93 | 1.62 | 0.78 | 0.01 | 0.02 | 0 |
| | Avg | 67.65 | 16.72 | 10.97 | 2.14 | 1.58 | 0.76 | 0.14 | 0.04 | 0.03 |
| Max | | 67.95 | 23.14 | 11.87 | 4.79 | 43.44 | 9.38 | 0.53 | 0.1 | 16.47 |
| Min | | 17.66 | 9.48 | 1.43 | 1.6 | 1.32 | 0.67 | 0 | 0 | 0 |
| Average | | 59.46 | 17.61 | 7.42 | 2.68 | 8.03 | 2.51 | 0.13 | 0.04 | 2.12 |
| Standard Deviation | | 16.84 | 4.39 | 3.92 | 1.18 | 14.44 | 3.58 | 0.19 | 0.03 | 5.22 |

Firstly, the bulk austenitic matrix observed as the lighter phase has an average Cr and Mo composition of 16.72 % and 2.14 %, whilst the darker δ-ferrite phase returns average Cr and Mo readings of 6.34 % and 2.12 % greater, respectively. This is offset by average reductions in the Fe and Ni composition from the austenite to the δ-ferrite of 1.81 % and 6.69 %, respectively. Whilst there are other variations across the other elements, their absolute changes are not as significant. Although 3 attempts were made to detect the composition of the circular inclusions observed in Figure 50, the data in Table 28 suggests that only 2 were successful, with spectrum 6 exhibiting a composition similar to that of the austenitic region, suggesting that either the spectrum was misplaced or that the inclusion is very shallow, and the kV used is resulting in the detection of an austenitic phase beneath it. Spectra 4 and 5, when compared, present substantial compositional differences. However, the most noteworthy elemental variations are those of Mn, Si and S, with increases in their weight % compared to the austenitic matrix from an average of 1.58 %, 0.76 % and 0.03 % to 34.15 %, 9.30 % and 10.43 %, respectively. These inclusions, whilst significantly depleted of Fe, also contain the least mass of Cr, Ni, and Mo per phase, all of which are important elements when studying the corrosion resistance of the steel. The compositions of spectra 4 and 5 are indicative of MnS inclusions, which are well known to occur when S content is not kept beneath certain levels [79].

5.5.3 CR

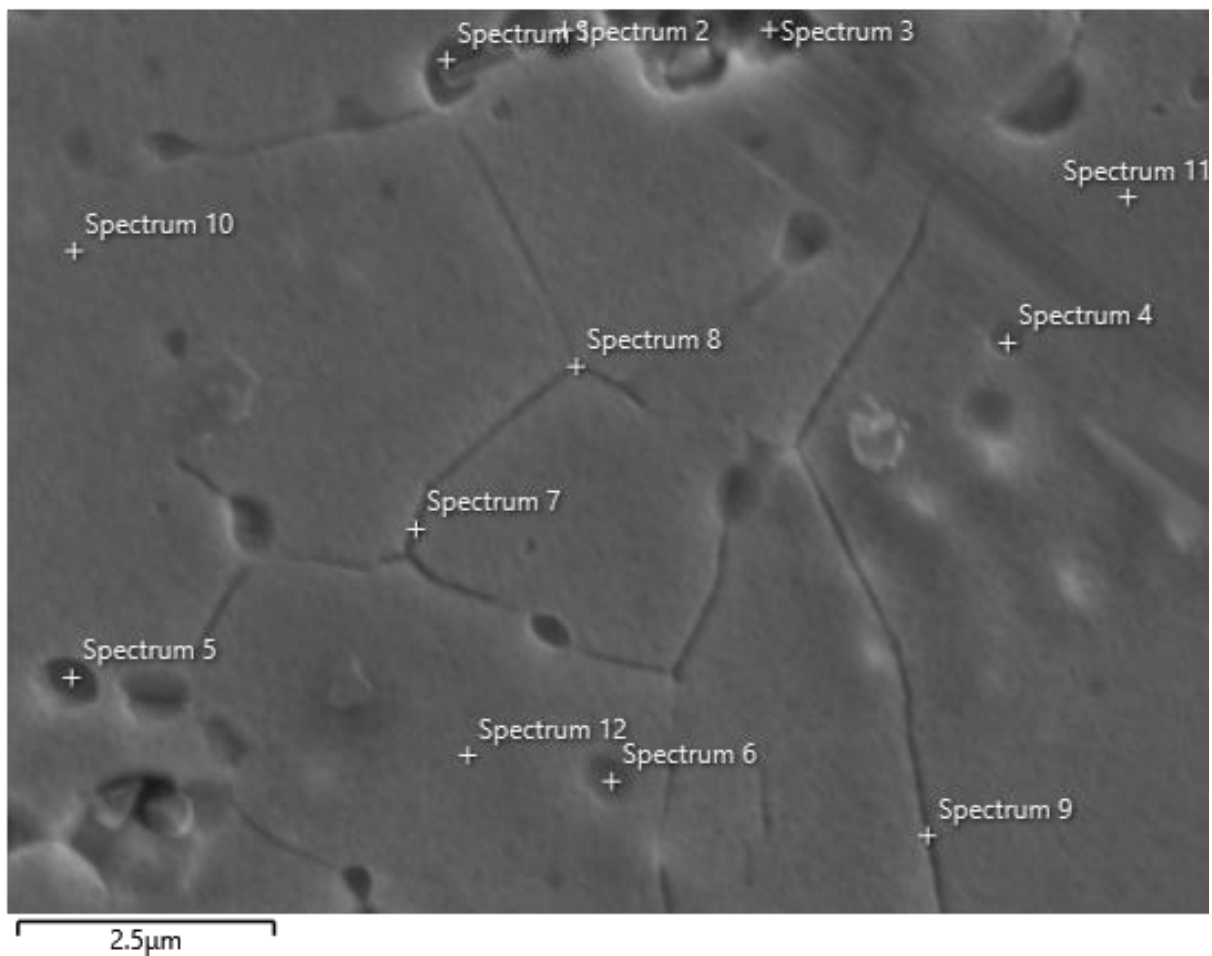
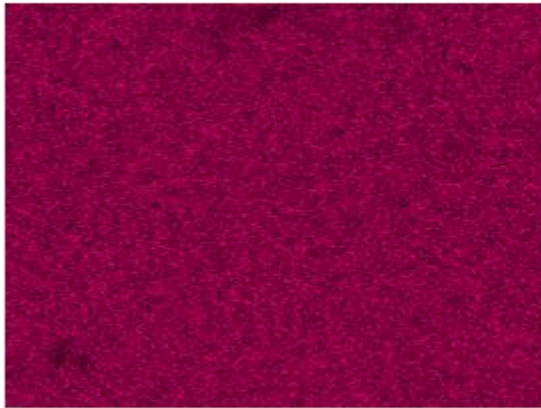


Figure 51 EDS point scan map of CR 316L at 10kx magnification

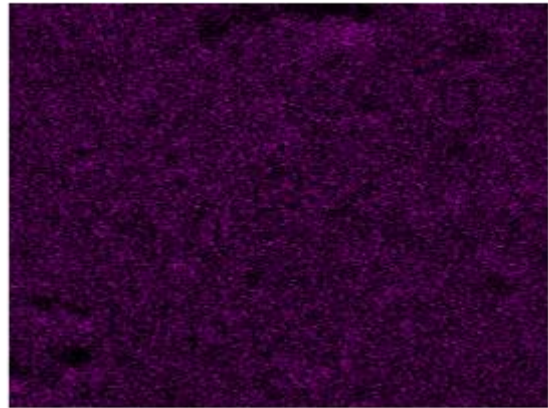
The CR 316L area investigated in Figure 51 shows signs of the targeted cellular structure seen previously in Figure 38 and Figure 39, with an approximate grain size of between 2.5 μm and 12.5 μm . Whilst this has been achieved, there are multiple surface defects present at this magnification. Small craters are observed along the grain boundaries as well as in the bulk, some of which are clear and others that have angular geometries within them. Additionally, there are some raised inclusions of varying structures present on the surface of the sample. These defects were investigated with a combination of EDS maps and subsequent point scans to determine if any additional phases or inclusions were present, or whether these defects were simply ornamental.

Fe K α 1



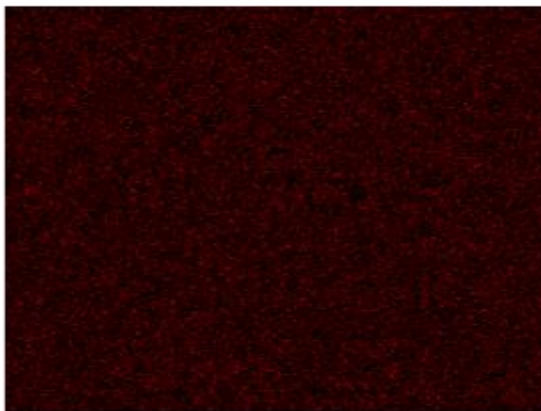
2.5 μ m

Ni L α 1,2



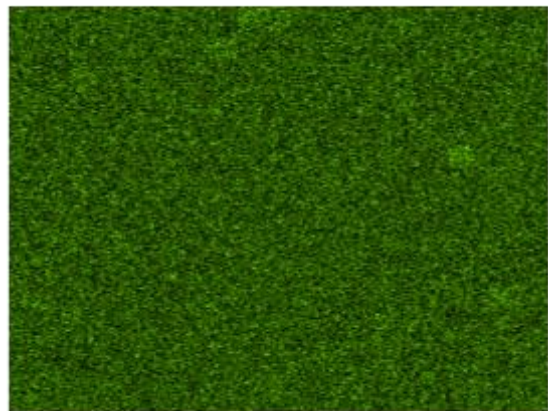
2.5 μ m

Mn K α 1



2.5 μ m

Cr K α 1



2.5 μ m

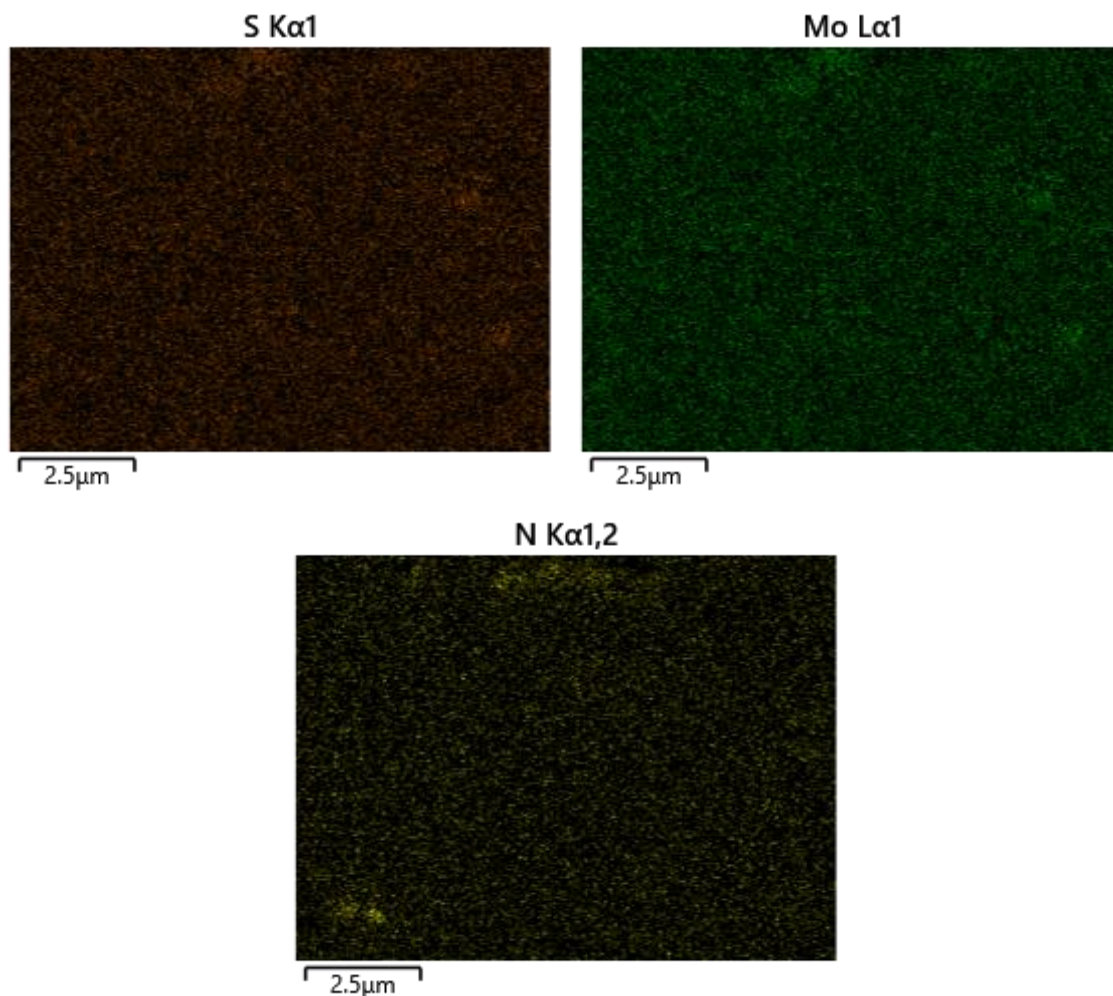


Figure 52 EDS Maps for CR 316L on the sample area shown in Figure 51

Table 29 Composition of CR 316L from EDS Maps in Figure 52

| Element | Fe | Cr | Ni | Mn | Mo | Si | N | P | S |
|----------|-------|-------|------|------|------|------|------|------|------|
| Weight % | 63.71 | 18.43 | 12.6 | 2.73 | 1.57 | 0.73 | 0.17 | 0.03 | 0.02 |

Whilst the composition provided through the EDS maps generated in Figure 52 and displayed in Table 29 differs from the levels anticipated in 316L and seen through the other manufacturing processes; this is likely due to the highly localised nature of this scan, with a specific focus on points of interest such as grain boundaries and variances in surface morphology. Largely homogenous maps are realised across the bulk of the region investigated; however, areas are identified with diminished levels of Fe and Ni whilst simultaneously having elevated levels of Mo, N, S and Cr. Figure 51 outlines the locations across the sample from which point scans were taken to quantify the inhomogeneity.

Table 30 Point scan analysis from spectrum in Figure 51 (wt.%)

| Region | Spectrum No. | Fe | Cr | Ni | Mn | Mo | Si | N | S | P |
|---------------------------|--------------|-------|-------|-------|------|------|------|------|------|------|
| Grain Boundary Inclusion | 1 | 63.17 | 18.68 | 12.28 | 2.85 | 1.65 | 0.74 | 0.56 | 0.03 | 0.04 |
| | 2 | 56.62 | 27.00 | 7.65 | 2.57 | 4.43 | 0.94 | 0.50 | 0.19 | 0.09 |
| | 3 | 64.07 | 18.87 | 12.51 | 2.86 | 1.02 | 0.44 | 0.12 | 0.1 | 0.02 |
| | Avg | 61.29 | 21.52 | 10.81 | 2.76 | 2.37 | 0.71 | 0.39 | 0.11 | 0.05 |
| Bulk Inclusion | 4 | 59.73 | 23.59 | 9.68 | 2.37 | 3.63 | 0.78 | 0 | 0.15 | 0.05 |
| | 5 | 63.27 | 20.43 | 10.77 | 2.76 | 2.15 | 0.62 | 0 | 0 | 0 |
| | 6 | 64.63 | 18.55 | 11.78 | 2.38 | 1.96 | 0.66 | 0 | 0 | 0.03 |
| | Avg | 62.54 | 20.86 | 10.74 | 2.50 | 2.58 | 0.69 | 0.00 | 0.05 | 0.03 |
| Grain Boundary | 7 | 64.11 | 17.94 | 12.75 | 2.75 | 1.41 | 0.78 | 0.15 | 0.03 | 0.08 |
| | 8 | 63.5 | 18.05 | 13.02 | 2.87 | 1.31 | 0.77 | 0.33 | 0.06 | 0.10 |
| | 9 | 64.47 | 18.39 | 12.24 | 2.66 | 1.36 | 0.74 | 0.11 | 0 | 0.03 |
| | Avg | 64.03 | 18.13 | 12.67 | 2.76 | 1.36 | 0.76 | 0.20 | 0.03 | 0.07 |
| Bulk | 10 | 61.84 | 20.60 | 11.95 | 2.44 | 2.08 | 0.89 | 0.05 | 0.15 | 0.01 |
| | 11 | 64.45 | 18.29 | 12.42 | 2.91 | 0.99 | 0.73 | 0.01 | 0.16 | 0.03 |
| | 12 | 64.37 | 18.65 | 11.9 | 2.55 | 1.58 | 0.77 | 0.12 | 0.01 | 0.06 |
| | Avg | 63.55 | 19.18 | 12.09 | 2.63 | 1.55 | 0.80 | 0.06 | 0.11 | 0.03 |
| Max | | 64.63 | 27.00 | 13.02 | 2.91 | 4.43 | 0.94 | 0.56 | 0.19 | 0.10 |
| Min | | 56.62 | 17.94 | 7.65 | 2.37 | 0.99 | 0.44 | 0 | 0 | 0 |
| Average | | 62.92 | 19.81 | 11.66 | 2.67 | 1.93 | 0.74 | 0.16 | 0.07 | 0.04 |
| Standard Deviation | | 2.32 | 2.66 | 1.50 | 0.19 | 1.01 | 0.12 | 0.19 | 0.07 | 0.03 |

Analysis of the point scan data for the average grain boundary and bulk compositions in Table 30, the most significant change in elemental magnitude is that of Cr, with a 1.05 wt.% decrease at the grain boundary. The regions in the table defined as 'bulk inclusion' and 'grain boundary inclusion', when their average compositions are scrutinised, offer little to suggest that these areas are anything other than deformities on the surface of the alloy. However, spectrums 2 and 4 exhibit higher levels of Cr and Mo with noticeable reductions in Ni and Fe compared to the bulk, suggesting some form of inclusion. C readings were retrospectively taken around these areas and, whilst potentially more unreliable under EDS, returned readings at ~2 wt.% at the boundaries and inclusions, reducing the likelihood of these formations being chromium carbides.

5.5.4 Grain Size Analysis

Grain size analysis was conducted on the 316L variants using the procedure outlined in section 3.14.3, the results of which are presented in Table 31. The data from the AM sample is displayed in Figure 53.

Table 31 Grain size analysis of AM, cast, and CR specimens

| Process | d_{\min} (μm) | d_{\max} (μm) | d_m (μm) |
|---------|------------------------------|------------------------------|-------------------------|
| AM | 3.2 | 119.6 | 16.7 ± 3.2 |
| Cast | 4.9 | 414.1 | 96.1 ± 147.3 |
| CR | 3.0 | 12.1 | 4.1 ± 0.1 |

Analysis of the 3 manufacturing methods showed distinct differences in their grain sizes, and also their variability. Interestingly, the d_{\min} of the samples were tightly grouped at between 3 μm and 4.9 μm ; however, the d_{\max} of the cast sample was significantly bigger at 414.1 μm compared to 119.6 μm and 12.1 μm for AM and CR, respectively. The significantly larger range of grain sizes detected for the cast sample has resulted in a substantial uncertainty in the d_m value, of ± 147.3 μm . One issue encountered with this sample was the dendritic arms, seen in Figure 50, which were identified as formed from multiple grains, when it is far likelier that each dendrite was one grain, propagating through the bulk microstructure. These were removed from the analysis as all BCC phases could be easily discounted. The majority of the AM grain sizes detected were in the 3.2 μm to 65.4 μm range, with just two higher at 119.56 μm and 105.08 μm . If these are considered errors in the analysis and subtracted, the d_m falls to 15.5 ± 1.5 μm , corresponding with literature [79].

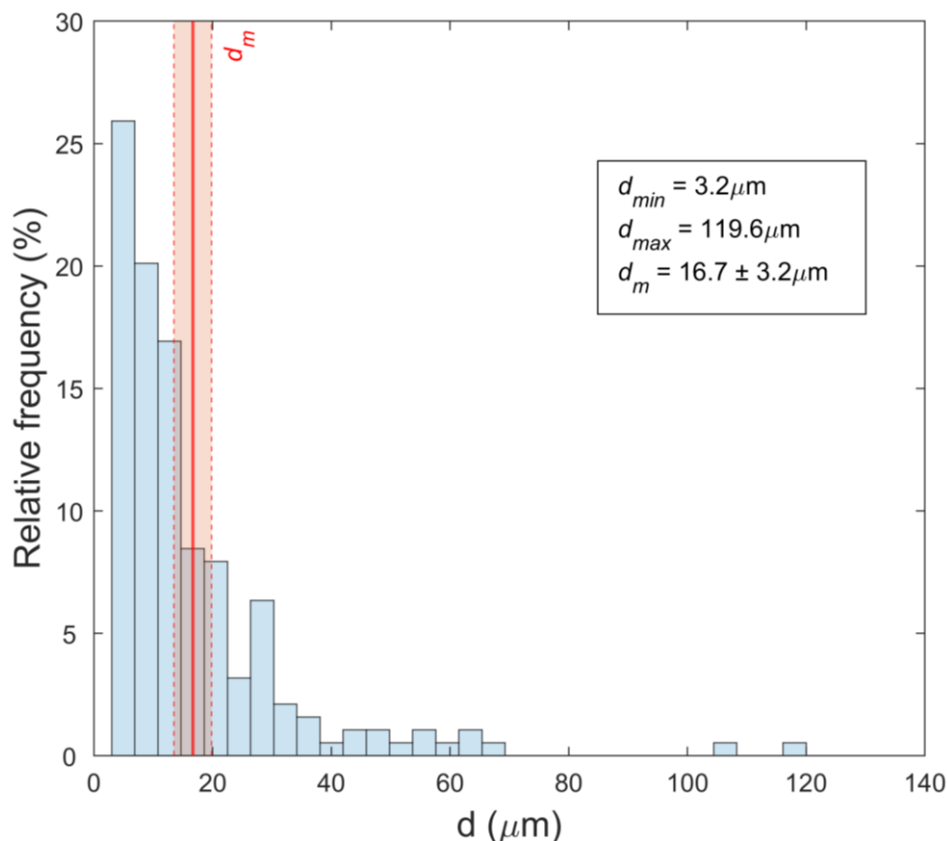


Figure 53 Histogram of 316L AM grain size analysis

5.6 Corrosion Testing

Table 32 Summary of 316L corrosion data for each manufacturing method

| Sample | Optical Density (%) | Avg OCP (V) | Error (SD) | Avg E_{corr} (V) | E_{corr} (SD) | Avg E_{pit} (V) | E_{pit} (SD) | Avg E_r (V) |
|--------|---------------------|-------------|------------|--------------------|-----------------|-------------------|----------------|---------------|
| AM 22 | 99.88 | 0.067 | 0.077 | 0.024 | 0.098 | 1.018 | 0.096 | -0.183 |
| Cast | 99.65 | -0.109 | 0.070 | -0.123 | 0.056 | 0.433 | 0.038 | -0.218 |
| CR | 99.89 | -0.126 | 0.095 | -0.085 | 0.076 | 0.479 | 0.086 | -0.214 |
| WRT | 100 | 0.113 | 0.037 | 0.030 | 0.038 | 0.415 | 0.049 | 1.164 |

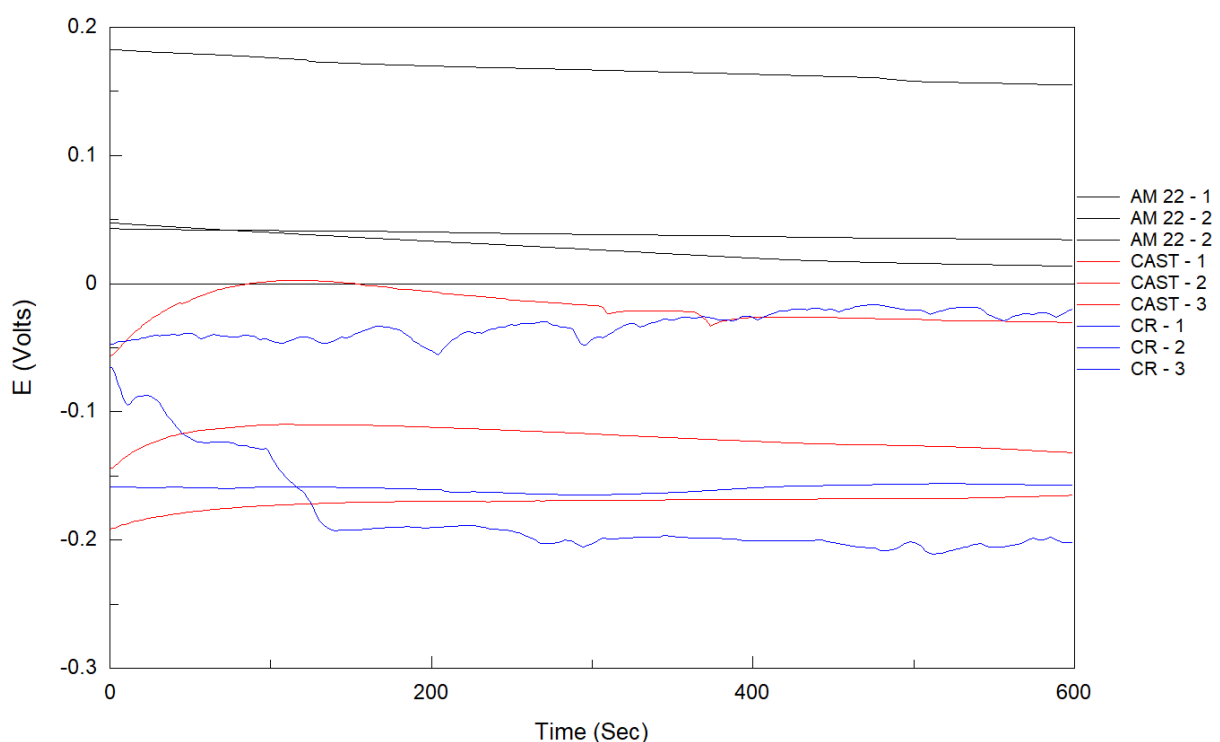


Figure 54 OCP plots for 316L AM 22, cast and CR over 600s

OCP measurements for each manufacturing process shown in Figure 54 indicate the greatest stability during the scan in the AM samples, with no noticeable deviations from the early equilibrium achieved. The cast sample's potential, when measured, was observed to exhibit trajectorial similarities, with an initial increase in OCP before levelling out and a subsequent slow reduction, returning to a similar level to the beginning of the test with minimal erraticism and an average OCP of -0.109 V. The CR samples, in contrast, show more disorder during their scans, particularly with sample 3, which shows a significant drop in potential of 0.126 V before levelling out. CR – 1 and 2, however, do exhibit more stability with both starting and finishing at a similar potential, with the former demonstrating a similar equilibrium to those in the cast and AM, albeit at a lower potential. The CR samples also had the lowest average OCP achieved of the 4 manufacturing routes shown in

Table 32, followed by the cast samples. However, the deviation in the cast OCP was lower than that of AM, even though the magnitude of the OCP was lower.

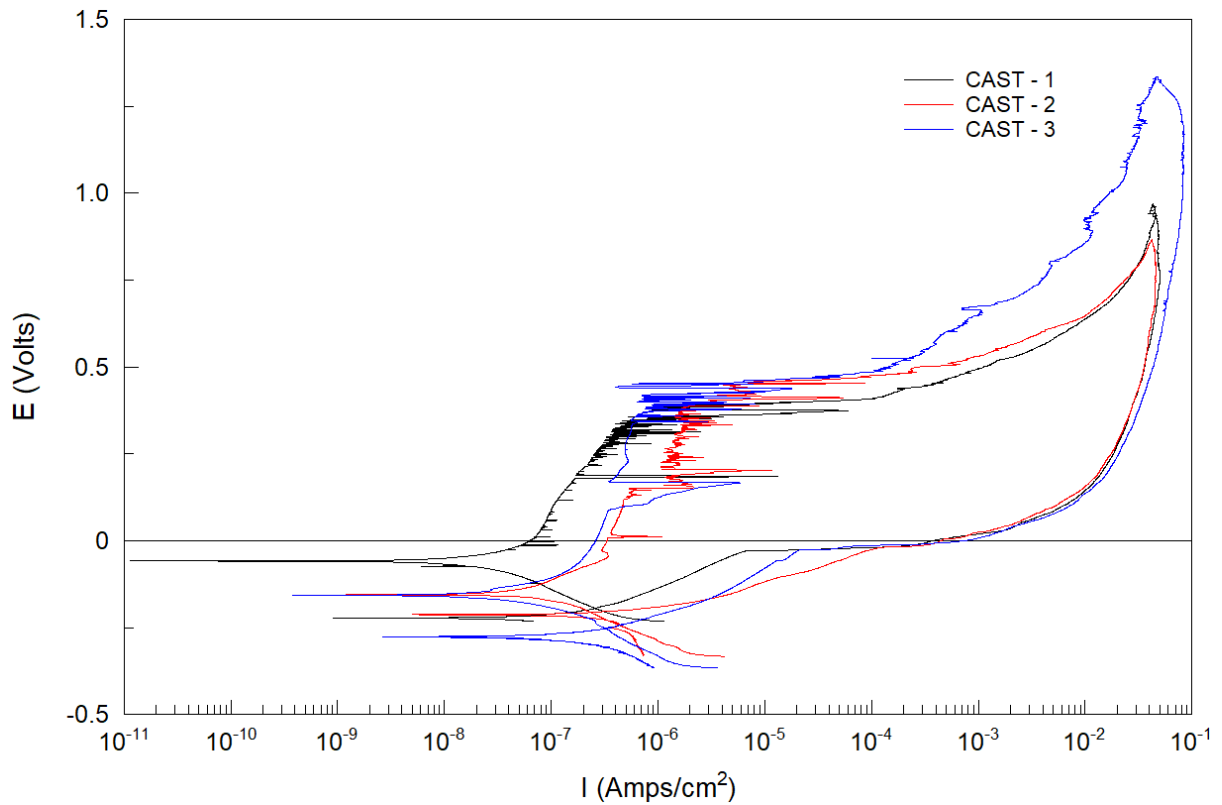


Figure 55 Cyclic polarisation plots for cast 316L

The CP scans of cast 316L shown in Figure 55 and the data extracted from them in

Table 32 show excellent repeatability in their E_{corr} and E_{pit} values, with standard deviations of 0.056 and 0.038, respectively, and comparable scan profiles. All 3 scans also suggest the presence of an oxide layer forming over the pitting sites, with passive regions indicated between the E_{corr} and E_{pit} . A small quantity of metastable pitting is observed in each scan before a significant but brief increase in current between 0.15 V and 0.2 V before it becomes more prominent. The profiles and key data points are very similar to those of the wrought specimens shown in Figure 46.

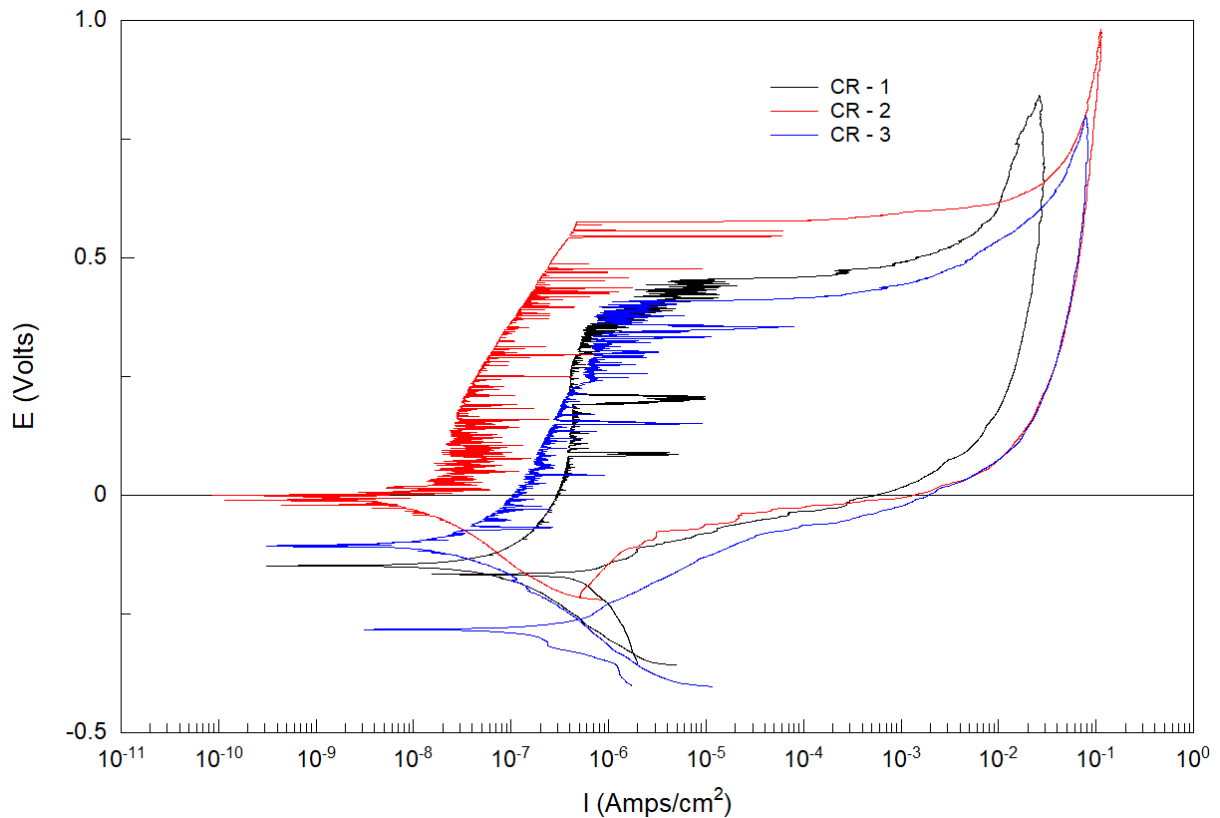


Figure 56 Cyclic polarisation plots for CR 316L

The CP scans shown in Figure 56 show similar levels of concurrence to that of the wrought and cast samples, with evident passive regions and metastable pitting before E_{pit} is reached. The average E_{pit} value is also higher than that of the cast samples at 0.479 V. However, this is most likely due to the results from CR – 2, which has a significantly higher E_{pit} than samples 1 and 3. This resulted in an E_{pit} standard deviation in the CR samples tested of 0.86, over 2x that of the cast specimens. Once again, the profiles are very similar to those of the wrought samples.

5.7 Discussion

The results from the 316L XRD presented in Table 26 show that all 4 manufacturing methods produce very similar phase proportions, with the highest and lowest FCC ratios being separated by 1.66 %, with the maximum FCC percentage at 98.39 %, similar to ratios present in literature [183–186]. Whilst there may be various inclusions or intermetallic phases, they were not present in a great enough quantity to be visible. The high percentage of FCC present correlates with literature and the Thermo-Calc predictions that 316L is a fully austenitic stainless steel with small concentrations of δ -ferrite, presenting as the BCC phase [29,79,81,170,172]. The AM sample produced the highest level of FCC of the 3 manufacturing routes produced by the author from the feedstock. This is likely due to the rapid cooling rates associated with LPBF preventing the majority of elemental segregation into discrete phases [184]. This correlates with the AM EDS maps and point scans that revealed very few

compositional inhomogeneities and, of those that did exist, did not fit with the profiles predicted by Thermo-Calc. Conversely, the cast sample presents a more distinguishable variation in composition with δ -ferrite dendrites present throughout the bulk, point scan analysis of which correlates closely with the BCC phase predicted by Thermo-Calc at 1174 °C and literature. The analysis detects multiple small MnS inclusions; however, there is no implication of chromium carbides. The more obvious δ -ferrite dendrites in the cast sample vs the AM are due to the slower cooling rate, giving the alloying elements time to diffuse into distinct phases [185,187]. The point scan analysis of the CR sample in Figure 51 and Table 30 shows a largely homogenous bulk composition with only 2 spectrums outside this range. Spectrums 2 and 4, as described previously, deviate from the bulk with decreases in Fe and Ni, with increases in Cr and Mo. Whilst not extreme, these variations follow trends outlined by Thermo-Calc for δ -ferrite and chromium carbide but do not directly mirror either of them. The latter, however, was somewhat contradicted due to the significant differences in Fe and Mn detected. In addition to the AM grain size being in line with that reported in literature, the annealing and rolling cycles produced a microstructure in the CR sample with an average grain size of 4.1 μm . This was very similar to the 6 μm grain size seen in the literature this production method was based on and in line with reports that grain sizes below $\sim 4 \mu\text{m}$ in austenitic stainless steels increase yield strength [172,188,189].

The cast and CR samples proved to have similar average OCPs at -0.109 V and -0.126 V, respectively, both of which were below the values set by the wrought and optimum AM, with the cast samples providing a slightly more stable equilibrium than the CR during the test. The CP profiles of these samples are comparable in shape with each other and with the wrought samples, with clear passive regions after E_{corr} is reached, as well as metastable pitting before E_{pit} is reached. The average E_{pit} values of the cast and CR samples surpass that of the wrought with values of 0.433 V and 0.479 V, respectively, suggesting a more effective passive oxide layer formed over pit initiation sites. This, however, could be due to compositional differences. The increase in the CR passive layer relative to the cast sample compares with literature suggesting that cold rolling reductions of greater than 50 %, and in some cases 70 %, result in a more effective passivation [74,75,77,172]. The AM 22 sample's corrosion resistance outweighed that of the cast and CR samples. This could be due to the more significant compositional differences exhibited in their respective EDS analysis as well as the greater incidence of inclusions and surface defects. MnS, for example, observed in the cast sample, is well documented as operating as a preferential site for pitting corrosion to initiate [81,154,190–193]. The effect of the grain size outlined in Table 31 on the corrosion resistance is difficult to determine with certainty, as that microstructural variable has not been isolated in these experiments and the surface chemistry is often a driving factor [29]. However, in line with existing literature, the E_{pit} values of the

two samples with lower grain sizes, AM and CR, are larger than those of the cast [188]. It is suggested that the number of pits in coarsely grained steel are fewer than those with a finer structure, but these pits tend to be larger and propagate much deeper into the alloy, increasing the corrosion rate [188].

5.8 Conclusions

- 316L was successfully produced in-house by 3 manufacturing methods: AM, cast, and CR.
- XRD spectra of the 3 methods observed similar, almost entirely austenitic crystallographic structures with maximum and minimum δ -ferrite proportions of 3.27 % and 1.76 % detected in the CR and AM samples, respectively. The distinction between austenitic and δ -ferrite phases was most prominent in the SEM images of the cast sample, as was the magnitude of compositional variation in these phases. MnS inclusions are also observed in the microstructure of the cast alloy. The CR sample achieved bulk homogeneity and a cellular microstructure similar to that seen in the wrought specimen; however, defects in the microstructure of the alloy are observed, the compositions of some of which suggest the presence of chromium carbide precipitates towards the grain boundaries.
- The optimal AM sample outperformed the cast and CR samples across all key metrics except the standard deviation of these metrics. Whilst the CR process displayed a less stable OCP than the cast samples, it presented higher values for E_{corr} and E_{pit} , suggesting the formation of a more effective passive film. The CR sample was expected to have a higher corrosion resistance than was observed; however, this could be due to the formation of detrimental chromium carbides at the grain boundaries, amongst other defects.
- The poorer than expected CR performance suggests the need to refine the thermomechanical processes undergone during its manufacture.

6 An Investigation into the Different Manufacturing Methods of a High Entropy Alloy (HEA1) and their Effects on Microstructure and Corrosion Resistance

6.1 Introduction

HEAs have existed under various nomenclatures for decades; however, only recently are they being studied in greater depth, specifically within the realms of AM. They are associated with improved mechanical properties as well as high corrosion resistance and design flexibility. HEA1 is a non-equimolar high entropy alloy system based on Al-Cr-Mn-Ni-Fe and was developed as a gas atomised powder for additive manufacturing at Swansea University under the Combinational Metallurgy (COMET) project through rapid alloy prototyping [106]. Certain desirable properties were outlined prior to the alloy design, such as minimising cost and environmental factors, achieving a density below 7.75 kg/m^3 , and achieve a tensile strength of $\geq 800 \text{ MPa}$. A high FCC phase proportion was also preferred to increase ductility to compensate for any issues occurring due to the high cooling rates and residual stresses that transpire in AM. The complete HEA1 composition was gas atomised by Sandvik-Osprey and used as the feedstock for 3 manufacturing processes to determine the effect these routes have on the microstructure and corrosion resistance of the alloy.

6.2 Powder Analysis

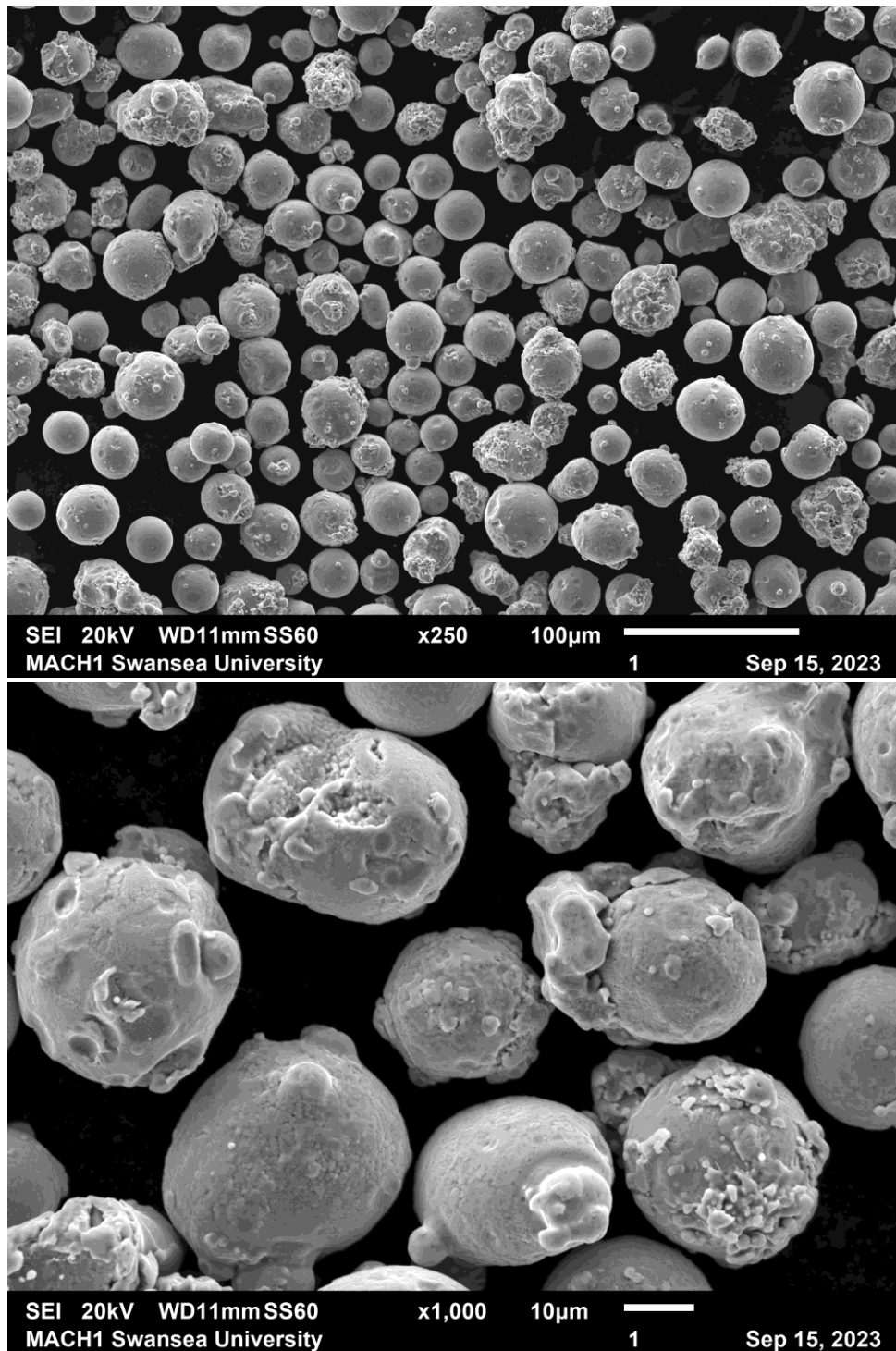


Figure 57 SEM images of HEA1 powder at 250x and 1000x magnification

The powder morphology of the virgin HEA1 powder gas atomised by Sandvik is displayed in Figure 57 at 250x and 1000x magnification. The powder has a largely homogenous morphology, with the majority of the particles exhibiting a spherical structure. However, on further magnification, it is observed that there is a level of agglomeration on some of the particles as well as increased surface roughness due to both additional and absent material. There are also some particles within the

powder that present as prolate spheroids, as opposed to the more desirable fully spherical elements. These irregularities could be due to the single-run nature of the manufacture of the HEA1 powder, meaning that an optimisation of the gas atomisation process for this composition would not be as complete as one for an industrially standard alloy such as 316L or Ti-6Al-4V. The optimal morphology provides ideal flowability and packing density, leading to uniform compaction and improved sintering properties, resulting in better part quality.

EDS analysis was conducted on the powder to identify measured composition relative to that which was supplied with the delivery of the powder, as well as its compositional homogeneity. It is compared with the target composition for the alloy as well as the ICP-OES measurements supplied on delivery in Table 33.

Table 33 Composition of the target, actual, and EDS HEA1 Powder, in w.%

| | Fe | Cr | Ni | Mn | Al | Si | N | C |
|---------------------------|-----------|--------------|--------------|------------|-------------|------------|-------------|-------------|
| Target | Bal | 30.9 ±1.5 | 24.5 ±1.5 | 10.0 ±1 | 3.0 ±0.5 | 0.5 max | 0.32 max | 0.02 max |
| Sandvik Osprey | 33.97 | 27.30 | 25.0 | 10.30 | 2.80 | 0.4 | 0.21 | 0.02 |
| Powder EDS | 32.11 | 28.84 | 23.28 | 11.75 | 2.98 | 0.31 | 0.71 | N/A |

The PSD measurements for the virgin HEA1 powder are displayed in Figure 58 and Table 34. The powder range measured during the test was between ~ 12.7 µm and 66.9 µm, the same array 316L previously presented. However, no particles outside this range were detected. The size fractions calculated and displayed in Table 34 shows that approximately 80 % of the powder by volume lies within the 15 µm to 45 µm range expected, with the SMD for the distribution given as 30.6 µm.

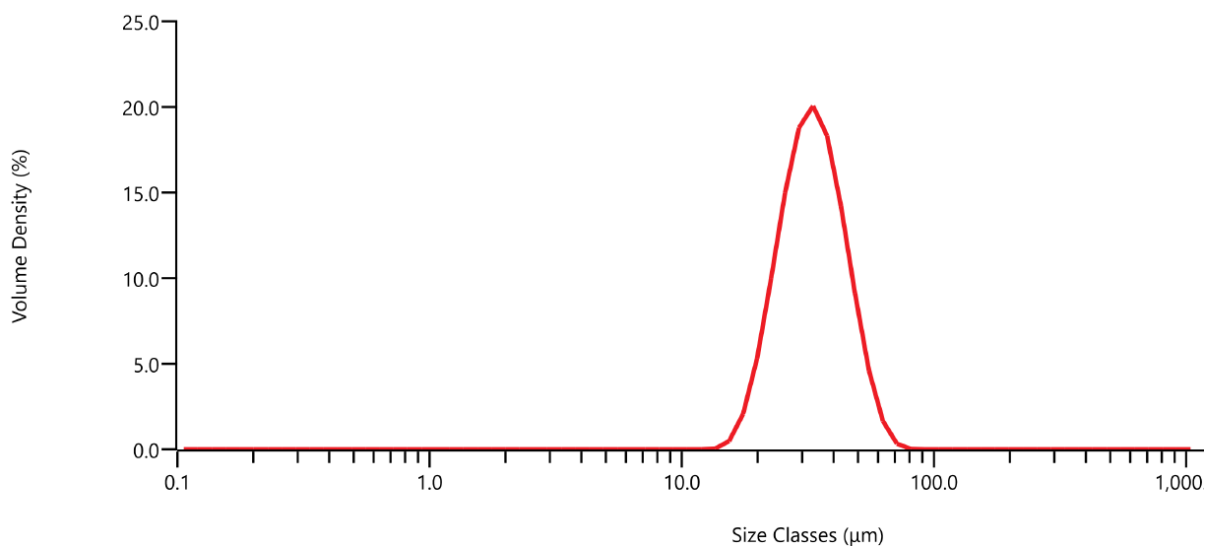


Figure 58 HEA1 powder PSD

Table 34 Particle size by volume for HEA1 powder

| Percentile | Size (µm) |
|----------------|-----------|
| Dv (10) | 22.5 |
| Dv (50) | 32.8 |
| Dv (90) | 47.8 |
| D [3,2] | 31.5 |
| D [4,3] | 34.1 |

A low FRI of 1.11 observed in Table 35 as well as a low BFE of 633.47 mJ suggests strong flowability characteristics and the powder's stability under changing flow conditions. This will likely result in an efficient and uniform distribution on the powder bed, reducing processing errors and leading to a high quality output.

Table 35 Rheometric characteristics of the HEA1 powder

| BFE (mJ) | SE (mJ/g) | FRI | CBD (g/ml) | Split Mass (g) |
|----------|-----------|------|------------|----------------|
| 633.47 | 2.53 | 1.11 | 3.93 | 98.17 |

6.3 Optimisation and Build Setup

The optimisation of HEA1 took place initially on the RBV. Due to its compositional and thermomechanical similarities to 316L, the initial parameters used were based on those optimised for 316L. An L9 array was created with the parameters varied by 20 % on either side of the optimum. In normal circumstances, this could be characterised as excessive; however, as this was a novel alloy, a broad approach was deemed necessary so as not to omit promising parameter sets.

Once the build had been completed, the samples were dipped and optically analysed, with the parameter set responsible for the highest optical density being used as the foundation for a 4-factor, 16-run Central Composite Design (CCD) full build volume optimisation with 3 repeated builds, created by Minitab. The repetitive nature of the builds allowed the software to account for factors such as part location on the build plate and, therefore, indicate the most stable parameters. For this stage of the optimisation, the parameter set only varied by 10 % on either side of the L9 optimum as there was greater certainty of the suitable range. This could possibly have been reduced further; however, there are many set up differences between the two builds beyond the volume, such as the heating of the build plate and the optimisation of the gas deflectors, which need to be accounted for. After the build was finished, the cubes were once again analysed for bulk density, the results for which are displayed in Figure 59, before selecting the best performing optical analysis.

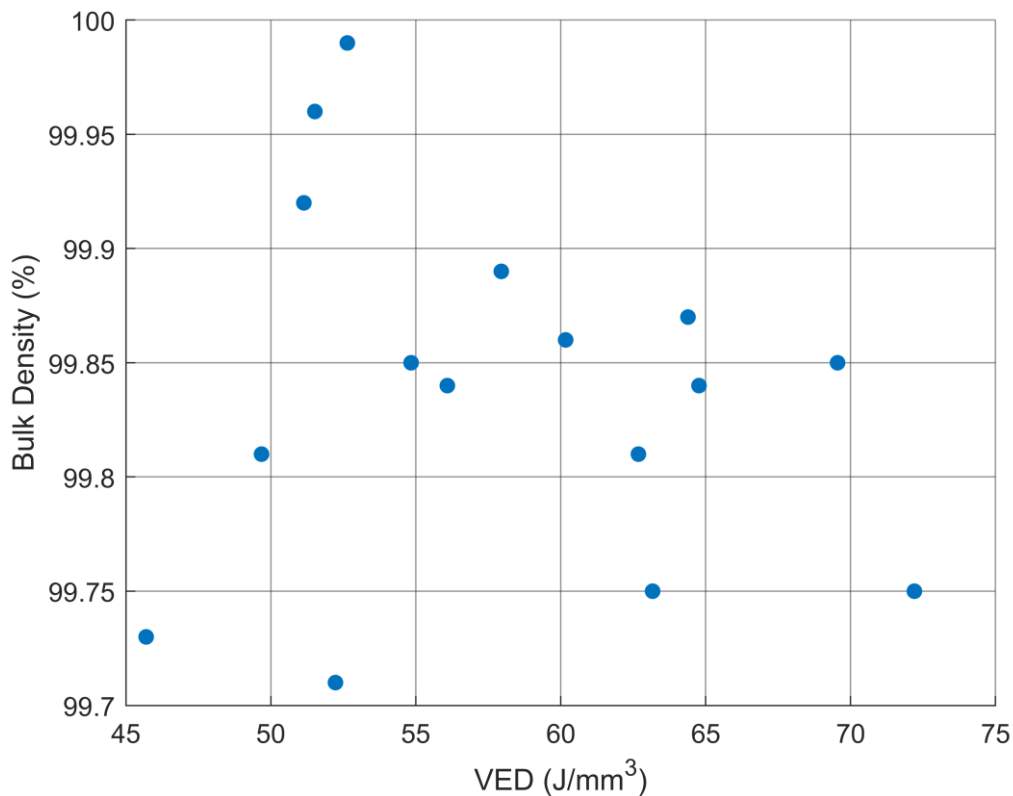


Figure 59 Measured bulk density vs VED during HEA1 optimisation

Whilst the bulk density analysis suggested an optimum parameter set with a VED of 52.64 J/mm³, the optical analysis revealed more porosity in addition to microcracks. After processing more samples, the highest optical density returned was 99.75 % through the parameters outlined in Table 36.

Table 36 Optimum parameter set used for HEA1

| P (W) | PD (µm) | ET (ms) | HS (µm) | LT (µm) | VED (J/mm ³) |
|-------|---------|---------|---------|---------|--------------------------|
| 225 | 50 | 85 | 0.11 | 50 | 69.55 |

Unlike the 316L build, the optimum parameter set was used to manufacture all cubes, as density variation was not the primary focus of this chapter. 9 cubes were manufactured on a single build using these parameters for the ensuing analysis.

6.4 Density Analysis

Table 37 displays the bulk density analysis for HEA1 cubes printed on the full build plate. Due to time, cost, and powder constraints, these were built around the perimeter of other components built for mechanical testing. Whilst this is not optimum, as the increased population of a build plate leads to a decrease in part quality, it is more representative of an industrial build schedule.

Table 37 Bulk density analysis of AM HEA1 cubes

| Cube Number | T (air) (°C) | T(water) (°C) | Mass (g) | Change (g) | Density | Porosity | Density (%) | Normalised (%) |
|-------------|--------------|---------------|----------|------------|---------|----------|-------------|----------------|
| 1 | 23.63 | 22.20 | 9.199 | 1.218 | 7.529 | -0.92 | 100.92 | 99.94 |
| 2 | 23.55 | 22.52 | 9.160 | 1.212 | 7.533 | -0.98 | 100.98 | 100 |
| 3 | 23.93 | 22.43 | 9.067 | 1.203 | 7.513 | -0.71 | 100.71 | 99.73 |
| 4 | 23.86 | 22.41 | 8.982 | 1.193 | 7.505 | -0.60 | 100.60 | 99.62 |
| 5 | 23.78 | 22.31 | 9.161 | 1.220 | 7.485 | -0.34 | 100.34 | 99.36 |
| 6 | 24.44 | 22.15 | 9.006 | 1.198 | 7.494 | -0.46 | 100.46 | 99.48 |
| 7 | 24.15 | 22.20 | 8.874 | 1.178 | 7.509 | -0.66 | 100.66 | 99.68 |
| 8 | 24.15 | 22.04 | 8.775 | 1.163 | 7.522 | -0.83 | 100.83 | 99.85 |
| 9 | 24.02 | 22.26 | 8.558 | 1.150 | 7.418 | 0.56 | 99.44 | 98.47 |

The calculated density resulted in 8 of the 9 cubes having a ‘density’ of over 100 %. This is, of course, impossible to achieve, with even a fully dense part unlikely, and therefore suggests that the theoretical density value of 7.460 kg/m³ needs adjusting. To counter this, the bulk density values have been normalised against the highest value (cube 2). Nevertheless, the data across the build plate, whilst varied, shows a tight spread of measured densities, bar an anomaly in cube 9. Considering the cubes were manufactured in non-optimum locations on the build plate, built alongside other parts which would significantly increase the interlayer time and intensify the likelihood of potential contamination from factors such as spatter expected in AM, this spread is considered satisfactory, with a standard deviation of 0.22 when discounting cube 9.

A selection of samples were then sectioned, mounted, and polished before being optically analysed for density. The images were then processed using ImageJ thresholding, the results for which are presented in Table 38. The table shows that both the cast and CR samples had significantly higher porosity than the optimum AM sample.

Table 38 Optical density measurements for AM, cast, and CR HEA1

| Sample | AM | Cast | CR |
|---------------------|-------|-------|-------|
| Optical Density (%) | 99.47 | 96.25 | 97.95 |

6.5 Thermo-Calc

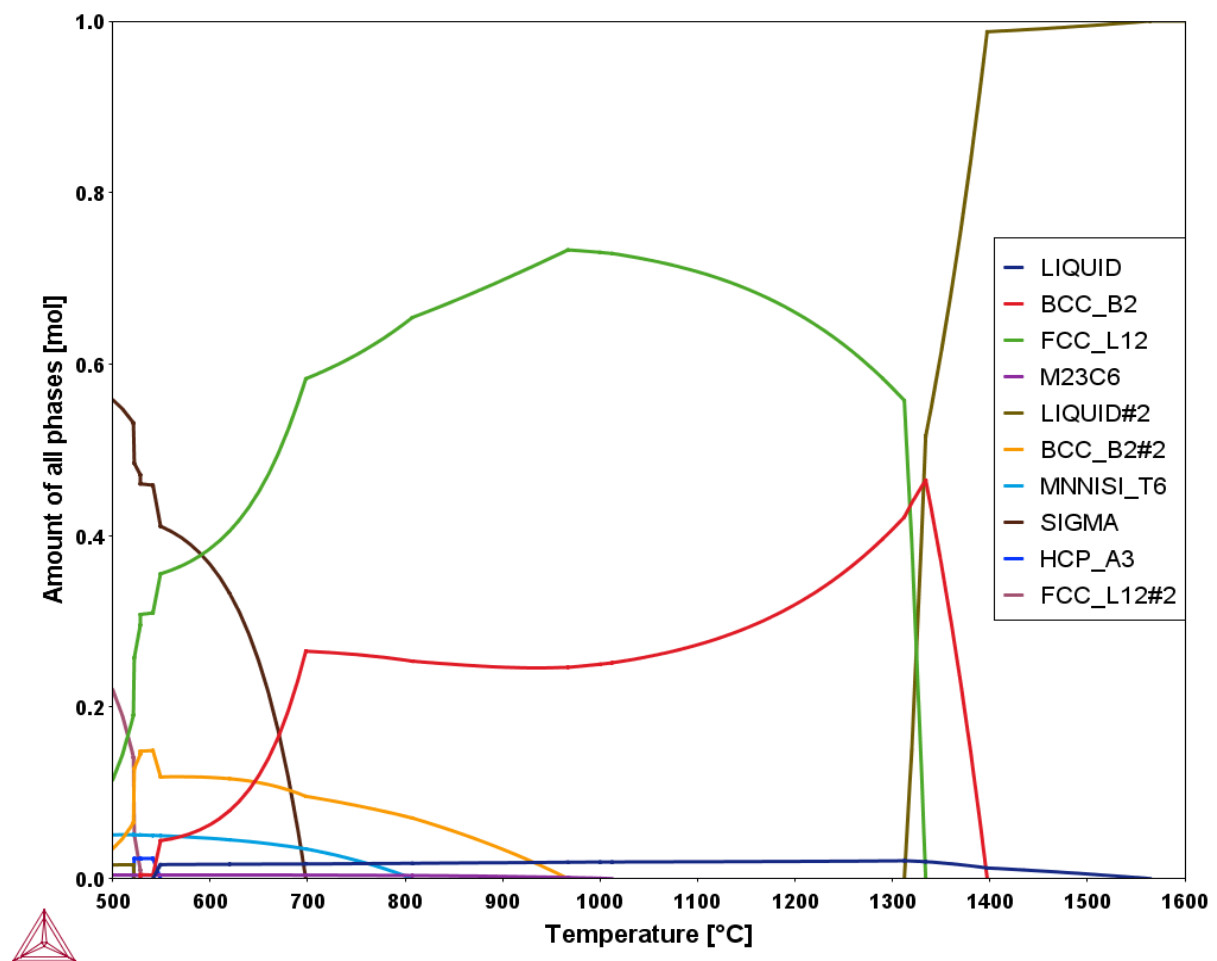


Figure 60 Thermo-Calc prediction of HEA1 in 2021

Figure 60 displays the 2021 simulation of HEA1 produced by Sandvik-Osprey based on the achieved composition of HEA1 in Table 33. Whilst the Y-axis is in moles instead of φ_i , this does not drastically affect the proportions, nor the temperatures, that different phases exist at. Approximately 2.5 years separate this simulation from that of the one presented in Figure 61 and the transformations are dramatic, most notably the reduction in the σ phase initiation temperature from 1193 °C to 704 °C. The lowering of the σ initiation temperature results in a much simpler solid solution containing a majority 1 FCC and 1 BCC structure for a large proportion of the equilibrium diagram. The comparison between Figure 60 and Figure 61 shows how much development has occurred within the realms of HEAs in this time, and indicates that there are still significant aspects that are still not fully understood.

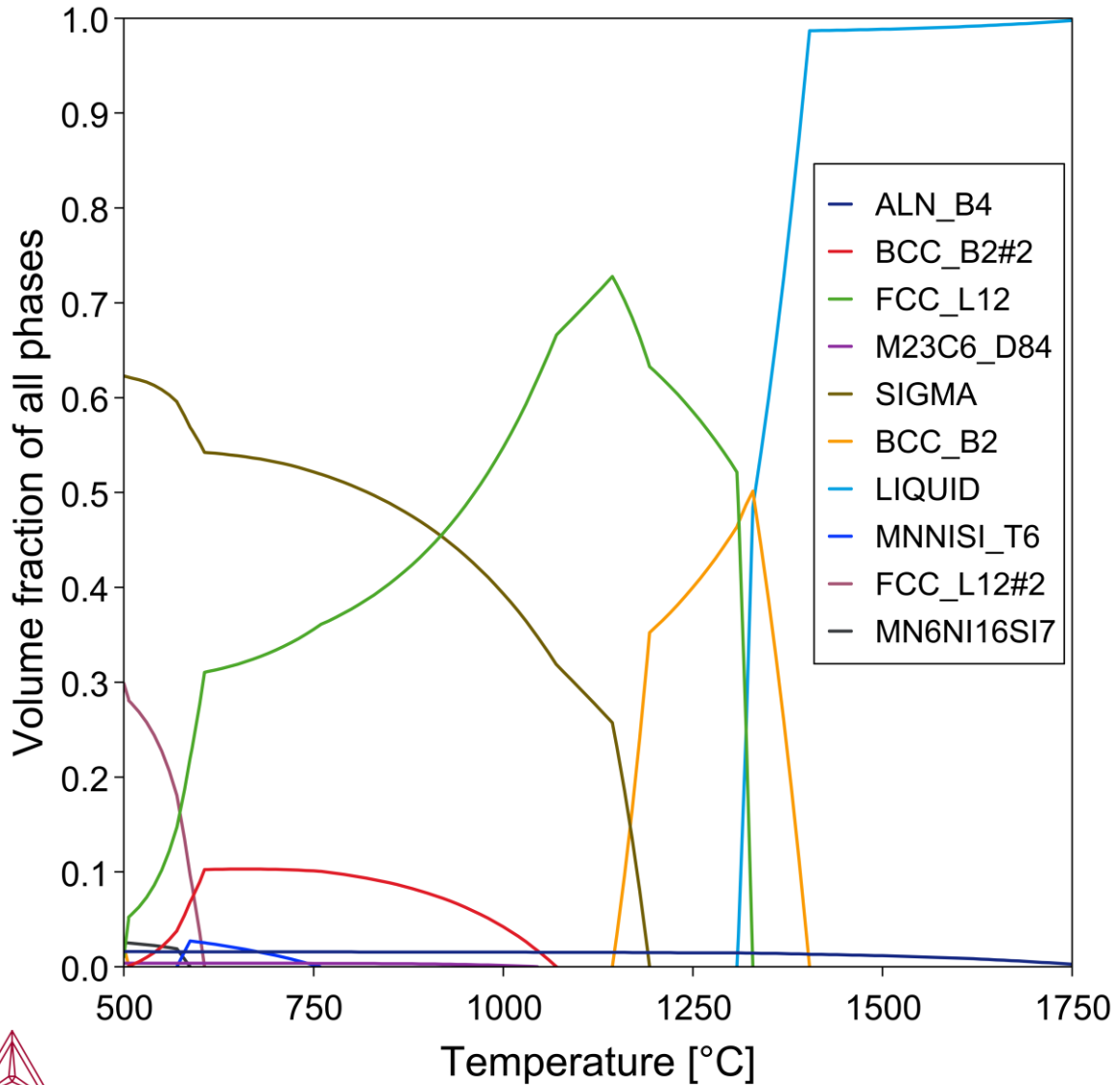


Figure 61 Volume fraction of all phases for HEA1 produced by Thermo-Calc

Figure 61 exhibits the phase diagram for HEA1 produced by Thermo-calc using the TCHEA5: High Entropy Alloys v5.1 database, based on the achieved composition measured by Sandvik-Osprey. As the alloy cools, ALN_B4 forms in small quantities at 1755 °C due to the limited availability of N in the system, reaching a ϕ_i of 0.015 by 1180 °C and only increasing to 0.016 by 500 °C. BCC_B2 is the first major phase to form at 1404 °C, peaking with a ϕ_i of 0.502 at 1329 °C at which point it begins to reduce as FCC_L12 formation takes over. At 1144 °C, this reaches its maximum abundance at 0.728 which is just after the σ phase has begun to figure, initialising at 1193 °C but not peaking till 500 °C. Finally, the BCC_B2#2 phase begins to form at 1070 °C, reaching a peak ϕ_i of 0.103 at 660 °C. The other phases presented in Figure 61 either occur in very small quantities, or only form at temperatures well below the solidus of the alloy and therefore are unlikely to occur without specific, targeted heat treatments. The compositions of each of the phases described at their maximum ϕ_i are presented in Table 39.

Table 39 Composition of selected HEA1 phases at their highest respective volume fraction (wt.%)

| | Fe | Cr | Ni | Mn | Al | Si | N | C |
|-----------------|-------|-------|-------|-------|--------|-------|-------|-------|
| BCC_B2 | 37.64 | 30.90 | 19.57 | 9.29 | 2.44 | 0.14 | 0.003 | 0.001 |
| FCC_L12 | 34.14 | 21.15 | 30.79 | 10.15 | 3.22 | 0.52 | 0.001 | 0.027 |
| SIGMA | 38.85 | 42.63 | 3.63 | 14.89 | 0.0003 | 0.001 | 0 | 0 |
| BCC_B2#2 | 10.73 | 1.27 | 60.75 | 10.43 | 16.56 | 0.25 | 0 | 0 |
| ALN_B4 | 0 | 0 | 0 | 0 | 65.83 | 0 | 34.17 | 0 |

The 4 major phases that are predicted to occur in HEA1 in large quantities vary significantly in composition and are presented in the first 4 rows of Table 39. The BCC_B2 phase that is forecast to form first sees increases in Fe and Cr as well as a reduction in Ni, whereas the second major phase to form, FCC_L12, shows reduced Cr as well as a richer concentration of Ni, Al, Si and C. The σ phase follows a similar pattern to that of the BCC but to a greater extent, with Cr levels anticipated to be at 42.63 % at peak as well as significant depletion of Ni to 3.63 % and only trace levels of Al and Si. The BCC_B2#2 phase forming below 1070 °C contains substantial levels of Ni and Al compared to the other phases as well as a Fe and Cr concentration over 20 % and 26 % lower than the bulk given in Table 33.

6.6 XRD

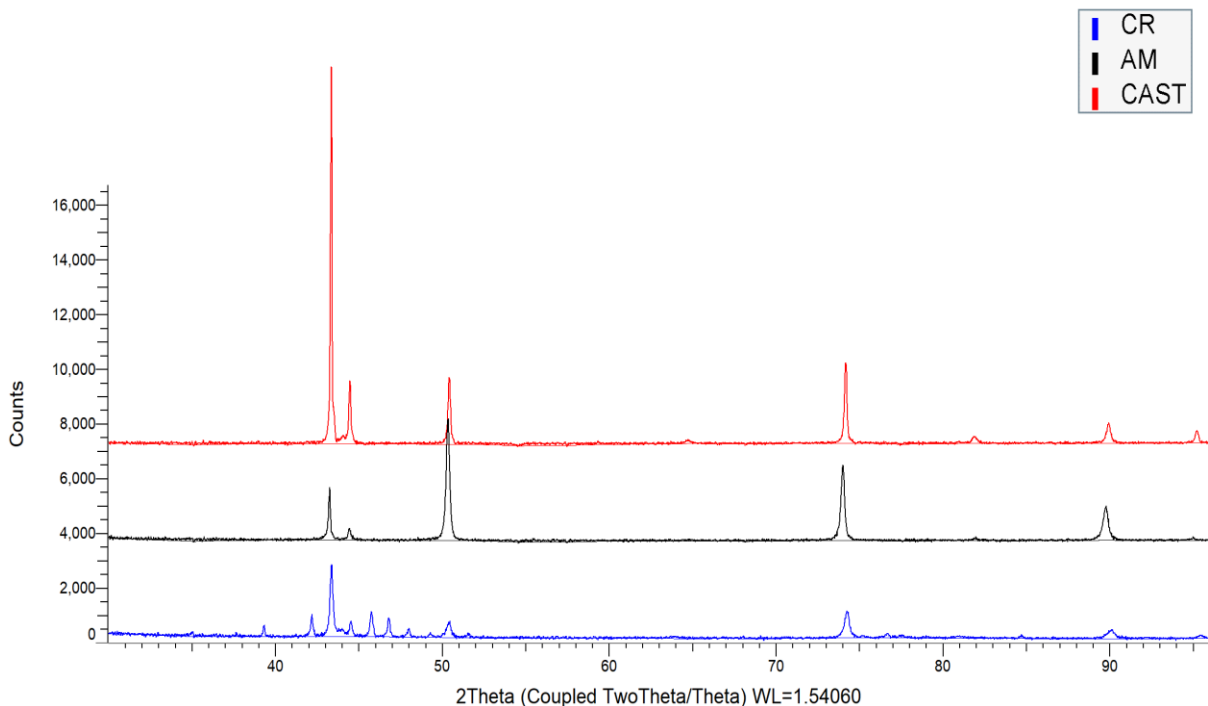


Figure 62 XRD scans for CR, AM, and cast HEA1 samples

Figure 62 shows XRD scans of CR, AM and cast HEA1, the extracted data from the relevant counts are displayed in Table 40. All 3 scans contain 5 clear peaks from the two major phases, outlined in Table 40 as 1,2, 3, 5 and 7, with the cast sample also exhibiting clear peaks at this scale at $\sim 65^\circ$, 90° and 95°

°. The magnitude of the intensity of these peaks is greatest in the cast scan, as was the case with 316L in Figure 48, followed by AM and then CR. The most substantial peak in the cast and CR samples is that of peak 1 at approximately 43.54 °, however the AM sample's is the 3rd peak at ~50.67 °. These peaks, however, both belong to the FCC phase and therefore, it is due to the orientation of the crystal structure. Some issues were encountered when defining the peaks using the pattern matching software, with misalignment of peaks at higher angles of 2θ. This was likely down to slight distortion of the cubic structure. Whilst it is possible to identify the 8 main peaks set out in Table 40 within the CR scan, there are significantly more distinct peaks present, particularly within the range of 39 ° to 52 °. These are very difficult to identify with the crystallographic database available. However, it is theorised, based initially on Thermo-Calc predictions, followed by pattern matching and literature, that AlN could be responsible for peaks at ~39.3 °, 45.8 ° and 84.7 ° [194]. MnS, whilst not predicted in Thermo-Calc due to the absence of S from the input composition, could easily occur due to S residuals in the manufacturing process of the HEA1 powder or other contamination. MnS, if present, could, based on literature, be responsible for peaks at ~ 35 ° and 49.3 °. However, the other anticipated peaks either do not exist or are not present at a high enough intensity to be distinctly visible [195]. The remaining peaks are attributed to secondary BCC and FCC phases however based on the prominence of the σ phase in Figure 61, this could equally be accountable. If any other phases are present in the alloy, it is likely they are not in sufficient quantities to be detectable.

Table 40 XRD data extracted from scans shown in Figure 62

| HEA1 XRD Intensities (cts) | | | | | | | | |
|----------------------------|--------------------|---------------|---------------|---------------|---------------|--------------------|---------------|---------------|
| | FCC Peak Intensity | | | | | BCC Peak Intensity | | |
| | 1 (43.54°) | 3 (50.67°) | 5 (74.25°) | 7 (90.07°) | 8 (95.42°) | 2 (44.42°) | 4 (64.71°) | 6 (81.97°) |
| CR | 2622.5 | 564.374 | 979.443 | 300.43 | 115.711 | 562.842 | 71.7028 | 50.02 |
| AM | 1887.34 | 4399.19 | 2742.81 | 1234.72 | 131.686 | 425.473 | 70.3347 | 140.487 |
| Cast | 13566.9 | 2417.08 | 583.703 | 736.07 | 445.744 | 2305.42 | 147.547 | 258.636 |

Table 41 Major phase ratios for HEA1 CR, cast and AM

| Sample | FCC/BCC |
|--------|-----------------|
| CR | 87.00 %/13.00 % |
| AM | 94.23 %/5.77 % |
| Cast | 86.75 %/13.25 % |

Table 41 shows the FCC/BCC phase ratio calculated for each manufacturing process based on the sum of counts for their respective peaks. The AM sample has a significantly higher FCC proportion than that of CR and cast, with exhibiting very similar magnitudes. Whilst all the visible peaks in the cast and AM samples are accounted for and used in this calculation, the same cannot be said for the CR

specimen. There are multiple uncertainties with these scans, hence why it is a comparison of the major phases present through each production route.

6.7 Microstructure

6.7.1 AM

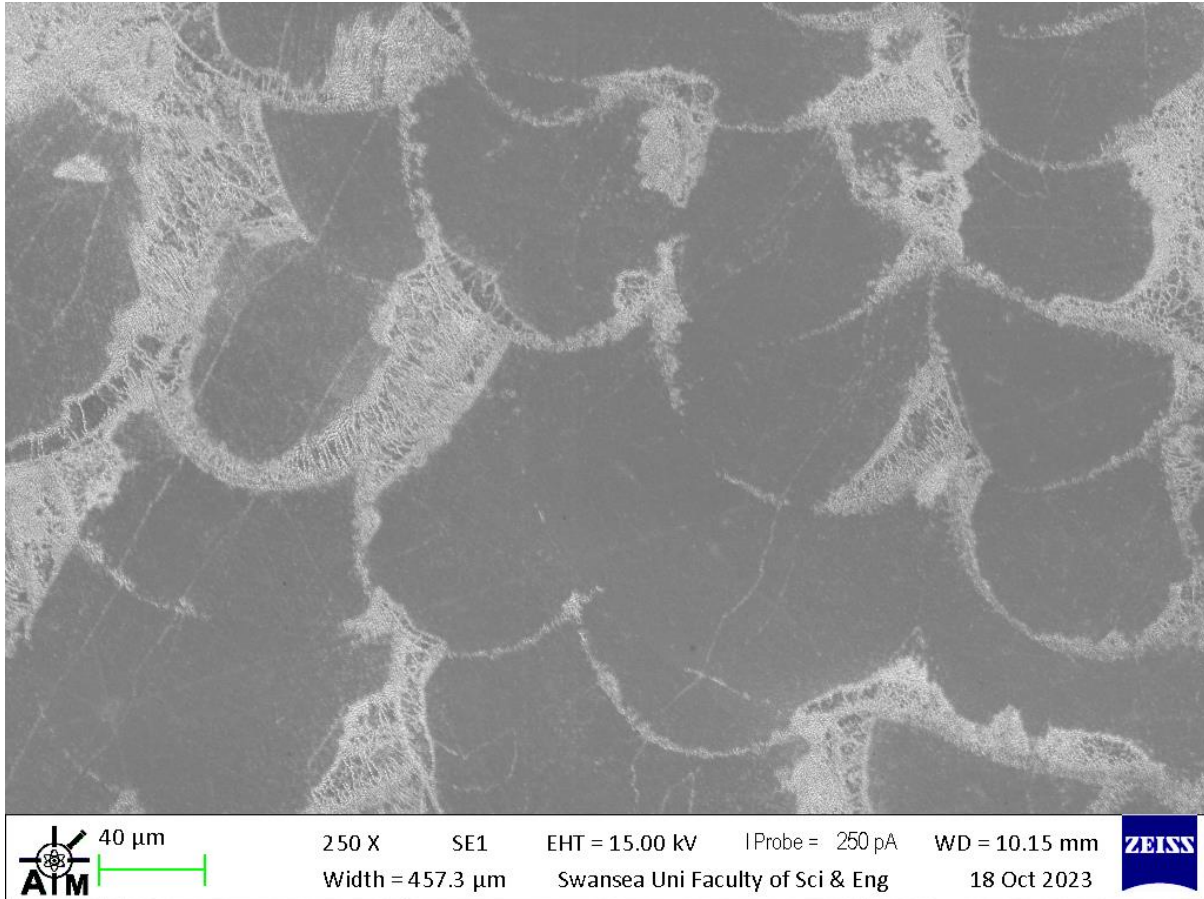


Figure 63 SEM micrograph of HEA1 produced by AM in the XZ plane

Figure 63 and Figure 64 depict SEM micrographs of a HEA1 specimen in the XZ and XY planes, respectively. After polishing and etching, the melt pools and laser paths become visible, the boundaries of which are contrastingly lighter in these images compared to the bulk. At these scales, it is still possible to distinguish the incredibly fine grain microstructures forming at these boundaries. Both these figures exhibit degrees of remelting, more obvious in Figure 64 where laser paths from subsequent layers intersect in varying directions with those tracks already created.

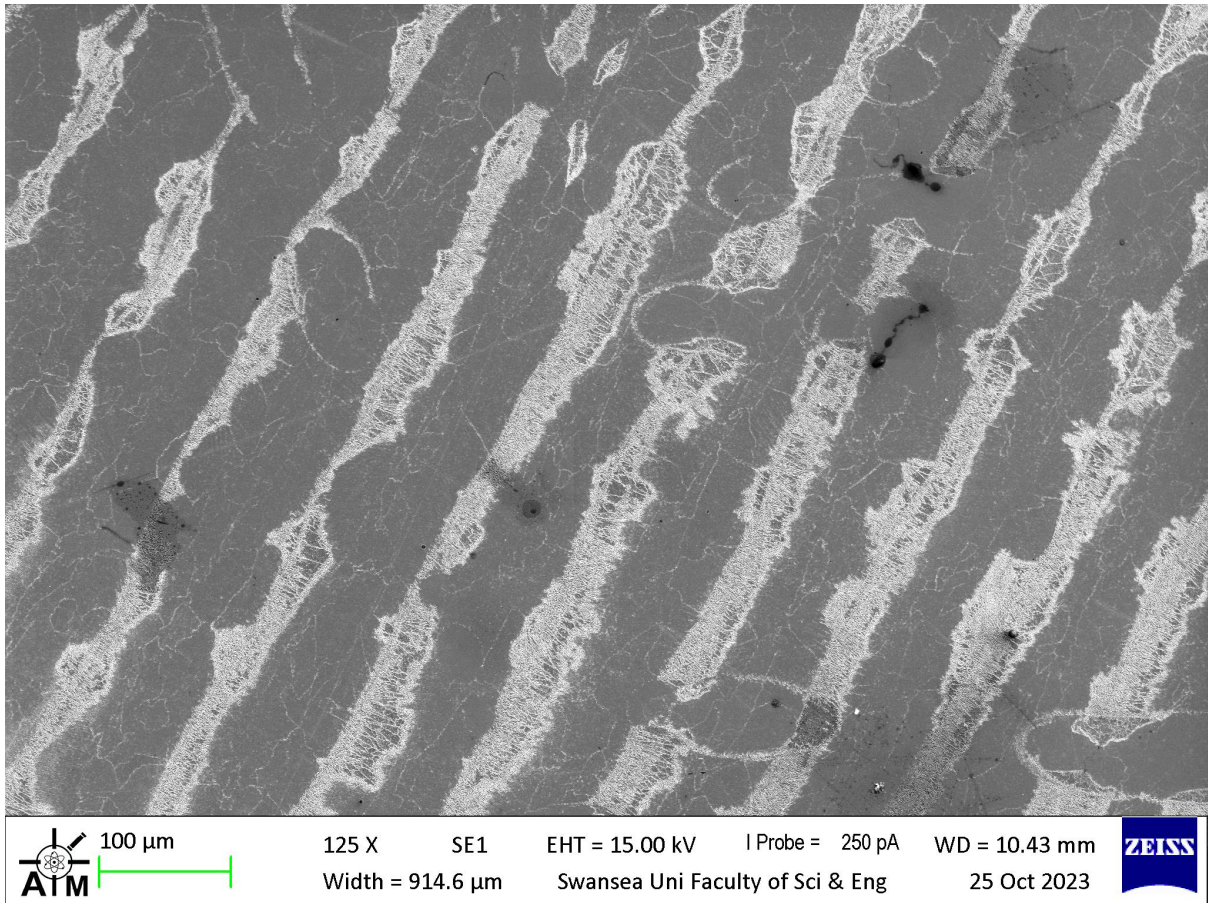


Figure 64 SEM micrograph of HEA1 produced by AM in the XY plane

This also demonstrates the hatch scanning pattern used in its production. Pores and hairline cracks are also detected in Figure 64, however, the congregation of many of these suggests more of a sample preparation issue than an outcome of the processing. Either way, there appears to be no correlation when observing at this scale that the location of defects tends to the laser path boundaries, nor are any observed at the melt pool boundaries seen in Figure 63.

EDS map analysis was applied to both these samples at 1000x magnification, specifically focusing on these areas; however, compositional distinctions were not apparent when evaluating the maps produced. The resultant EDS composition from these scans is shown in Table 42.

Point scans, as well as a linescan, were then acquired at 1000x and 2000x, respectively, to increase the likelihood of observing evidence of the hypothesised phase duality. The results of these are displayed in Figure 65, Table 43, and Figure 66, Table 44.

Table 42 Composition of AM HEA1 from EDS maps

| Element | Fe | Cr | Ni | Mn | Al | Si | N |
|----------|-------|-------|-------|-------|------|------|---|
| Weight % | 33.18 | 27.99 | 25.38 | 10.28 | 2.78 | 0.38 | 0 |

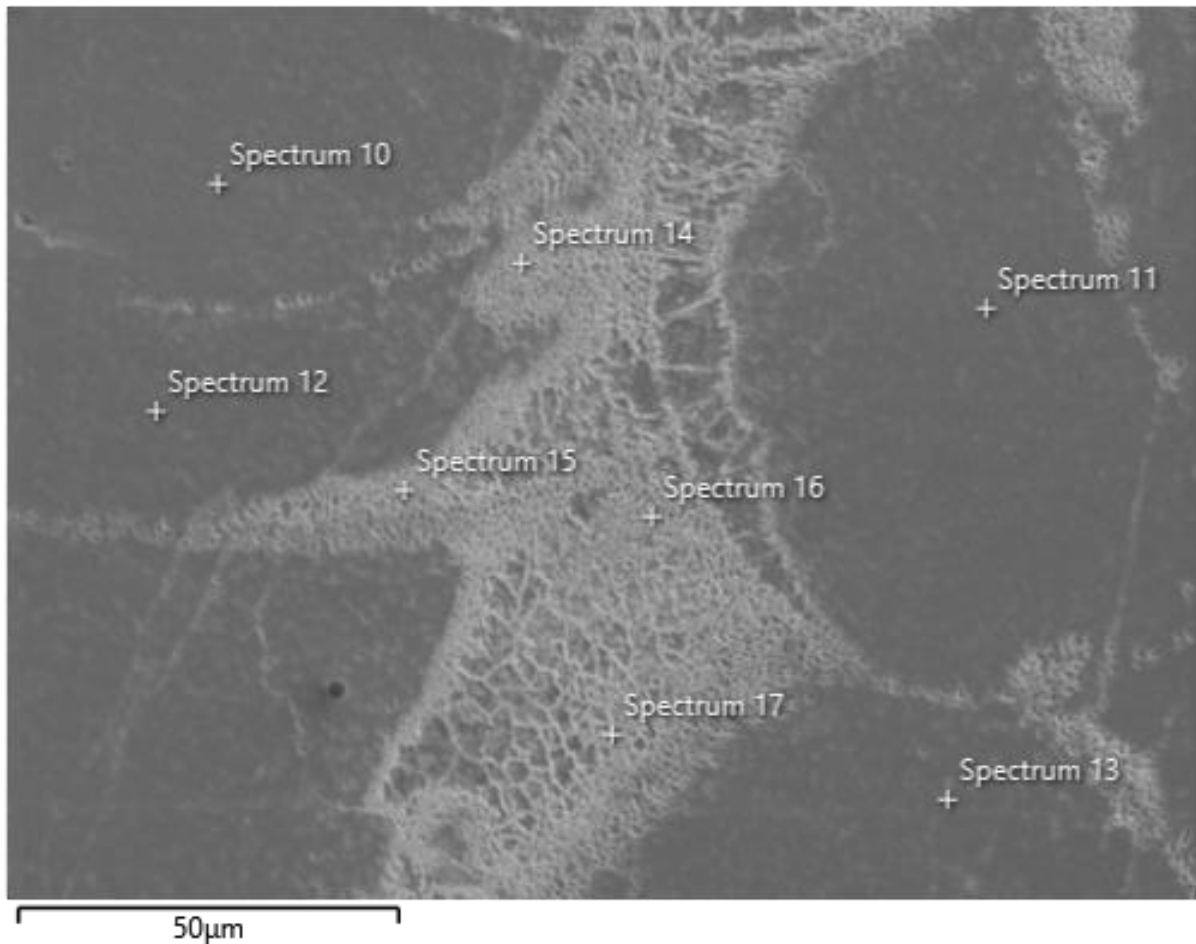


Figure 65 Point scan EDS for HEA1 AM XZ at 1000x magnification

Table 43 Summary of point scan EDS on HEA1 AM on the XZ plane (wt.%)

| Statistic | Fe | Cr | Ni | Mn | Al | Si | N | S |
|--------------------|-------|-------|-------|-------|------|------|------|------|
| Max | 33.99 | 29.02 | 26.33 | 10.39 | 4.09 | 0.45 | 0.65 | 0.06 |
| Min | 32.63 | 26.83 | 24.48 | 9.67 | 2.4 | 0.34 | 0 | 0 |
| Bulk Avg | 33.15 | 28.16 | 25.36 | 10.24 | 2.66 | 0.42 | 0.01 | 0.01 |
| Grain Avg | 33.37 | 27.93 | 25.17 | 9.95 | 2.97 | 0.38 | 0.22 | 0.03 |
| Average | 33.24 | 28.02 | 25.3 | 10.13 | 2.79 | 0.4 | 0.1 | 0.02 |
| Standard Deviation | 0.4 | 0.62 | 0.53 | 0.24 | 0.48 | 0.03 | 0.21 | 0.02 |

Table 43 outlines the results of the point scans undertaken in Figure 65, with minimal variation across the area investigated. The only point that differed significantly from the average was spectrum 15, with elevated values of Al and N to 4.09 % and 0.65 % by weight respectively. Whilst this does potentially indicate some AlN segregation, it is not at the magnitude expected of a precipitate.

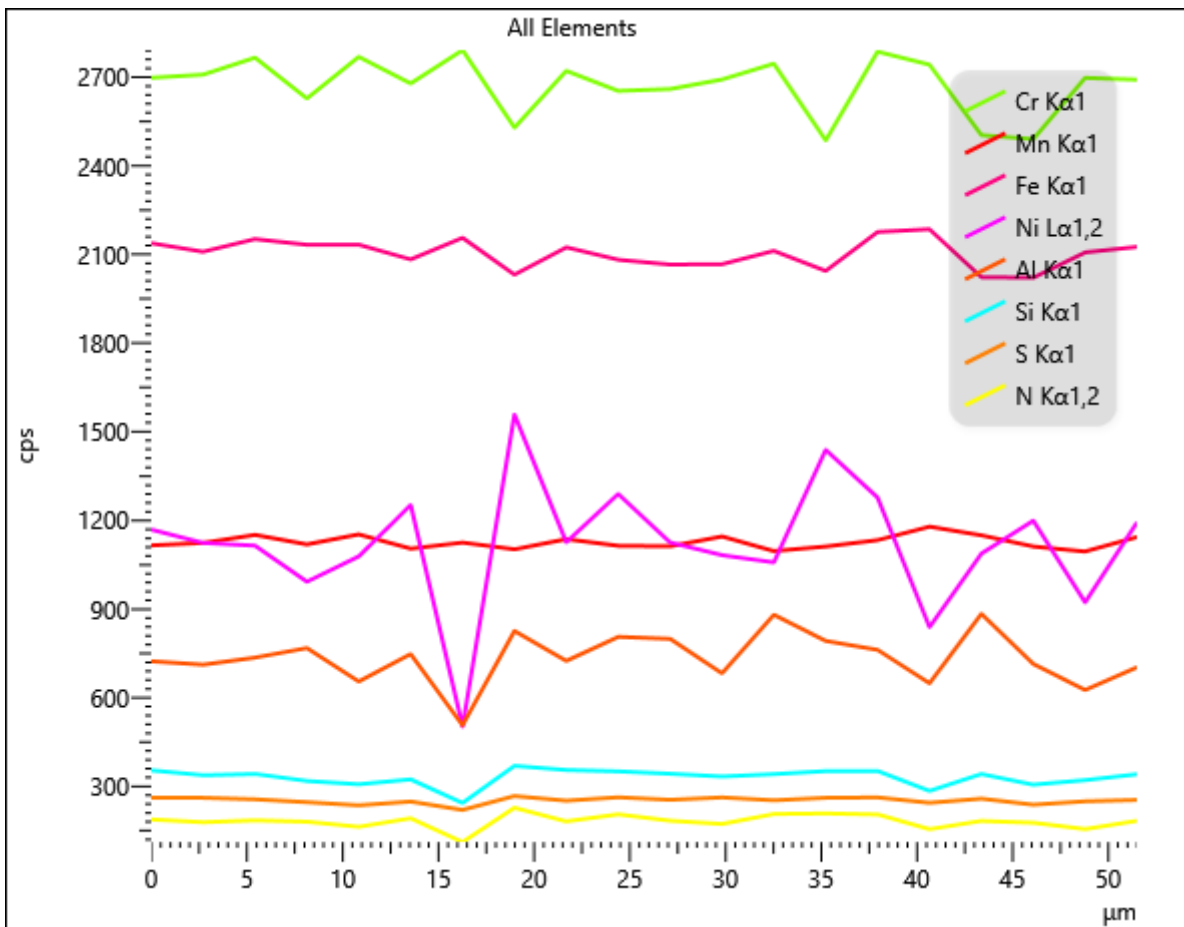
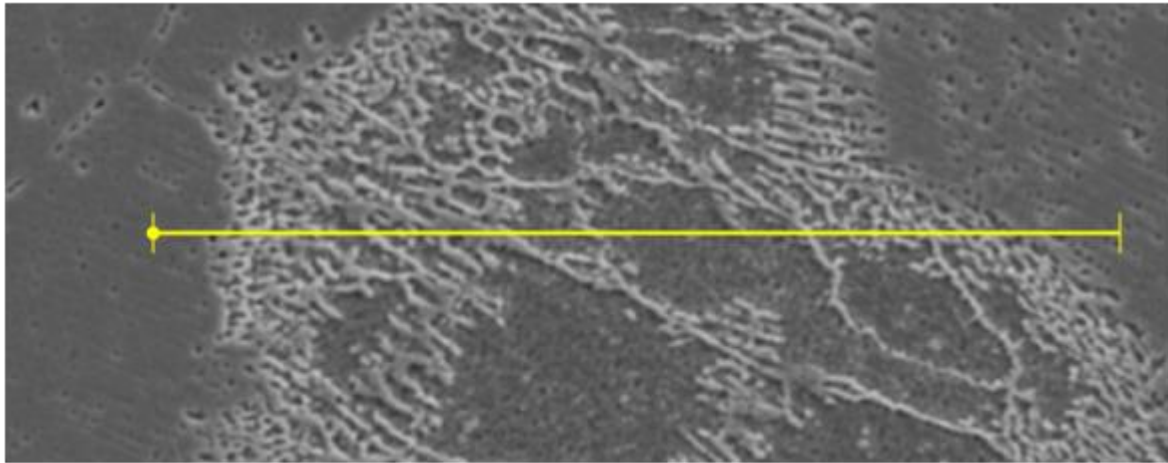


Figure 66 EDS linescan one HEA1 across a melt pool boundary at 2000x magnification

The linescan in Figure 66 occurs over a 53µm range which includes both the bulk and the melt pool grain boundaries observed in the previous SEM images. This was used in addition to the EDS maps and point scans to better ascertain whether there were any compositional variations across these boundaries that would indicate the existence of more than one phase. Whilst counts per second (cps) is not a direct measurement of composition, it does identify relative changes, hence it can be suggested that Ni has the least consistent composition across this line, with its variations being most clearly compensated for by changes Cr.

Table 44 Summary of linescan EDS on HEA1 AM on the XY plane (wt.%)

| Statistic | N | Al | Si | S | Cr | Mn | Fe | Ni |
|--------------------|------|------|------|------|-------|-------|-------|-------|
| Max | 0.13 | 3.59 | 0.47 | 0.07 | 29.43 | 10.96 | 34.19 | 27.08 |
| Min | 0.00 | 1.98 | 0.27 | 0.00 | 26.40 | 9.77 | 32.40 | 23.54 |
| Average | 0.03 | 2.76 | 0.38 | 0.01 | 28.06 | 10.20 | 33.31 | 25.25 |
| Standard Deviation | 0.04 | 0.38 | 0.05 | 0.02 | 0.86 | 0.26 | 0.48 | 0.91 |

As can be seen from Table 43 and Table 44, whilst compositional differences across both scans are observed, the magnitude of these variations are not significant enough to suggest the presence of multiple distinct phases.

6.7.2 Cast

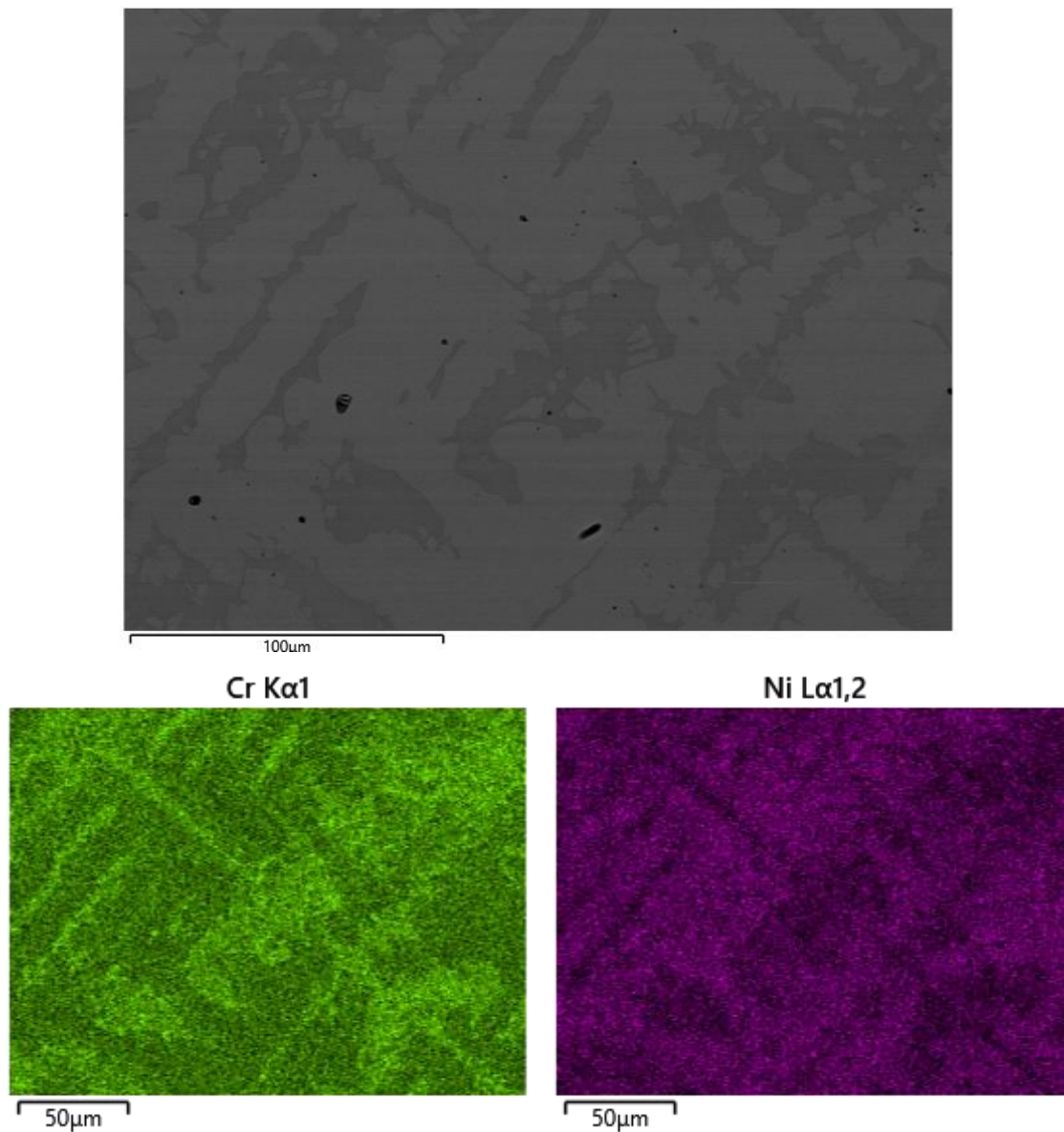


Figure 67 SEM BSD of cast HEA1 and accompanying EDS maps for Cr and Ni at 750x magnification

Table 45 Composition of cast HEA1 from EDS maps in Figure 67

| Element | Fe | Cr | Ni | Mn | Al | Si | N |
|----------|-------|-------|-------|-------|------|------|---|
| Weight % | 33.44 | 28.78 | 24.76 | 10.41 | 2.21 | 0.42 | 0 |

Figure 67 shows an SEM BSD image of cast HEA1 accompanied by Cr and Ni EDS maps of the same area. The BSD image shows two discrete phases; the bulk FCC phase appearing as the lighter region with the inverse is true for the BCC, which has a bi-directional dendritic formation that propagates through the bulk. The EDS maps indicate that the FCC phase is richer in Ni than the BCC, whereas the Cr has a higher abundance in the BCC. The composition of the area presented in Table 45 has a higher Cr and lower Ni wt.% than that expected of the bulk alloy, but that is likely due to the area investigated having a greater than average proportion of the Cr rich BCC phase. There are some surface defects present in Figure 67 however, these do not appear to present any compositional alterations at this magnification.

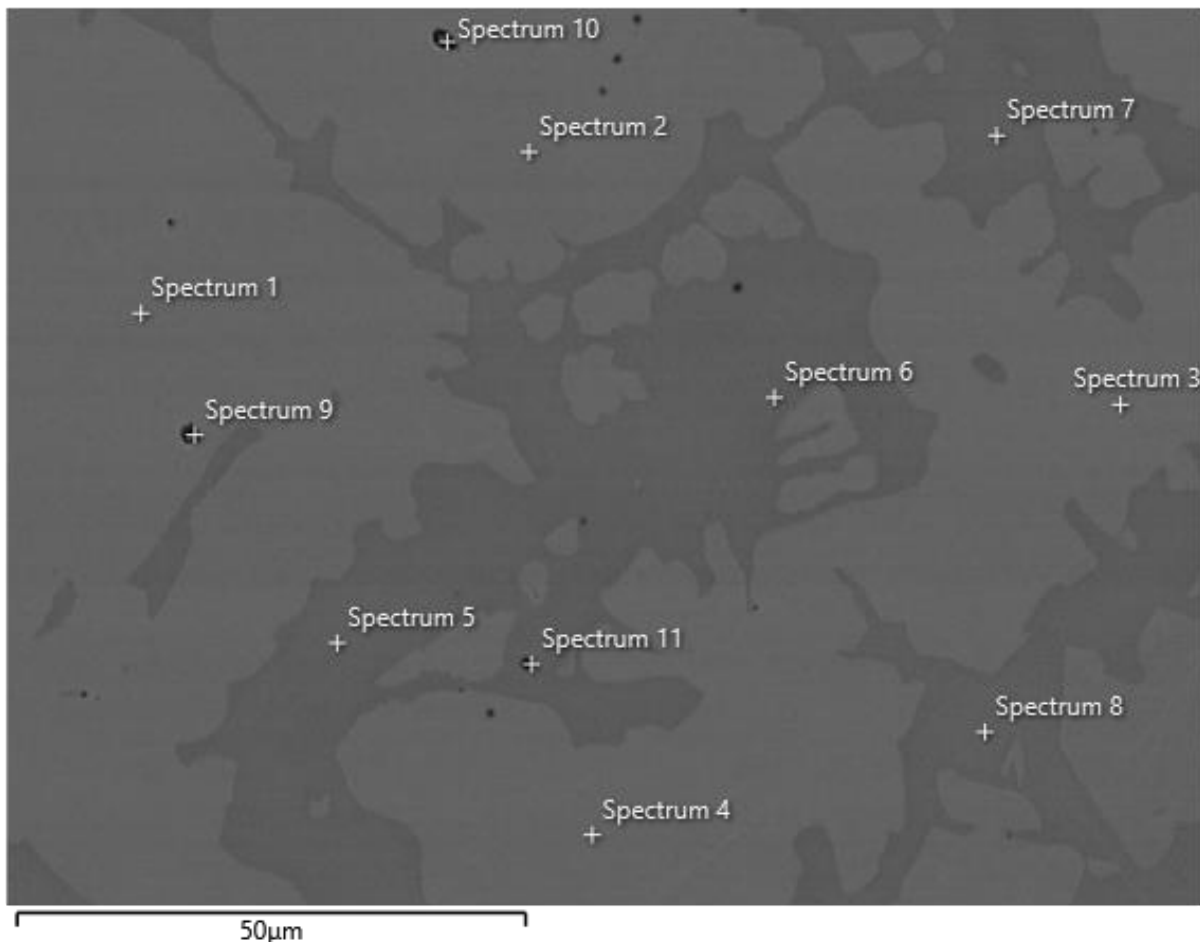


Figure 68 BSD EDS point scan map of cast HEA1 at 1000x magnification

Table 46 Point scan data for HEA1 cast in Figure 68 (wt.%)

| Region | Spectrum No. | Fe | Cr | Ni | Mn | Al | S | Si | N |
|--------------------|--------------|-------|-------|-------|-------|--------|------|-------|-------|
| FCC | 1 | 33.34 | 24.85 | 28.26 | 10.91 | 2.27 | 0.03 | 0.35 | 0 |
| | 2 | 34.28 | 25.07 | 27.27 | 10.74 | 2.21 | 0.01 | 0.42 | 0 |
| | 3 | 33.37 | 24.88 | 28.45 | 10.66 | 2.21 | 0.02 | 0.41 | 0 |
| | 4 | 33.41 | 24.8 | 28.43 | 10.71 | 2.26 | 0.02 | 0.36 | 0 |
| | Avg | 33.60 | 24.90 | 28.10 | 10.76 | 2.24 | 0.02 | 0.39 | 0.00 |
| FCC_L12 | ThermoCalc | 34.14 | 21.15 | 30.79 | 10.15 | 3.22 | 0 | 0.52 | 0.001 |
| BCC | 5 | 30.35 | 32.5 | 22.21 | 11.05 | 3.35 | 0.03 | 0.51 | 0 |
| | 6 | 38 | 41.78 | 11.41 | 7.41 | 0.92 | 0 | 0.48 | 0 |
| | 7 | 36.57 | 38.6 | 14.4 | 8.31 | 1.61 | 0 | 0.51 | 0 |
| | 8 | 30.77 | 31.12 | 23.57 | 10.86 | 3.24 | 0.01 | 0.43 | 0 |
| | Avg | 33.92 | 36.00 | 17.90 | 9.41 | 2.28 | 0.01 | 0.48 | 0.00 |
| BCC_B2 | ThermoCalc | 37.64 | 30.90 | 19.57 | 9.29 | 2.44 | 0 | 0.14 | 0.003 |
| BCC-B2#2 | ThermoCalc | 10.73 | 1.27 | 60.75 | 10.43 | 16.56 | 0 | 0.25 | 0 |
| Sigma | ThermoCalc | 38.85 | 42.63 | 3.63 | 14.89 | 0.0003 | 0 | 0.001 | 0 |
| Inclusion | 9 | 22.81 | 18.9 | 17.97 | 32.78 | 0 | 7.32 | 0.21 | 0.01 |
| | 10 | 25.1 | 21.92 | 34.38 | 15.58 | 2.39 | 0.1 | 0.52 | 0 |
| | 11 | 31.04 | 40.53 | 14.98 | 9.16 | 3.61 | 0 | 0.69 | 0 |
| | Avg | 28.22 | 29.34 | 21.31 | 16.73 | 2.07 | 1.86 | 0.48 | 0.00 |
| Max | | 38 | 41.78 | 34.38 | 32.78 | 3.61 | 7.32 | 0.69 | 0.01 |
| Min | | 22.81 | 18.9 | 11.41 | 7.41 | 0 | 0 | 0.21 | 0 |
| Average | | 31.73 | 29.54 | 22.85 | 12.56 | 2.19 | 0.69 | 0.44 | 0 |
| Standard Deviation | | 4.52 | 7.88 | 7.3 | 7.02 | 1.06 | 2.2 | 0.12 | 0 |

Point scans were taken from both the major phases as well as the inclusions to quantify the magnitude of the compositional variations exhibited in Figure 67. The locations of these point scans and their relevant compositions are outlined in Figure 68 and Table 46 respectively. The compositions of relevant phases predicted by Thermo-Calc are added for ease of comparison. The FCC scans returned consistent compositions with only minimal deviations, which is to be expected, whereas the BCC phase presents more inconsistency across the scans, with Cr and Ni being the most volatile. The maximum and minimum values of these elements differ by 10.66 wt.% and 12.16 wt.%, respectively, which is significant considering the points analysed appear to be located in the same phase. Even so, the BCC points all display higher Cr and lower Ni abundance than the average; therefore, points 1-8 concur with the assumptions made that the FCC phase is rich in Ni and depleted in Cr, the inverse being true for the BCC. Points 6 and 7 deviate from the trends set by 5 and 8, with an increase in Fe observed alongside reductions in Mn and Al. These variations suggest a σ or secondary BCC phase, however, there is no visual evidence in Figure 68 to advocate this.

The inclusions investigated by points 9-11 show 3 distinct compositions. Spectrum 9 shows reduced levels of all elements with 0 wt.% Al, as well as significant increases in Mn and S, indicating a MnS inclusion. Spectrum 10 again shows reduced readings of Fe and Cr, with the largest Ni level shown across the 11 points, and a rise in Mn, although not to the same magnitude as that in spectrum 9 and no rise in S is recorded. Spectrum 11 however, exhibits a similar trend in composition as that of the proposed secondary BCC phase, which could indicate that the point overlaps the boundary between the inclusion and the phase it resides in.

6.7.3 CR

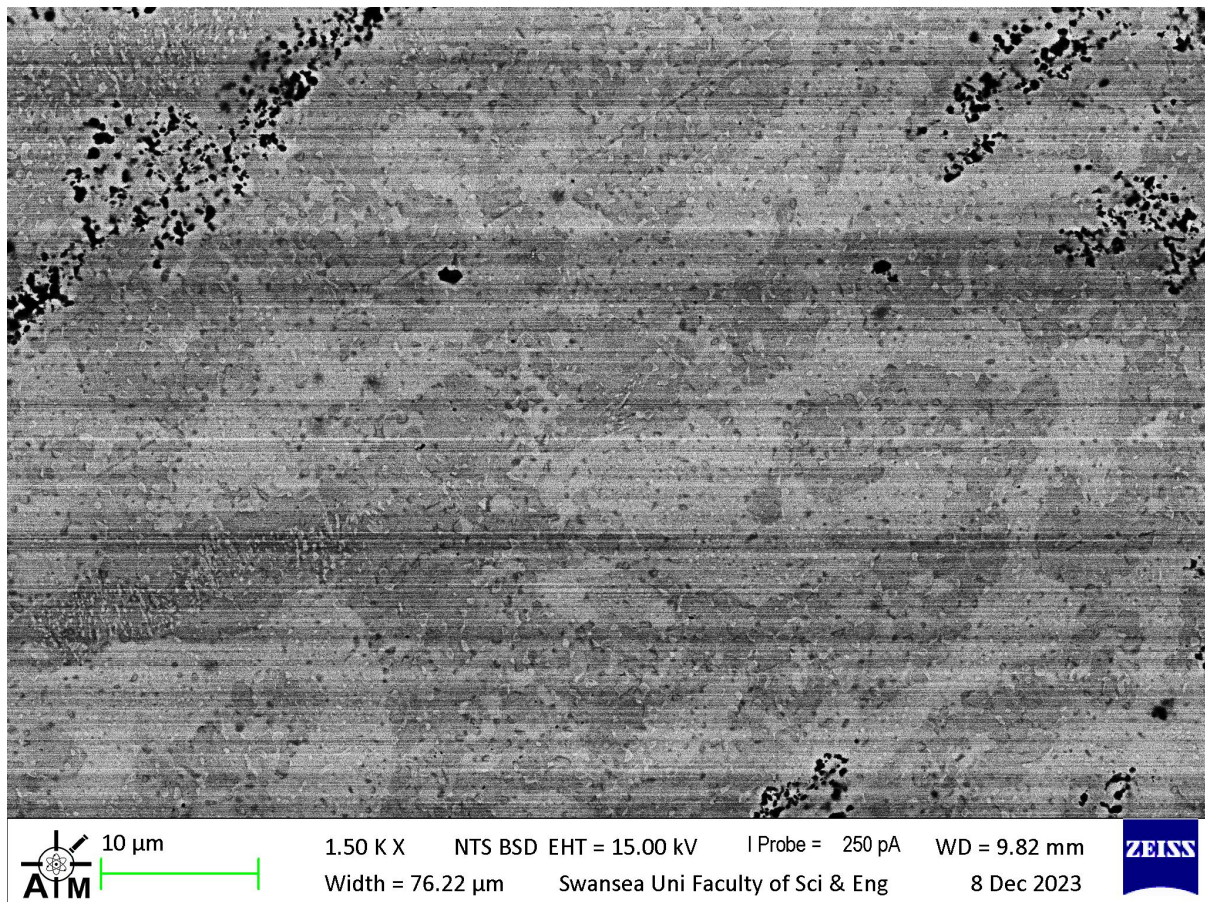
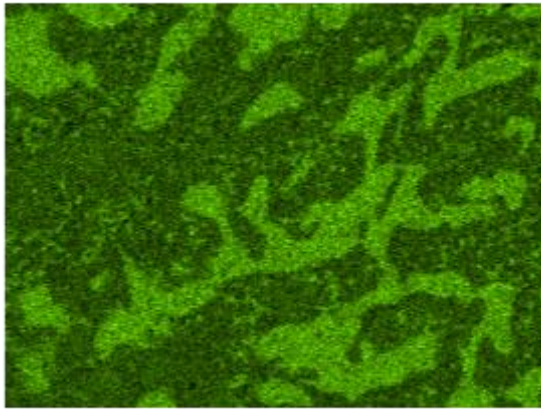


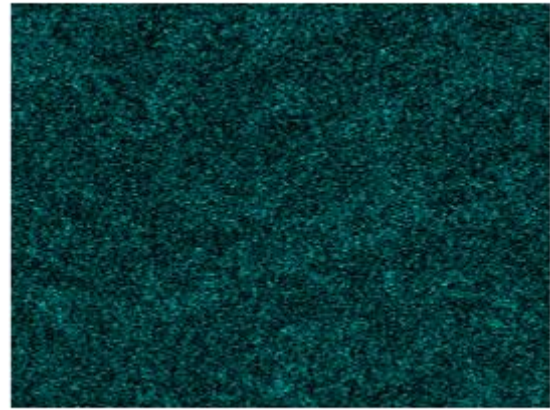
Figure 69 BSD SEM of CR HEA1 at 1500x magnification

Figure 69 shows a BSD SEM image of CR HEA1 with two clear phases present, light and dark, with what appears to be process induced defects in the top corners of the image. The formation of the two main phases has less of a dendritic pattern than that of the cast sample displayed in Figure 67, with no obvious directionality. Speckling is also observed at this magnification across both phases with no obvious arrangement. EDS maps were conducted on the area to initially distinguish any compositional variations and are presented in Figure 70. The maps produced appear to have shifted approximately 20 μm upwards compared to the image in Figure 69.

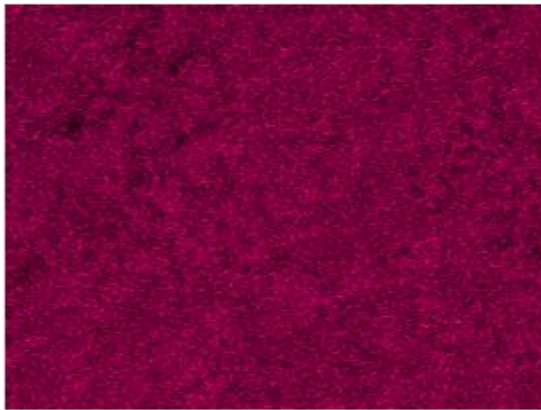
Cr K α 1



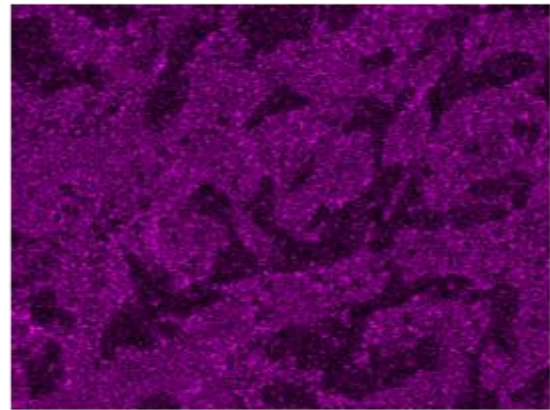
Si K α 1



Fe K α 1



Ni L α 1,2



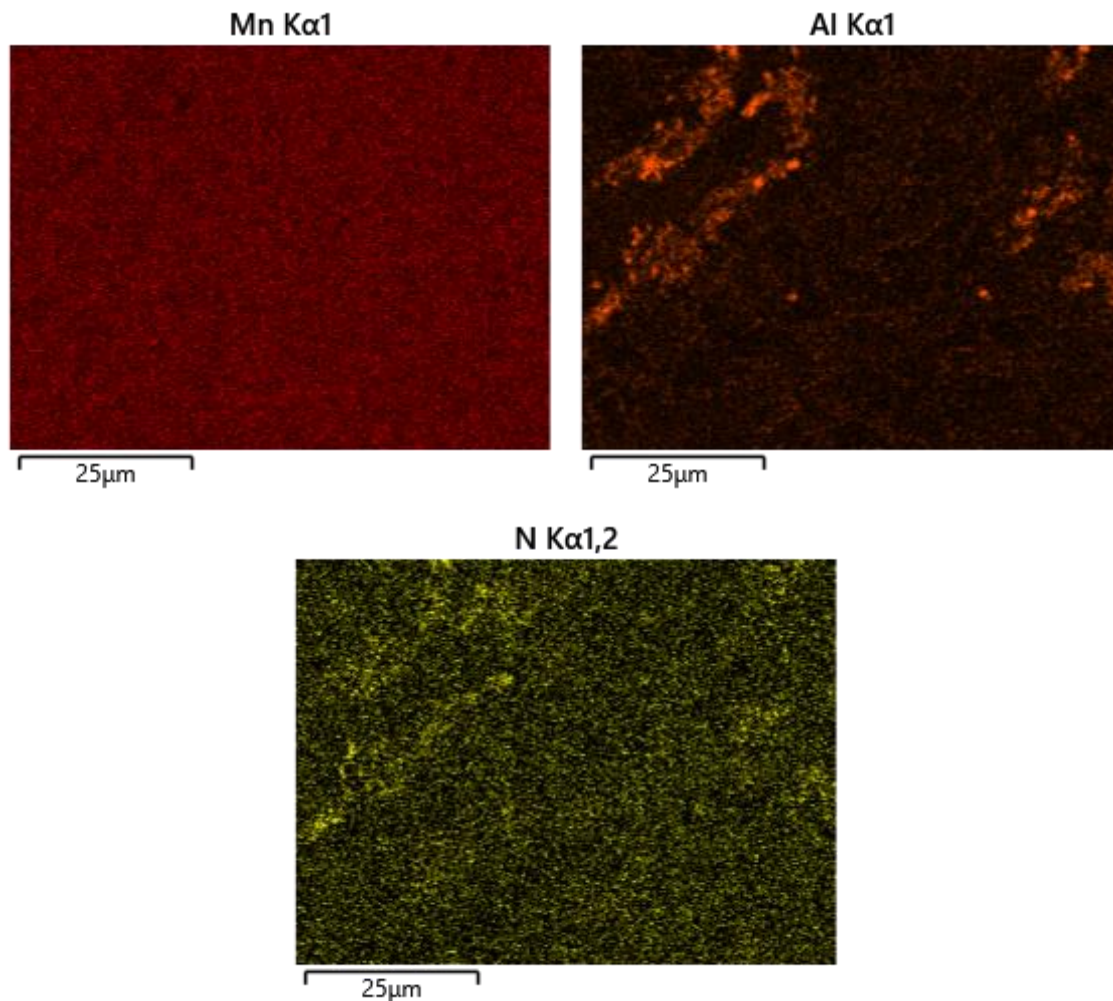


Figure 70 EDS maps of CR HEA1 area in Figure 69

As seen in the cast EDS maps for HEA1 in Figure 67, the abundance of Cr and Ni invert each other, with the former segregating to the lighter BCC phase and the Ni to the darker FCC. Si and Fe also appear to preferentially tend to the BCC; however, compared to the Cr and Ni, the contrast is unsubstantial. The areas previously designated as a processing defect appear significantly richer in Al and N than the bulk material, with Al also appearing to favour the FCC phase.

Table 47 Composition of CR HEA1 from maps in Figure 70

| Element | Fe | Cr | Ni | Mn | Al | Si | N |
|-----------------|-------|-------|-------|------|------|------|------|
| Weight % | 33.01 | 28.05 | 25.54 | 9.62 | 3.17 | 0.48 | 0.13 |

The Al concentration in Table 47 is higher than expected in HEA1; however, this is likely due to the large amounts of what appears to be AlN present in the area chosen for investigation and is, therefore, not totally representative of the bulk alloy.

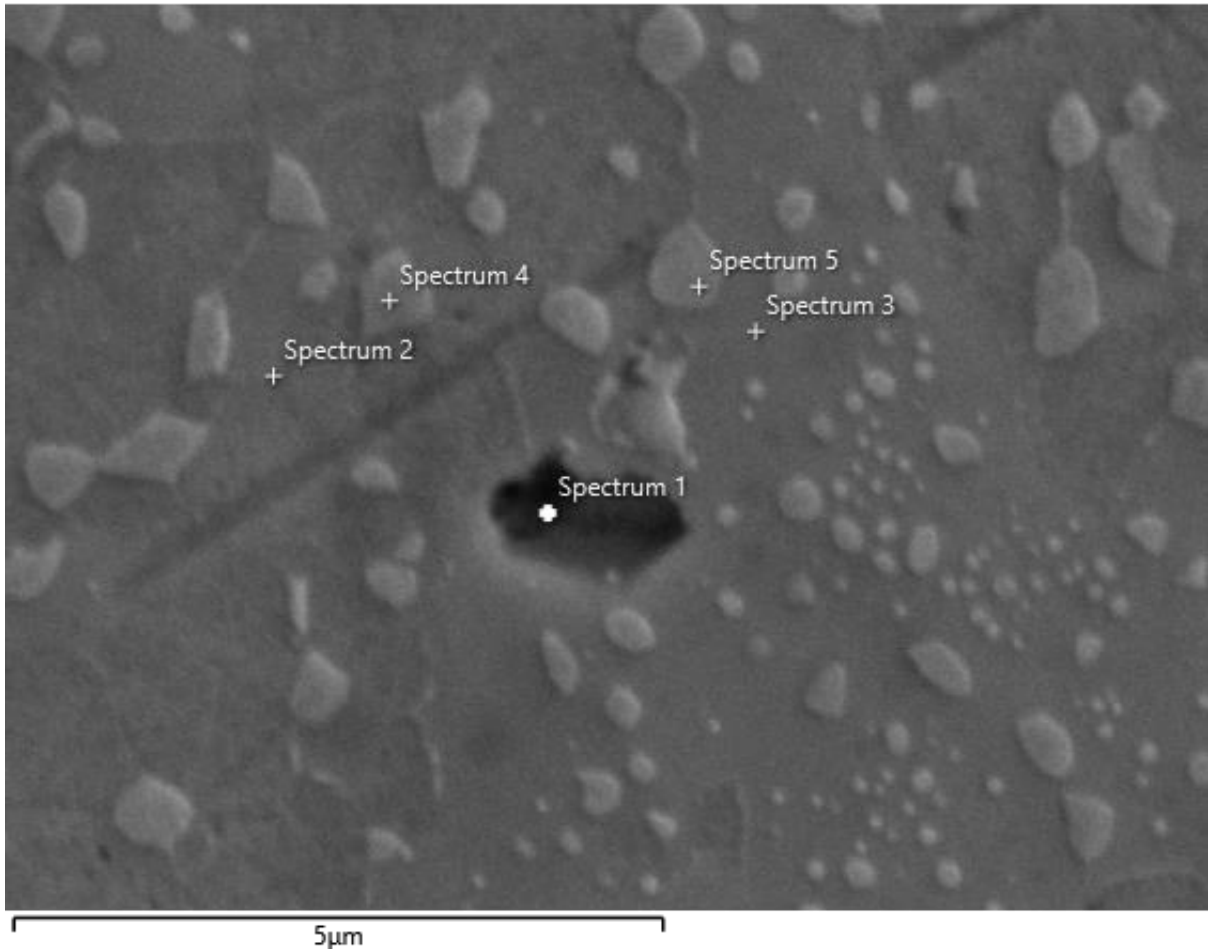


Figure 71 EDS point scan map of CR HEA1 at 12.6kx magnification

Table 48 Composition summary of CR HEA1 point scans in Figure 71 (wt.%)

| Spectrum No. | Fe | Cr | Ni | Mn | Al | N | Si |
|---------------------------|-------|-------|-------|-------|-------|------|------|
| 1 (Inclusion) | 27.09 | 17.05 | 21.94 | 8.11 | 18.84 | 6.74 | 0.21 |
| 2 (FCC) | 32.29 | 26.59 | 27.99 | 10.18 | 2.39 | 0.12 | 0.44 |
| 3 (BCC) | 35.63 | 40.4 | 14.2 | 8.08 | 0.97 | 0 | 0.73 |
| 4 (FCC Inc) | 20.1 | 18.82 | 40.28 | 12.64 | 7.83 | 0 | 0.34 |
| 5 (BCC Inc) | 18.94 | 12.31 | 45.86 | 13.69 | 8.71 | 0.22 | 0.28 |
| Max | 35.63 | 40.4 | 45.86 | 13.69 | 18.84 | 6.74 | 0.73 |
| Min | 18.94 | 12.31 | 14.2 | 8.08 | 0.97 | 0 | 0.21 |
| Average | 26.81 | 23.03 | 30.05 | 10.54 | 7.75 | 1.42 | 0.4 |
| Standard Deviation | 7.33 | 10.99 | 13 | 2.57 | 7.05 | 2.98 | 0.2 |

Point scans were taken at 12.6kx magnification at the locations shown in Figure 71, with the compositions presented in Table 48. The image shows in more detail the speckling previously mentioned within the phases. At this scale, a clearer pattern is observed, with these speckles/inclusions located in both phases, but with different structures. The inclusions that appear within the BCC appear small and with more sphericity, whereas those in the FCC are larger with a more

angular geometry and well as what seems to be links or grains between them. The inclusion analysed by spectrum 1 reveals lower elemental concentrations across Fe, Cr, Ni, Mn and Si, but dramatic increases in Al and N. The increase in Al and N would suggest the presence of an AlN inclusion; however, the existence of other alloying elements in the spectrum contradicts this assumption. Nevertheless, it is predicted that this area is that of an AlN inclusion, with the detector identifying regions both beneath and around the point that represents the bulk alloy. The perceived FCC phase investigated by spectrum 2 only shows minimal compositional differences to that of the bulk in Table 47, whereas spectrum 3 shows elevated levels of Fe, Cr and Si with reductions of Ni, Al and Mn. Levels of Cr and Al of > 40 wt.% and <1 wt.%, respectively, however, could indicate the presence of the σ phase outlined in Table 39 as it correlates with similar compositional tendencies. The inclusions inspected by points 4 and 5 exhibit similar trends, with elevated concentrations of Ni, Mn and Al, with noticeable declines in Fe and Cr. Whilst the exact compositions do not match perfectly with the Thermo-Calc predictions in Table 39 for the BCC_B2#2 phase, the tendencies observed do match with those presented by these points.

6.8 Corrosion Testing

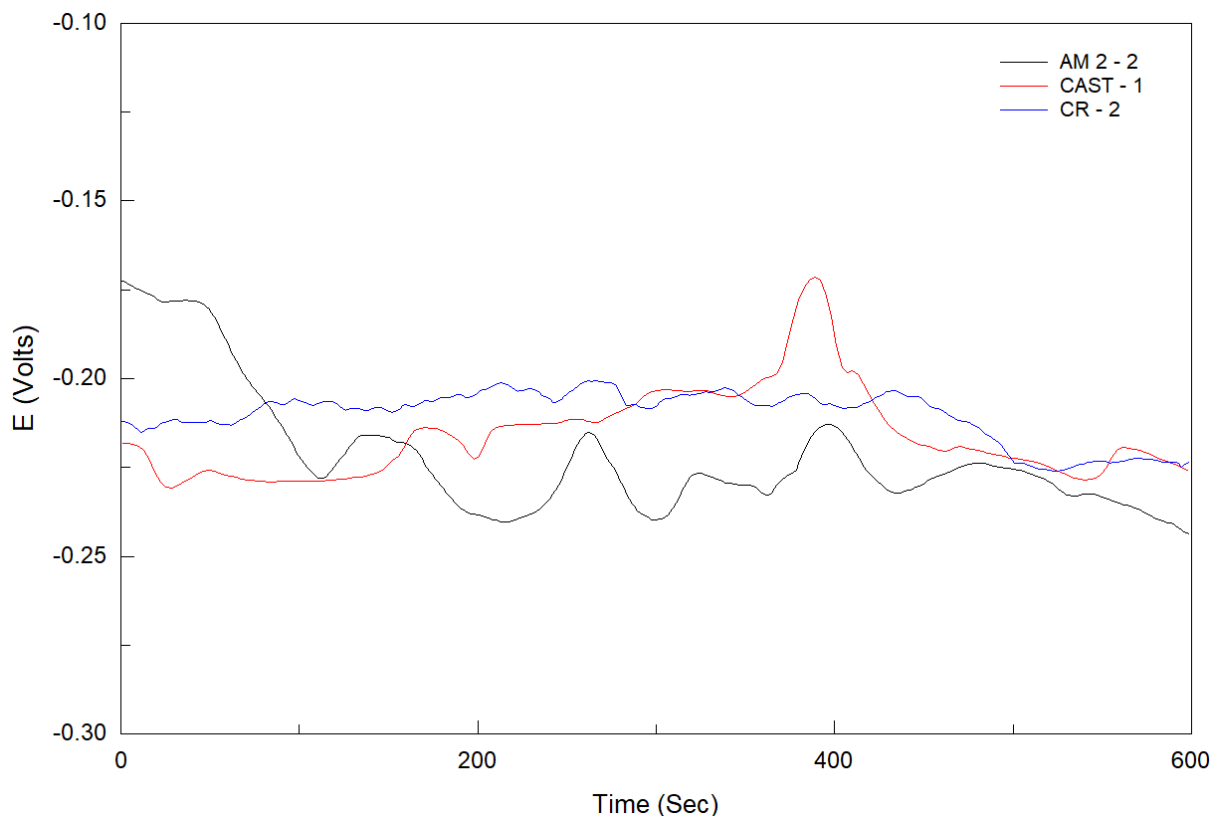


Figure 72 OCP plots for HEA1 AM, cast and CR over 600s

Table 49 Summary of HEA1 corrosion data for each manufacturing method

| Sample | Optical Density (%) | Avg OCP (V) | Error (SD) | Avg E_{corr} (V) | E_{corr} (SD) | Avg E_{pit} (V) | E_{pit} (SD) | Avg E_r (V) |
|--------|---------------------|-------------|------------|--------------------|-----------------|-------------------|----------------|---------------|
| AM 2 | 99.47 | -0.291 | 0.059 | -0.289 | 0.060 | 0.006 | 0.037 | -0.242 |
| Cast | 96.25 | -0.243 | 0.046 | -0.227 | 0.042 | 0.071 | 0.183 | -0.274 |
| CR | 97.95 | -0.212 | 0.019 | -0.207 | 0.017 | -0.049 | 0.068 | -0.342 |

The modal OCP plots for HEA1 AM, cast and CR presented in Figure 72 were selected because their repeats offered little to the graph, as the OCP values extracted and profiles of the plots had limited deviation. The most stable sample by OCP value is that of the CR samples, followed by the cast, as their readings were less anodic and, therefore, more noble AM sample 2 data. This is mirrored by the smoothness of the equilibrium plots, with the CR samples offering the least deviation from the normal across the duration of the scans, whereas the AM samples exhibited multiple peaks and troughs. The repeatability of the CR OCP was also the greatest, with a standard deviation of 0.019 followed by cast at 0.059, further establishing this conclusion.

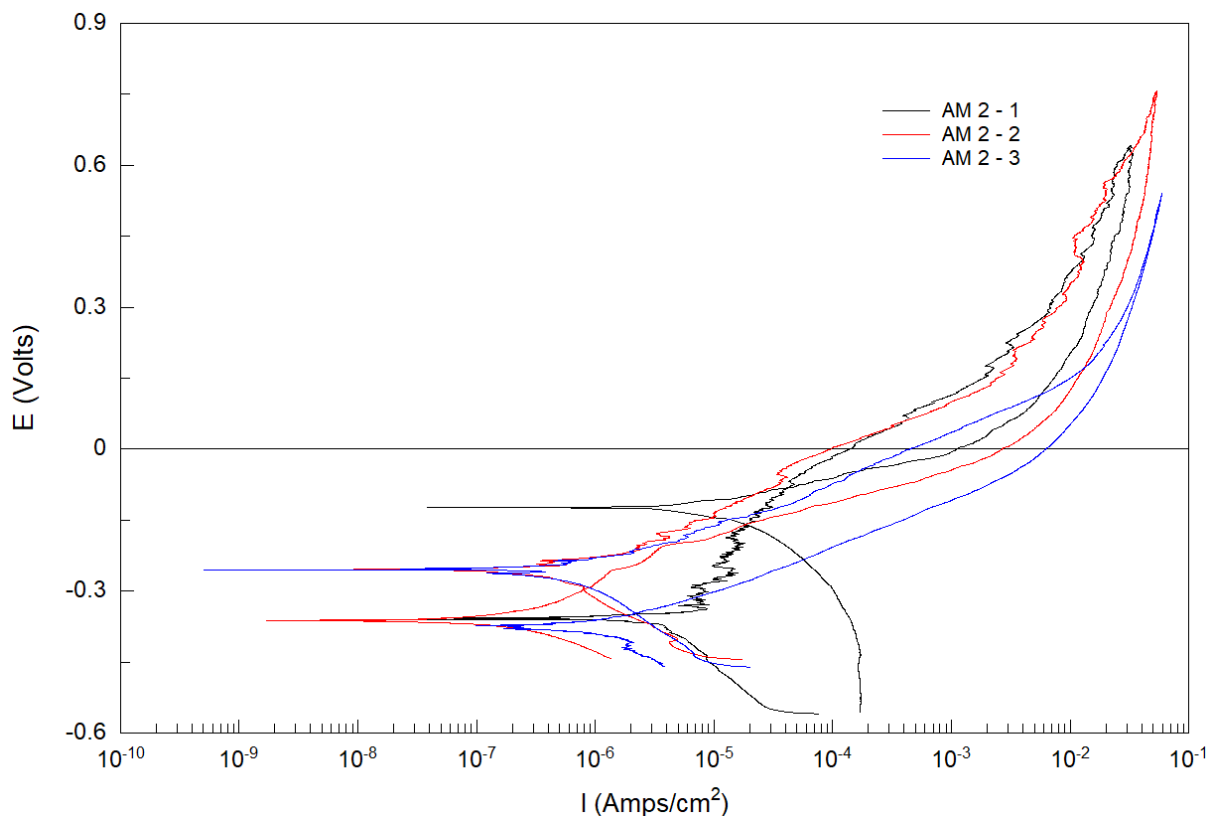


Figure 73 Cyclic polarisation plots for HEA1 AM, sample 2

The E_{pit} values are more difficult to distinguish in the HEA plots compared to those of 316L, as more often than not, there is no distinct pit where the current rapidly increases, caused by a minimal rise in potential. Due to the limited passivation seen in these curves and the lack of any clear pitting corrosion occurring, 0.0002 A was designated as the point at which the potential across these scans could be

compared, as this is greater than the current expected at most E_{pit} . This point will still be referred to as E_{pit} .

Figure 73 shows that the AM repeats 2 and 3 have an almost identical E_{corr} at -0.254 V and -0.255 V, respectively, whereas AM 1's is 0.105 V below. This is a possible justification as to why the passive region after AM 1 has reached its E_{corr} is more established, because the passive layer that does form can protect the pitting sites up until a less negative potential. Repeats 2 and 3 follow similar profiles after E_{corr} is reached, with only brief indications of metastable pitting, suggesting that as the potential approaches 0, the passive layer is too feeble to protect the corroded sites. It is difficult to appoint a potential where the E_{pit} was reached across all 3 scans, and therefore, using the predesignated current, the average E_{pit} was calculated as 0.006 V. On analysing the other extracted data, one promising statistic that is revealed is the minimal level of error affecting the E_{pit} values, with a standard deviation of 0.037, the lowest of the 3 manufacturing routes.

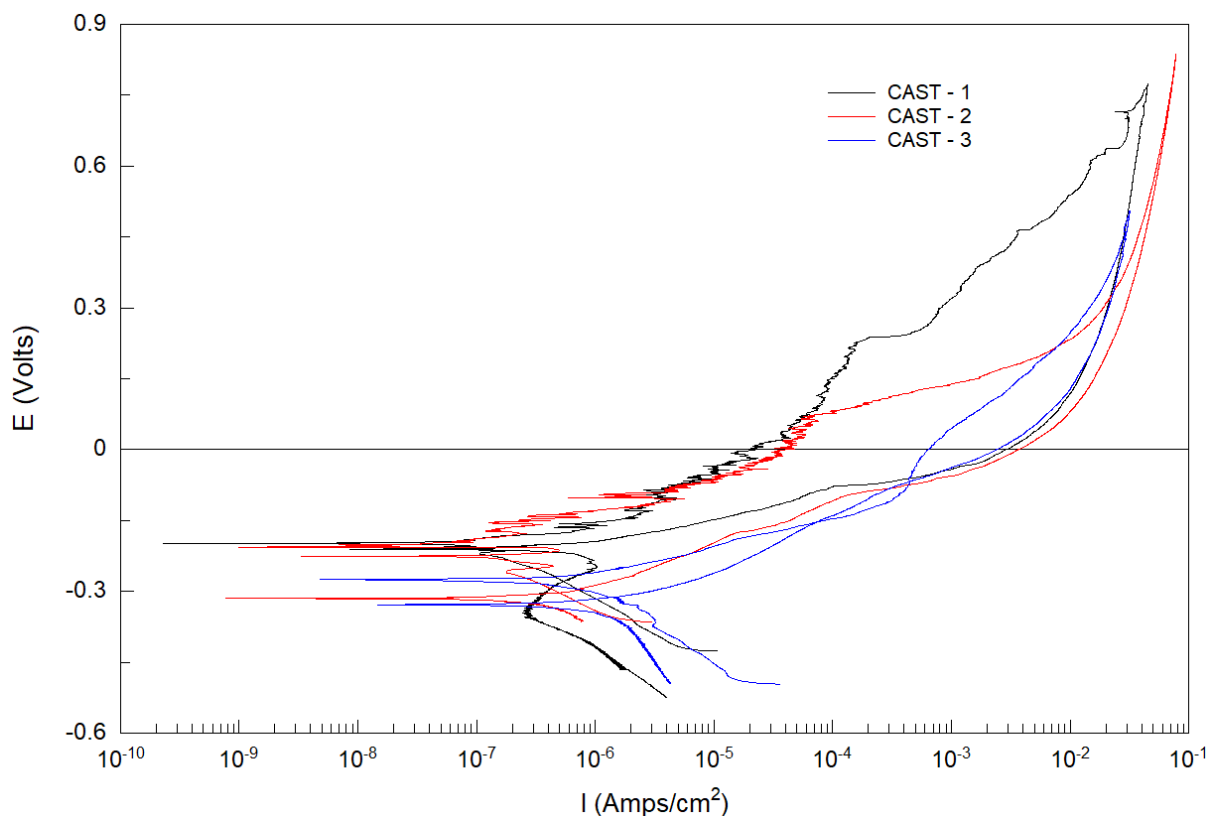


Figure 74 Cyclic polarisation plots for cast HEA1

The cast samples CP results shown in Figure 74 offer both similarities and differences to those seen with the AM results. The overall profile of the CP scans follows a comparable trend. However, a passive phase is more distinguishable in the cast scans when compared, with casts 1 and 2 exhibiting clear metastable pitting between their respective E_{corr} and E_{pit} values. They also present clear points on their scan profiles where the E_{pit} is reached at 0.238 V and 0.1 V, respectively. The reliability of these results

is, however, questioned when the third sample is considered, with no passivity or clear E_{pit} shown, and a much lower value for E_{pit} when defined by a current of 0.0002 A of -0.125 V. This raises the overall standard deviation to 0.183 as presented in Table 49.

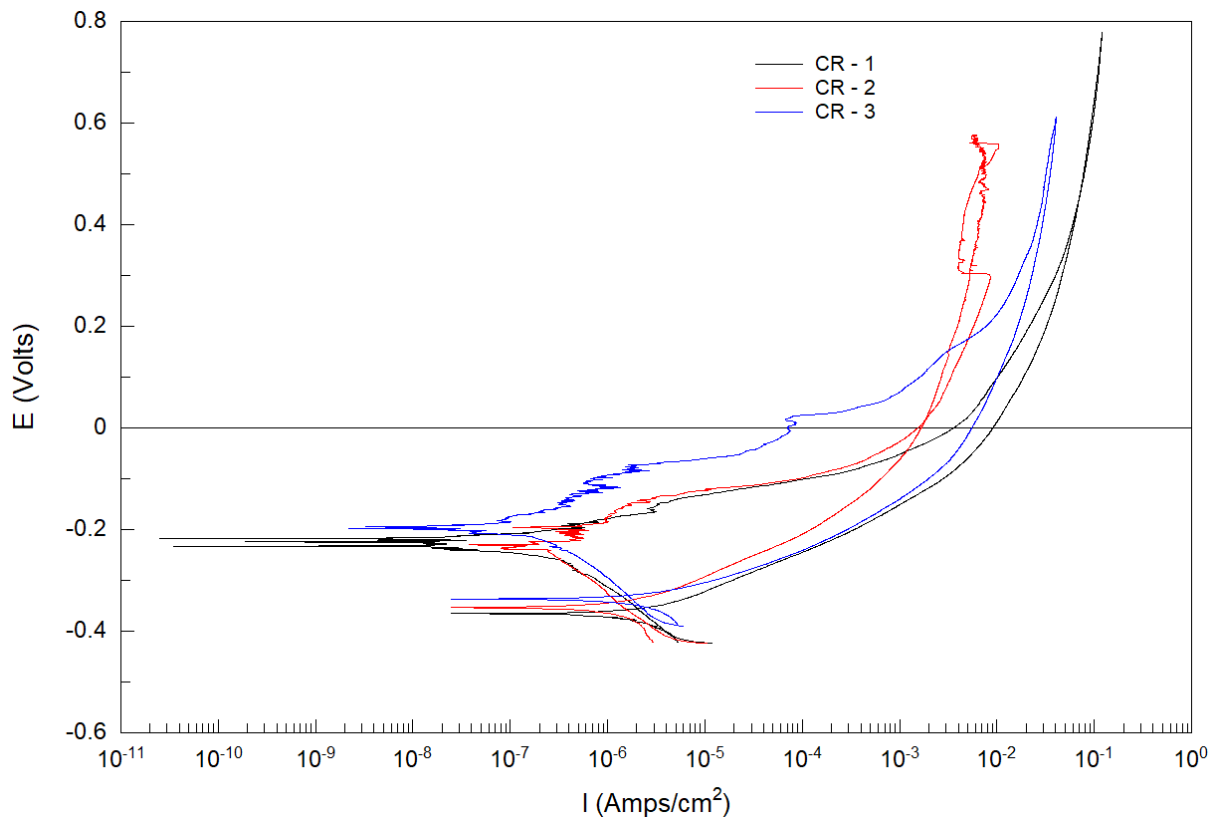


Figure 75 Cyclic polarisation plots for CR HEA1

The CR scans in Figure 75 have the lowest deviation of E_{corr} values across the 3 manufacturing methods at 0.017 as well as the most consistent E_r , with a deviation of 0.013. Tests 2 and 3 follow very similar profiles throughout the scans with E_{pit} values within 0.008 V; however, both of these values were extracted at the nominated current due to a lack of an obvious E_{pit} . This, added to the observation that both scans, whilst showing some signs of passive layer formation, showed a minor metastable pitting and only for a short duration, suggests that the passive oxide that did form was weak and easily broken down by increasing the potential. The first test, however, showed more promise with a stronger passive phase indicated by a larger potential difference between the E_{corr} and E_{pit} , and a more identifiable E_{pit} . Whilst this E_{pit} value was 0.118 V higher than the other repeats, it still resulted in the CR samples having the worst average E_{pit} of the 3 manufacturing methods.

6.9 Discussion

The investigation into the reproducibility of HEA1 AM parts showed that, irrespective of build location and suboptimal build conditions, high density > 99.3 % was achieved across 8/9 samples. The optical density results in Table 38 reveal much more significant porosity observed in the cast and CR samples in comparison to the AM. It is noted that the density of the CR sample is greater than that of the cast, and whilst the cast samples that were taken through the thermomechanical stages were not the same as the cast, this would indicate that the cold rolling process has eliminated some of the porosity present.

One of the key effects of HEAs outlined in literature is the high entropy effect, as it improves the formation of solid solutions and reduces the likelihood of intermetallics forming. The specific composition achieved for HEA1 when simulated in Thermo-Calc does not appear to benefit from this, with a large φ_i of an σ phase forming at temperatures 1193 °C and below. The XRD major phase proportions outlined in Table 41 display high proportions of FCC achieved for all 3 manufacturing routes (>86 %). However, that does not take into account the CR peaks from 39 ° to 52 °. Some literature suggests that these could be a Cr rich σ phase, similar to the one outlined by the Thermo-Calc predictions [119]. The greater number of peaks in the CR XRD spectra is likely a result of the thermomechanical processes undergone, with heat treatments at 1080 °C and 900 °C creating FCC_L12/ σ and FCC_L12/ σ /BCC_B2#2 microstructures, respectively. The compositional homogeneity and microstructure of the 3 manufacturing processes differ greatly, with the AM route exhibiting a largely uniform composition with only minor differences realised. These variations are likely small due to the rapid heating and cooling experienced during LPBF, preventing elements from diffusing into separate phases [196–198]. Contrastingly, the cast and CR samples show clear phase separation in SEM images in Figure 64 and Figure 65, with unmistakable elemental segregation into phases observed in their EDS maps in Figure 63 and Figure 66, the FCC of which exhibits increased Ni and lower Cr, the inverse of which is true for the BCC. The FCC provides consistent compositions across the majority of point scans in these areas. However, the BCC presents much more instability, with Cr ranging from 31.12 wt.% to 41.78 wt.%, the latter of which is outside the range predicted by Thermo-Calc for the BCC_B2 which has a maximum forecast Cr concentration of 36.92 wt.% at 1193 °C. This, therefore, suggests the presence of a third phase belonging to either BCC_B2#2 or σ . Based on the overall compositions detected at the points of high Cr, for example, spectrum 6 in Table 46 shows high Fe and Cr, and low Ni and Al correlating with the σ prediction in Table 39; however, the Mn concentration is also noticeably lower, whereas the table suggests it should have increased by approximately 30 %. This could be due to cooling conditions present in the cast sample, the heat treatments in the CR, and possibly a lack of mobility often associated with HEAs [91,92,104]. However, based on the balance of

probability and literature attributing the unidentified peaks to σ , the likelihood is that it does indeed belong to the σ phase, provided it is not just a compositional variation of the BCC_B2. Inclusions of MnS are also detected in the cast HEA1 sample, and whilst they are not in the area investigated during the CR analysis, it is unlikely they are not also present there. The inverse is also true when considering the AlN identified in the CR sample during point scan analysis in Table 48. The BCC_B2#2 predicted is more obvious in the CR sample, with the inclusions defined by spectrums 4 and 5 in Table 48 correlating with the Ni/Al rich and Fe/Cr depleted composition predicted by Thermo-Calc.

The number of defects present on a metal's surface significantly impacts its corrosion resistance. Defects are not limited to porosity but extend to imperfections in composition, such as inclusions or large compositional heterogeneity. Defects like MnS inclusions and σ phases are known to act as preferential sites for pitting corrosion to occur and reduce overall corrosion resistance, whilst compositional variations can act as a localised galvanic cell, preferentially corroding one over the other [119,124]. Literature suggests that in multi-phase HEAs of similar elemental composition, Ni and Al are preferentially corroded over Fe and Cr [199]. Applying that theory to cast HEA1, the BCC presents a Cr concentration on average 11.10 wt.% higher than that of the FCC with Ni 10.20 wt.% higher in the FCC. The XRD phase proportions suggest a FCC/BCC ratio of 86.75/13.25, so 86.75 % of the alloy is being hypothetically preferentially corroded over the remaining BCC. There are factors outside of this, such as a higher packing factor in the FCC, which promotes corrosion resistance, but literature suggests this is outweighed by the phase proportion [121].

The corrosion mechanisms of HEA1 differ from those seen with other alloys known for strong passive oxide formation, such as 316L. Across the manufacturing routes, there is little to indicate that pitting corrosion occurs, with poor passivation after E_{corr} is reached, and instead, more generalised corrosion is present. The corrosion testing of the different HEA1 manufacturing routes resulted in conflicting findings. The CR sample had the most stable OCP, followed by cast and AM with -0.212 V, -0.243 V and -0.292 V, respectively, whilst also having the lowest standard deviation. However, the CP data declares the CR samples having the lowest average E_{pit} , 0.055 V and 0.120 V below the AM and cast, respectively. The AM samples, whilst having the 2nd best E_{pit} of the 3 routes, exhibit the greatest reliability of this metric and also the highest E_r , and the potential difference between its E_{corr} and E_{pit} values are very similar to those of the cast at 0.297 V vs 0.303 V, showing similar qualities of passive layer formation. The CR samples, on the other hand, show poor passivation after corrosion is initiated at E_{corr} , at a potential difference of 0.163 V. Further testing is required to identify the makeup and characteristics of the protective coatings formed on these alloys. This will aid in understanding the

corrosion mechanisms taking place, as well as the impact of the relative proportions and compositions of each phase on the selective dissolution of specific elements.

6.10 Conclusions

- A novel HEA was successfully printed, and its build parameters were successfully optimised, resulting in a maximum theoretical bulk density of 100 % and a maximum optical density of 99.47 %.
- Minimal density variation was observed in parts distributed around the build plate measured by bulk density, suggesting high repeatability.
- HEA1 AM, cast, and CR samples were successfully manufactured in-house and prepared for analysis and electrochemical testing.
- XRD spectra revealed similar bulk phase proportion ratios, with a maximum FCC percentage of 94.23 % observed in the AM sample and a minimum proportion of 86.75 % in the cast. SEM imaging and EDS analysis of the different processes showed good phase and compositional homogeneity in the AM sample. The cast and CR both presented two major distinct phases, an FCC_L12 rich in Ni and Cr depleted, and a BCC_B2 showing the inverse. Inclusions were observed in both of these samples, suggesting the presence of competing BCC_B2#2 and σ phases, as predicted by Thermo-Calc. These were more dominantly located within the primary BCC than the FCC. MnS inclusions and AlN precipitates were also detected across both samples.
- The increase in distinction of the competing BCC and σ phases in the CR sample suggests the need to refine the thermomechanical processes used for its manufacture.
- The different atomistic, arithmetic and stimulatory mechanisms used to predict phases and compositions of HEAs still need significant refinement.
- Overall, the cast sample displayed the most consistent corrosion resistance. Whilst the CR route presented the most stable OCP and an accompanying low standard deviation, its E_{pit} values were the lowest of the 3 manufacturing processes, implying the formation of the weakest passive oxide layer. This could be due to the increased phase complexity of the CR samples relative to the cast and AM, predicted by Thermo-Calc and observed through XRD and SEM-EDS analysis, with increases in σ phase formation known to negatively impact corrosion resistance.
- Further work needs to be done to optimise the production processes to optimise the corrosion resistance.

7 An Investigation into the Different Manufacturing Methods of a High Entropy Alloy (HEA1) with a 2.4 wt.% Molybdenum Addition and their Effects on Microstructure and Corrosion Resistance

7.1 Introduction

The Pitting Resistance Equivalent Number (PREN) is a corrosion resistance parameter used to assess the susceptibility of stainless steel and other alloys to pitting corrosion [200]. It is particularly valuable in predicting the performance of materials in chloride-containing environments, such as seawater or brine solutions. The PREN is calculated using the alloy's composition, considering the content of key corrosion-resistant elements such as Cr and Mo and is outlined in equation 18 [201]. It is important to note that while the PREN is a useful guideline, the actual corrosion resistance of an alloy can be influenced by factors such as heat treatment, manufacturing processes, finishing, and specific environmental conditions.

$$PREN = Cr + 3.3 \times Mo + 16 \times N \quad 18$$

The PREN number, whilst applicable to steels, identifies that additions of certain elements will increase the corrosion resistance of an alloy. Following on from this theory and concurring with the literature, Mo additions have also been used in conjunction with HEAs to successfully improve corrosion resistance by increasing the thickness of the passive layer and forming insoluble MoO_3 [119,120,123,124]. Because of this, a Mo addition of 2.4 wt.% was made in situ to HEA1, creating HEAX, to see if these results could be replicated through AM, cast, and CR manufacturing processes and to develop further understanding of the microstructure evolution caused by this addition and its effect on corrosion resistance. This new alloy is henceforth dubbed HEAX.

7.2 Powder Analysis

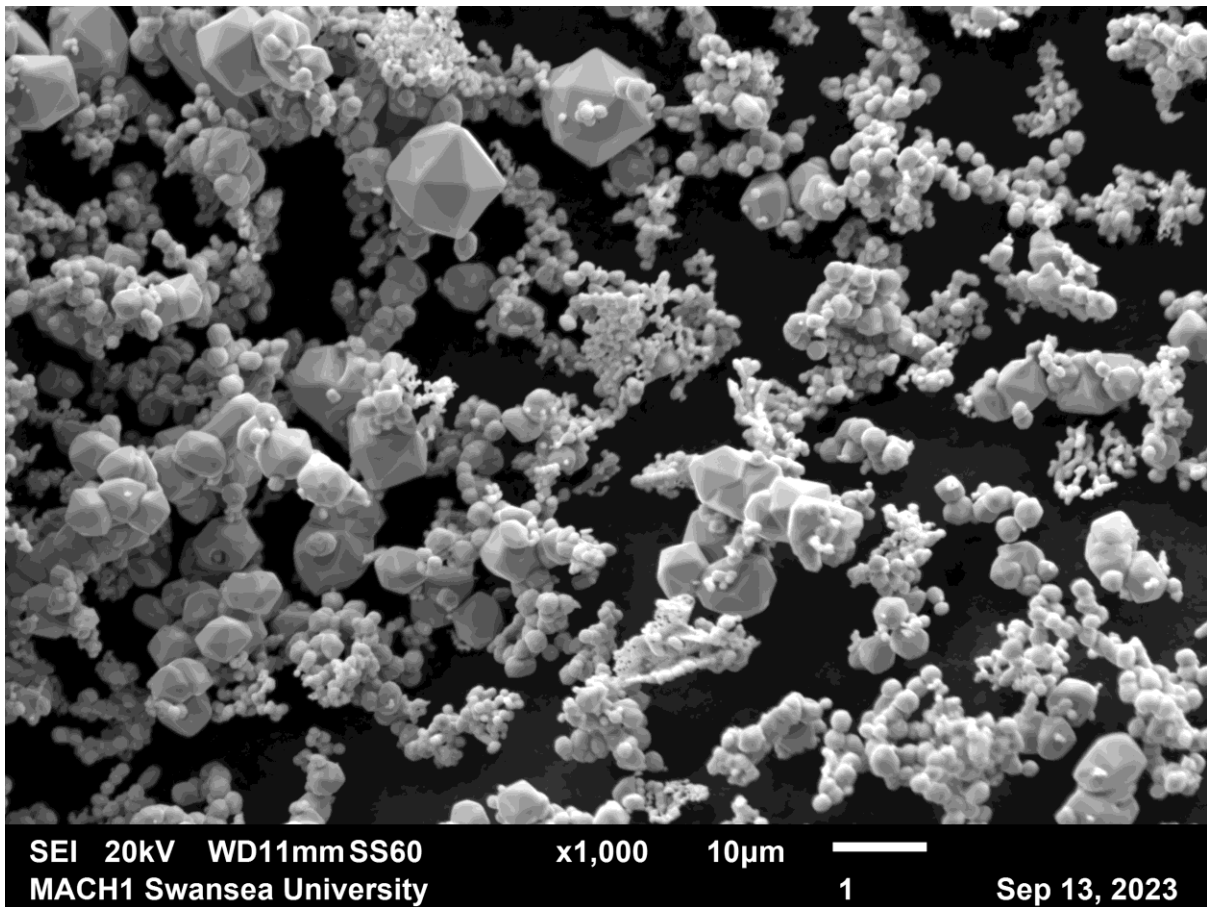


Figure 76 SEM micrograph of Mo powder used for in-situ addition

Figure 76 shows an SEM image of the Mo powder that was mixed with HEA1 as described in section 3.2. The morphology of this powder appears far more polyhedral, with a significant agglomeration of particles in branch-like formations, the latter occurring more prominently on those particles with an apparent lesser diameter.

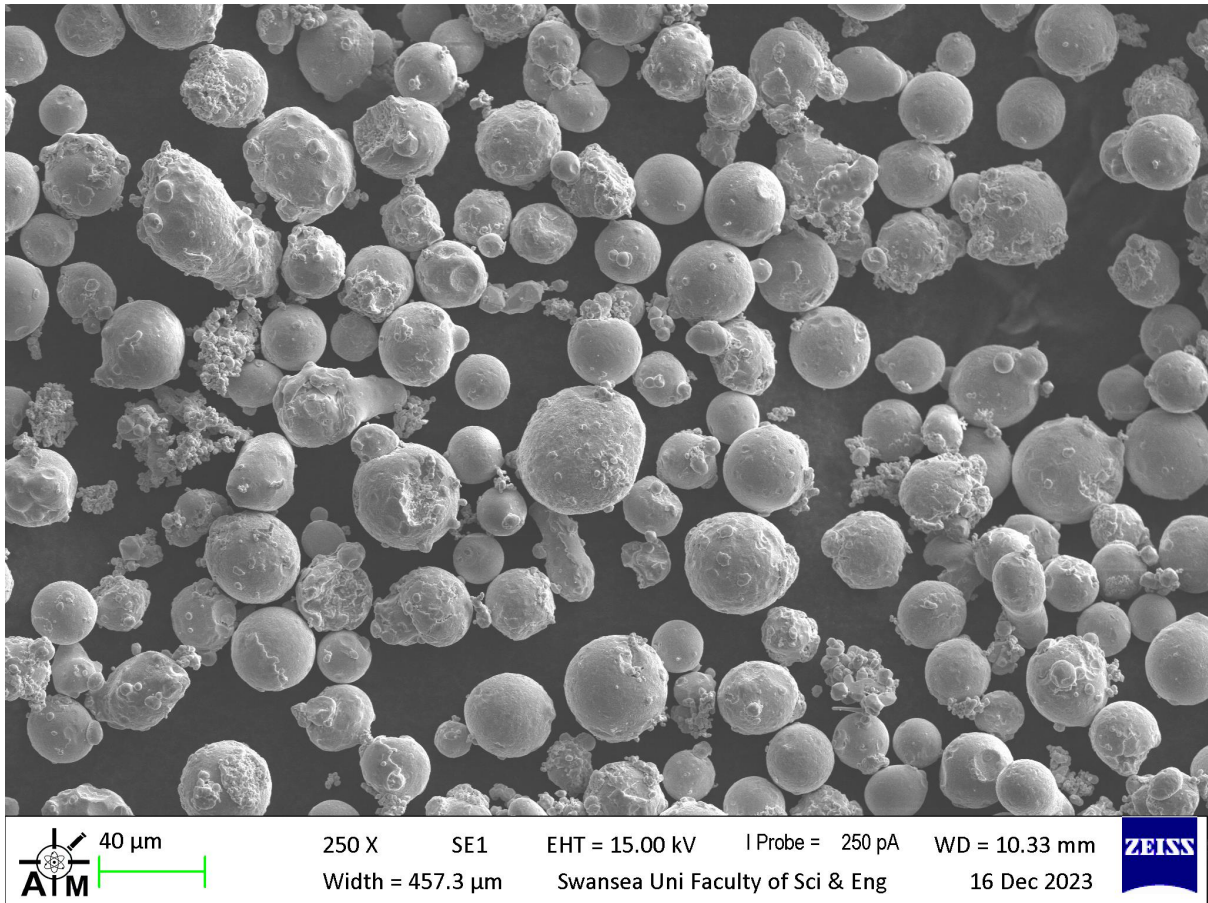


Figure 77 SEM micrograph of HEAX powder

Figure 77 shows the resultant powder mixture after the Mo had been combined with virgin HEA1. The Mo appears relatively evenly distributed, however there are areas of agglomeration, both of the Mo alone, and in combination with HEA1 particles. This depiction clarifies the size disparity between the Mo and HEA1 particles, the former being significantly smaller.

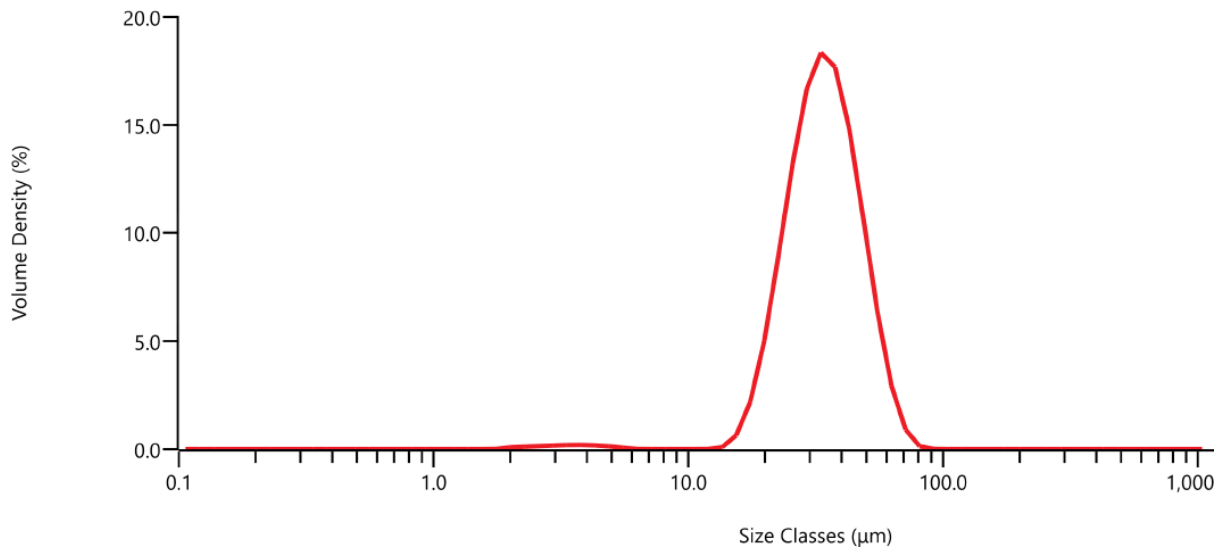


Figure 78 HEAX powder PSD

Figure 78 and Table 50 exhibit the data for the PSD tests performed on the powder mixture and concur with this inference, with the former showing a distinct break in volume density and data suggesting that no particles are perceived within the approximate range of 5.92 μm and 11.2 μm . The Mo is responsible for size fractions smaller than this, with particles detected between 1.88 μm – 5.21 μm , whereas HEA1 is accountable for the values from 12.7 μm to 76.0 μm . 80 % of the powder is stated to be within the range of 22.2 μm and 50.6 μm , with the SMD at 29.5 μm .

Table 50 Particle size by volume for HEAX powder

| Percentile | Size (μm) |
|------------|------------------------|
| Dv (10) | 22.2 |
| Dv (50) | 33.8 |
| Dv (90) | 50.6 |
| D [3,2] | 29.5 |
| D [4,3] | 35.2 |

The rheometric data displayed in Table 51 suggests that the HEAX blended powder had good flowability, with a FRI of 1.11 in the region described in Table 5 as insensitive to flow rate.

Table 51 Rheometric characteristics of the HEAX powder

| BFE (mJ) | SE (mJ/g) | FRI | CBD (g/ml) | Split Mass (g) |
|----------|-----------|------|------------|----------------|
| 1045.23 | 3.95 | 1.11 | 3.63 | 90.86 |

7.3 Optimisation and Build Setup

The optimisation of HEAX proved to be a far more difficult endeavour than the previous alloys tested. Only 5 kg of mixed powder could be created to use as feedstock, meaning that the RBV was the only feasible AM production method.

Initially, the optimum parameters for HEA1 were used to attempt to manufacture 9 density cubes of HEAX on the RBV, as shown in Figure 79. However, this build failed due to delamination and poor fusion of the build plate, approximately 20 layers after the supports had concluded. To eliminate the possibility of the failure being associated with machine set-up, the same build was run again but with the concurrent results.

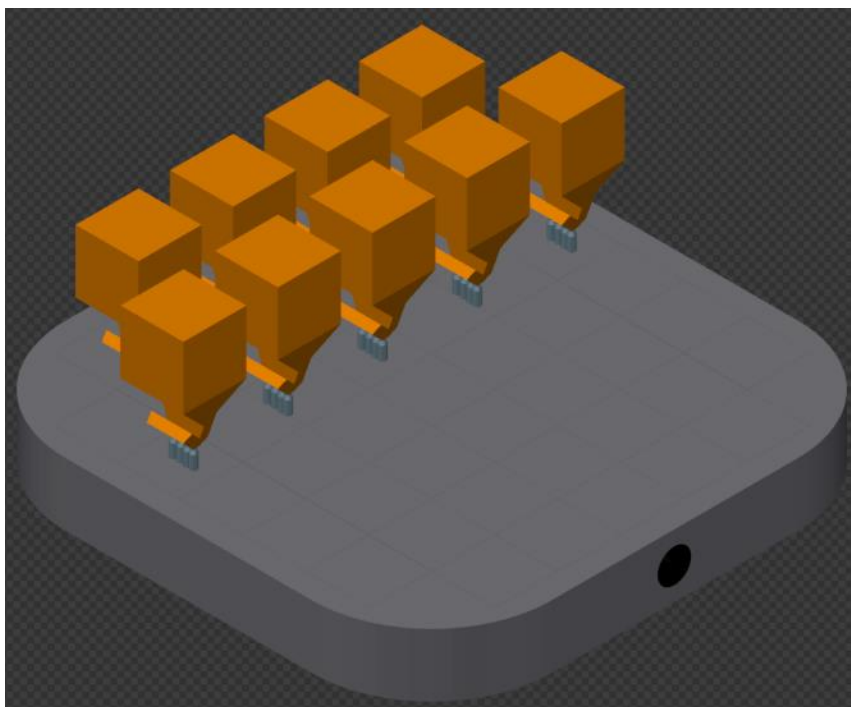


Figure 79 Initial build setup for HEAX on the RBV

Multiple different parameter sets, including extremes, were tested with minimal success. A 3 mm tall disc geometry was then tested, the hypothesis being that the cube edges had previously been a focal point for delamination and removing them could enhance the prospect of success. The first build with the discs was built straight to the plate without any supports, hoping this larger fusion area would also limit delamination. Whilst more success was experienced than with the cube before failure, not enough material was constructed to be made into samples. Finally, the build setup in Figure 80 was successful enough to produce sufficient material to begin testing. The small number of components on the plate and the rotation of the square geometries resulted in reduced delamination, and any failures that did occur did not affect any of the surrounding parts.

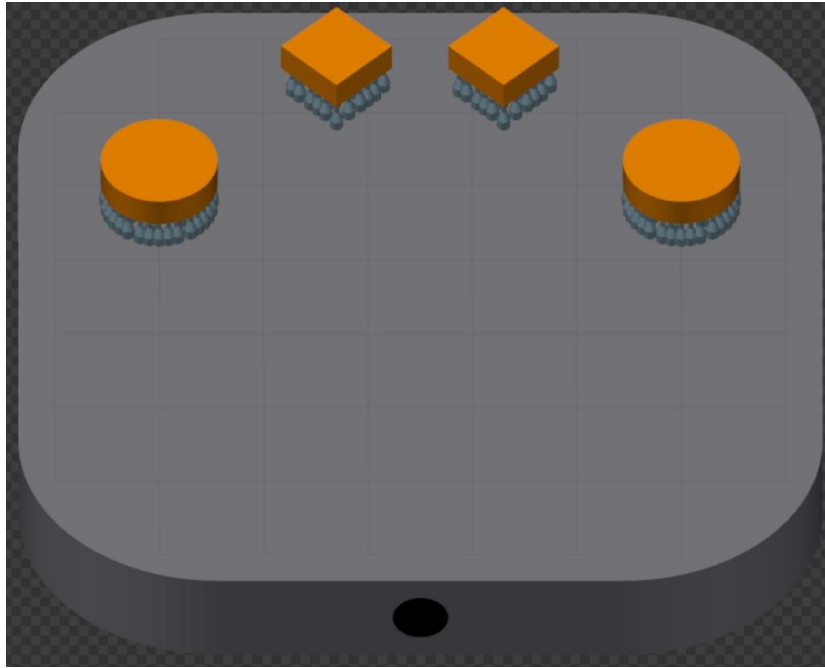


Figure 80 Successful build layout for HEAX on the RBV

Once removed from the plate, the parts were taken to the workshop to be machined flat whilst preserving the largest area of material possible. The parameters used for the successful parts are displayed in Table 52.

Table 52 Laser parameters used for AM HEAX

| P (W) | PD (μm) | ET (ms) | HS (μm) | LT (μm) | VED (J/mm^3) |
|-------|----------------------|---------|----------------------|----------------------|--------------------------------|
| 215 | 60 | 85 | 0.11 | 50 | 55.38 |

7.4 Density Analysis

The densities of each processing route were calculated using ImageJ as outlined in section 3.13.2 and are displayed in Table 53. Due to the geometries manufactured, obtaining a bulk density measurement for the AM sample in the same way as in previous chapters was impossible.

Table 53 Optical density measurements for AM, cast, and CR HEAX

| Sample | AM | Cast | CR |
|---------------------|-------|-------|-------|
| Optical Density (%) | 98.81 | 98.98 | 99.05 |

7.5 Thermocalc

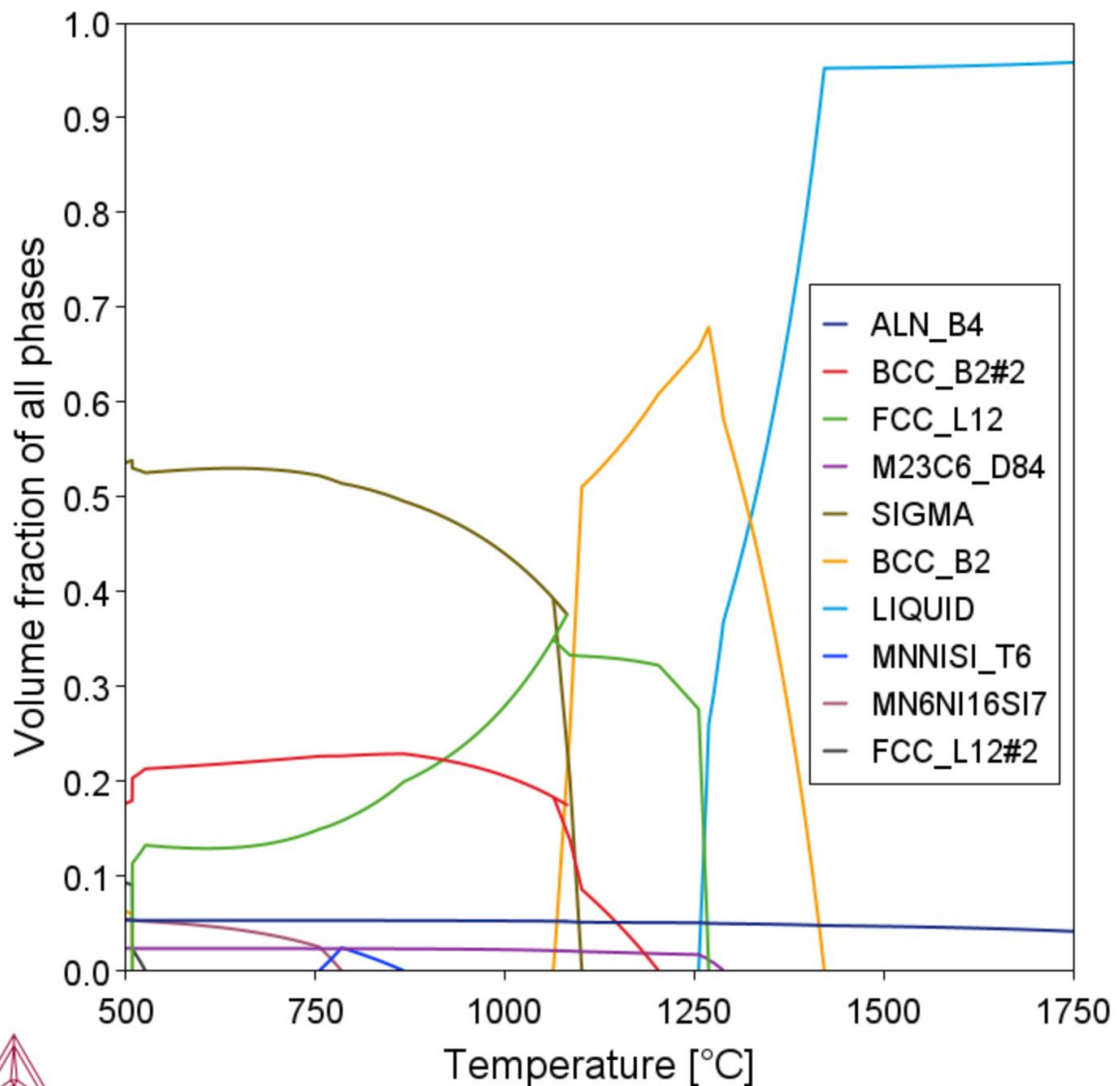


Figure 81 Volume fraction of all phases for HEAX produced by Thermo-Calc

Figure 81, produced by Thermo-calc using the TCHEA5: High Entropy Alloys v5.1 database, exhibits similarities to HEA1, with ALN being the first solid phase to form at 1886 °C, but reaches a higher φ_i of 0.053 once the system is cooled to 1000 °C. Once again, the BCC_B2 is the first major phase to form, as seen in Figure 81, beginning at 1416 °C and peaking at a φ_i of 0.68. Similarly to HEA1, this phase contains elevated levels of Fe and Cr and a reduced concentration of Ni, but by a lesser magnitude, according to the data in Table 54. Al is also noted at 1.4 wt.% higher than the target level. The FCC again shows similar trends to HEA1, with Cr dropping to a predicted concentration of 18.4 wt.% when its φ_i peaks at 0.376 at 1082 °C. Between the temperatures of 1102 °C and 1064 °C Figure 81 exhibits considerable competition between the 4 major phases present as the BCC_B2#2 and σ phases initiate, both of which follow the same compositional trends as HEA1, with the former showing vastly

diminished Fe, Cr and Mo, with increases in Ni, Al and Si. The σ appears high in Cr with slightly elevated levels of Mo, whereas the concentrations of Ni and Al have been drastically diluted. Figure 81 also shows the presence of a phase identified as M23C6_D84, which, based on its composition and literature, is understood to be a chromium carbide and occurs at a maximum φ_i of 0.024.

Table 54 Composition of selected HEAX phases at their highest respective volume fraction (wt.%)

| | Fe | Cr | Ni | Mn | Al | Mo | Si | N | C |
|------------------|-------|-------|-------|-------|-------|-------|-------|--------|-------|
| BCC_B2 | 35.23 | 29.00 | 19.25 | 9.54 | 4.17 | 2.33 | 0.45 | 0.001 | 0.004 |
| FCC_L12 | 36.73 | 18.40 | 28.78 | 9.44 | 3.41 | 1.97 | 1.23 | 0.0004 | 0.03 |
| SIGMA | 37.90 | 43.80 | 2.37 | 12.59 | 0.001 | 3.35 | 0.002 | 0 | 0 |
| BCC_B2#2 | 12.47 | 1.71 | 57.60 | 11.03 | 15.91 | 0.040 | 1.23 | 0 | 0 |
| ALN_B4 | 0 | 0 | 0 | 0 | 65.83 | 0 | 0 | 34.17 | 0 |
| M23C6_D84 | 5.36 | 69.59 | 0.245 | 0.009 | 0 | 19.65 | 0 | 0 | 5.15 |

7.6 XRD

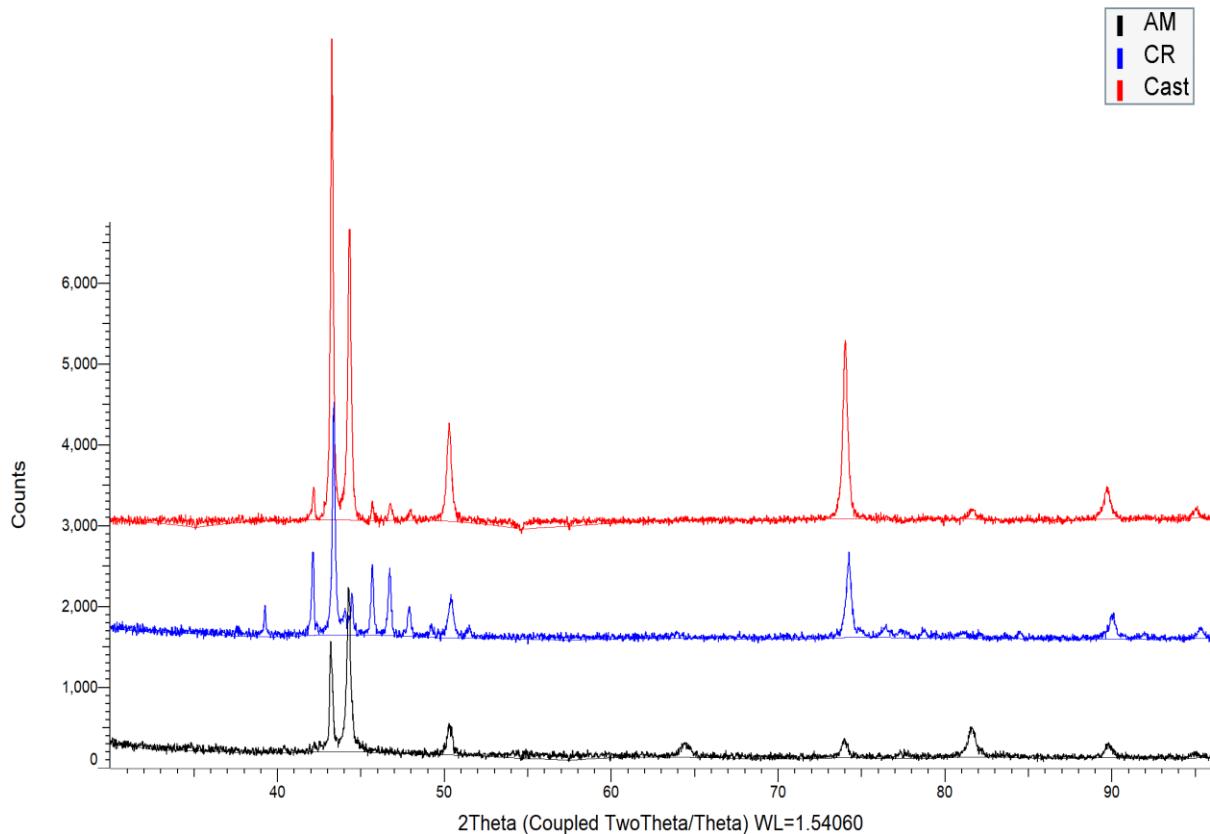


Figure 82 XRD scans for CR, AM, and cast HEAX samples

The XRD scans for AM, CR and cast HEAX in Figure 82 show peaks at varying intensities associated with the two major FCC and BCC phases located at the angles presented in Table 55. Peaks 1-3, 5 and 7 are seen prominently across all 3 scans, with the AM sample showing clearer summits at ~64.71 ° and 81.97 ° than the CR and cast. The CR and cast samples show significant similarities, with the most visible peaks mirrored across their scans, albeit at contrasting strengths. The additional peaks between 2θ angles of 38 ° and 52 ° in these scans and not the AM are comparable to those evident in the CR HEA1 scan shown in Figure 62. Once again, these peaks are difficult to define using pattern matching software, but similar assumptions can be made regarding the presence of MnS and AlN.

Table 55 XRD data extracted from scans shown in Figure 82

| HEAX XRD Intensities (cts) | | | | | | | | |
|----------------------------|--------------------|---------------|---------------|---------------|---------------|--------------------|---------------|---------------|
| | FCC Peak Intensity | | | | | BCC Peak Intensity | | |
| | 1 (43.54°) | 3 (50.67°) | 5 (74.25°) | 7 (90.07°) | 8 (95.42°) | 2 (44.42°) | 4 (64.71°) | 6 (81.97°) |
| CR | 2863.98 | 537.38 | 1055.29 | 305.95 | 141.59 | 518.35 | 64.63 | 82.00 |
| AM | 1349.57 | 385.45 | 241.80 | 185.16 | 81.29 | 2028.26 | 187.15 | 375.98 |
| Cast | 5912.30 | 1213.90 | 2198.67 | 393.58 | 123.28 | 3601.39 | 51.23 | 124.96 |

Table 56 Major phase ratios for HEAX CR, cast and AM

| Sample | FCC/BCC |
|-------------|-----------------|
| CR | 88.06 %/11.94 % |
| AM | 46.4 %/53.60 % |
| Cast | 72.26 %/27.74 % |

The most significant comparison comes when calculating the phase proportions of each manufacturing process. When considering the major FCC and BCC phases calculated in Table 56 based on the sum of peak intensities in Table 55, all 3 processes return significantly different ratios, with the FCC at its highest in the CR sample and lowest in the AM, with a 41.66 % reduction.

This is attributed to the large BCC peak at approximately 44.42 ° in the AM sample relative to the primary FCC peak at ~43.54 °, contrary to the CR and cast intensities, superior BCC peaks at ~64.71 ° and 81.97 °, and a diminished FCC peak at ~74.25 °.

7.7 Microstructure

7.7.1 AM

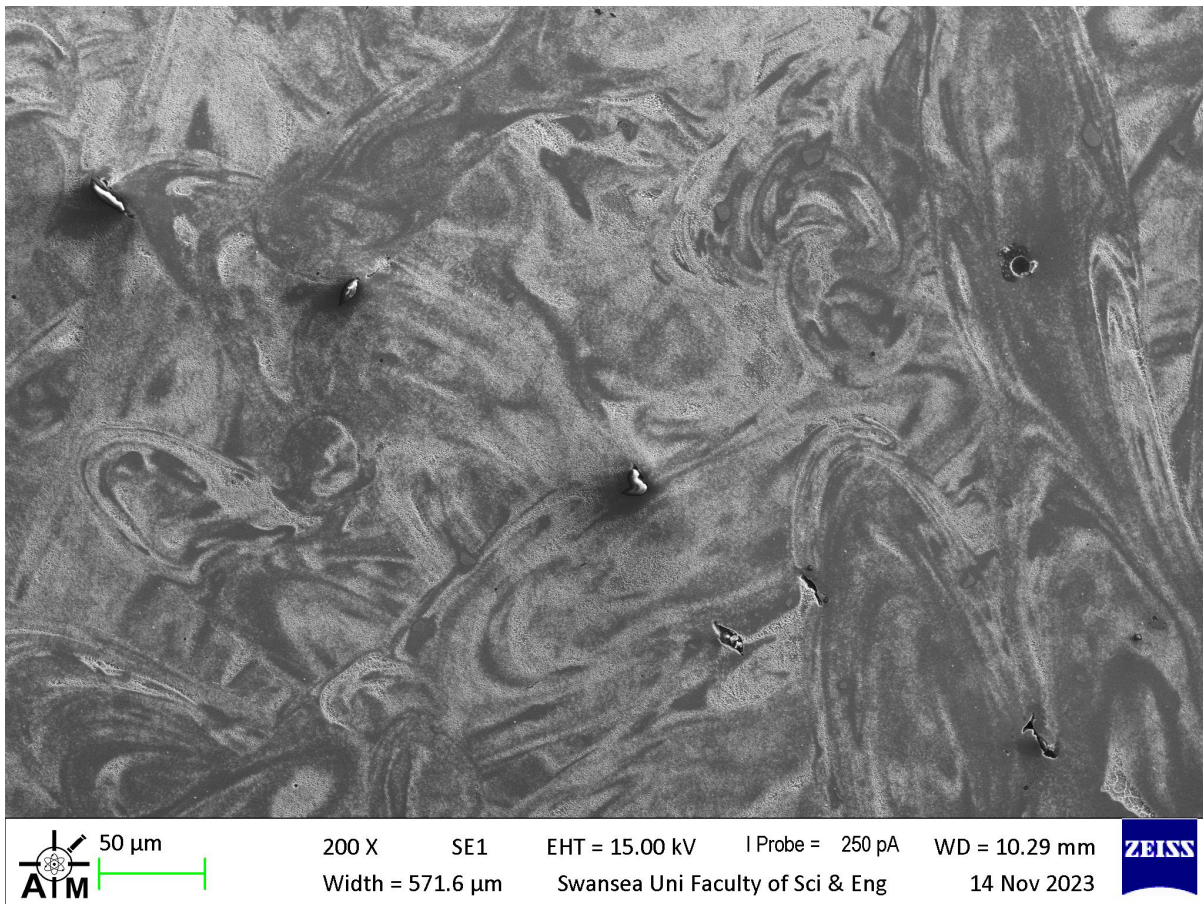


Figure 83 SEM micrograph of AM HEAX in the XY plane

The microstructure observed in Figure 83 is of AM HEAX in the XY plane and shows a chaotic array of refined grains that appear to follow the laser scan path. Significant multidirectional remelting across the sample is shown, as well as minor cracks and porosity. It is impossible to discern whether there is any pattern to this porosity, such as along the laser boundaries, due to its disordered features.

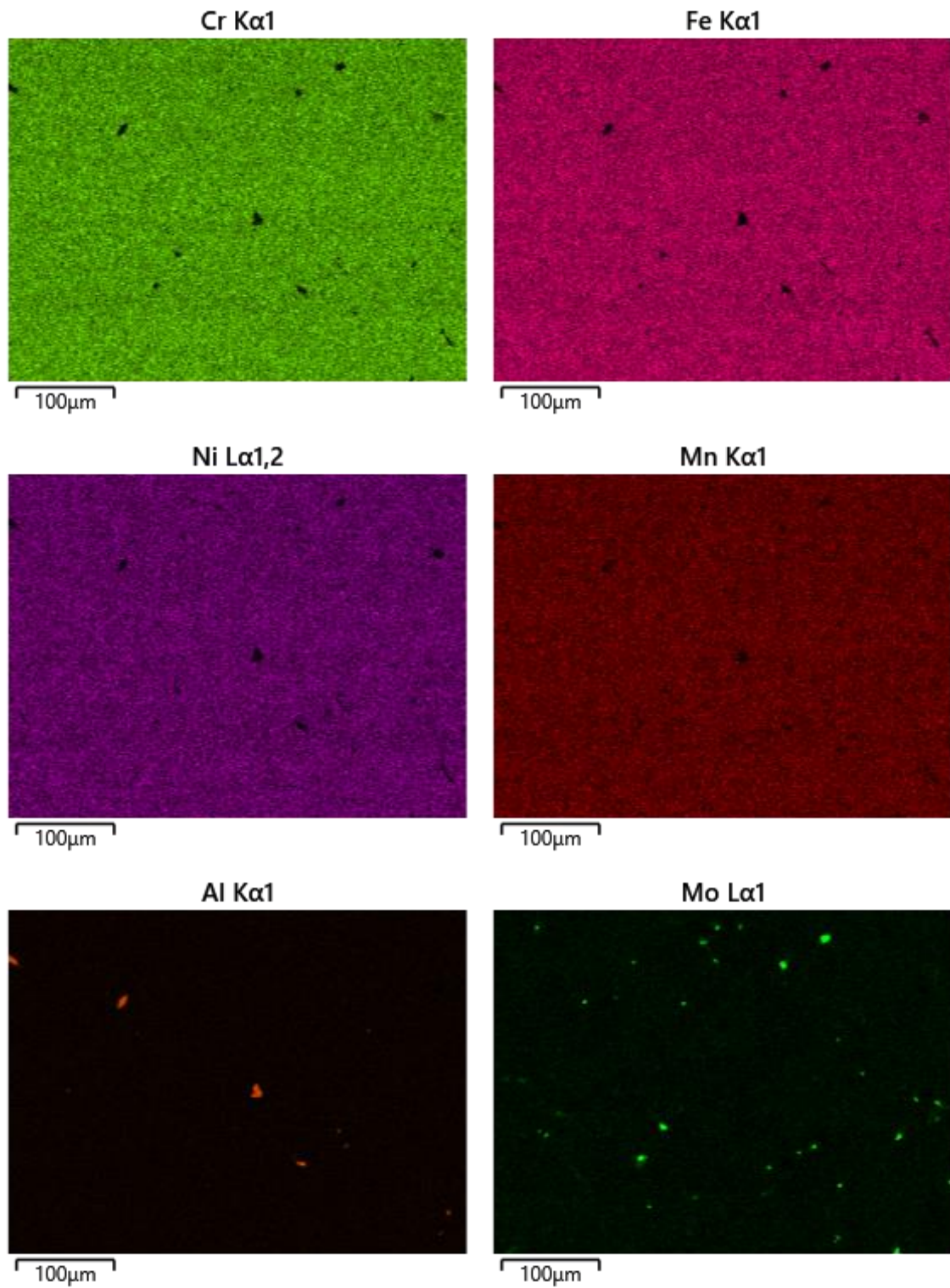


Figure 84 EDS maps for AM HEAX

Table 57 Composition of AM HEAX from EDS (wt.%)

| Element | Fe | Cr | Ni | Mn | Al | Mo | Si | N |
|----------|-------|-------|-------|-------|------|------|------|---|
| Weight % | 32.25 | 27.21 | 24.82 | 10.04 | 2.73 | 2.38 | 0.57 | 0 |

EDS mapping was used to investigate the level to which the sample had alloyed during the AM process, the results of which are presented in Figure 84 and Table 57. The overall composition measured initially suggests that the process had succeeded, with 2.38 wt.% of Mo being detected, just missing out on the 2.4 wt.% target. However, significant inhomogeneity is observed when consulting the EDS maps, with numerous areas detected with low counts of Cr, Fe, Ni, and Mn relative to the bulk. These regions have conversely high concentrations of Al and Mo.

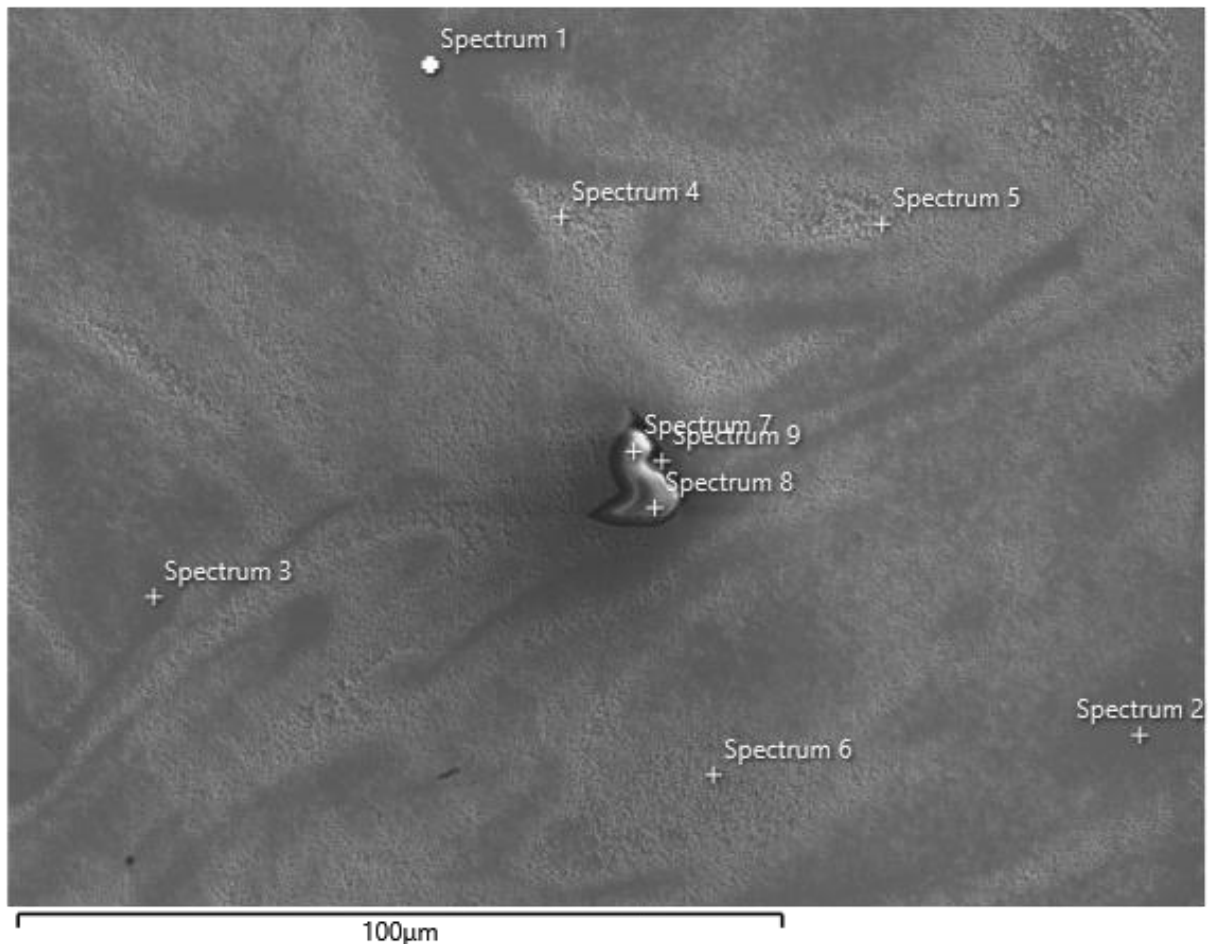


Figure 85 SEM micrograph and point scan map of AM HEAX at 750x magnification

Figure 85 shows the point scan analysis undertaken around one of the areas identified as high in Al based on the EDS maps in Figure 84. 3 areas of interest were examined, namely the centralised inclusion, the darker, more uniform region, and the lighter area interpreted as the edges of the laser scan path. The light and dark areas, which could collectively be defined as the bulk alloy, present very similar compositions, except when comparing their Mo content, which occurs at 4.06 wt.% and 0.90 wt.%, respectively. An increase or decrease in the other constituent elements offsets this variation. The inclusion and the area surrounding it were previously identified as high in Al and demonstrated significantly elevated levels of this element when consulting spectra 7-9, with an average wt.% of 81.35. The only non-residual element that appears close to its forecasted value is that of Mn at an

average of 6.17 wt.%. Thermocalc would suggest that this region with such a high Al concentration would be an inclusion of AlN; however, this is disproved by the complete absence of N at these points.

Table 58 Point scan spectrum analysis relating to the HEAX AM sample in Figure 85 (wt.%)

| Region | Spectrum No. | Fe | Cr | Ni | Mn | Mo | Al | Si | N | S |
|---------------------------|--------------|-------|-------|-------|-------|------|-------|------|------|------|
| Dark | 1 | 31.5 | 26.53 | 25.36 | 10.13 | 3.15 | 2.61 | 0.61 | 0.1 | 0.02 |
| | 2 | 32.68 | 27.54 | 23.99 | 10.02 | 2.76 | 2.45 | 0.53 | 0 | 0.05 |
| | 3 | 31.59 | 27.26 | 22.49 | 9.22 | 6.26 | 2.63 | 0.56 | 0 | 0 |
| | Avg | 31.92 | 27.11 | 23.95 | 9.79 | 4.06 | 2.56 | 0.57 | 0.03 | 0.02 |
| Light | 4 | 32.48 | 28.84 | 24.81 | 10.77 | 0.51 | 2.05 | 0.54 | 0 | 0 |
| | 5 | 31.81 | 27.38 | 25.48 | 10.58 | 0.99 | 2.86 | 0.76 | 0.14 | 0 |
| | 6 | 32.96 | 27.66 | 25.33 | 9.78 | 1.21 | 2.54 | 0.42 | 0 | 0.1 |
| | Avg | 32.42 | 27.96 | 25.21 | 10.38 | 0.90 | 2.48 | 0.57 | 0.05 | 0.03 |
| Inclusion | 7 | 1.32 | 5.11 | 0.18 | 7.28 | 0.35 | 85.68 | 0.03 | 0 | 0.05 |
| | 8 | 1.62 | 4.66 | 1.35 | 6.69 | 0.13 | 85.17 | 0.36 | 0 | 0.02 |
| | 9 | 5.47 | 10.04 | 1.81 | 4.55 | 3.6 | 73.19 | 1.34 | 0 | 0 |
| | Avg | 2.80 | 6.60 | 1.11 | 6.17 | 1.36 | 81.35 | 0.58 | 0.00 | 0.02 |
| Max | | 32.96 | 28.84 | 25.48 | 10.77 | 6.26 | 85.68 | 1.34 | 0.14 | 0.1 |
| Min | | 1.32 | 4.66 | 0.18 | 4.55 | 0.13 | 2.05 | 0.03 | 0 | 0 |
| Average | | 22.38 | 20.56 | 16.75 | 8.78 | 2.11 | 28.8 | 0.57 | 0.03 | 0.03 |
| Standard Deviation | | 14.74 | 10.59 | 11.77 | 2.13 | 2.02 | 39.57 | 0.35 | 0.05 | 0.03 |

SEM analysis was retrospectively conducted on the repolished corrosion sample, shown in Figure 86, as its surface integrity was higher than that of the previously analysed sample. Whilst unetched, the sample surface only shows small aspects of heterogeneity with a few tiny pores, a single, much larger defect and a lighter mark beneath it by the markers for spectrums 5 and 6.

EDS analysis in Figure 87 confirms this at an elemental level, with the 5 original bulk elements appearing to be evenly distributed across the sample, with the exception of the significant central defect. The Mo addition also seems that it has alloyed homogenously, except at the location of the previously mentioned mark by spectrums 5 and 6. The overall composition of this EDS map, shown in Table 59, was similar to that of the previous AM sample analysed, with the exception of an additional 1 % Mo.

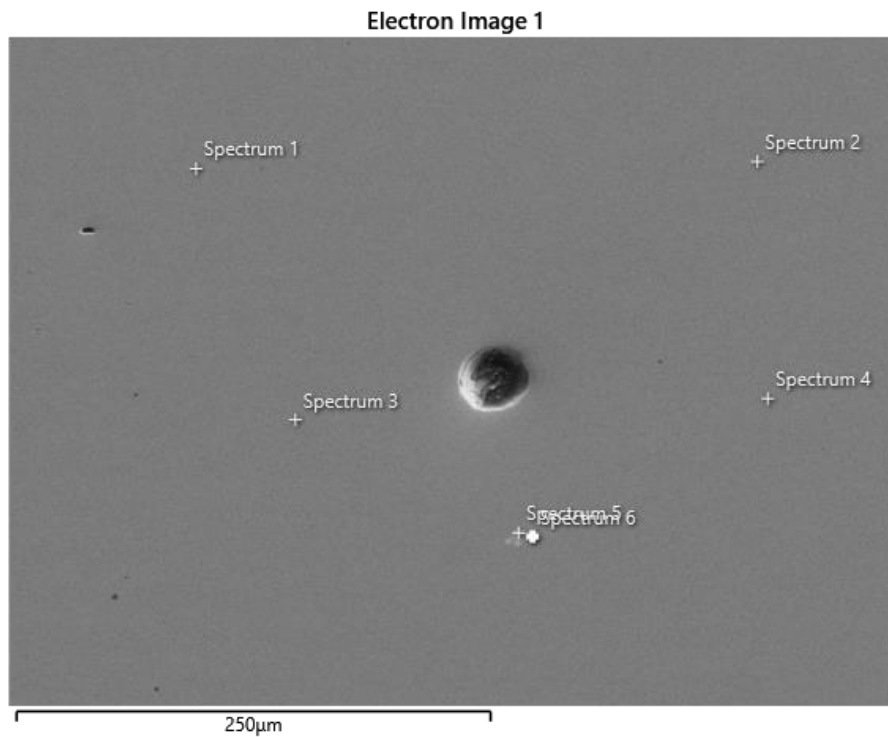


Figure 86 SEM image of AM HEAX corrosion sample with point scan locations at 250x magnification

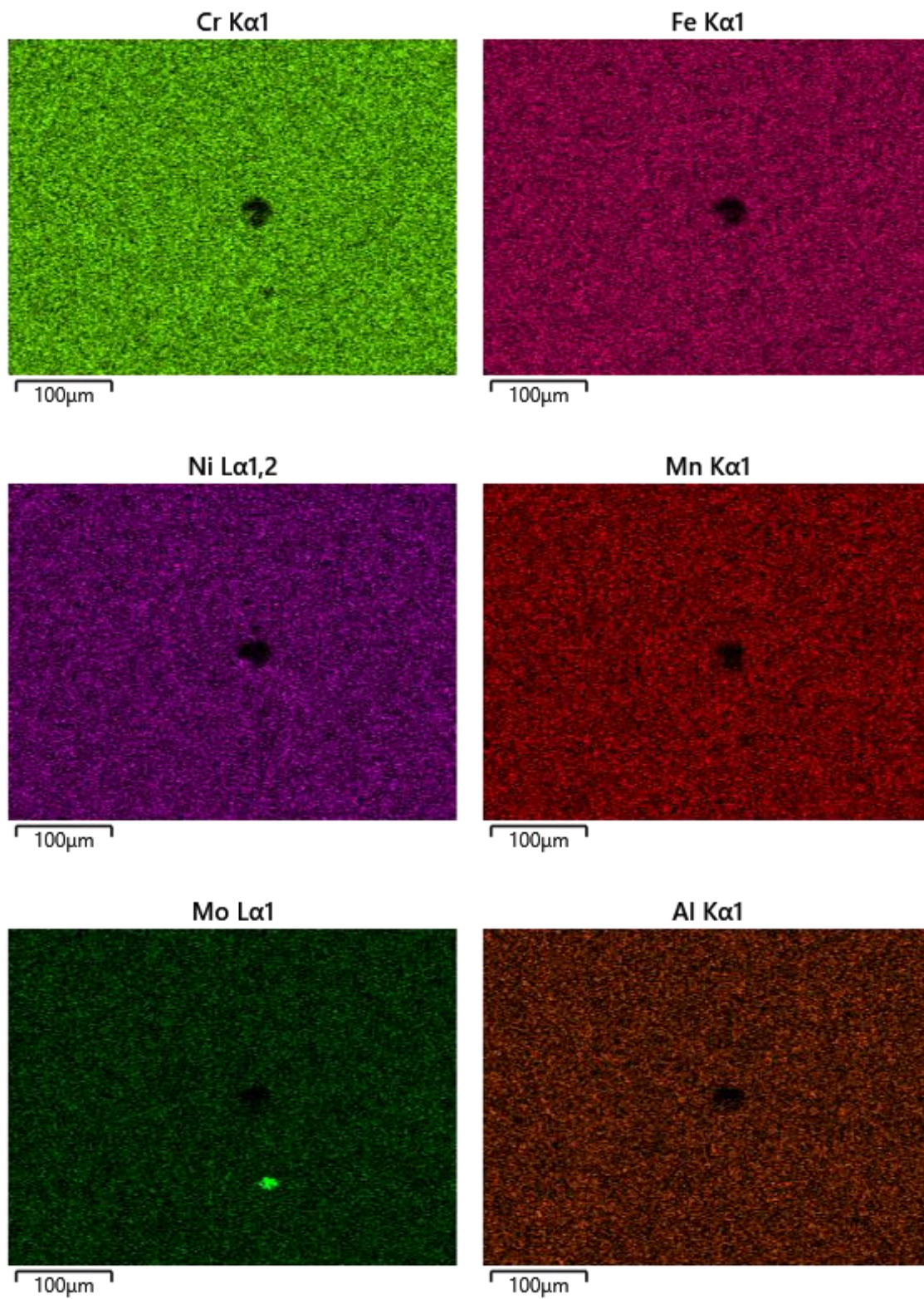


Figure 87 EDS maps for HEAX corrosion sample

Table 59 Composition of AM HEAX corrosion sample from EDS maps

| Element | Fe | Cr | Ni | Mn | Mo | Al | Si | S | N |
|-----------------|-------|-------|-------|------|------|------|------|------|------|
| Weight % | 32.48 | 26.99 | 24.61 | 9.29 | 3.42 | 2.50 | 0.57 | 0.07 | 0.06 |

Point scans were taken at 4 points in the homogenous bulk microstructure, two at the site of high Mo from the initial EDS map, and the rectangular area around that region shown in Figure 88, the results of which are presented in Table 60.

Table 60 Point scan analysis of AM HEAX corrosion sample (wt.%)

| Spectrum No. | Fe | Cr | Ni | Mn | Mo | Al | Si | S | N |
|---------------------------|-------|-------|-------|------|-------|------|------|------|------|
| 1 | 32.40 | 26.70 | 25.08 | 9.41 | 3.18 | 2.39 | 0.57 | 0.13 | 0.14 |
| 2 | 32.43 | 27.06 | 24.67 | 8.86 | 3.88 | 2.55 | 0.54 | 0.00 | 0.01 |
| 3 | 32.55 | 27.34 | 24.43 | 8.86 | 3.61 | 2.59 | 0.58 | 0.04 | 0.00 |
| 4 | 32.29 | 27.29 | 24.88 | 9.17 | 3.27 | 2.43 | 0.62 | 0.05 | 0.00 |
| 5 | 32.59 | 27.39 | 24.50 | 9.23 | 3.23 | 2.42 | 0.61 | 0.04 | 0.00 |
| 6 | 32.76 | 27.03 | 24.59 | 9.60 | 2.88 | 2.55 | 0.57 | 0.00 | 0.02 |
| Max | 32.76 | 27.39 | 25.08 | 9.60 | 3.88 | 2.59 | 0.62 | 0.13 | 0.14 |
| Min | 32.29 | 26.70 | 24.43 | 8.86 | 2.88 | 2.39 | 0.54 | 0.00 | 0.00 |
| Average | 32.50 | 27.11 | 24.68 | 9.20 | 3.35 | 2.49 | 0.58 | 0.05 | 0.03 |
| Standard Deviation | 0.15 | 0.24 | 0.23 | 0.27 | 0.32 | 0.08 | 0.03 | 0.04 | 0.05 |
| Rectangular Area | 22.92 | 18.94 | 14.53 | 8.56 | 33.38 | 1.64 | 0.03 | 0.00 | 0.00 |

Interestingly, all 6 point scan locations returned very similar compositions, with the average almost identical to the bulk composition in Table 59. However, the same cannot be said for the rectangular area encapsulating spectrums 5 and 6 as well as the entire Mo hotspot, which instead reveals a composition dominant in Mo at 22.28 wt.%, with significant reductions across all the other elements. It is theorised that the reason spectrums 5 and 6 did not display the same compositional structure is due to the incident electrons primarily revealing the surface chemistry directly beneath the Mo rich region, or due to beam drift during the time between the initial image being taken and the point scans being completed. What these additional images, scans, and compositions show is that, in this case, there were significant compositional differences between two samples made with the same parameters, highlighting the need for further optimisation to increase stability.

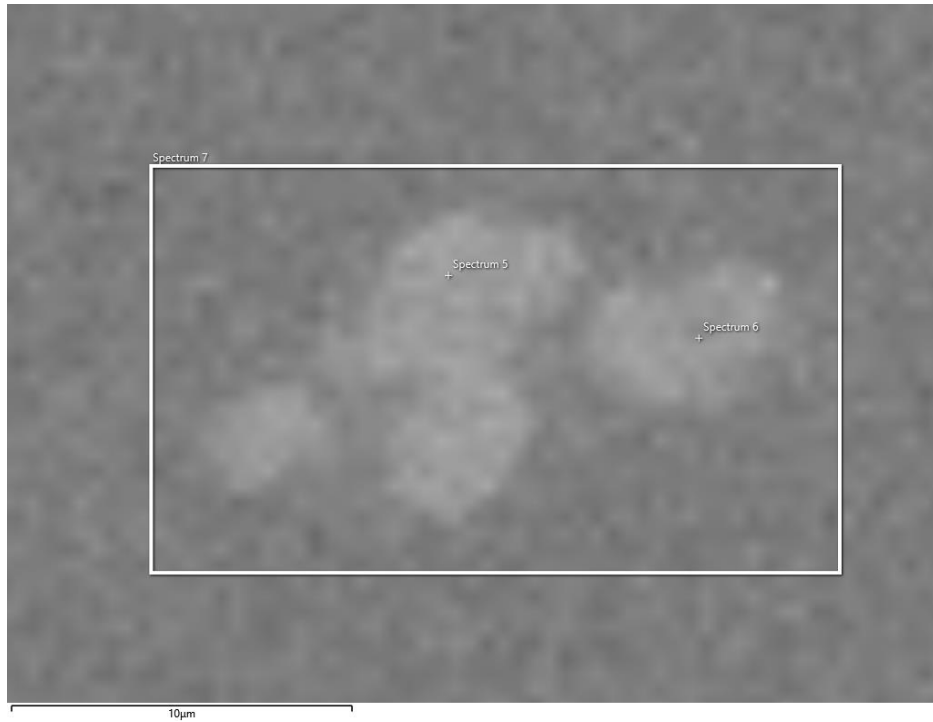


Figure 88 Rectangular area around the region of high Mo in AM HEAX

7.7.2 Cast

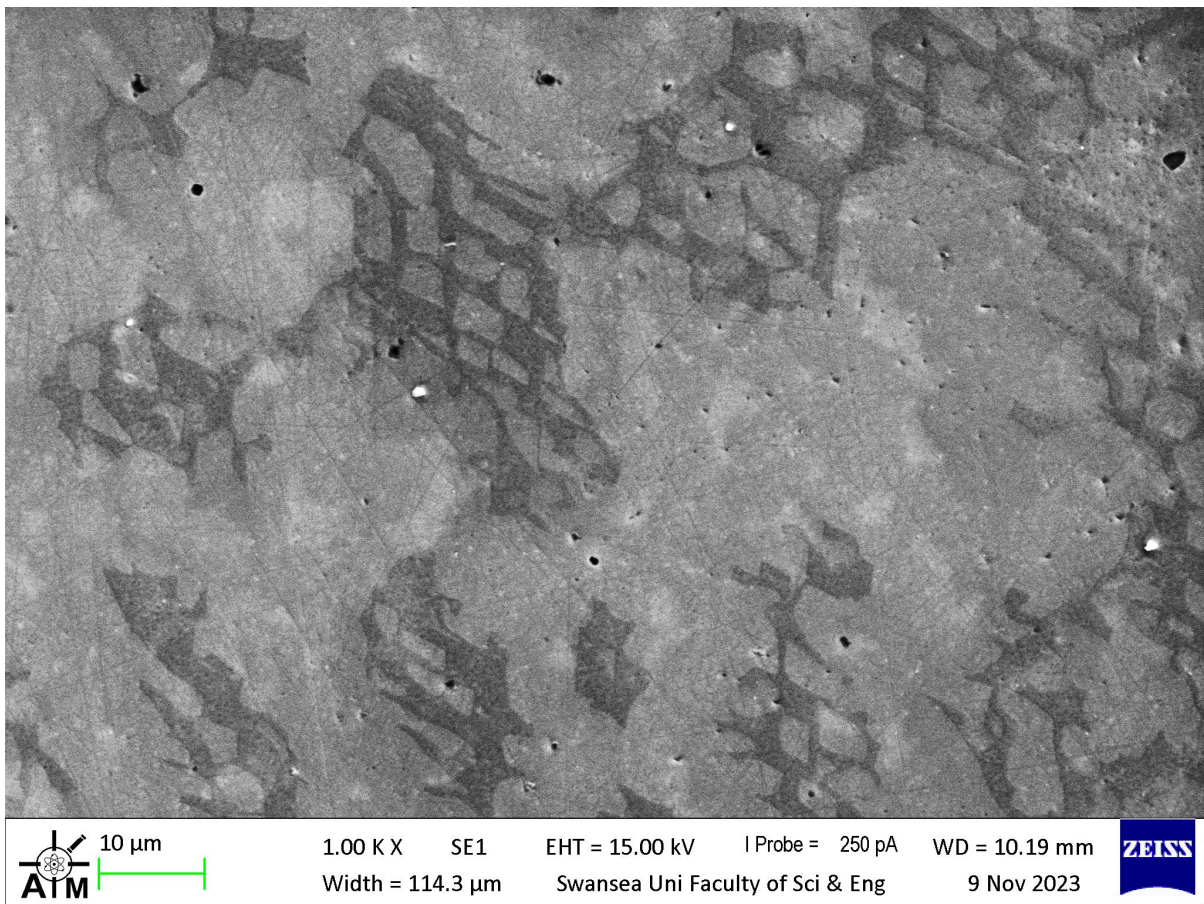


Figure 89 SEM image of cast HEAX at 1000x magnification

Figure 89 shows an SEM image of cast HEAX at 1000x magnification. In this image, two distinct phases are apparent, the bulk appearing as a lighter phase with a darker dendritic structure throughout. The dendrites are observed to have two growth directions, the majority of which are primary dendrites, some with small secondary arms. The BCC dendrites also appear to internally intersect, often forming diagonal enclosures around FCC regions cut off from the bulk.

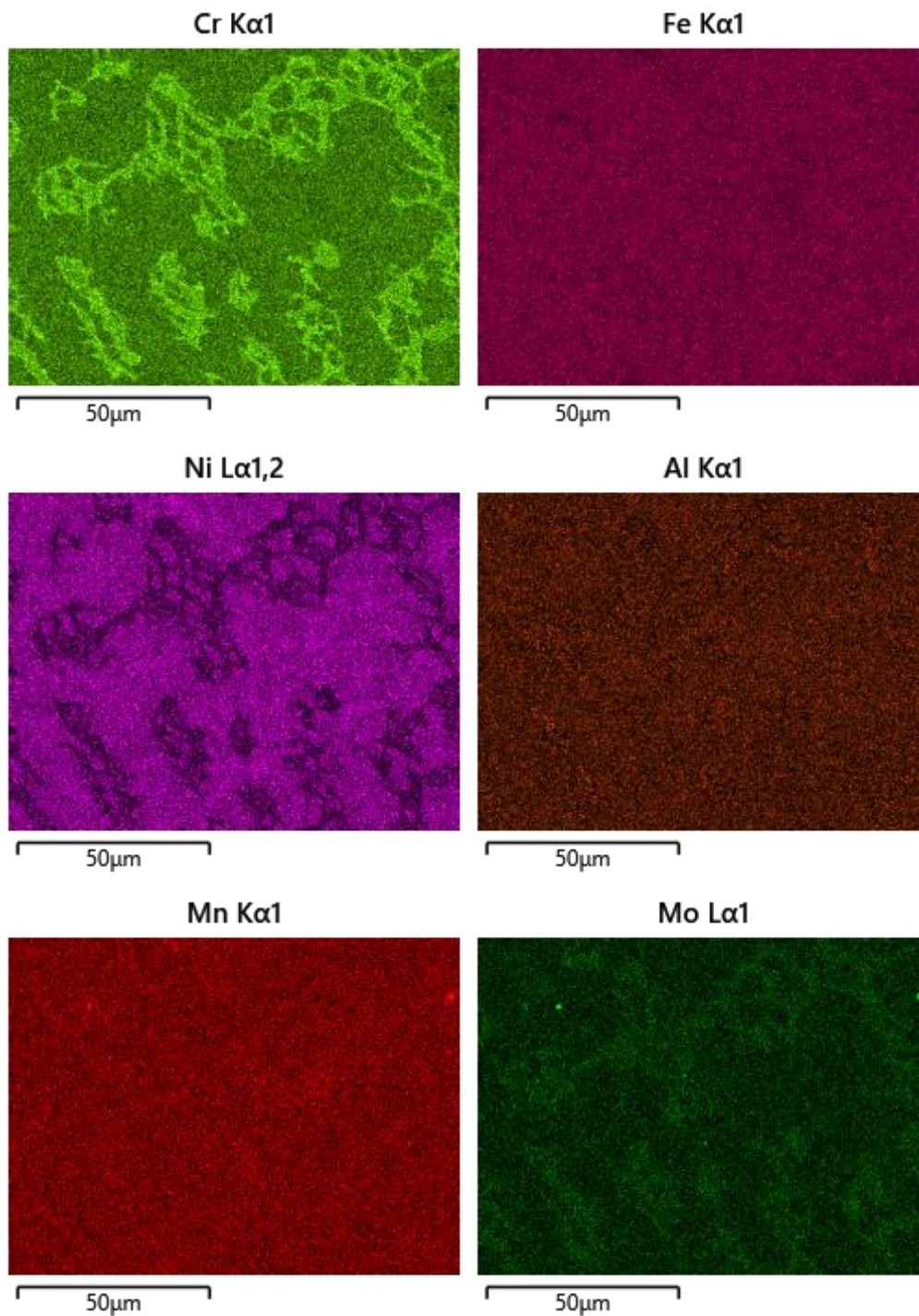


Figure 90 EDS maps of cast HEAX at 1000x magnification

Table 61 Composition of cast HEAX from EDS maps (wt.%)

| Element | Fe | Cr | Ni | Mn | Al | Mo | Si | N |
|----------|------|------|------|------|-----|-----|-----|---|
| Weight % | 32.4 | 26.8 | 25.5 | 10.5 | 2.2 | 2.0 | 0.6 | 0 |

The EDS maps presented in Figure 90 suggest that there are significant compositional differences between the bulk FCC phase and that of the dendritic BCC. Most notable is the segregation of Cr to the BCC phase, depleting the bulk, with the inverse occurring with Ni. Mo and S appear to follow the same trend as Cr, with additional spots of relatively high concentration. However, it is difficult to differentiate between Mo and S using EDS as the characteristic X-rays they emit overlap, occurring at 2.293 KeV and 2.307 KeV, respectively. In addition, Mn, whilst having a much more homogenous distribution as is seen with Fe, Al, Si and N, also appears in a higher concentration at the same spots previously mentioned.

To confirm the magnitude of the compositional variations, point scans were taken from the FCC and BCC phases as well as from multiple inclusions. The locations of these points and their resultant compositions are outlined in Figure 91 and Table 62 respectively.

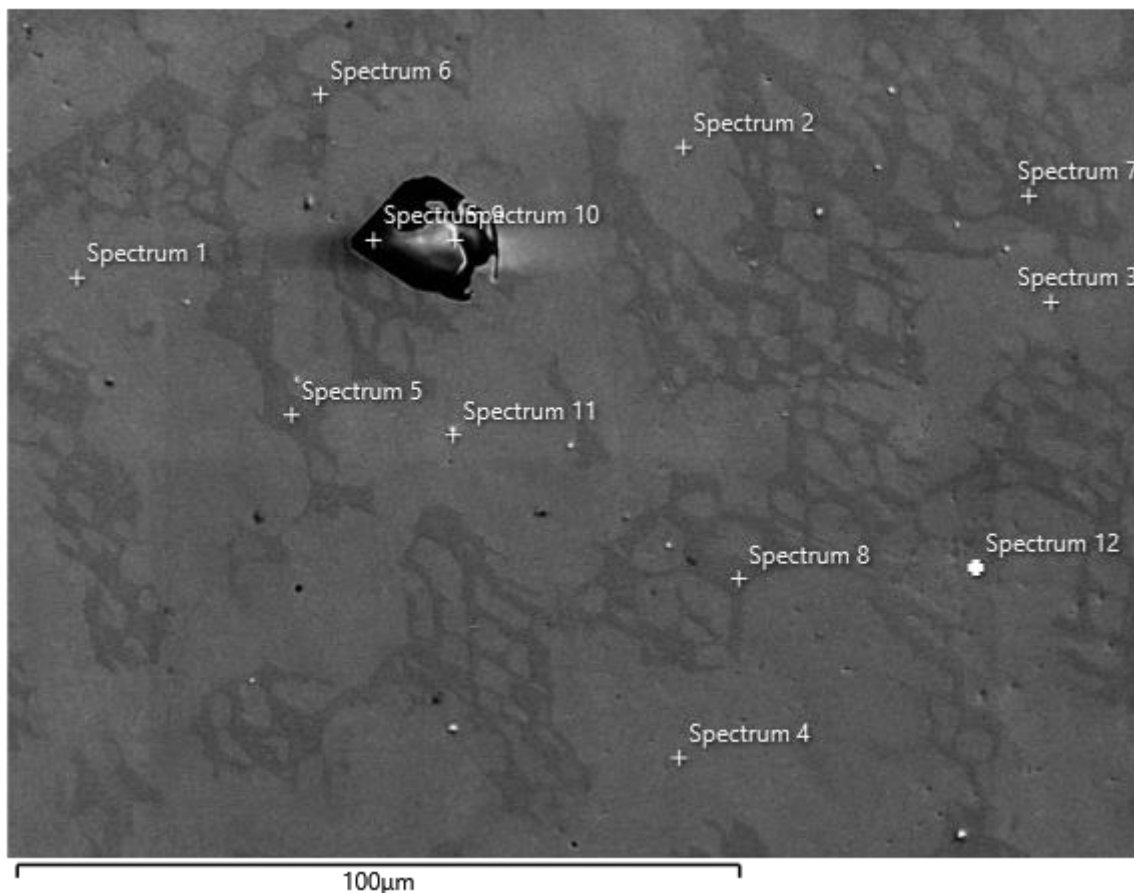


Figure 91 SEM micrograph and point scan map of cast HEAX at 750x magnification

Table 62 Point scan analysis of cast HEAX shown in Figure 91(wt.%)

| Region | Spectrum No. | Fe | Cr | Ni | Mn | Al | Mo | Si | S | N |
|---------------------------|--------------|-------|-------|-------|-------|-------|------|------|-------|-------|
| FCC | 1 | 31.73 | 23.75 | 29.07 | 11.15 | 2.34 | 1.30 | 0.51 | 0.15 | 0.00 |
| | 2 | 31.78 | 23.48 | 28.84 | 11.18 | 2.20 | 1.96 | 0.55 | 0.00 | 0.00 |
| | 3 | 32.00 | 23.95 | 28.37 | 10.91 | 2.21 | 1.97 | 0.58 | 0.00 | 0.00 |
| | 4 | 30.65 | 23.39 | 29.77 | 11.48 | 2.49 | 1.51 | 0.60 | 0.12 | 0.00 |
| | Avg | 31.54 | 23.64 | 29.01 | 11.18 | 2.31 | 1.69 | 0.56 | 0.07 | 0.00 |
| BCC | 5 | 35.98 | 39.79 | 11.20 | 7.82 | 0.89 | 3.56 | 0.74 | 0.04 | 0.00 |
| | 6 | 28.84 | 31.84 | 22.16 | 10.47 | 3.41 | 2.62 | 0.60 | 0.06 | 0.00 |
| | 7 | 36.93 | 38.25 | 11.92 | 7.51 | 1.01 | 3.62 | 0.74 | 0.03 | 0.00 |
| | 8 | 34.13 | 37.26 | 14.29 | 8.36 | 1.91 | 3.27 | 0.67 | 0.06 | 0.05 |
| | Avg | 33.97 | 36.79 | 14.89 | 8.54 | 1.81 | 3.27 | 0.69 | 0.05 | 0.01 |
| AIN | 9 | 0.33 | 0.37 | 0.50 | 0.00 | 74.56 | 0.21 | 0.03 | 0.00 | 24.00 |
| | 10 | 0.88 | 0.74 | 0.23 | 0.33 | 73.45 | 0.00 | 0.10 | 0.03 | 24.25 |
| | Avg | 0.61 | 0.56 | 0.37 | 0.17 | 74.01 | 0.11 | 0.07 | 0.02 | 24.13 |
| Inclusion | 11 | 29.53 | 23.00 | 29.89 | 12.40 | 2.45 | 2.00 | 0.60 | 0.00 | 0.14 |
| | 12 | 9.78 | 9.15 | 9.94 | 51.42 | 0.00 | 1.87 | 0.21 | 17.57 | 0.06 |
| | Avg | 19.66 | 16.08 | 19.92 | 31.91 | 1.23 | 1.94 | 0.41 | 8.79 | 0.10 |
| Max | | 36.93 | 39.79 | 29.89 | 51.42 | 74.56 | 3.62 | 0.74 | 17.57 | 24.25 |
| Min | | 0.33 | 0.37 | 0.23 | 0.00 | 0.00 | 0.00 | 0.03 | 0.00 | 0.00 |
| Average | | 25.21 | 22.91 | 18.02 | 11.92 | 13.91 | 1.99 | 0.49 | 1.50 | 4.04 |
| Standard Deviation | | 13.40 | 13.47 | 11.40 | 13.11 | 28.09 | 1.17 | 0.24 | 5.06 | 9.38 |

As previously discussed, there are significant differences observed in the magnitude of Cr and Ni levels in the FCC and BCC phases. Spectrum numbers 1-4 and 5-8, respectively, investigate these more closely, and as expected, the FCC phase presents much richer in nickel, at an average of 29.01 wt.% compared to the BCC, where it is observed at 14.89 wt.%. The inverse occurs with Cr, where it is in abundance in the BCC at 36.79 wt.%, with it depleted to 23.64 wt.% in the FCC. Whilst not having the most significant absolute difference between these two phases, Mo presents the 2nd largest relative variation after Ni, almost doubling in abundance from 1.69 wt.% to 3.27 wt.% from FCC to BCC. Both Mn and Al follow the same trend as Ni, with slight depletions in the BCC relative to the FCC.

The large inclusion probed by spectrums 9 and 10 returns significantly higher levels of Al and N at 74.01 wt.% and 24.13 wt.%, respectively, heavily indicating that it is an AlN precipitate. Other elements are detected; however, they are all present in trace quantities, which is possibly due to the background interference around or underneath the precipitate.

Spectrums 11 and 12 inspected the final areas previously identified in the EDS maps as having higher-than-average levels of Mn, Mo, and S. Spectrum 11 appears to have been misplaced based on its composition, which closely replicated that of the FCC. 12, however, detects significantly higher levels of Mn and S at 51.42 wt.% and 17.57 wt.%, respectively. This indicates the presence of MnS inclusions.

7.7.3 CR

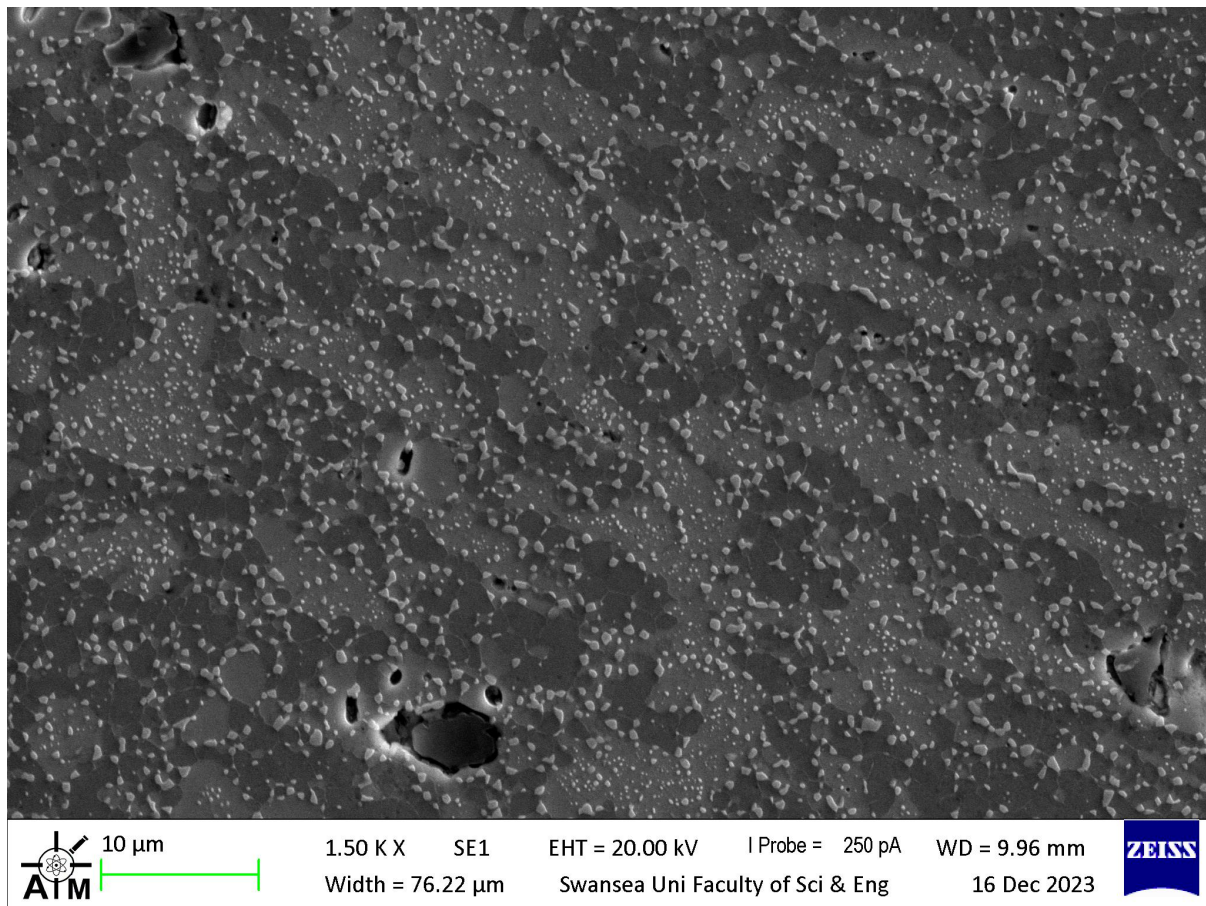


Figure 92 SEM micrograph of CR HEAX at 1500x magnification

The microstructure of CR HEAX in Figure 92 shares similarities with that of Figure 69 and Figure 71, with two major phases present interspersed by numerous small inclusions $<1 \mu\text{m}$ in diameter as well as irregular but larger inclusions of between $2 \mu\text{m}$ and $8 \mu\text{m}$ in diameter. What is more distinctive in Figure 92 is the locations of the smaller inclusions relative to the two main phases. Whilst they are regularly observed in the perceived lighter BCC phase, they are small in size and scattered erratically throughout. However, in the FCC, they appear larger, with the majority tending towards the phase boundaries, whilst there is also an indication of a cellular like structure with grain boundaries linking these inclusions. This may also be present in the BCC; however, there is less contrast and therefore makes it less evident.

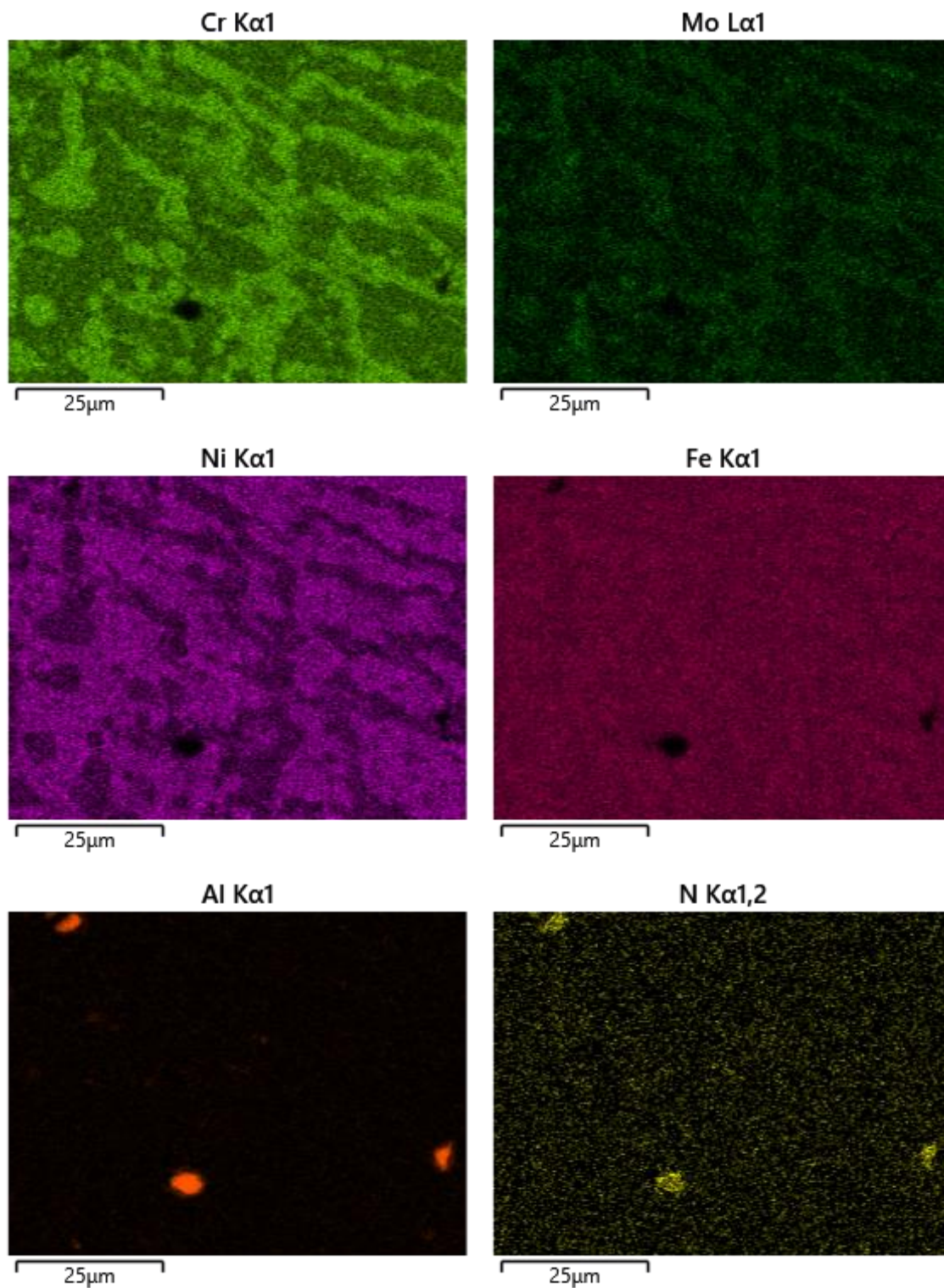


Figure 93 EDS maps of CR HEAX

Table 63 Composition of CR HEAX from EDS maps in Figure 93

| Element | Fe | Cr | Ni | Mn | Al | Mo | Si | N |
|----------|------|-------|-------|------|------|------|-----|------|
| Weight % | 31.9 | 27.73 | 24.49 | 9.63 | 3.18 | 2.29 | 0.5 | 0.28 |

EDS maps in Figure 93 of the area in Figure 92 show increases in Cr and Mo levels in the BCC phase, a diminished Ni concentration, and a slight decrease in Fe relative to the FCC. The large inclusions described previously show a deprivation of all elements except those of Al and N, implying they are AlN inclusions, and at this magnification, it is difficult to distinguish any compositional differences at the sites of the smaller inclusions in the EDS maps. No obvious variations were observed in maps depicting Si and Mn, other than impoverished regions coinciding with the aforementioned AlN inclusions.

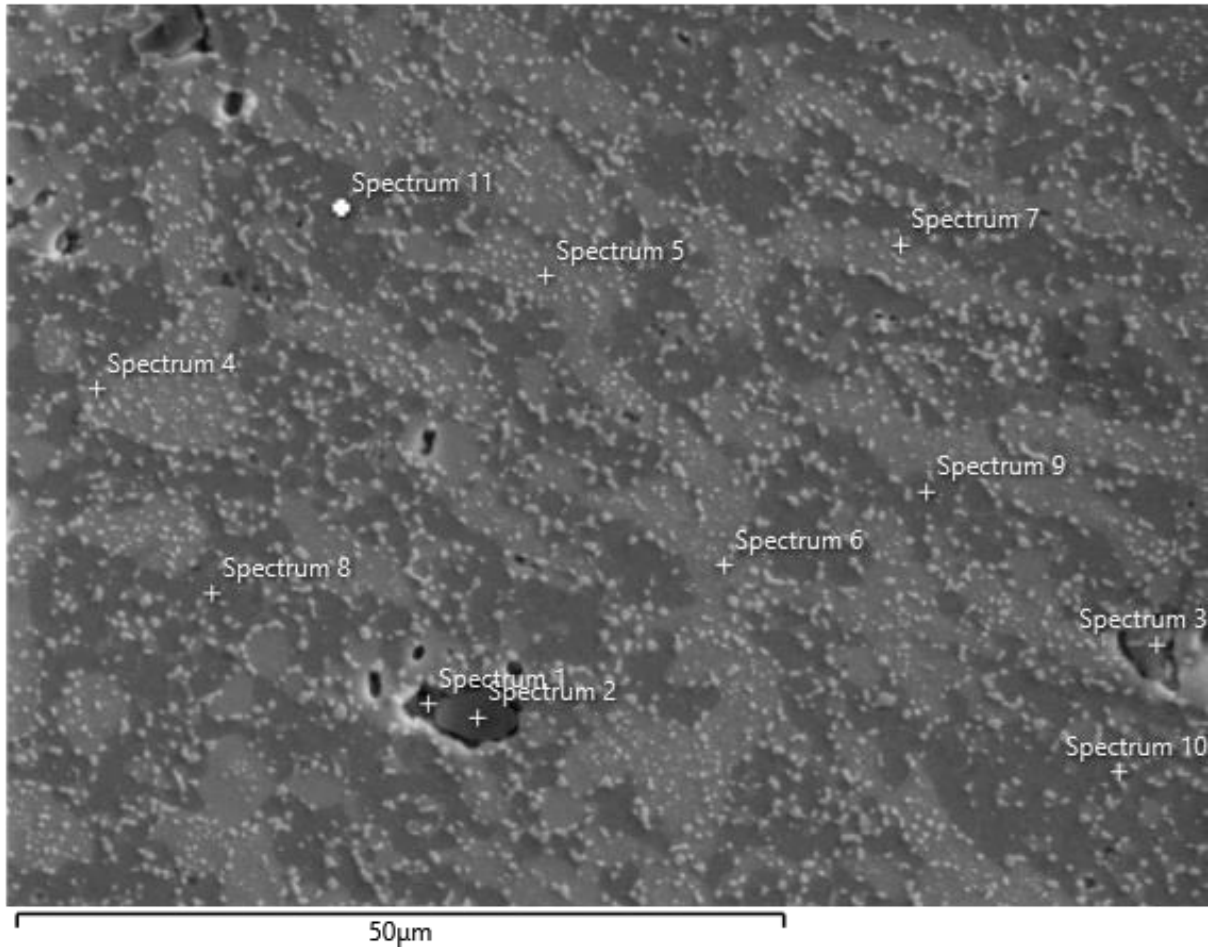


Figure 94 EDS point scan map of CR HEAX

Table 64 Point scan analysis of CR HEAX shown in Figure 94 (wt.%)

| Region | Spectrum No. | Fe | Cr | Ni | Mn | Al | Mo | N | Si |
|---------------------------|--------------|-------|-------|-------|-------|-------|------|-------|------|
| AIN | 1 | 28.82 | 32.97 | 22.39 | 11.16 | 2.36 | 1.33 | 0.34 | 0.61 |
| | 2 | 1.65 | 2.03 | 0.96 | 0.68 | 70.27 | 0.3 | 23.97 | 0.15 |
| | 3 | 9.64 | 11.51 | 5.4 | 3.09 | 54.52 | 1.17 | 14.38 | 0.28 |
| | Avg | 13.37 | 15.50 | 9.58 | 4.98 | 42.38 | 0.93 | 12.90 | 0.35 |
| BCC | 4 | 28.83 | 35.36 | 20.38 | 9.02 | 2.14 | 3.59 | 0 | 0.69 |
| | 5 | 32.69 | 36.21 | 17.14 | 8.38 | 1.1 | 3.77 | 0 | 0.71 |
| | 6 | 21.16 | 22.1 | 34.63 | 11.32 | 8.06 | 2.19 | 0.1 | 0.45 |
| | 7 | 32.23 | 36.42 | 16.74 | 8.61 | 1.68 | 3.66 | 0.04 | 0.62 |
| | Avg | 28.73 | 32.52 | 22.22 | 9.33 | 3.25 | 3.30 | 0.04 | 0.62 |
| FCC | 8 | 34.56 | 21.28 | 29.8 | 10.67 | 1.97 | 1.08 | 0.2 | 0.44 |
| | 9 | 33.07 | 21.53 | 30.31 | 10.65 | 2.64 | 1.17 | 0.22 | 0.41 |
| | 10 | 25.49 | 23.58 | 33.1 | 10.72 | 5.35 | 1.03 | 0.44 | 0.29 |
| | 11 | 29.38 | 19.31 | 33.33 | 11.32 | 4.94 | 0.89 | 0.47 | 0.36 |
| | Avg | 30.63 | 21.43 | 31.64 | 10.84 | 3.73 | 1.04 | 0.33 | 0.38 |
| Max | | 34.56 | 36.42 | 34.63 | 11.32 | 70.27 | 3.77 | 23.97 | 0.71 |
| Min | | 1.65 | 2.03 | 0.96 | 0.68 | 1.1 | 0.3 | 0 | 0.15 |
| Average | | 25.23 | 23.85 | 22.2 | 8.69 | 14.09 | 1.83 | 3.65 | 0.46 |
| Standard Deviation | | 10.55 | 10.91 | 11.46 | 3.57 | 24.22 | 1.26 | 7.97 | 0.18 |

Spectra 1-3 in Table 64 were placed to identify the compositions of some of the AIN inclusions throughout the alloy. 2 and 3 were successful, returning average Al and N concentrations of 62.40 wt.% and 19.18 wt.%, respectively; however, the composition of spectrum 1 is very similar to that of the BCC phase, and it is therefore concluded that there are cavities around the AIN inclusion. At the 1500x magnification in Figure 94 it is difficult to accurately identify whether the points lie precisely on the small inclusions running through the phases, or on the phase itself. However, significant compositional differences identified when investigating these regions facilitate assumptions to be made.

Spectrums 4, 5 and 7 record similar compositions with elevated levels of Cr and reduced Ni concentration, indicative of the BCC_B2 phase. However, it could be postulated that, based on the reduced Al, increased Mo, and a Cr reading over 6 wt.% higher than the predicted BCC_B2, these spectrums could be identifying the σ phase. Conversely, spectrum 6 appears to be located on one of the inclusions within the phase, producing a composition that correlates more with the BCC_B2#2 composition predicted by Thermo-Calc. Spectra 8-11 exhibit similar compositions for Cr, Mn and Mo; however, there are notable differences between 8/9 and 10/11. The former two points return an average Fe concentration 6.38 wt.% higher and average Ni and Al levels 3.16 wt.% and 2.84 wt.% lower, respectively than the latter. Spectra 8 and 9 therefore show compositions that suggest the

presence of the FCC phase in Table 54, whereas 10 and 11 compare with the BCC_B2#2 also presented by spectrum 6.

7.8 Corrosion Testing

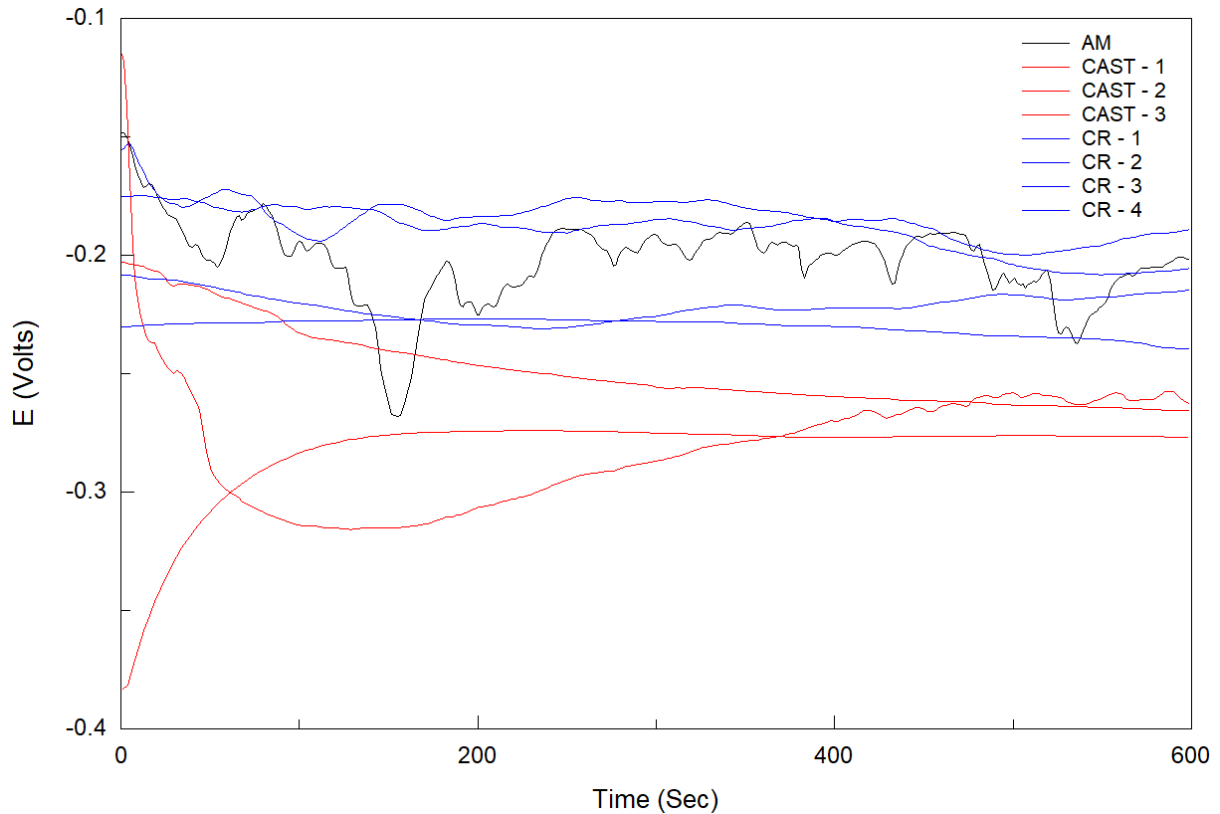


Figure 95 OCP plots for HEAX AM, cast and CR over 600s

The OCP plots for HEAX in Figure 95 show repeatable equilibrium profiles within each manufacturing route. Both the CR and cast specimens show smooth scan patterns across the duration of the tests; however, the AM is notably less stable, with sharp variations in potential of up to 0.065 V. Whilst there was only one sample to conduct analysis on, this erraticism could indicate a larger range of OCP values had more samples been manufactured. The OCP data extracted and displayed in Table 65 does, however, show that the AM sample had the noblest OCP at -0.202 V, whereas the cast sample had the lowest at -0.269. The exceptionally low OCP error observed in the cast and CR samples shows superb reliability with standard deviations of 0.007 and 0.021, respectively.

Table 65 Summary of HEAX corrosion data for each manufacturing method

| Sample | Optical Density (%) | Avg OCP (V) | Error (SD) | Avg E_{corr} (V) | E_{corr} (SD) | Avg E_{pit} (V) | E_{pit} (SD) | Avg E_r (V) |
|--------|---------------------|-------------|------------|--------------------|-----------------|-------------------|----------------|---------------|
| AM | 98.81 | -0.202 | N/A | -0.208 | N/A | 0.038 | N/A | -0.324 |
| Cast | 98.98 | -0.269 | 0.007 | -0.303 | 0.050 | 0.308 | 0.339 | 0.036 |
| CR | 99.05 | -0.212 | 0.021 | -0.205 | 0.011 | -0.057 | 0.024 | -0.321 |

As with HEA1, the majority of HEAX samples do not appear to enter a passive phase after E_{corr} is reached. Once again, the predefined current of 0.0002A is used to define a point across the scans at which point the E_{pit} would be reached if it indeed occurred. This also allows comparisons to be made across the manufacturing processes and with different alloys.

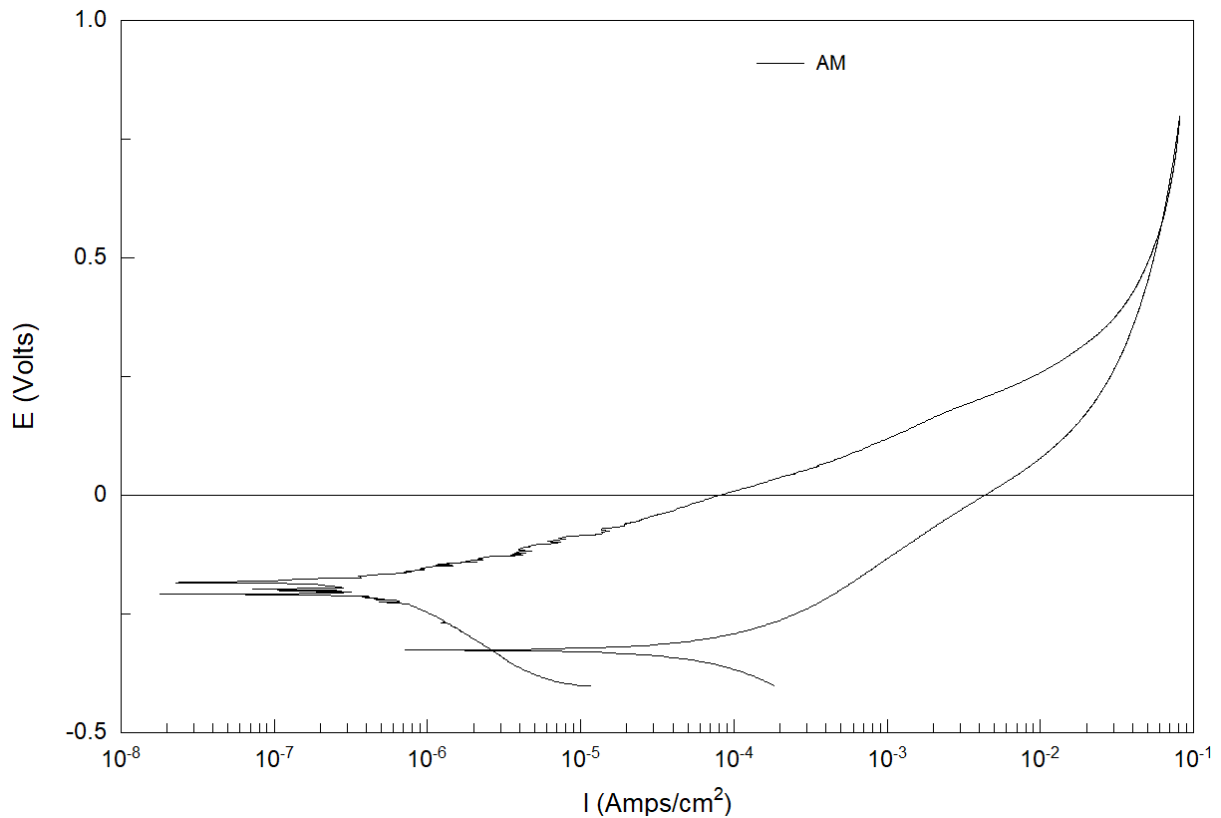


Figure 96 Cyclic polarisation plot for AM HEAX

The AM specimen for HEAX presented in Figure 96 presents a smooth increase in current density once E_{corr} is reached at -0.208 V, before reaching an E_{pit} of 0.038 V at the predetermined point of 0.0002A. Other than a slightly unstable region between the E_{corr} and -0.0035 V, there are no indications that a strong enough passive layer has formed to protect the corrosion sites and prevent further degradation.

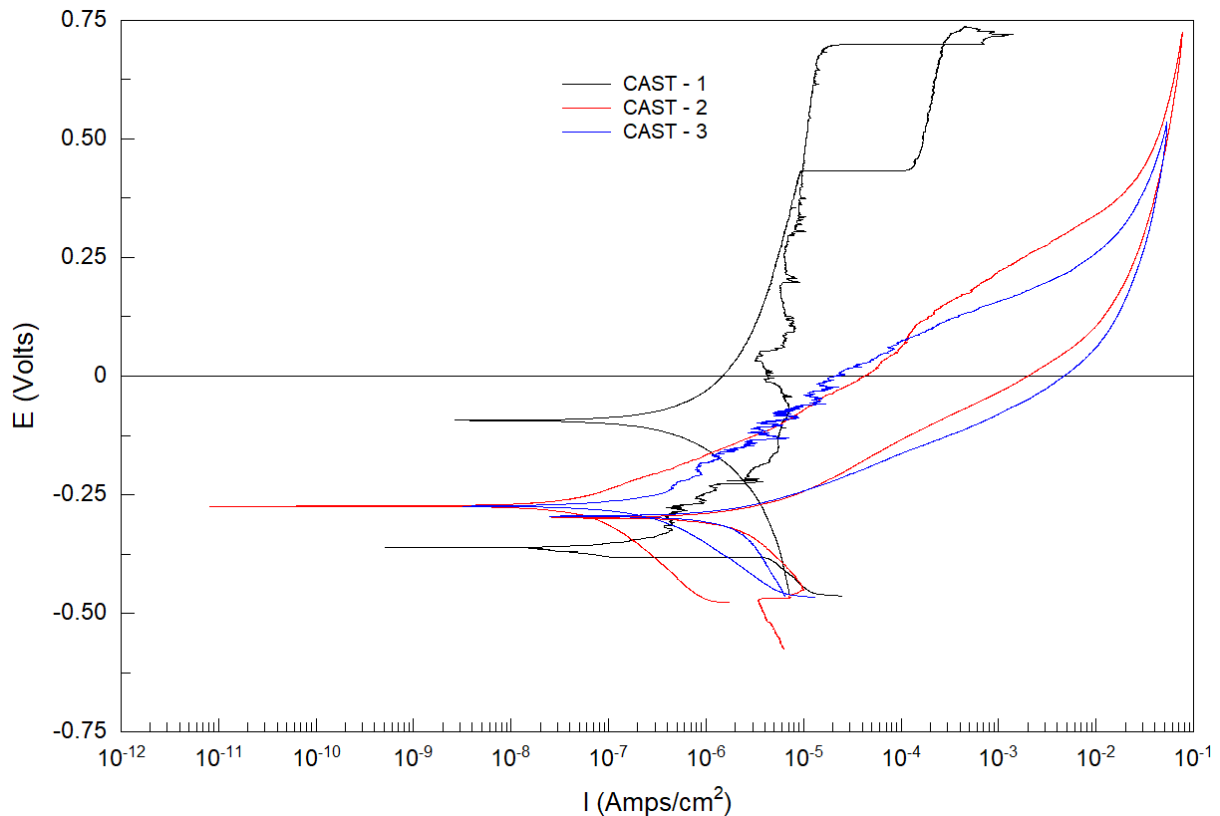


Figure 97 Cyclic polarisation plots for cast HEAX

The CP scans of cast HEAX in Figure 97 show 2 repeats with a high degree of similarity with identical E_{corr} values of -0.274 V and one with a vastly different profile. Cast 1 presents an unusually low E_{corr} of -0.361 V compared to its OCP of -0.263 V, before entering a clear passive phase as the potential is further increased up till the E_{pit} is reached at 0.699 V. Contrary to samples 2 and 3, this E_{pit} is distinct instead of having to be defined by a set current density. Samples 2 and 3 both see increases in their current densities as the potential is increased, showing a more generalised corrosion attack, with only sample 3 showing signs of passivation, whilst not significant enough to change the trajectory of the scan profile in the region before E_{pit} is defined. Whilst the average E_{pit} across the 3 tests is 0.308 V, this decreases dramatically to 0.113 V when test 1 is discounted. The standard deviation of these two values also drops from 0.339 to 0.020 when the same process is applied. Due to this, more data is necessary to determine whether CAST - 1 was an anomaly, or whether its apparent superior E_{pit} was due to any number of possible causes.

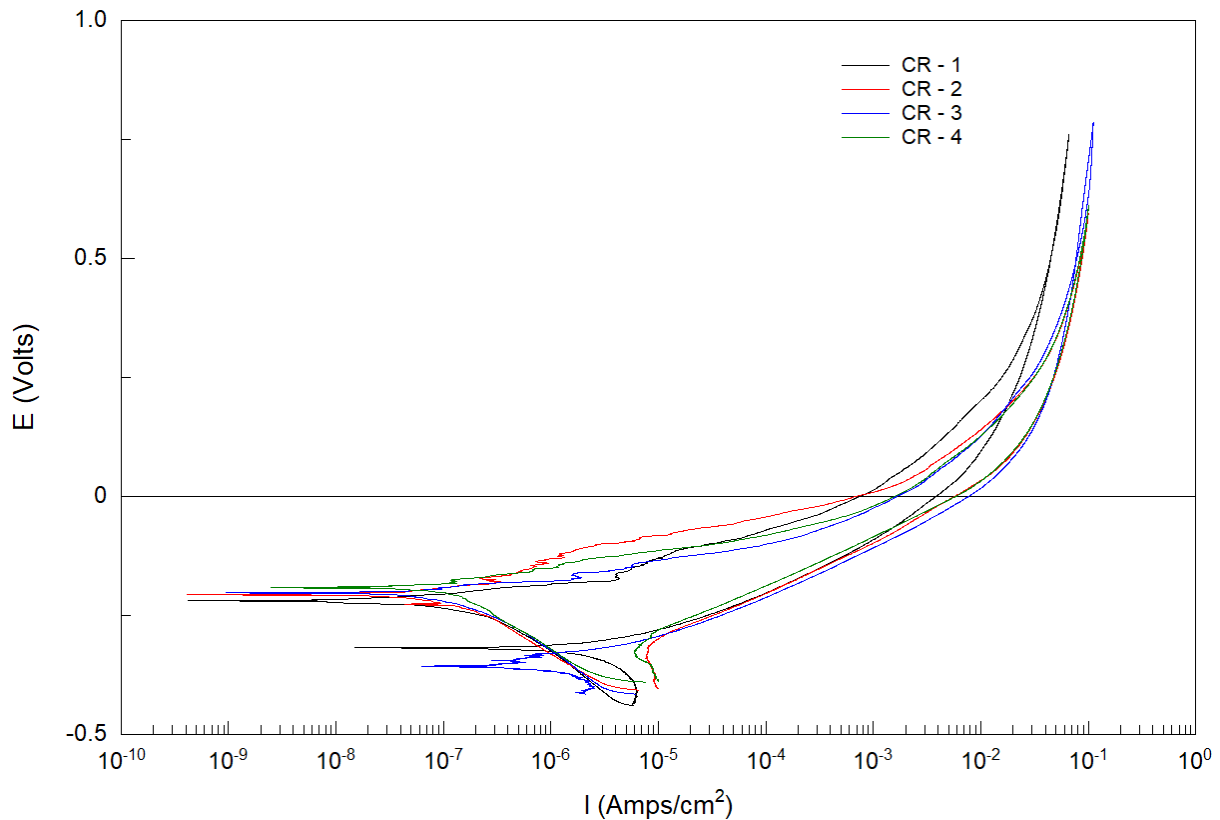


Figure 98 Cyclic polarisation plots for CR HEAX

The 4 CP scans for CR HEAX presented in Figure 98 display exceptional repeatability. This is amplified when considering the error of key metrics in Table 65 such as the E_{pit} and E_{corr} , with the standard deviations calculated as 0.011 and 0.024. However, the region between the E_{corr} and E_{pit} does not imply much, if any, passivation occurred, with the potential only having to increase on average by 0.148 V before the current density of 0.0002A is reached, defining the E_{pit} .

7.9 Discussion

The issues related to the production of the HEAX alloy through AM were down to numerous factors such as, but not limited to, the differences in thermomechanical properties of the Mo and bulk alloy, the discrete PSDs noted in Figure 76, Figure 77, and Figure 78, and in turn, the rheological differences these generated. The flowability of metal powders is crucial, significantly influencing part quality [202]. Flowability refers to the ability of powder particles to distribute uniformly during processes like spreading and layering. Key factors that impact flowability include particle size and distribution, particle shape, surface properties, density, and agglomeration [51,180,202]. Figure 76 of the Mo powder shows a significantly smaller particle size fraction with a sub-optimal polyhedral morphology and significant agglomeration, which could have led to poor flowability or a variation in the powder bed's packing density.

The Thermo-Calc equilibrium phase diagram for HEAX in Figure 81 shows much more disorder between 800 °C and 1250 °C due to the addition of Mo with a significant reduction in the maximum φ_i of the FCC_L12 phase as well as an increase in the φ_i of the BCC_B2#2 and a broadening of the equilibrium range of the BCC_B2#2 and BCC_B2 phases. Literature also suggests that the addition of Mo is likely to increase the σ phase formation [119,124].

This increased disorder is also observed in the cast and CR XRD spectra in Figure 82, however, the AM only clearly presents the BCC and FCC phases due to the rapid cooling rates preventing other phases from forming in addition to the sluggish diffusion effect of HEAs [91–93,105,196–198]. The additional peaks between 39 ° and 52 °, as seen in CR HEA1, are attributed to σ formation; however, some of the additional peaks likely belong to the secondary BCC phase. The AM and cast sample's phase proportions are vastly different from those of HEA1, with the former presenting a majority BCC phase. Both changes are theorised to have occurred due to the extension of the BCC_B2 phase from 1144 °C in HEA1 to 1064 °C in HEAX and the less substantial φ_i of FCC_L12.

EDS of the first AM sample showed alloying of the Mo addition within the bulk but not a homogenous distribution, with a range of 0.9 wt.% to 6.26 wt.% of the points analysed. A significant lack of fusion pore is also seen with a high concentration of Al. The analysis of the AM corrosion sample, however, shows a much greater compositional homogeneity, with even elemental distribution across the majority of the surface than the first. The significant difference in surface chemistry between these two samples built with the same parameters highlights the instability of the alloy in this manufacturing method. Further parameter optimisation and changes to component geometry, amongst other factors, need to be evaluated before additional testing. MnS inclusions are observed in the EDS maps of the cast HEAX sample, as well as a prominent AlN inclusion. Similar questions are posed about discerning between the composition of the BCC and σ phase with much higher Cr and much lower Ni and Al present than expected in the BCC. Replicating the structure of CR HEA1, CR HEAX images and EDS show significant amounts of high Ni, high Al BCC_B2#2 forming at the BCC_B2 and FCC_L12 boundary, potentially creating further opportunity for selective dissolution and reducing the alloys corrosion resistance [199].

As discussed previously, controlling defects such as compositional heterogeneity and porosity is paramount when attempting to improve the corrosion resistance of an alloy [190,192,193]. Like HEA1, there is little to suggest that any of the manufacturing routes consistently result in samples that have any inherent passivation; therefore, E_{pit} values do not signify the breakdown potential of an oxide layer over a pit.

7.10 Conclusions

- Whilst HEAX was produced by AM, significant difficulties were encountered in the printing process due to the differences in the two materials PSD as well as powder morphologies and thermomechanical properties. The alloying of the Mo addition was shown to be largely successful in the corrosion sample; however, areas of inhomogeneity are observed on the alloy where complete diffusion has not occurred.
- The 2.4 wt.% Mo addition is predicted by Thermo-Calc to increase the magnitude of phase competition between 1000 °C and the formation of the first BCC phase at 1416 °C. This disorder is replicated in the XRD spectra of the cast and CR samples with an increase in the number of peaks in the 39 ° to 52 ° range of 2θ , suggesting the presence of a σ and secondary BCC phase. The phase proportions calculated from these spectra show drastic changes in the primary FCC/BCC ratio. Dendritic structures are observed in the cast HEAX microstructure comparable to HEA1, with similar trends of elemental segregation. The CR microstructure is again similar to HEA1, with the secondary BCC phase present at the inter-phase boundaries.
- The OCP and CP tests performed to determine whether HEAX had a greater corrosion resistance than HEA1 were inconclusive due to a mixture of results supporting both arguments. AM HEAX was the only route to show a greater corrosion resistance than its HEA1 counterpart across all metrics.

8 Final Discussion

Whilst in-situ additions have been shown in literature to produce parts with high density and improved properties, it has been documented that problems can arise when the alloying fraction tends to and exceeds 5 at.% [136,139–141]. This has been encountered within the work presented in Chapter 7, but distinguishing between the causes based on the current data is more difficult. Comparing the rheometric results of 316L, HEA1, and HEAX, their FRI are very similar at 1.17, 1.11 and 1.11, respectively, suggesting all are insensitive to changes in flow rate. However, there are a 0.3 g/ml and 7.32 g reduction in the CBD and split masses between HEA1 and HEAX. This suggests that whilst the Mo in HEAX was theorised to increase the packing density of the powder due to its smaller PSD, this has not occurred. An explanation for this could be the agglomeration of Mo particles, as seen in Figure 76, actually reducing the ability for the particles to tessellate, reducing the CBD and, therefore, the split mass. When comparing the SE of the 3 powders, HEA1 reports the lowest value of 2.53 mJ/g, followed by 316L and HEAX and 2.89 mJ/g and 3.95 mJ/g, respectively. The values for 316L and HEA1 correlate with similar results reported in literature for 316L using the same testing apparatus, of between 1.84 mJ/g and 2.58 mJ/g, whereas HEAX exceeds it by over 54 % [202]. This suggests that relative to the 316L and HEA1 powder, HEAX demonstrates significantly more cohesion and, therefore, poorer flowability. However, literature also states that a SE of below 5 is considered to demonstrate low cohesion, so it is, therefore, less likely that the PSD of the HEAX is the leading cause of the processing issues reported previously [202]. Due to this, it is hypothesised that the thermomechanical properties of the 2.4 wt.% Mo addition was the primary cause for the difficulties encountered.

One of the features of 316L that provides excellent corrosion resistance is its fully austenitic microstructure [29,81,184]. The majority single phase microstructure, absent of inclusions or precipitates, eliminates the effects of galvanic corrosion, creates a consistent passive oxide layer and results in its superb corrosion resistance [29,66]. This single phase is displayed in Figure 48 and Table 26, with all 4 manufacturing methods achieving an austenitic phase proportion of 96.73 % or above. HEAs are renowned for their preference for forming single solid solutions; however, this has not been seen in the majority of the analysis of the microstructures of both HEA1 or HEAX [91,102,104]. The AM HEA1 is closest to achieving this, with an FCC proportion of 94.23 %, with cast and CR at 86.75 % and 87 %, respectively; however, the CR sample does present additional competing phases, seen by the XRD peaks between 43 ° and 59 ° in Figure 62, and the point scan analysis in Table 48. Cast and CR HEAX have similar XRD peaks and microstructures to their HEA1 counterparts, suggesting that the Mo addition has moved the microstructure further away from the single solid solution, including promoting intermetallic phases.

Mixed results were seen when comparing the corrosion resistance of HEAX with HEA1. The AM HEAX sample proved to have a more noble OCP and a higher E_{pit} than its HEA1 counterpart; however, a slight reduction in the potential difference between these values suggests a weakening in the passive oxide layer. This is also indicated by its more negative E_r , perhaps down to large pores, as seen in Figure 85, or due to the non-uniform distribution of the Mo addition. The cast HEAX sample had a more anodic OCP than the HEA1 but outperformed its E_{pit} , indicating a more effective passive film. However, its optical density was more significant and, therefore, should have superior corrosion resistance, assuming all other factors are equal. The CR samples of each HEA exhibited almost identical averaged metrics, with OCPs of -0.212 V and their E_{pit} values separated by just 0.008 V. However, the error in the E_{pit} values of HEA1 was almost 3x that of HEAX. Again, density could be a significant factor when comparing these performances with HEA1 cast and CR densities of 96.25 % and 97.95 %, respectively, vs HEAX densities of 98.98 % and 99.05 %. Comparing the corrosion resistance of both HEAs with the 316L baselines presented in sections 4 and 5 shows a stark relationship, with 316L outperforming the HEAs in every category, particularly with its well-documented high pitting potential [79,81]. The cast samples provide the most even comparison in the absence of factors such as processing parameters, with 316L returning an average E_{pit} of 0.433 V to 0.71 V and 0.133 V for HEA1 and HEAX, respectively. The HEA's relatively poor corrosion resistance could be down to a number of factors analysed during the experimental chapters, including porosity, microstructure, elemental homogeneity, the presence of inclusions and precipitates, and the optimisation of heat treatments in the case of the CR samples. Whilst HEAs and their documented effects are known in some cases to improve certain properties beyond the sum of their elements, this work shows that it is not the case for all HEAs [203].

9 Conclusions and Future Work

9.1 Conclusions

- 316L was produced by LPBF with a range of intentional, process induced porosity to investigate the effect this has on the corrosion resistance and compared to wrought. Increased porosity was observed to have a negative effect on the corrosion resistance of the AM samples as well as their reliability. The high density samples displayed excellent corrosion resistance with E_{pit} values 603 mV greater than that of the wrought, with only slightly poorer reliability.
- A heat treatment and cold rolling schedule was observed to increase the corrosion resistance of 316L, but not by the magnitude anticipated. This demonstrated the critical role surface defects beyond porosity, such as carbide and inclusion formation, play in corrosion resistance.
- There was little to separate the corrosion resistance of HEA1 produced by AM, casting and CR. However, the latter was created with what was later discovered as suboptimal heat treatments. This highlights the vast developments that have been made within the field of HEAs but also that significant knowledge gaps remaining.
- Mo additions to HEA1 creating HEAX were observed through XRD to increase the disorder in the alloy system as predicted by Thermo-Calc. Even in its small quantity, it was seen to increase the BCC phase proportion by 14.49 % in the cast sample and 47.83 % in the AM.
- The benefits of a 2.4 wt.% addition of Mo to HEA1 on its corrosion resistance across 3 different manufacturing processes were inconclusive in all but the AM sample, which did improve slightly. The increased disorder and phase competition and its impact on compositional homogeneity and defects are thought to be a factor in these results.
- Computational tools such as Thermo-Calc for predicting microstructures are incredibly useful and, for the most part, highly accurate. However, their limitations are displayed in this thesis, particularly with new alloy systems like HEAs, shown by the significant variation in phase prediction observed over 2 years.
- The HEAs in this work underperformed in comparison to the corrosion resistance of 316L, showing that HEAs are not inherently corrosion resistant, with a focus needed on reducing the number of phases present and limiting surface defects such as inclusions

9.2 Future Work

Future work, building on what has been presented here, will include investigating the influence of process parameters on the grain size of AM 316L and its effect on passive film formation. Additionally, the newly acquired powder atomiser will be used to create pre-alloyed HEAX powder, amongst other alloys, to better investigate the effect of this addition and the possibility of RAP for AM. Furthermore, design a test that facilitates the corrosion of a tiny examination area ($\sim 500 \mu\text{m}^2$) on the HEA cast and CR specimens that can be analysed before and after to investigate whether a phase or inclusion corrodes preferentially to the bulk. Finally, investigate the effect of the cooling rate on the phase formation and elemental segregation in HEAs in the induction casting process.

10 References

- [1] Bowman E, Koch G, Varney J, Thompson N, Moghissi O, Gould M, et al. International Measures of Prevention, Application, and Economics of Corrosion Technologies Study. NACE International. 2016;(February).
- [2] Cicek V. Corrosion Engineering. John Wiley & Sons; 2014.
- [3] ASTM. ASTM F2792 - 12a Standard Terminology for Additive Manufacturing Technologies, (Withdrawn 2015). ASTM International. 2012.
- [4] Wohlers T, Gornet T, Mostow N, Campbell I, Diegel O, Kowen J, et al. History of Additive Manufacturing. Wohlers Report 2014 - 3D Printing and Additive Manufacturing State of the Industry. 2014.
- [5] Lavery N. Additive Manufacturing. Swansea; 2019 Feb.
- [6] Wohlers T. 3D Printing and Additive Manufacturing State of the Industry. Annual Worldwide Progress Report. Wohlers Report, Executive summary. 2017.
- [7] Larimian T, Kannan M, Grzesiak D, AlMangour B, Borkar T. Effect of energy density and scanning strategy on densification, microstructure and mechanical properties of 316L stainless steel processed via selective laser melting. *Materials Science and Engineering A*. 2020;770.
- [8] Dilip JJS, Zhang S, Teng C, Zeng K, Robinson C, Pal D, et al. Influence of processing parameters on the evolution of melt pool, porosity, and microstructures in Ti-6Al-4V alloy parts fabricated by selective laser melting. *Progress in Additive Manufacturing*. 2017;2(3).
- [9] Gibson I, Rosen D, Stucker B, Khorasani M. *Additive Manufacturing Technologies*. Additive Manufacturing Technologies. Cham: Springer; 2021.
- [10] Frazier WE. Metal additive manufacturing: A review. *J Mater Eng Perform*. 2014 Apr 8;23(6):1917–28.
- [11] Blakey-Milner B, Gradl P, Snedden G, Brooks M, Pitot J, Lopez E, et al. Metal additive manufacturing in aerospace: A review. *Mater Des*. 2021 Nov 1;209:110008.
- [12] Guo N, Leu MC. Additive manufacturing: Technology, applications and research needs. Vol. 8, *Frontiers of Mechanical Engineering*. 2013. p. 215–43.
- [13] Bikas H, Lianos AK, Stavropoulos P. A design framework for additive manufacturing. *International Journal of Advanced Manufacturing Technology*. 2019 Aug 1;103(9–12):3769–83.
- [14] Yang S, Tang Y, Zhao YF. A new part consolidation method to embrace the design freedom of additive manufacturing. *J Manuf Process*. 2015 Oct 1;20:444–9.

- [15] Busachi A, Erkoyuncu J, Colegrove P, Martina F, Watts C, Drake R. A review of Additive Manufacturing technology and Cost Estimation techniques for the defence sector. *CIRP J Manuf Sci Technol*. 2017 Nov 1;19:117–28.
- [16] Günther D, Heymel B, Günther JF, Ederer I. Rapid Prototyping Journal Continuous 3D-printing for additive manufacturing Continuous 3D-printing for additive manufacturing. *Rapid Prototyping Journal Assembly Automation Surface Mount Technology Iss Assembly Automation*. 2006;20(1).
- [17] Ahmed R. Stratasys Showcases New H2000 Infinite Build 3D Printer to Prospects - 3D Printing [Internet]. 2020 [cited 2020 Jul 27]. Available from: <https://3dprinting.com/news/stratasys-showcases-new-h2000-infinite-build-printer-potential-buyers/>
- [18] Seifi M, Gorelik M, Waller J, Hrabe N, Shamsaei N, Daniewicz S, et al. Progress Towards Metal Additive Manufacturing Standardization to Support Qualification and Certification. *JOM*. 2017 Mar 1;69(3):439–55.
- [19] Heiden MJ, Deibler LA, Rodelas JM, Koepke JR, Tung DJ, Saiz DJ, et al. Evolution of 316L stainless steel feedstock due to laser powder bed fusion process. *Addit Manuf*. 2019;25.
- [20] Malekipour E, El-Mounayri H. Common defects and contributing parameters in powder bed fusion AM process and their classification for online monitoring and control: a review. *International Journal of Advanced Manufacturing Technology*. 2018;95(1–4).
- [21] Dev Singh D, Mahender T, Raji Reddy A. Powder bed fusion process: A brief review. *Mater Today Proc*. 2021 Jan 1;46:350–5.
- [22] Ladani L, Sadeghilaridjani M. Review of Powder Bed Fusion Additive Manufacturing for Metals. *Metals* 2021, Vol 11, Page 1391. 2021 Sep 1;11(9):1391.
- [23] Sames WJ, List FA, Pannala S, Dehoff RR, Babu SS. The metallurgy and processing science of metal additive manufacturing. Vol. 61, *International Materials Reviews*. 2016.
- [24] Ziaee M, Crane NB. Binder jetting: A review of process, materials, and methods. *Addit Manuf*. 2019 Aug 1;28:781–801.
- [25] Lores A, Azurmendi N, Agote I, Zuza E. A review on recent developments in binder jetting metal additive manufacturing: materials and process characteristics. *Powder Metallurgy*. 2019 Oct 20;62(5):267–96.
- [26] Mirzababaei S, Pasebani S. A Review on Binder Jet Additive Manufacturing of 316L Stainless Steel. *Journal of Manufacturing and Materials Processing* 2019, Vol 3, Page 82. 2019 Sep 9;3(3):82.

- [27] Dass A, Moridi A. State of the Art in Directed Energy Deposition: From Additive Manufacturing to Materials Design. *Coatings* 2019, Vol 9, Page 418. 2019 Jun 29;9(7):418.
- [28] Ahn DG. Directed Energy Deposition (DED) Process: State of the Art. *International Journal of Precision Engineering and Manufacturing-Green Technology* 2021 8:2. 2021 Feb 15;8(2):703–42.
- [29] Trelewicz JR, Halada GP, Donaldson OK, Manogharan G. Microstructure and Corrosion Resistance of Laser Additively Manufactured 316L Stainless Steel. *JOM*. 2016;68(3).
- [30] Gibson I, Rosen DW, Stucker B, Gibson I, Rosen DW, Stucker B. Medical Applications for Additive Manufacture. In: *Additive Manufacturing Technologies*. 2010.
- [31] Cooper DE, Stanford M, Kibble KA, Gibbons GJ. Additive Manufacturing for product improvement at Red Bull Technology. *Mater Des*. 2012;41.
- [32] FIA. 2020 FORMULA ONE TECHNICAL REGULATIONS. 2019.
- [33] Bray P. Breaking the mould: new horizons in 3D printing [Internet]. 2015 [cited 2020 Mar 12]. Available from: <https://www.telegraph.co.uk/education/stem-awards/power-systems/new-horizons-in-3d-printing/>
- [34] Bandyopadhyay A, Krishna B V., Xue W, Bose S. Application of Laser Engineered Net Shaping (LENS) to manufacture porous and functionally graded structures for load bearing implants. In: *Journal of Materials Science: Materials in Medicine*. 2009.
- [35] Harrysson OLA, Marcellin-Little DJ, Horn TJ. Applications of Metal Additive Manufacturing in Veterinary Orthopedic Surgery. *JOM*. 2015;67(3).
- [36] Bertol LS, Júnior WK, Silva FP da, Aumund-Kopp C. Medical design: Direct metal laser sintering of Ti-6Al-4V. *Mater Des*. 2010;31(8).
- [37] Williams E, Lavery N. Laser processing of bulk metallic glass: A review. *J Mater Process Technol*. 2017;247:73–91.
- [38] Butcher D, Christie S, Brown SGR, Lavery NP. Validated computational modelling techniques for simulating melt pool ejecta in laser powder bed fusion processing. In: *2019 International Solid Freeform Fabrication Symposium*. 2019.
- [39] Philo AM, Brown SGR, Cherry J, Sienz J, Lavery NP. Effects of Hatch Pattern and Laser Parameters on the Multi-Scale Thermal Modelling of Selective Laser Melting. *23rd UK Conference of the Association for Computational Mechanics in Engineering*. 2015;(April):453–6.

- [40] Milward SS, Swygart H, Eccles L, Brown SGR, Lavery NP. Controlling Thermal Expansion with Lattice Structures Using Laser Powder Bed Fusion. In: Solid Freeform Fabrication 2017: Proceedings of the 28th Annual International Solid Freeform Fabrication Symposium. 2017. p. 2139–47.
- [41] Rosser J, Megahed M, Mindt H-W, Brown SGR, Lavery NP. Computational modelling and experimental validation of single in625 line tracks in laser powder bed fusion. In: 2019 International Solid Freeform Fabrication Symposium. 2019.
- [42] Sillars SA, Sutcliffe CJ, Philo AM, Brown SGR, Sienz J, Lavery NP. The three-prong method: a novel assessment of residual stress in laser powder bed fusion. *Virtual Phys Prototyp.* 2018;13(1):20–5.
- [43] Cherry JA, Davies HM, Mehmood S, Lavery NP, Brown SGR, Sienz J. Investigation into the effect of process parameters on microstructural and physical properties of 316L stainless steel parts by selective laser melting. *International Journal of Advanced Manufacturing Technology.* 2015;76(5–8):869–79.
- [44] Philo AMM, Butcher D, Sillars S, Sutcliffe CJ, Sienz J, Brown SGR, et al. A multiphase CFD model for the prediction of particulate accumulation in a laser powder bed fusion process. In: *Minerals, Metals and Materials Series.* 2018. p. 65–76.
- [45] Philo AM, Mehraban S, Holmes M, Sillars S, Sutcliffe CJ, Sienz J, et al. A pragmatic continuum level model for the prediction of the onset of keyholing in laser powder bed fusion. *International Journal of Advanced Manufacturing Technology.* 2019;101(1–4):697–714.
- [46] Philo A, Lavery NP, Brown SGR, Cherry J, Sienz J, Joannou J, et al. Comparison and Validation of Gas Flow Models in a Powder Bed Selective Laser Melting Process. In: *23rd UK Conference of the Association for Computational Mechanics in Engineering (ACME 2015).* 2015.
- [47] Philo AM, Sutcliffe CJ, Sillars S, Sienz J, Brown SGR, Lavery NP. A Study into the Effects of Gas Flow Inlet Design of the Renishaw AM250 Laser Powder Bed Fusion Machine Using Computational Modeling. In: *2017 International Solid Freeform Fabrication Symposium.* 2017.
- [48] Murray K, Kearns MA, Davies PA, Lavery NP, Brown SGR, Sienz J, et al. The influence of powder ageing characteristics on 316L stainless steel processed by laser based powder bed fusion. In: *Proceedings Euro PM 2017: International Powder Metallurgy Congress and Exhibition.* 2017.
- [49] Peng T, Chen C. Influence of energy density on energy demand and porosity of 316L stainless steel fabricated by selective laser melting. *International Journal of Precision Engineering and Manufacturing - Green Technology.* 2018;5(1).

- [50] Giordimaina A. Physical Verification of the Melt Pool in Laser-Bed Fusion. Swansea University; 2017.
- [51] Mathias LET, Pinotti VE, Batistão BF, Rojas-Arias N, Figueira G, Andreoli AF, et al. Metal powder as feedstock for laser-based additive manufacturing: From production to powder modification. *Journal of Materials Research* 2023 39:1. 2023 Dec 29;39(1):19–47.
- [52] Carpenter A. Comparison of Plasma and Electrode Inert Gas Atomized Powder [Internet]. 2020. Available from: https://cdn2.hubspot.net/hubfs/6205315/carpenter_additive/pdf/20200416_EB-PBF_Ti_Equivalency_Whitepaper_Screen-combo.pdf
- [53] Moghimian P, Poirié T, Habibnejad-Korayem M, Zavala JA, Kroeger J, Marion F, et al. Metal powders in additive manufacturing: A review on reusability and recyclability of common titanium, nickel and aluminum alloys. *Addit Manuf.* 2021 Jul 1;43:102017.
- [54] Grainger L. Investigating the effects of multiple re-use of Ti6Al4V powder in additive manufacturing (AM). White Paper, Renishaw. 2016;
- [55] Tan KL, Yeo SH. Surface modification of additive manufactured components by ultrasonic cavitation abrasive finishing. *Wear.* 2017;378–379.
- [56] Kumbhar NN, Mulay A V. Post Processing Methods used to Improve Surface Finish of Products which are Manufactured by Additive Manufacturing Technologies: A Review. *Journal of The Institution of Engineers (India): Series C.* 2018 Aug 1;99(4):481–7.
- [57] Gisario A, Barletta M, Veniali F. Laser polishing: a review of a constantly growing technology in the surface finishing of components made by additive manufacturing. *The International Journal of Advanced Manufacturing Technology* 2022 120:3. 2022 Feb 21;120(3):1433–72.
- [58] Zhang B, Zhu L, Liao H, Coddet C. Improvement of surface properties of SLM parts by atmospheric plasma spraying coating. *Appl Surf Sci.* 2012 Dec 15;263:777–82.
- [59] Jr Callister W, Rethwisch D. *Callister's materials science and engineering.* 2020.
- [60] Lavery NP, Cherry J, Mehmood S, Davies H, Girling B, Sackett E, et al. Effects of hot isostatic pressing on the elastic modulus and tensile properties of 316L parts made by powder bed laser fusion. *Materials Science and Engineering A.* 2017;693(March):186–213.
- [61] Grech IS, Sullivan JH, Lancaster RJ, Plummer J, Lavery NP. The optimisation of hot isostatic pressing treatments for enhanced mechanical and corrosion performance of stainless steel 316L produced by laser powder bed fusion. *Addit Manuf.* 2022;58.

- [62] Raes HDB. Hot isostatic press technology. Powder Metallurgy. 1983;26(4).
- [63] M2A. Advanced Metallurgy. Swansea University; 2018.
- [64] Ashby M. Teach Yourself Phase Diagrams and Phase Transformations Phase Diagrams and Phase Transformations [Internet]. 2009 [cited 2021 Jun 4]. Available from: www.teachingresources.grantadesign.com
- [65] Llewellyn DT, Hudd RC. Steels - Metallurgy and Applications (3rd Edition). Elsevier. 1998.
- [66] Lodhi MJK, Deen KM, Haider W. Corrosion behavior of additively manufactured 316L stainless steel in acidic media. Materialia (Oxf). 2018;2.
- [67] Inc LA. What is the difference between duplex and super duplex stainless steels? [Internet]. [cited 2020 Apr 16]. Available from: <https://www.langleyalloys.com/en/knowledge-advice/difference-duplex-super-duplex-stainless-steels/>
- [68] Global stainless steel production 2019 [Internet]. 2020 [cited 2020 Jul 17]. Available from: <https://www.statista.com/statistics/223028/world-stainless-steel-production/>
- [69] Stainless Steel Grades - Continental Steel & Tube Company [Internet]. [cited 2021 Jun 4]. Available from: <https://continentalsteel.com/stainless-steel/grades/>
- [70] Stainless Steel - Grade 316L (UNS S31603) [Internet]. [cited 2021 Jun 4]. Available from: <https://www.azom.com/article.aspx?ArticleID=2382>
- [71] Stainless steel: The role of nickel | Nickel Institute [Internet]. [cited 2021 Jun 4]. Available from: <https://nickelinstitute.org/about-nickel/stainless-steel/>
- [72] Miller JT, Martin HJ, Cudjoe E. Comparison of the effects of a sulfuric acid environment on traditionally manufactured and additive manufactured stainless steel 316L alloy. Addit Manuf. 2018;23.
- [73] Zhou C, Hu S, Shi Q, Tao H, Song Y, Zheng J, et al. Improvement of corrosion resistance of SS316L manufactured by selective laser melting through subcritical annealing. Corros Sci. 2020;164.
- [74] Ravi Kumar B, Mahato B, Singh R. Influence of cold-worked structure on electrochemical properties of austenitic stainless steels. Metall Mater Trans A Phys Metall Mater Sci. 2007 Sep;38 A(9):2085–94.
- [75] Tayyab K, Farooq A, Alvi A, Nadeem A, Deen K. Corrosion behavior of cold-rolled and post heat-treated 316L stainless steel in 0.9 wt% NaCl solution. International Journal of Minerals, Metallurgy and Materials. 2021 Mar 1;28(3):440–9.

- [76] Xu Y, Jiao H, Qiu W, Devesh R, Misra K, Li J. Effect of cold rolling process on microstructure, texture and properties of strip cast Fe-2.6% Si steel. *Materials*. 2018;11(7).
- [77] Wu W, Ni S, Liu Y, Song M. Effects of cold rolling and subsequent annealing on the microstructure of a HfNbTaTiZr high-entropy alloy. *J Mater Res*. 2016 Dec 28;31(24):3815–23.
- [78] Kong D, Dong C, Ni X, Li X. Corrosion of metallic materials fabricated by selective laser melting. *Npj Mater Degrad*. 2019;3(1).
- [79] Vignal V, Voltz C, Thiébaud S, Demésy M, Heintz O, Guerraz S. Pitting Corrosion of Type 316L Stainless Steel Elaborated by the Selective Laser Melting Method: Influence of Microstructure. *J Mater Eng Perform*. 2021 Jul 1;30(7):5050–8.
- [80] Paulraj P, Garg R. EFFECT OF INTERMETALLIC PHASES ON CORROSION BEHAVIOR AND MECHANICAL PROPERTIES OF DUPLEX STAINLESS STEEL AND SUPER-DUPLEX STAINLESS STEEL. *Advances in Science and Technology Research Journal*. 2015 Aug 13;9(27):87–105.
- [81] Sander G, Thomas S, Cruz V, Jurg M, Birbilis N, Gao X, et al. On The Corrosion and Metastable Pitting Characteristics of 316L Stainless Steel Produced by Selective Laser Melting. *J Electrochem Soc*. 2017;164(6).
- [82] Williams G. *Electrochemistry*. 2019.
- [83] Lodhi MJK, Deen KM, Haider W. Corrosion behavior of additively manufactured 316L stainless steel in acidic media. *Materialia (Oxf)*. 2018;2.
- [84] Miller JT, Martin HJ, Cudjoe E. Comparison of the effects of a sulfuric acid environment on traditionally manufactured and additive manufactured stainless steel 316L alloy. *Addit Manuf*. 2018;23.
- [85] Trelewicz JR, Halada GP, Donaldson OK, Manogharan G. Microstructure and Corrosion Resistance of Laser Additively Manufactured 316L Stainless Steel. *JOM*. 2016;68(3).
- [86] Sander G, Thomas S, Cruz V, Jurg M, Birbilis N, Gao X, et al. On The Corrosion and Metastable Pitting Characteristics of 316L Stainless Steel Produced by Selective Laser Melting. *J Electrochem Soc*. 2017;164(6).
- [87] Cantor B, Chang ITH, Knight P, Vincent AJB. Microstructural development in equiatomic multicomponent alloys. *Materials Science and Engineering A*. 2004 Jul 1;375–377(1-2 SPEC. ISS.):213–8.
- [88] Chen TK, Shun TT, Yeh JW, Wong MS. Nanostructured nitride films of multi-element high-entropy alloys by reactive DC sputtering. *Surf Coat Technol*. 2004 Nov 1;188–189(1-3 SPEC.ISS.):193–200.

- [89] Hsu CY, Yeh JW, Chen SK, Shun TT. Wear resistance and high-temperature compression strength of Fcc CuCoNiCrAl_{0.5}Fe alloy with boron addition. *Metall Mater Trans A Phys Metall Mater Sci* [Internet]. 2004 [cited 2021 Jun 7];35 A(5):1465–9. Available from: <https://link.springer.com/article/10.1007/s11661-004-0254-x>
- [90] Huang PK, Yeh JW, Shun TT, Chen SK. Multi-principal-element alloys with improved oxidation and wear resistance for thermal spray coating. *Adv Eng Mater* [Internet]. 2004 Feb 5 [cited 2021 Jun 7];6(1–2):74–8. Available from: <http://www.aem-journal.de>
- [91] Murty BS, Yeh JW, Ranganathan S, Bhattacharjee PP. *High-Entropy Alloys*. 2019.
- [92] Miracle DB, Senkov ON. A critical review of high entropy alloys and related concepts. *Acta Mater*. 2017;122:448–511.
- [93] Miracle DB, Miller JD, Senkov ON, Woodward C, Uchic MD, Tiley J. Exploration and development of high entropy alloys for structural applications. *Entropy*. 2014;16(1):494–525.
- [94] Zhang Y, Zhou YJ, Lin JP, Chen GL, Liaw PK. Solid-solution phase formation rules for multi-component alloys. *Adv Eng Mater*. 2008;10(6):534–8.
- [95] Yusenkov KVK V, Riva S, Crichton WAWA, Spektor K, Bykova E, Pakhomova A, et al. High-pressure high-temperature tailoring of High Entropy Alloys for extreme environments. *J Alloys Compd*. 2018;738:491–500.
- [96] Butcher D, Cullen JCT, Barron N, Mehraban S, Calvo-Dahlborg M, Brown SGR, et al. Development of a High Entropy Alloy AlX(CoCrCuFeNi)_{1-X} for Diverse Security Applications. In: *TMS 2022 151st Annual Meeting & Exhibition Supplemental Proceedings*. Cham: Springer International Publishing; 2022. p. 543–54.
- [97] Cieslak J, Tobola J, Przewoznik J, Berent K, Dahlborg U, Cornide J, et al. Multi-phase nature of sintered vs. arc-melted Cr_xAlFeCoNi high entropy alloys - experimental and theoretical study. *J Alloys Compd*. 2019;801.
- [98] Riva S, Yusenkov KVK V, Lavery NPNP, Jarvis DJDJ, Brown SGRSGR. The scandium effect in multicomponent alloys. *International Materials Reviews*. 2016;61(3):203–28.
- [99] Riva S, Brown SGR, Lavery NP, Yusenkov K V. Scandium-Based Hexagonal-Closed Packed Multi-Component Alloys. *Physics of Metals and Metallography*. 2018;119(8):735–40.
- [100] Riva S, Brown SGR, Lavery NP, Tudball A, Yusenkov K V. Spark plasma sintering of high entropy alloys. In: *Spark Plasma Sintering of Materials: Advances in Processing and Applications*. Springer International Publishing; 2019. p. 517–38.

- [101] Riva S, Tudball A, Mehraban S, Lavery NP, Brown SGR, Yusenko K V. A novel High-Entropy Alloy-based composite material. *J Alloys Compd.* 2018;730:544–51.
- [102] Yeh JW. Recent progress in high-entropy alloys. *Annales de Chimie: Science des Materiaux.* 2006;31(6):633–48.
- [103] Zhang Y, Zuo TT, Tang Z, Gao MC, Dahmen KA, Liaw PK, et al. Microstructures and properties of high-entropy alloys. Vol. 61, *Progress in Materials Science.* Elsevier Ltd; 2014. p. 1–93.
- [104] Tsai MH, Yeh JW. High-entropy alloys: A critical review. *Mater Res Lett.* 2014;2(3):107–23.
- [105] Pickering EJ, Jones NG. High-entropy alloys: a critical assessment of their founding principles and future prospects. *International Materials Reviews.* 2016 Apr 2;61(3):183–202.
- [106] Farrugia D, Brown S, Lavery NP, Pleydell-Pearce C, Davis C. Rapid Alloy Prototyping for a range of strip related advanced steel grades. *Procedia Manuf.* 2020;50:784–90.
- [107] Lavery NP, Mehraban S, Pleydell-Pearce C, Brown SGR, Jarvis DJ, Voice W, et al. Combinatorial development and high throughput materials characterisation of steels. *Ironmaking and Steelmaking.* 2015;42(10):727–33.
- [108] Yar MA, Norrish C, Cullen JCT, Zhang L, Brown S, Underhill R, et al. Small-Scale Rapid Alloy Prototyping of Extra-Low Carbon Steel to Investigate the Effects of Cu and Cr Residuals. In: *TMS 2022 151st Annual Meeting & Exhibition Supplemental Proceedings.* Cham: Springer International Publishing; 2022. p. 1202–13.
- [109] Zhang L, Harrison W, Abdullah T, Mehraban S, Lavery NP. Formability prediction of interstitial-free steel via miniaturized tensile specimen for Rapid Alloy Prototyping. *Appl Math Model.* 2023;124:713–33.
- [110] Zhang L, Harrison W, Yar MA, Mehraban S, Brown SGR, Lavery NP. Use of miniaturized tensile specimens to evaluate the ductility and formability of dual phased steels for Rapid Alloy Prototyping. *Materials Science and Engineering: A.* 2023;875.
- [111] Zhang L, Harrison W, Mehraban S, Brown SGR, Lavery NP. Size Effect on the Post-Necking Behaviour of Dual-Phase 800 Steel: Modelling and Experiment. *Materials.* 2023;16(4).
- [112] Zhang L, Harrison W, Yar MA, Brown SGR, Lavery NP. The development of miniature tensile specimens with non-standard aspect and slimmness ratios for rapid alloy prototyping processes. *Journal of Materials Research and Technology.* 2021;15:1830–43.

- [113] Zhang L, Harrison W, Yar MA, Brown SGR, Lavery NP. Influence of aspect ratio (AR) on the necking angle of tensile specimens for different alloys. In: 2nd International Workshop on Plasticity, Damage and Fracture of Engineering Materials. Ankara, Turkey; 2021.
- [114] Abdullah TS, Zhang L, Evans P, Ludwig G, Lavery NP. Scaling effects in miniaturised tensile testing on mechanical properties and plastic anisotropy r -values in Interstitial Free Steel. Available at SSRN 4399446. 2023;
- [115] Ritchie M, Shahin M, Brown S, Butcher D, Jonathan C, Calvo-Dahlborg M, et al. In-situ Modification of a High Entropy Alloy With 2.4% Molybdenum Using LPBF, and its Effect on Microstructure and Corrosion Resistance. In: Annual International Solid Freeform Fabrication Symposium. Austin, Texas, USA; 2022.
- [116] Calvo-Dahlborg M, Dahlborg U, Brown SGR, Juraszek J. Influence of the electronic polymorphism of Ni on the classification and design of high entropy alloys. *J Alloys Compd.* 2020 May 25;824:153895.
- [117] Calvo-Dahlborg M, Mehraban S, Lavery NPP, Brown SGRGR, Cornide J, Cullen J, et al. Prediction of phase, hardness and density of high entropy alloys based on their electronic structure and average radius. *J Alloys Compd.* 2021;865:158799.
- [118] Calvo-Dahlborg M, Dahlborg U, Cornide J, Mehraban S, Leong Z, Hansen TC, et al. Structural investigation of the stability in temperature of some high entropy/multi major components alloys as a function of their electronic structure. *J Alloys Compd.* 2020;837:155496.
- [119] Chou YL, Yeh JW, Shih HC. The effect of molybdenum on the corrosion behaviour of the high-entropy alloys $\text{Co}_{1.5}\text{CrFeNi}_{1.5}\text{Ti}_{0.5}\text{Mo}_x$ in aqueous environments. *Corros Sci.* 2010 Aug;52(8):2571–81.
- [120] Hsu W, Kao W, Yeh J, Tsai C. Effect of Mo on the Mechanical and Corrosion Behaviors in Non-Equal Molar AlCrFeMnNi BCC High-Entropy Alloys. *Materials.* 2022;15(3).
- [121] Parakh A, Vaidya M, Kumar N, Chetty R, Murty B. Effect of crystal structure and grain size on corrosion properties of AlCoCrFeNi high entropy alloy. *Journal of Alloys and Compounds.* 2021;863.
- [122] Lee CP, Chang CC, Chen YY, Yeh JW, Shih HC. Effect of the aluminium content of $\text{Al}_x\text{CrFe}_{1.5}\text{MnNi}_{0.5}$ high-entropy alloys on the corrosion behaviour in aqueous environments. *Corros Sci.* 2008 Jul;50(7):2053–60.
- [123] Shang XL, Wang ZJ, Wu QF, Wang JC, Li JJ, Yu JK. Effect of Mo Addition on Corrosion Behavior of High-Entropy Alloys CoCrFeNiMo_x in Aqueous Environments. *Acta Metallurgica Sinica (English Letters).* 2019 Jan 2;32(1):41–51.

- [124] Niu Z, Wang Y, Geng C, Xu J, Wang Y. Microstructural evolution, mechanical and corrosion behaviors of as-annealed CoCrFeNiMox ($x = 0, 0.2, 0.5, 0.8, 1$) high entropy alloys. *J Alloys Compd.* 2020 Apr 15;820.
- [125] Lu P, Saal JE, Olson GB, Li T, Swanson OJ, Frankel GS, et al. Computational materials design of a corrosion resistant high entropy alloy for harsh environments. *Scr Mater.* 2018 Aug 1;153:19–22.
- [126] Muangtong P, Rodchanarowan A, Chaysuwan D, Chanlek N, Goodall R. The corrosion behaviour of CoCrFeNi-x ($x = \text{Cu, Al, Sn}$) high entropy alloy systems in chloride solution. *Corros Sci.* 2020 Aug 1;172:108740.
- [127] Hsu YJ, Chiang WC, Wu JK. Corrosion behavior of FeCoNiCrCux high-entropy alloys in 3.5% sodium chloride solution. *Mater Chem Phys.* 2005 Jul 15;92(1):112–7.
- [128] Li QH, Yue TM, Guo ZN, Lin X. Microstructure and corrosion properties of alcocrfeni high entropy alloy coatings deposited on AISI 1045 steel by the electrospark process. *Metall Mater Trans A Phys Metall Mater Sci.* 2013 Apr 8;44(4):1767–78.
- [129] Lin CM, Tsai HL, Bor HY. Effect of aging treatment on microstructure and properties of high-entropy Cu_{0.5}CoCrFeNi alloy. *Intermetallics (Barking).* 2010 Jun 1;18(6):1244–50.
- [130] Chen YY, Hong UT, Shih HC, Yeh JW, Duval T. Electrochemical kinetics of the high entropy alloys in aqueous environments—a comparison with type 304 stainless steel. *Corros Sci.* 2005 Nov 1;47(11):2679–99.
- [131] Chen YY, Duval T, Hung UD, Yeh JW, Shih HC. Microstructure and electrochemical properties of high entropy alloys—a comparison with type-304 stainless steel. *Corros Sci.* 2005 Sep 1;47(9):2257–79.
- [132] Qiu Y, Gibson MA, Fraser HL, Birbilis N. Corrosion characteristics of high entropy alloys. *Materials Science and Technology (United Kingdom).* 2015 Jul 1;31(10):1235–43.
- [133] Peng Z, Li B, Luo Z, Chen X, Tang Y, Yang G, et al. A Lightweight AlCrTiV_{0.5}Cux High-Entropy Alloy with Excellent Corrosion Resistance. *Materials.* 2023 Apr 1;16(7).
- [134] Qiu Y, Thomas S, Gibson MA, Fraser HL, Pohl K, Birbilis N. Microstructure and corrosion properties of the low-density single-phase compositionally complex alloy AlTiVCr. *Corros Sci.* 2018 Apr 1;133:386–96.
- [135] Chen P, Li S, Zhou Y, Yan M, Attallah MM. Fabricating CoCrFeMnNi high entropy alloy via selective laser melting in-situ alloying. *J Mater Sci Technol.* 2020 Apr 15;43:40–3.

- [136] Zhang Z, Zhou Y, Zhou S, L Zhang. Mechanically blended Al: simple but effective approach to improving mechanical property and thermal stability of selective laser-melted Inconel 718. *Metallurgical and Materials Transactions A*, Springer. 2019 Aug 15;50(8):3922–36.
- [137] Farquhar L, Maddison G, Hardwick L, Livera F, Todd I, Goodall R. In-Situ Alloying of CoCrFeNiX High Entropy Alloys by Selective Laser Melting. *Metals* 2022, Vol 12, Page 456. 2022 Mar 8;12(3):456.
- [138] Zhang H, Zhao Y, Huang S, Zhu S, Wang F, Li D. Manufacturing and Analysis of High-Performance Refractory High-Entropy Alloy via Selective Laser Melting (SLM). *Materials* 2019, Vol 12, Page 720. 2019 Mar 1;12(5):720.
- [139] Melia MA, Whetten SR, Puckett R, Jones M, Heiden MJ, Argibay N, et al. High-throughput additive manufacturing and characterization of refractory high entropy alloys. *Appl Mater Today*. 2020 Jun 1;19:100560.
- [140] Polozov I, Sufiiarov V, Popovich A, Masaylo D, Grigoriev A. Synthesis of Ti-5Al, Ti-6Al-7Nb, and Ti-22Al-25Nb alloys from elemental powders using powder-bed fusion additive manufacturing. *J Alloys Compd*. 2018 Sep 30;763:436–45.
- [141] Cagirici M, Wang P, Ng FL, Nai MLS, Ding J, Wei J. Additive manufacturing of high-entropy alloys by thermophysical calculations and in situ alloying. *J Mater Sci Technol*. 2021 Dec 20;94:53–66.
- [142] Wu Y, Liaw PK, Zhang Y. Preparation of bulk tizrnbmov and nbtialtav high-entropy alloys by powder sintering. *Metals (Basel)*. 2021 Nov 1;11(11):1748.
- [143] Shaw BA, Kelly RG. What is corrosion? Vol. 15, *Electrochemical Society Interface*. 2006.
- [144] Sullivan J. *Degradation of Materials*. Swansea; 2019.
- [145] Fontana MG. *Corrosion engineering*. Third edition. 1986;
- [146] Lewis T. *An Investigation into the Corrosion Behaviour and Effect of Inhibitor Additions on Commercial Zn-Mg-Al Alloys*. Swansea University; 2018.
- [147] Shukla P. Thermodynamics of corrosion and potentiometric methods for measuring localized corrosion. In: *Techniques for Corrosion Monitoring*. 2008.
- [148] Marcus P, Protopopoff É, Maurice V. Surface chemistry and passivation of metals and alloys. In: *Mechanics - Microstructure - Corrosion Coupling: Concepts, Experiments, Modeling and Cases*. 2019.
- [149] Nishikata A, Ichihara Y, Tsuru T. An application of electrochemical impedance spectroscopy to atmospheric corrosion study. *Corros Sci*. 1995;37(6).

- [150] Tomashov ND, Mikhailovskii YN, Leonov V V. Mechanism of Electrochemical Corrosion Of Metals Under Insulating Coatings. II. Kinetics of Cathodic Processes On Insulated Metals in Electrolytes. *Corrosion*. 1964;20(7).
- [151] Yildiz R, Dehri I. Investigation of the cut-edge corrosion of organically-coated galvanized steel after accelerated atmospheric corrosion test. *Arabian Journal of Chemistry*. 2015;8(6).
- [152] Zhang X, Leygraf C, Odnevall Wallinder I. Atmospheric corrosion of Galvan coatings on steel in chloride-rich environments. *Corros Sci*. 2013;73.
- [153] Wu H. Highly Accelerated UV Weathering: When and How to Use it. In: *Service Life Prediction of Polymers and Plastics Exposed to Outdoor Weathering*. 2017.
- [154] Frankel GS. Pitting Corrosion of Metals: A Review of the Critical Factors. *J Electrochem Soc*. 1998 Jun 1;145(6):2186–98.
- [155] Horvath J, Uhlig HH. Critical Potentials for Pitting Corrosion of Ni, Cr-Ni, Cr-Fe, and Related Stainless Steels. *J Electrochem Soc*. 1968;115(8):791.
- [156] Howard RL, Lyon SB, Scantlebury JD. Accelerated tests for prediction of cut edge corrosion of coil-coated architectural cladding. Part II: Cyclic immersion. *Prog Org Coat*. 1999;37(1).
- [157] Howard RL, Lyon SB, Scantlebury JD. Accelerated tests for the prediction of cut-edge corrosion of coil-coated architectural cladding. Part I: Cyclic cabinet salt spray. *Prog Org Coat*. 1999;37(1).
- [158] Perez N. *Electrochemistry and Corrosion Science*. Electrochemistry and Corrosion Science. 2004.
- [159] Trethewey KR, Chamberlain J. *Corrosion for students of science and engineering*. Longman Scientific & Technical; 1988.
- [160] Bagotsky VS. *Fundamentals of Electrochemistry: Second Ed*. Fundamentals of Electrochemistry: Second Ed. 2005.
- [161] Sun Q, Chen K, Fang H, Xu J, Dong P, Hu G, et al. Effect of grain refinement on electrochemical behavior of Al-Zn-Mg-Cu alloys. *Int J Electrochem Sci*. 2016;11(7).
- [162] Silverman DC. *Practical Corrosion Prediction Using Electrochemical Techniques*. In: *Uhlig's Corrosion Handbook: Third Edition*. 2011.
- [163] Sun Q, Chen K. Potential difference of cyclic polarization curve of an aircraft alloy: Δe ($e_{sec,corr} - e_{corr}$). *Journal of Electrochemical Science and Technology*. 2020;11(2).

- [164] Worsley DA, McMurray HN, Sullivan JH, Williams IP. Quantitative assessment of localized corrosion occurring on galvanized steel samples using the scanning vibrating electrode technique. *Corrosion*. 2004;60(5).
- [165] Bastos AC, Quevedo MC, Karavai O V., Ferreira MGS. Review—On the Application of the Scanning Vibrating Electrode Technique (SVET) to Corrosion Research. *J Electrochem Soc*. 2017;164(14).
- [166] Williams G, Neil McMurray H. Localized Corrosion of Magnesium in Chloride-Containing Electrolyte Studied by a Scanning Vibrating Electrode Technique. *J Electrochem Soc*. 2008;155(7).
- [167] L. Collins J, van Knippenberg B, Ding K, V. Kofman A. Time-Lapse Microscopy. In: *Cell Culture*. IntechOpen; 2019.
- [168] Sullivan J, Cooze N, Gallagher C, Lewis T, Prosek T, Thierry D. In situ monitoring of corrosion mechanisms and phosphate inhibitor surface deposition during corrosion of zinc-magnesium-aluminium (ZMA) alloys using novel time-lapse microscopy. *Faraday Discuss*. 2015;180:361–79.
- [169] Mehraban S, Sullivan JH, Elvins J. In Situ Monitoring of Phosphate Inhibitor Surface Deposition during Corrosion of a Zinc Magnesium Aluminium (ZMA) Alloy Using Time-Lapse Microscopy and Energy Dispersive X-ray Spectroscopy. *ECS Trans*. 2013 May 1;50(31):377–90.
- [170] Turnbull A, Ryan M, Willetts A, Zhou S. Corrosion and electrochemical behaviour of 316L stainless steel in acetic acid solutions. *Corros Sci*. 2003;45(5):1051–72.
- [171] Ghafouri SN, Faulkner RG, Chung TE. Microstructural developments in type 316L stainless steel during low-cycle fatigue at 350–550°C and their effects on cyclic strength and life. *Materials Science and Technology (United Kingdom)*. 1986 Jan 1;2(12):1223–32.
- [172] Ravi Kumar B. Influence of crystallographic textures on tensile properties of 316L austenitic stainless steel. *J Mater Sci*. 2010 May;45(10):2598–605.
- [173] Tamiri T, Zitrin S. Explosives: Analysis. *Encyclopedia of Forensic Sciences: Second Edition*. 2013 Jan 1;64–84.
- [174] Gumustas M, Sengel-Turk CT, Gumustas A, Ozkan SA, Uslu B. Effect of Polymer-Based Nanoparticles on the Assay of Antimicrobial Drug Delivery Systems. *Multifunctional Systems for Combined Delivery, Biosensing and Diagnostics*. 2017 Jan 1;67–108.
- [175] Wang P, Tan X, He C, Nai M, Huang R, Tor S, et al. Scanning optical microscopy for porosity quantification of additively manufactured components. *Addit Manuf*. 2018;21:350–8.

- [176] Wilson-Heid AE, Novak TC, Beese AM. Characterization of the Effects of Internal Pores on Tensile Properties of Additively Manufactured Austenitic Stainless Steel 316L. *Exp Mech*. 2019 Jul 15;59(6):793–804.
- [177] Buhairi MA, Foudzi FM, Jamhari FI, Sulong AB, Radzuan NAM, Muhamad N, et al. Review on volumetric energy density: influence on morphology and mechanical properties of Ti6Al4V manufactured via laser powder bed fusion. *Progress in Additive Manufacturing*. 2023 Apr 1;8(2):265–83.
- [178] Smoqi Z, Gaikwad A, Bevans B, Kobir MH, Craig J, Abul-Haj A, et al. Monitoring and prediction of porosity in laser powder bed fusion using physics-informed melt pool signatures and machine learning. *J Mater Process Technol*. 2022 Jun 1;304:117550.
- [179] Foster BK, Reutzel EW, Nassar AR, Hall BT, Brown SW, Dickman CJ. Optical, layerwise monitoring of powder bed fusion. In: *International Solid Freeform Fabrication Symposium*. 2015.
- [180] Vukkum VB, Gupta RK. Review on corrosion performance of laser powder-bed fusion printed 316L stainless steel: Effect of processing parameters, manufacturing defects, post-processing, feedstock, and microstructure. *Mater Des*. 2022 Sep 1;221:110874.
- [181] Sullivan J, Cooze N, Gallagher C, Lewis T, Prosek T, Thierry D. In situ monitoring of corrosion mechanisms and phosphate inhibitor surface deposition during corrosion of zinc-magnesium-aluminium (ZMA) alloys using novel time-lapse microscopy. *Faraday Discuss*. 2015;180:361–79.
- [182] Filimonov AM, Rogozin OA, Firsov DG, Kuzminova YO, Sergeev SN, Zhilyaev AP, et al. Hardening of additive manufactured 316L stainless steel by using bimodal powder containing nanoscale fraction. *Materials*. 2020 Jan 1;14(1):1–14.
- [183] Mataya MC, Nilsson ER, Brown EL, Krauss G. Hot Working and Recrystallization of As-Cast 316L. *Metallurgical and Materials Transactions A*. 2003;34:1683–703.
- [184] Apolinario R, Daianezi I, Borges S, de Sousa L, Pinto H, Mariano N. Effect of rapid solidification processing on the microstructure and corrosion of 316L austenitic stainless steel. *Materials Research*. 2022;25.
- [185] Padilha A, Tavares C, Martorano M. Delta ferrite formation in austenitic stainless steel castings. *Materials Science Forum*. 2013;730:733–8.
- [186] Martorano MA, Tavares CF, Padilha AF. Predicting delta ferrite content in stainless steel castings. *ISIJ International*. 2012;52(6):1054–65.
- [187] Li Y, Zou D, Li M, Tong L, Zhang Y, Zhang W. Effect of Cooling Rate on δ -Ferrite Formation and Sigma Precipitation Behavior of 254SMO Super-Austenitic Stainless Steel During Solidification. *Metallurgical and Materials Transactions B*:

Process Metallurgy and Materials Processing Science. 2023 Dec 1;54(6):3497–507.

- [188] Di Schino A, Barteri M, Kenny JM. Effects of grain size on the properties of a low nickel austenitic stainless steel. *J Mater Sci*. 2003 Dec 1;38(23):4725–33.
- [189] Di Schino A, Salvatori I, Kenny JM. Effects of martensite formation and austenite reversion on grain refining of AISI 304 stainless steel. *J Mater Sci*. 2002 Nov 1;37(21):4561–5.
- [190] Stewart J, Williams D. The initiation of pitting corrosion on austenitic stainless steel: on the role and importance of sulphide inclusions. *Corros Sci*. 1992;33(3):457–74.
- [191] Ryan M, Williams DE, Chater R, Hutton B, McPhail D. Why stainless steel corrodes. *Nature*. 2002;
- [192] Ke R, Alkire R. Initiation of corrosion pits at inclusions on 304 stainless steel. *J Electrochem Soc*. 1995;142:4056.
- [193] Ke R, Alkire R. Surface Analysis of Corrosion Pits Initiated at MnS Inclusions in 304 Stainless Steel. *J Electrochem Soc*. 1992 Jun 1;139(6):1573–80.
- [194] Panda P, Mantry S, Mohapatra S, Singh SK, Satapathy A. A study on erosive wear analysis of glass fiber-epoxy-AlN hybrid composites. *J Compos Mater*. 2014 Jan;48(1):107–18.
- [195] Mi L, Chen Y, Zheng Z, Hou H, Chen W, Cui S. Beneficial metal ion insertion into dandelion-like MnS with enhanced catalytic performance and genetic morphology. *RSC Adv*. 2014;
- [196] Xiong K, Huang L, Wang X, Yu L, Feng W. Cooling-Rate Effect on Microstructure and Mechanical Properties of Al_{0.5}CoCrFeNi High-Entropy Alloy. *Metals* 2022, Vol 12, Page 1254. 2022 Jul 26;12(8):1254.
- [197] Ma L, Li C, Jiang Y, Zhou J, Wang L, Wang F, et al. Cooling rate-dependent microstructure and mechanical properties of Al_xSi_{0.2}CrFeCoNiCu_{1-x} high entropy alloys. *J Alloys Compd*. 2017 Feb 15;694:61–7.
- [198] Molnár D, Vida Á, Huang S, Chinh NQ. The effect of cooling rate on the microstructure and mechanical properties of NiCoFeCrGa high-entropy alloy. *J Mater Sci*. 2019 Mar 1;54(6):5074–82.
- [199] Cui P, Bao Z, Liu Y, Zhou F, Lai Z, Zhou Y, et al. Corrosion behavior and mechanism of dual phase Fe_{1.125}Ni_{1.06}CrAl high entropy alloy. *Corros Sci*. 2022 Jun 1;201:110276.
- [200] Köhler ML, Kunz J, Herzog S, Kaletsch A, Broeckmann C. Microstructure analysis of novel LPBF-processed duplex stainless steels correlated to their mechanical

and corrosion properties. *Materials Science and Engineering: A*. 2021 Jan 13;801:140432.

- [201] Gunn R. *Duplex stainless steels: microstructure, properties and applications*. 1997.
- [202] Groarke R, Danilenkoff C, Karam S, McCarthy E, Michel B, Mussatto A, et al. 316L Stainless Steel Powders for Additive Manufacturing: Relationships of Powder Rheology, Size, Size Distribution to Part Properties. *Materials* 2020, Vol 13, Page 5537. 2020 Dec 4;13(23):5537.
- [203] Kim D, Kim K, Park J, Chung W, Shin BH. Microstructure and corrosion performance of high-entropy alloy and austenite and super duplex stainless steels in 3.5% NaCl solution. *Int J Electrochem Sci*. 2023 Apr 1;18(4):100074.